# UNIVERSITA' DEGLI STUDI DI VERONA

DEPARTMENT OF

Biotechnology

GRADUATE SCHOOL OF

Science Engineering Medicine

DOCTORAL PROGRAM IN

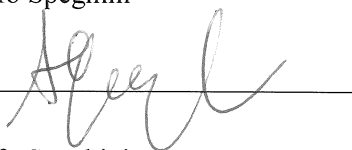Nanotechnologies and Nanomaterials for Biomedical Application

*XXVIII Cycle*

## Nanocrystalline Materials for Photovoltaic and Nanomedicine Applications
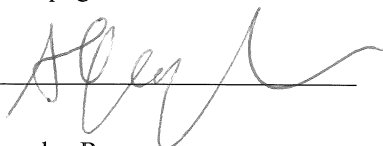
S.S.D. CHIM03-FIS07

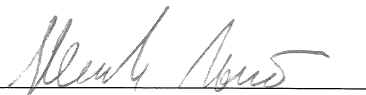Coordinator: Prof.   Adolfo Speghini

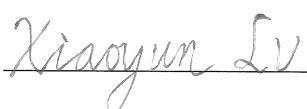Signature _____

Tutor:        Prof.   Adolfo Speghini

Signature _____

Tutor:        Prof.   Alessandro Romeo

Signature _____

Doctoral Student:      Xiaoyun Lv

Signature _____

# Contents

# Abstract

The aim of this thesis is to investigate the property of some typical photovoltaic and luminescent materials, and the possible application of these materials in the fields of solar energy, light emitting diode and biomedical imaging.

Earth abundant and nontoxic material quaternary semiconductor copper zinc tin sulfide (CZTS) provides a photovoltaic capability with favorable optical and electronic properties. Crystalized into either kesterite or wurtzite phases in aqueous or organic solution, CZTS represents potential application in the field of solar cell.

Low cost and easy producing material methylammonium lead halide perovskite $CH_3NH_3PbX_3$ (X=I, Br and Cl) possess superior optoelectronic properties, it represents a great potential for a variety of applications, such as high-efficiency photovoltaic cells and light-emitting diodes, but the involvement of toxic element and the instability is a concerning issue. Some efforts are in progress in the recent years to replace it with nontoxic and stable varieties such as cesium tin halide ($CsSnX_3$, X=Cl, Br, I) and the derivative $Cs_2SnX_6$ (X=Cl, Br, I).

Ternary I–III–VI semiconductor $CuInS_2$ possesses unique properties such as large Stokes shift and high absorption coefficient. By doping with lanthanide ion $Gd^{3+}$, the dual-modal MRI contrast agent with good relaxivity and fluorescent probe-CuInS2@ZnS:$Gd^{3+}$ quantum dots have been investigated.

Synthesized in a very simple way, the copper thiolate compounds exhibit bright emission in the optical region of green, yellow to white. The life time of copper thiolate is in the range of micrometers. These compounds possess interesting mechanochromic and thermochromism luminescent properties.

The $\alpha$-NaYbF$_4$, $\beta$-NaGdF$_4$, $\beta$-NaGdF$_4$:(Yb,Tm), orthorhombic KYb$_2$F$_7$, $\alpha$-KGdF$_4$, $\alpha$-KGdF$_4$:(Yb,Tm), MGdF$_4$:Ce@MGdF$_4$:Eu/Tb, MGdF$_4$:(Yb,Tm)@MGdF$_4$:Eu/Tb, and MGdF$_4$:Yb,Tm@MGdF$_4$:Eu/Tb@MGdF$_4$:Ce (M: Na or K) NPs have been synthesized hydrothermally. Under 365-400 nm UV excitation, the $Eu^{3+}$/$Tb^{3+}$ doped NaYbF$_4$, NaGdF$_4$ and KGdF$_4$ samples emit red or green light. Not only by longer UV excitation, MGdF$_4$:Ce@MGdF$_4$:$Eu^{3+}$/$Tb^{3+}$ NPs and MGdF$_4$:Yb,Tm@MGdF$_4$:$Eu^{3+}$/$Tb^{3+}$@MGdF$_4$:Ce NPs can also emit red or green light under short UV excitation 254 nm by a $Ce^{3+} \rightarrow Gd^{3+} \rightarrow Eu^{3+}$/$Tb^{3+}$ energy transfer process. Under 980 nm NIR laser excitation, these potassium and sodium based core shell and core-shell-shell NPs emit red or green light by an energy transfer process of $Yb^{3+} \rightarrow Tm^{3+} \rightarrow Gd^{3+} \rightarrow Eu^{3+}$/$Tb^{3+}$. The potassium based NPs exhibit brighter UCPL than sodium based NPs.

# List of abbreviations

| | |
|---|---|
| ACF | Autocorrelation function |
| ACQ | Aggregation caused quenching |
| AFM | Atomic force microscopy |
| AIE | Aggregation induced emission |
| BCP | 2,9-dimethyl-4,7-diphenyl-1,10-phenanthroline |
| BSA | Bovine serum albumin |
| CB | Chlorobenzene |
| CBD | Chemical bath deposition |
| CCD | Charge coupled device |
| CdTe | Cadmium telluride |
| CEs | Counter electrodes |
| CIE | International Commission on Illumination |
| CIGS | Copper indium gallium sulfide/selenide |
| CIS | Copper indium sulfide ($CuInS_2$) |
| CQ | Concentration quenching |
| CZTS | Copper zinc tin sulfide/selenide |
| DAP | Donor acceptor pair |
| DCPL | Down converting photo luminescence |
| DDT | 1-dodecanethiol |
| DLS | Dynamic light scattering |
| DMF | N,N-dimethylformamide |
| DMSO | Dimethyl sulfoxide |
| DSSC | Dye-sensitized solar cells |
| EC | Ethyl cellulose |
| EDS (EDX) | Energy-dispersive X-ray spectroscopy |
| EPA | Environmental Protection Agency |
| EQE | External quantum efficiency |
| ETL | Electron transport layer |
| EVA | Ethylene-vinyl acetate |
| FAI | Formamidinium iodide |
| FETs | Field-effect transistors |
| FF | Fill factor |
| FIR | Fluorescence Intensity Ratio |
| FTIR | Fourier-transform infrared spectroscopy |
| FTO | Fluorine tin oxide |
| FWHM | Full width at half-maximum |
| GBL | γ-butyrolactone |
| GOF | goodness of fit |
| HAC | Acetic acid |
| H&E stain | Haematoxylin and eosin stain |
| HOMO | Highest occupied molecular orbital |

| | |
|---|---|
| HTL | Hole transport layer |
| HTM | Hole transport materials |
| ICP-MS | Inductively coupled plasma mass spectrometry |
| IQE | Internal quantum efficiency |
| IR | Infra-red |
| ITO | Indium tin oxide |
| Jsc | Short circuit current density |
| LED | Light emitting diode |
| LMCT | Ligand-to-metal charge transfer |
| LMMCT | Ligand-to-metal-metal charge transfer |
| LUMO | Lowest unoccupied molecular orbital |
| MAI | Methylammonium iodide ($CH_3NH_3I$) |
| MRI | Magnetic resonance imaging |
| NCs | Nanoclusters |
| NIR | Near-infrared |
| NPs | Nanoparticles |
| ODE | 1-octadecene |
| OLA | Oleylamine |
| P3HT | Poly 3-hexylthiophene |
| PBS | Phosphate buffer saline |
| PCBM | [6,6]-phenyl-C61-butyric acid methyl ester |
| PCE | Power conversion efficiency |
| PDMS | Polydimethylsiloxane |
| PEDOT:PSS | Poly (3,4-ethylenedioxythiophene):poly (styrenesulfonate) |
| PEG | Poly (ethylene glycol) |
| PET | Positron emission tomography |
| PL | Photoluminescence |
| PMT | Photomultiplier tube |
| PSCs | Perovskite solar cells |
| PTAA | poly(triarlyamin)/poly[bis(4-phenyl)(2,4,6-trimethyl phenyl)amine |
| QY | Quantum yield |
| RES | Reticuloendothelial system |
| SEM | Scanning electron microscope |
| SILAR | Successive ionic adsorption and reaction |
| SNR | Signal to noise ratio |
| spiro-OMeTAD | 2,2',7,7'-tetrakis(N,N-di-p-methoxy-phenylamine)-9,9'-spirobifluorene |
| SPM | Scanning probe microscopy |
| TCO | Transparent conductive oxides |
| TEM | Transmission electron microscopy |
| TFSC | Thin film solar cells |
| TO | Toluene |
| TR | Repetition time |
| TTIP | Titanium (IV) isopropoxide |
| UC(NPs) | up converting (nanoparticles) |

| UCPL | up converting photoluminescence |
| UV | Ultra-violet |
| Voc | Open circuit voltage |
| XRD | X-ray powder diffraction |

# Chapter 1 Introduction

In order to maintain life, to study and work, humans need to consume energy. And we need a lot of energy to produce food and goods, to transport people, food and goods to other places, to warm up our water and house, and so on. As we know, energy is never produced but converted from one form to another form. We usually use energy by converting it to a more useable form from another form by our technologies. For example, automobile use fossil fuels like oil and natural gas to convert chemical energy to mechanical energy. As the world population and economy growing, the demands of energy are increasing throughout the world, but fossil fuels have limited storage on the earth and they are depleted much faster than produced. And furthermore, the burning of fossil fuels produces greenhouse gases like carbon dioxide to cause climate problem of global warming. The wood, coal, oil and gas are secondary form of solar energy which has been stored in the earth through millions of years and the sun is the only energy source we have for all the process on this planet. As a renewable energy source, nowadays the development of photovoltaic technology can directly convert the solar energy into electricity and we are entering a new era of which we utilize the solar energy to satisfy our energy demands. Since the discovery of photovoltaic effect in 1839 [1], up to now, many kinds of solar cell models have been developed with quite good efficiency achieved. Yet the desire to have a solar cell with nontoxic, stable and low-cost materials remains challenging. The aim of this research is to investigate some nontoxic, earth abandon photovoltaic materials. Because of the property of semiconductor material itself, some light absorbing photovoltaic materials fluoresce as well. So, except for the photovoltaic investigation, light emitting effect and the relevant materials, and the possible applications in lighting and biological imaging has been investigated in this work as well.

## 1.1 Semiconductor and band gap

A semiconductor is a material with electrical conductivity between that of a conductor and that of an insulator. It is the foundation of modern electronics, including transistors, digital integrated circuits, solar cells, light emitting diodes (LEDs) and quantum dots. Many elements and compounds display semiconductor properties, in which they pass current more easily in one direction than the other by controlled addition of impurities (doping) or by the application of electrical fields or light. A pure semiconductor is a poor electric conductor with electrons completely in its valence bonds. Current conduction in a semiconductor is fulfilled through the movement of "charge carriers" (free electrons and "holes"). Doping can greatly increase the number of charge carriers within semiconductor material. When a doped semiconductor contains excess of free electrons it becomes an n-type semiconductor; when it is modified to have deficiency of electrons it is called a p-type semiconductor. In both cases, the semiconductor becomes much more conductive [2].

Semiconductors are sensitive to light or heat such that under light irradiation or heating, electrons can be excited across the energy band gap of a semiconductor and consequently leave a hole in valence band. This process is known as exciton (electron hole pair) generation. In some semiconductor materials, such as $CuS$, $CuInS_2$, $ZnS$, $CdS$ and $CdTe$, these excited electrons can pass micrometers' distance before dissipating their energy into heat. This property is essential to the operation of solar cells that collect the movement of electrons in one direction and thus produce photovoltaic electric powder. While in certain other semiconductors, electron hole pairs are apt to recombine, the excited electrons can relax by emitting radiation light (in the form of photons) or thermal energy (in the form of phonons) instead of moving and generating electric current. These semiconductors, which we call fluorescent or phosphorescent materials, such as quantum dots, metal clusters or complex, up converting nanoparticles, are extensively used in lighting (include light emitting diodes), biological and medical imaging, signage, and other fields [2,3].

Semiconductors have unique electric conductive behavior between metal and insulator. Electrical conductivity arises since the presence of electrons in delocalized states that is partially filled when its energy is near to the Fermi level. Metals are good electrical conductors and have many delocalized and partially filled states with energies near their Fermi level. Oppositely, Insulators have few partially filled states and their Fermi levels locate within band gaps. The band gap refers to the energy difference between the top of the valence band and the bottom of the conduction band in the graph of the electronic band structure. It is the energy needed to promote a valence electron to become a conduction electron that can move freely within the crystal lattice to conduct electric current. In chemistry, we also call this energy difference the highest occupied molecular orbital (HOMO) and the lowest unoccupied molecular orbital (LUMO) gap. The HOMO level in organic semiconductors is equivalent to the valence band maximum in inorganic semiconductors, and the same between the LUMO level and the conduction band minimum [4]. Therefore, the band gap is the main factor that determines the electric conductivity of a material. Insulators have large band gap and the band gap of a semiconductor is smaller than that of an insulator, while conductors have very small band gaps or no gaps at all, since the valence and conduction bands overlap [5,6], see figure 1.1.
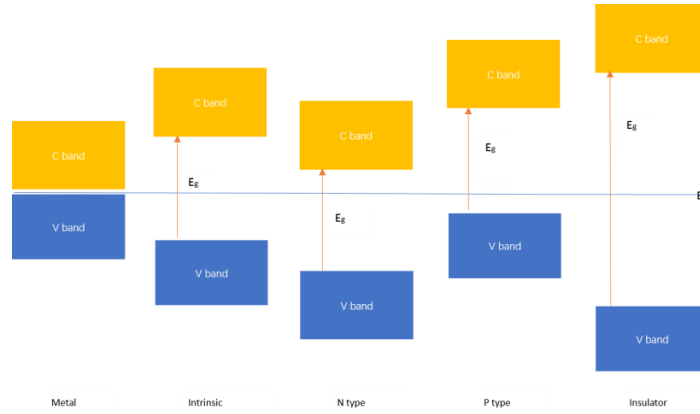
Figure 1.1 Electronic band structures in various types of materials at equilibrium (Eg: band gap). The Fermi level $E_F$ lie inside at least one band in metals and is inside a band gap in semiconductors and insulators. It shifts the position in n and p type semiconductors.

The band gap of a bulk semiconductor is temperature dependent; it tends to decrease as the temperature is increased. Generally, the band gap can be calculated by: [7]

$$E_g(T) = E_g(0) - \frac{\alpha T^2}{T+\beta}$$
(1.1)

where $E_g(0)$, α and β are material constants.

The band gap of a semiconductor is classified into direct band gap and indirect band gap. If the momentum of electrons and holes is the same in both the conduction band and the valence band, it is called a "direct gap" in which the electron-hole pairs (excitons) can be created by a photon and an electron can directly emit a photon when the excitons recombine, otherwise it is called an "indirect gap", in which the electron cannot emit a photon since it must pass through an intermediate state and transfer momentum to the crystal lattice. InAs, GaAs, CdTe, CIS and CZTS are direct band gap semiconductors while Si, Ge, and AlSb are indirect band gap semiconductor materials [8].

## 1.2 P-N junction

The conductivity of semiconductor can be increased by doping with impurities which can move either the conduction or valence band closer to the Fermi level, and thus greatly increase the number of partially filled states. By doping to the intrinsic (pure) semiconductors, the electrical conductivity of the obtained extrinsic semiconductors may be increased by factors of thousands or millions. Semiconductors doped with extra valence electron donor impurities to the conduction band are called n-type semiconductor, while those doped with electron acceptor impurities are known as p-type semiconductor. Excess electrons increase the electron carrier concentration ($n_0$) in n-type semiconductor and excess holes increase the hole carrier concentration ($p_0$) in p-type semiconductor.

Semiconductors are defined by the column of the periodic table in which the intrinsic semiconductors and dopant atoms positioned. For example, Group IV semiconductors (Si) have four valence electrons; they use group V (N) atoms as donors and group III (B) atoms as acceptors. Group III-V (GaN) semiconductors are compound semiconductors; they use group VI atoms (Se) as donors and group II (Zn) atoms as acceptors. They can also use group IV atoms (Si) as either donors or acceptors. Group IV atoms act as donors when they replace the group III atoms and act as acceptors when they replace the group V element in the semiconductor lattice.

When the n-type and p-type semiconductors contact each other, a p–n junction is formed in the joint interface between two types of semiconductor materials. Usually the p-n junctions are created in a single semiconductor crystal by doping each side with different dopants. p–n junctions are basically the building blocks of most electronic devices such as diodes, transistors, integrated circuits, solar cells, LEDs, and so on. The junction between relatively conductive n and p semiconductors become depleted of charge carriers and thus non-conductive. By applying forward bias or reverse bias through this non-conductive layer (depletion layer), p–n junctions can be used to conduct electric current in one direction, where the term bias refers to the application of electric voltage on the p–n direction.

The p-n junction can be classified into homojunction and heterojunction. Homojunction such as silicon diode is an interface between layers of similar semiconductors with equal band gaps but different doping. Heterojunction is the interface that occurs between two layers of different semiconductors with unequal band gaps. The different doping level and unequal band gaps will cause band bending [2].

When there is no external applied voltage, an equilibrium condition is reached in p-n junction and a potential difference (i.e., built-in potential) is formed across the junction. Specifically, electrons from the n region near the p–n interface tend to diffuse into the p region and thus leave positively charged ions (donors) in the n region. Likewise, holes from the p-type region near the p–n interface tend to diffuse into the n-type region, leaving fixed negative charged ions (acceptors) in p-type region. The regions nearby the p–n interfaces become charged and form the space charge region or depletion layer. The electric field and voltage difference (built-in voltage) created by the depletion layer opposes the diffusion process of both electrons and holes. There are two concurrent processes at equilibrium: the diffusion process that tends to generate more space charge region, and the counteract process of diffusion by the electric field created in the space charge region. The built-in potential in equilibrium can be expressed by: [9]

$$\varphi_0 = \frac{kT}{e} l_n \left( \frac{N_A N_D}{n_i^2} \right) \tag{1.2}$$

where $N_A$ and $N_D$ denote the density of acceptor and donor atoms; $n_i$ is the intrinsic carrier concentration. K is Boltzmann's constant (k = 1.38 * $10^{-23}$ J/K) and kT is the thermal energy (0.0258 eV at 300K).

When applied by forward bias, i.e., the p-type is connected to the positive terminal and the

n-type is connected to the negative terminal, the holes in the p-type region and the electrons in the n-type region are pushed toward the junction, which reduces the width of the depletion zone. This process makes the depletion zone thin, lowers the barrier potential (built-in voltage) and reducing electrical resistance. As a result, the p-n junctions become conductive. The electrons pushed by forward bias from n-type region toward p side do not flow too long distance since it is energetically favorable for them to recombine with holes. The average distance before the electrons recombine with holes (i.e., diffusion length) is usually on the order of micrometers [10,11]. The overall effect of electron and hole flowing and recombining is the current flow through the diode in a desired direction. The external net current density can be expressed by Shockley equation:

$$J(V_a) = J_{rec}(V_a) - J_{gen}(V_a) = J_0 \left( e^{\frac{eV_a}{kT}} - 1 \right) \tag{1.3}$$

where $V_a$ is external voltage; $J_0$ is the saturation current density; $J_{rec}$ is the recombination current of minority carriers and $J_{gen}$ is the thermal generation current of drifting minority carriers.

When applied by reverse bias, both the electrons and holes are pulled away from the junction and the depletion region widens. This process increases the voltage barrier and resistance to the flow of charge carriers and thus makes the junction an insulator. When the strength of the electric field in depletion zone increase along with the increasing reverse bias voltage and exceed a threshold, the p–n junction depletion zone breaks down by the Zener or avalanche processes and current begins to flow. The breakdown processes are reversible if the current intensity does not reach levels of overheating and following thermal damage. The net current density is given by:

$$J(V_a) = -J_0 \tag{1.4}$$

The current density and voltage (J-V) characteristic of an ideal p-n junction under forward and reverse bias is schematically shown in Figure 1.2.
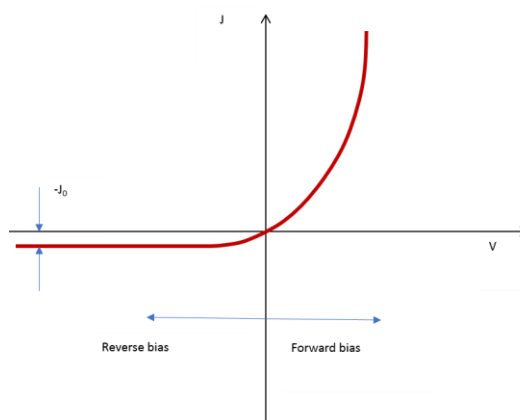


Figure 1.2 J-V Characteristic of P-N junction.

# 1.3 Principles of solar cells

A solar cell is an electrical device that converts the energy of light into electricity by the photovoltaic effect. The thin film solar cells (TFSC) are made of multiple layers with different functions on glass or flexible substrates. It is the building blocks of photovoltaic modules (solar panels). Since the first demonstration of photovoltaic effect in 1839 by French physicist Edmond Becquerel [1], after 178 years development, the solar cell technology has made significant progress and varieties of materials find application in solar cells. From monocrystalline silicon to polycrystalline silicon, to amorphous silicon thin film, GaAs thin film, CdTe thin film, CIGS and CZTS thin film, to perovskite thin film, the manufacturing cost keep declining and efficiency keep increasing. A new record efficiency of 26.3% was achieved by Japanese researchers for thin crystalline silicon cells with the heterojunction back contact and 26.6% was claimed to managed [12]. The conversion efficiency for Cu (In, Ga) (S, Se)$_2$ (CIGS) is increased to 22.8% with a Cd free (Zn, Mg)O buffer layer [13]. The record efficiency for superstrate CdTe solar cell device is up to 22.1% [14] and 13.6% for substrate CdTe cells [15]. The dye-sensitized solar cells (DSSC) have achieved 13% efficiency by the molecular engineering of porphyrin sensitizers [16]. The research in perovskite solar cells improving dramatically and the efficiency boost to the value of 21% recently [17].

In this thesis study, the non-toxic and low cost photovoltaic material $Cu_2ZnSnS_2$ (CZTS) was synthesized and characterized. Metal halide perovskite $CH_3NH_3PbCl_3$ solar cell device was fabricated and the non-toxic derivative $Cs_2SnI_6$ was synthesized.

## 1.3.1 Sun light

The Sun is the central star of solar system which contributes 99.68% of the total mass of the solar system. It consists mainly of hydrogen and helium that keep on the nuclear fusion reaction in which four protons react into a helium core, two positrons, two neutrinos, and the electromagnetic radiations $E = mc^2$. Solar radiation closely matches a black body radiation at about 5,800 K [18]. The solar radiation is attenuated by scattering and absorption when it passes through the atmosphere of the Earth, according to the distance it travels through. The distance is the shortest when the Sun is at the zenith, i.e., directly overhead. The ratio of an actual path length to this minimal distance is called the optical air mass. The spectrum is defined the air mass 1 (AM1) spectrum when the Sun is at zenith and AM0 spectrum outside the atmosphere of the Earth. When the Sun is at an angle θ to the zenith, the air mass is given as:

$$AM = \frac{1}{cos\theta} \tag{1.5}$$

For example, when the Sun is 60° from the zenith (i.e., 30° above the horizon), the AM is 2.
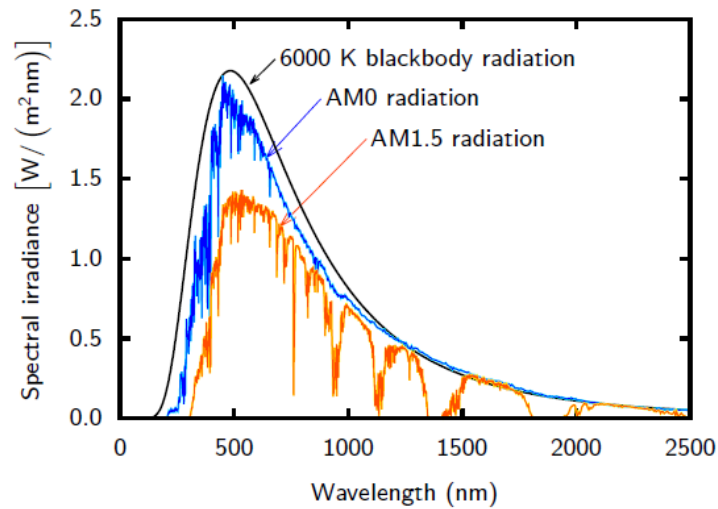
Figure 1.3 Comparison of solar spectrum (the extraterrestrial AM0 spectrum and the AM1.5 spectrum) and the blackbody spectrum at 6000 K [9].

There are many different solar cell technologies and photovoltaic modules investigated, produced and sold, therefore, it is important to define a reference solar spectrum that allows for the comparison of different solar cells and photovoltaic modules. The industrial standard is the AM1.5 spectrum (48.2°) and the irradiance of 1000 W/m$^2$ which is close to the maximum received at the surface of the Earth. A comparison of AM 0, AM 1.5 solar spectra and black body radiation is shown in figure 1.3.

## 1.3.2 Theories in solar cell

When a photon from the Sun hit on the solar cell, the photon can be absorbed by the solar cell if the photon energy is higher than the band gap value and its energy is given to an electron in the crystal lattice. This generates an electron hole pair (exciton) by exciting the electron from covalence band to conduction band where it is free to move around. The movement of electrons leads to the propagating of holes throughout the lattice as well.

The electron in the depletion region is pushed by the building potential toward the n side and the hole toward the p side. For the pairs created outside the space charge zone, diffusion acts to move the minority carriers (electrons in the p-type side and holes in the n-type side) toward the junction since the junction sweeps these minority carriers to the opposite side to become majority carriers (electrons in the n-type side and holes in the p-type side). If the cell is linked to the outside circuit, a reverse current $J_{ph}$ is generated and joins to thermal generation current $J_{gen}$. On the other hand, majority carriers are also driven into the depletion zone by diffusion resulted from the concentration gradient and forms the forward current $J_{rec}$. Therefore, the carrier distribution in the solar cell device is governed by a dynamic equilibrium between reverse current ($J_{gen}+J_{ph}$) and forward current $J_{rec}$ [9].

7

$$J(V_a) = J_{rec}(V_a) - J_{gen}(V_a) - J_{ph} = J_0 \left( e^{\frac{eV_a}{kT}} - 1 \right) - J_{ph} \tag{1.6}$$

$$J_{ph} = eG(L_N + W + L_P) \tag{1.7}$$

where $L_N$ and $L_P$ is the minority-carrier-diffusion length for electrons and holes, respectively, and W is the width of the depletion region. G is uniform generation rate.

Both the dark and illuminated J-V characteristics of the p-n junction (i.e., solar cell) are illustrated in Figure 1.4. The illuminated J-V characteristic of the p-n junction is the same as the dark J-V characteristic, only shifting down by the value of photo-generated current $J_{ph}$.
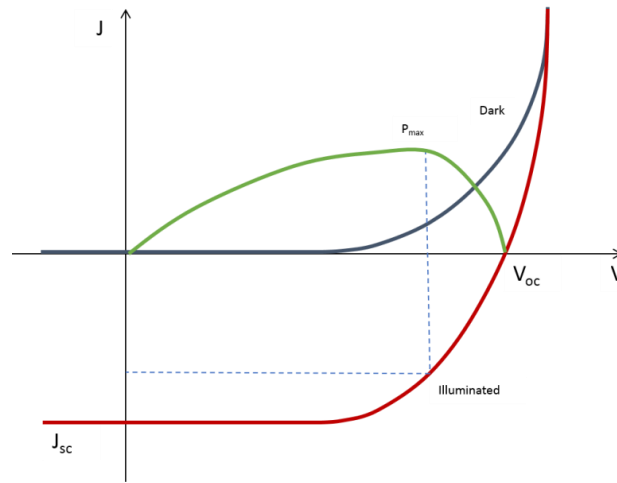


Figure 1.4 The illuminated J-V characteristic of the p-n junction

When the metal electrodes are connected to both sides of solar cell, the ohmic metal semiconductor contacts are made. The electrodes can then be connected to an external load to form a circuit. Electrons that are created on the n-type side, or created on the p-type side and then swept onto the n-type side by the junction travel through the wire until they reach the p-type metal semiconductor contact. Here, they recombine with the holes created on the p-type side, and swept across the junction from the n-type side. In this electron circulate process, the load is powered. The voltage measured is equal to the difference in the quasi Fermi levels of the majority carriers on the two terminals [19]. The behavior of solar cell as an idea diode in this case can be described by a simple equivalent circuit (Fig. 1.5).
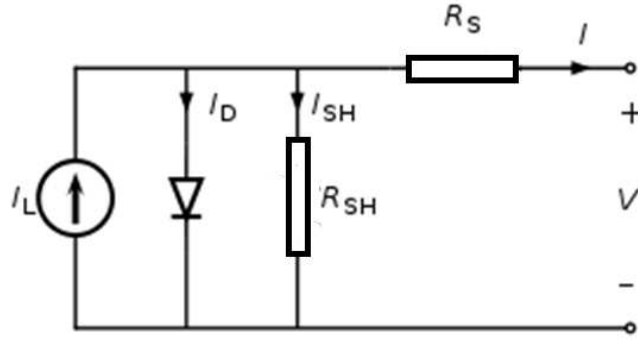
Figure 1.5 The equivalent circuit of a solar cell.

The J-V characteristic of the equivalent circuit with the series resistance $R_s$ and the shunt resistance $R_{SH}$ is given by

$$J = J_0 \left\{ exp \left[ \frac{e(V-AJR_s)}{kT} \right] - 1 \right\} + \frac{V-AJR_s}{R_{SH}} - J_{ph} \qquad (1.8)$$

where A is the area of the solar cell, $R_s$ and $R_{SH}$ is the series resistance and shunt resistance ($\Omega$), respectively.

The above equation can be solved further by the Lambert W function to give the J value. However, in a real solar cell, the equivalent circuit is replaced by a two-diode model. When external load is applied to the cell, its resistance can be simply added to Rs.

## 1.3.3 Parameters in solar cell

The main parameters that used to characterize the performance of solar cells are the short-circuit current density ($J_{sc}$), the open-circuit voltage ($V_{oc}$), the fill factor (FF) and conversion efficiency. These parameters are determined from the illuminated J-V characteristic.

When the circuit is open, J = 0 and the voltage on the output terminals is defined as the open-circuit voltage ($V_{oc}$). It is the maximum voltage that a solar cell can deliver. Assuming the shunt resistance is high enough and the open-circuit voltage $V_{oc}$ can be expressed as:

$$V_{oc} = \frac{kT}{e} l_n \left( \frac{J_{ph}}{J_0} + 1 \right) \qquad (1.9)$$

Similarly, when the circuit is shorted, V = 0 and the current J on the terminals is defined as the short-circuit current ($J_{sc}$) to describe the maximum current the solar cell can deliver. In the case of low $R_S$, $J_0$ and high $R_{SH}$, the short circuit current $J_{sc}$ is equal to $J_{ph}$:

$$J_{sc} = J_{ph} \qquad (1.10)$$

Another parameter to evaluate the performance of a solar cell is fill factor. The fill factor is

defined by the ratio between the maximum power generated by the cell ($P_{max} = J_{mp} \cdot V_{mp}$) and the product of $J_{sc}$ and $V_{oc}$:

$$\text{FF} = \frac{J_{mp}V_{mp}}{J_{sc}V_{oc}} \tag{1.11}$$

The most important parameter of a solar cell in terms of its ultimate performance is the conversion efficiency. The conversion efficiency is calculated as the ratio between the maximal generated power of the cell and the power of the incident irradiation. The irradiance value of $P_{in} = 1000$ W/m$^2$ for the AM1.5 spectrum has become a standard for measuring the conversion efficiency of solar cells.

$$\eta = \frac{P_{max}}{P_{in}} = \frac{J_{mp}V_{mp}}{P_{in}} = \frac{J_{sc}V_{oc}FF}{P_{in}} \tag{1.12}$$

The external quantum efficiency EQE ($\lambda_0$) is the fraction of photons incident on the solar cell that create charge carriers in the absorber layer and are successfully collected. It is dependent on the energy of individual photon and usually measured by illuminating the solar cell with monochromatic light $\lambda_0$ and measuring the photocurrent $I_{ph}$.

$$\text{EQE}(\lambda_0) = \frac{I_{ph}(\lambda_0)}{e\phi_{ph}(\lambda_0)} = EQE^{ref}(\lambda_0)\frac{I_{ph}(\lambda_0)}{I_{ph}^{ref}(\lambda_0)} \tag{1.13}$$

Where e is the elementary charge and $\phi_{ph}$ is the photon flux incident on the solar cell which is usually determined by measuring the EQE of a calibrated solar cell under the same light source and fixed bias voltage.

If only consider the photon absorbed by the solar cell and neglect the reflection and transmission, the quantity is then known as the internal quantum efficiency IQE ($\lambda_0$):

$$\text{IQE}(\lambda_0) = \frac{EQE}{1 - Reflection - Transmission} \tag{1.14}$$

# 1.4 Photoluminescence

## 1.4.1 Principles

Photoluminescence (PL) is light emission from any luminescent materials after the absorption of photons (electromagnetic radiation). In discipline of chemistry, it is often classified into fluorescence and phosphorescence.

The term of fluorescence was derived from the mineral fluorite ($CaF_2$). It is the emission of light by some substance that has absorbed other electromagnetic radiation or light. Fluorescence is a form of luminescence which produces spontaneous emission when the fluorophore molecules are excited by some means rather than heating [20]. Usually, the emitted light has lower energy with longer wavelength than the absorbed light. This energy difference is called Stokes shift, named after Irish physicist George G. Stokes [21].

The most remarkable fluorescence occurs when fluorophores are exposed to UV light and emit distinct visible light. Unlike phosphorescence which emits longer time, fluorescence has shorter life time and ceased to glow when the radiation source is removed.

When irradiated by certain electromagnetic irradiation, the energy level of an orbital electron in an atom, molecule, or nanoparticle will be elevated from ground state to excited state. Usually this excited state is singlet state, which means all electrons are paired and net angular momentum and spin quantum number S is zero so that there is only one spectra line. However, in some cases, the doublet and triplet state are also possible. A doublet state has one unpaired electron and spectral lines split into doublet; and a triplet state contains two unpaired electrons and spectral lines split by three folds.

When the excited electron relaxes from excited singlet state to ground state, fluorescence occurs. Usually the excited molecules decay to the lowest vibrational level of the excited state before fluorescence emission takes place. The nucleus does not move and the vibration levels of the excited state resemble the vibration levels of the ground state. The excitation and relaxation process, and fluorescence mechanism of excited state can be described by Jablonski diagram, in which it shows an electron absorbs a high energy photon and excited from ground state to the first excited singlet state, and then the system relaxes along with the occurring fluorescence emission at a lower energy or longer wavelength, see figure 1.6. It can also be described by the following formulas:

Excitation: $S_0 + h\nu_{ex} \rightarrow S_1$ (1.15)

Emission: $S_1 \rightarrow S_0 + h\nu_{ex}$ (1.16)

where $S_0$ is the ground state of the fluorophore, and $S_1$ is the first excited singlet state.

In most cases, the emitted light has a longer wavelength and lower energy than the absorbed radiation which is known as the Stokes shift, due to energy loss between the time a photon is absorbed and emitted. The causes and magnitude of Stokes shift are complex and dependent on the fluorophore and its environment. In principle, it is frequently due to non-radiative decay to the lowest vibrational energy level of the excited state. In other cases, the emission of fluorescence leaves a fluorophore in a higher vibrational level of the ground state. On the contrary, when the absorbed electromagnetic radiation is intense, it is possible to emit in a higher energy and shorter wavelength than the absorbed radiation. This energy difference is called an anti-Stokes shift, such as up conversion in lanthanides doped nanoparticles. In the case of "resonance fluorescence", the emission is of the same wavelength with the absorbed radiation.

Except for the relaxation of photon emission, the molecule in $S_1$ can relax thriugh other pathways by dissipating the energy as heat and vibrations to the environment and undergo a non-radiative relaxation. Excited electron can also relax by conversion to a triplet state, and subsequently may relax via phosphorescence or a secondary non-radiative relaxation step.

Related to fluorescence, but stores the absorbed energy and re-emits for a longer time, another photoluminescence phenomena called phosphorescence. The slower

re-emission time scales of phosphorescence are associated with a "forbidden" transition of spin multiplicity in quantum mechanics, which appears very slowly in certain materials and absorbed radiation is re-emitted at a lower intensity for up to several hours after excitation. In phosphorescence, the electron that absorbed the photon energy in a molecule with a singlet ground state is excited to the excited singlet state and undergoes an unusual intersystem crossing into excited triplet state. The triplet lifetimes of phosphorescent materials are on the order of milliseconds, and up to minutes or even hours. The radiative decay from an excited triplet state back to a singlet ground state is known as phosphorescence. If the phosphorescent quantum yield is high, these materials will release significant amounts of photon energy over long time scales, as we can see in glow-in-the-dark toys, stickers, paint, and clock dials. The process in phosphorescence can be described by following equation and the Jablonski diagram (Fig. 1.6)

$$S_0 + h\nu_{ex} \rightarrow S_1 \rightarrow T_1 \rightarrow S_0 + h\nu_{em} \tag{1.17}$$

where $S_0$ is the ground state of the fluorophore, $S_1$ is the first excited singlet state, $T_1$ is first excited triplet state.

Intersystem crossing is a process that a singlet state passes to a triplet state non-radiatively, or conversely a triplet state transition to a singlet state during which the spin of the excited electron is reversed. The occurring probability of intersystem crossing is more favorable when the vibrational levels of the two excited states overlap for the reason of little energy gained or lost in the transition. The intersystem crossing involves coupling of the electron spin with the orbital angular momentum of non-circular orbits and thus the process is also called "spin-orbit coupling". Intersystem crossing is a slow relaxation process and the time scale of which is on the order of $10^{-8}$ to $10^{-3}$ s. The presence of paramagnetic species in solution enhances intersystem crossing. A singlet state is a molecular electronic state such that the spin of the excited electron is still paired with the ground state electron. In a triplet state the excited electron is no longer paired with the ground state electron and they are parallel (same spin).
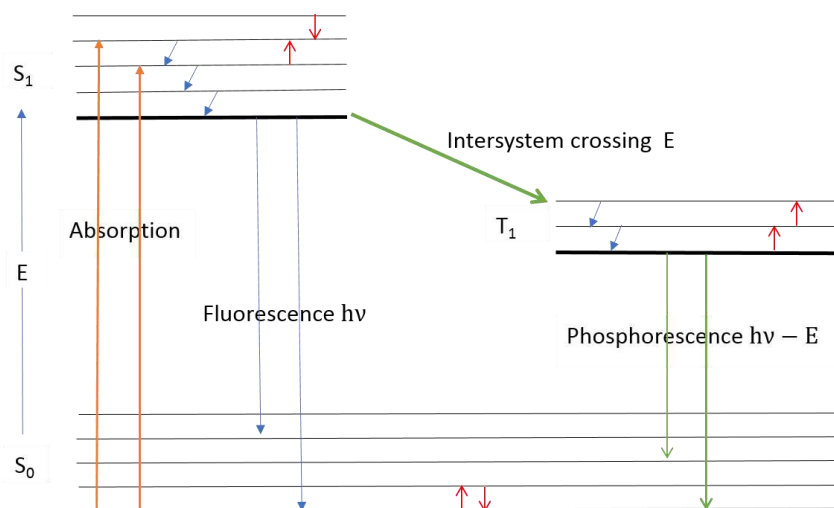
Figure 1.6 Jablonski diagram illustration of fluorescence and phosphorescence. An electron is excited electronically and vibrationally from ground state $S_0$ to singlet excited state $S_1$ after it absorbs a high energy photon. The system relaxes vibrationally and eventually fluoresces at a longer wavelength. The system may undergo vibrational relaxations and intersystem crossing to the triplet excited state ($T_3$) and then finally relaxes to the ground state by phosphorescence. The spin state of electron is also indicated with red arrow in each energy state.

## 1.4.2 Fluorescence Lifetime

The fluorescence lifetime refers to the average value of the time that the fluorophore molecule stays in excited state before return to the ground state. In the process discussed above, the life time is defined by:

$$\tau = \frac{1}{\Gamma + k_{nr}}$$ 
(1.18)

Suppose the fluorophore molecule is excited by an infinitely sharp light source, and it leads to the initial population n (0) of fluorophore molecule in excited state. The excited population decays with a rate $\Gamma + k_{nr}$ according to:

$$-\frac{dn(t)}{dt} = (\Gamma + k_{nr})n(t)$$ 
(1.19)

where n(t) is the population of excited molecules at time t following excitation, $\Gamma$ is the emissive rate, and $k_{nr}$ is the nonradiative decay rate. Solve this differential equation and it results in the exponential decay of the excited population:

$$n(t) = n(0)e^{-\frac{t}{\tau}}$$ 
(1.20)

Since the time dependent fluorescent intensity in experiment is proportional to the n(t), substituting the population with intensity yields the usual single exponential decay

expression: [21]

$$I(t) = I(0)e^{-\frac{t}{\tau}}$$ (1.21)

where I(t) and I(0) is the intensities at time t and 0, the lifetime $\tau$ is the inverse of the sum of the total decay rate which depopulate the excited state. It can be determined from the slope of a plot of log I(t) versus t, and more commonly determined by fitting the data to assumed decay models. For a single exponential decay, 63% of the molecules have decayed prior to $t = \tau$ and 37% ($n_0/e$) decay when $t > \tau$.

The lifetime is the average time a fluorophore remains in the excited state, which can be calculated by averaging t over the intensity decay of the fluorophore:

$$\bar{t} = \frac{\int_0^\infty tI(t)dt}{\int_0^\infty I(t)dt} = \frac{\int_0^\infty texp(-\frac{t}{\tau})dt}{\int_0^\infty exp(-\frac{t}{\tau})dt}$$ (1.22)

After integration by parts, the denominator is equal to $\tau$ and the numerator is equal to $\tau^2$. Thus the average time a fluorophore remains in the excited state is equal to the lifetime for a single exponential decay:

$$\bar{t} = \tau$$ (1.23)

Many samples that contain only a single fluorophore display more complex decay which commonly fitted with a multi-exponential model. The intensity is assumed to decay as the sum of individual single exponential decays in the multi-exponential model:

$$I(t) = \sum_{i=1}^n A_i exp(-\frac{t}{\tau_i})$$ (1.24)

Where $n$ is the number of decays, $\tau_i$ are the decay times, $A_i$ represent the amplitudes of each of the components at t = 0. The meaning of the pre-exponential factors $A_i$ is different for a mixture of fluorophores and for one fluorophore that displaying a complex decay. For the one fluorophore case, the $A_i$ values represent the fraction of the molecules in each conformation at ground-state equilibrium (t = 0). In the case of the mixture of fluorophores, it is more complex; the relative $A_i$ values depend on the concentration, quantum yield, absorption and emission intensity of each fluorophore at the observation wavelength.

It is often useful to determine the average lifetime when using the multi-exponential decay model, which is given by eq. 1.22. For a two-exponential decay it is given by

$$\bar{\tau} = \frac{A_1\tau_1^2 + A_2\tau_2^2}{A_1\tau_1 + A_2\tau_2}$$ (1.25)

The fluorescence lifetime is an important parameter in research and practical applications of fluorescence. There are numerous organic fluorophores and almost all of them display lifetimes from 1 to 10 ns. Pyrene has been derived by adding fatty acid chains and exceptionally has decay times near 100 ns. Metal–ligand probes display decay times ranging from 100 ns to 10 µs and lanthanides have millisecond decay times [21].

## 1.4.3 Photoluminescent materials

There are many natural and artificial compounds that exhibit fluorescence, and they have many applications. Many fishes, such as sharks, lizardfish, scorpionfish, wrasses, and flatfishes, exhibit biofluorescence. Fluorescent chromatophore cells in these fishes contain fluorosomes in which the movement, aggregation, and dispersion of fluorescent proteins inside that produce fluorescence. The well-studied example of biofluorescence in the ocean is the jellyfish which is identified as a carrier of green fluorescent protein (GFP). The gene for green fluorescent proteins has been isolated and widely used in genetic studies to indicate the expression of other genes [22]. The dragonfish in deep sea can harness the blue light emitted from their own bioluminescence to generate red fluorescence which can supply the dragonfish extra light in deep dark ocean but is invisible to other animals in case of attracting predators [23]. The wings of swallowtail butterflies contain pigment infused crystals. These crystals can produce fluorescent light when they absorb blue light radiance [24]. Fluorescence serves a variety of functions in coral such as photosynthesis [25].

Many gemstones and minerals such as rubies, emeralds, diamonds, calcite, amber, and opal have distinctive fluorescence under short-wave ultraviolet (UVC, 100-280nm), medium-wave ultraviolet (280-315nm), long-wave ultraviolet (315-400nm), visible light, or X-rays, A single mineral can fluoresce with different colors under shortwave and long wave light [26].

Fluorescence in minerals is caused by a wide range of activator elements. In most cases, the concentration of the activator must be restricted to under a certain level in order to prevent quenching of the fluorescent emission. For example, Low-iron sphalerite ((Zn, Fe) S) fluoresces and phosphoresces in a range of colors depend on the presence of various trace impurities [27,28]. Divalent manganese, with the concentrations of several percent, is responsible for the red or orange fluorescence of calcite ($CaCO_3$) [29]. Trivalent chromium in low concentration is the red fluorescence source of ruby [30]. Divalent europium is the source of the blue fluorescence in fluorite ($CaF_2$) [31]. $Er^{3+}$, $Ho^{3+}$, $Tm^{3+}$, $Tb^{3+}$ and other lanthanide ions activated up converting fluorescence materials, along with quantum dots and transition metal complexes or clusters triggered great research interest in recent years [32–36].

In this thesis study, fluorescent material quantum dots $CuZnS_2$@ZnS doped with gadolinium ions, phosphorescent copper thiolate compounds and lanthanide doped fluoride materials $NaGdF_4$ and $KGdF_4$ were investigated.

# Chapter 2 Instrumentation and spectroscopy

## 2.1 Instrumentation

### 2.1.1 Evolution 201 UV–visible spectrophotometer

The 201 UV-visible spectrophotometer (Thermo Scientific, Madison, USA) has a standard absorption/transmittance setup and can measure the absorbance and transmittance in the region of 190 - 1100 nm. The spectrophotometer has a xenon flash lamp for visible and ultraviolet ranges light source and dual silicon photodiodes detector. The display is a touchscreen LCD panel; 800 × 480; 17.8 cm (7 in) diagonal with software Microsoft Windows XP embedded. The obtained absorbance/transmittance data were then exported to Origin 9 software for analysis and presentation.



Figure 2.1 Scheme of the optical components of the Evolution 201 UV-visible spectrophotometer. Figure from http://www.thermofishersci.in/lit/Thermo%20Scientific%20Evolution%20201.pdf

### 2.1.2 FP-8200 spectrofluorometer (Japan)

The spectrofluorometer has a standard 10 mm rectangular cuvette holder with 90º between excitation beam and detection. The wavelength regions for λex and λem are 200 - 750 nm for the setup, and the scanning of the wavelengths is controlled by Spectra Manager$^{TM}$/CFR, iRM. The spectrometer has a xenon arc lamp with shielded lamp housing (150W). The instrument has holographic concave grating in modified Rowland

mount type monochromators. A silicon photodiode and a photomultiplier tube (PMT) are used to record excitation and emission spectrum, respectively. The data from the experiments were exported to and analyzed with origin 9 software.

## 2.1.3 NanoLog® spectrofluorometer

The standard NanoLog® spectrofluorometer system (Horiba Scientific, New Jersey, USA) is equipped with a double-grating monochromator in the excitation position. Double-grating monochromators offer a significant increase in sensitivity, resolution and stray-light rejection than single-grating ones. In the emission position, the NanoLog® is equipped with a single-grating iHR spectrometer which offers the option of detection with a CCD, to create an image of the dispersed fluorescence for subsequent analysis. There are movable grating turrets and multiple ports with mirrors to choose in iHR spectrometers. The sample compartment module is equipped with a silicon photodiode reference detector to monitor and compensate for variations in the xenon lamp output, and a Symphony InGaAs array cooled by liquid nitrogen to provide rapid and robust spectral characterization in the near infra-red.
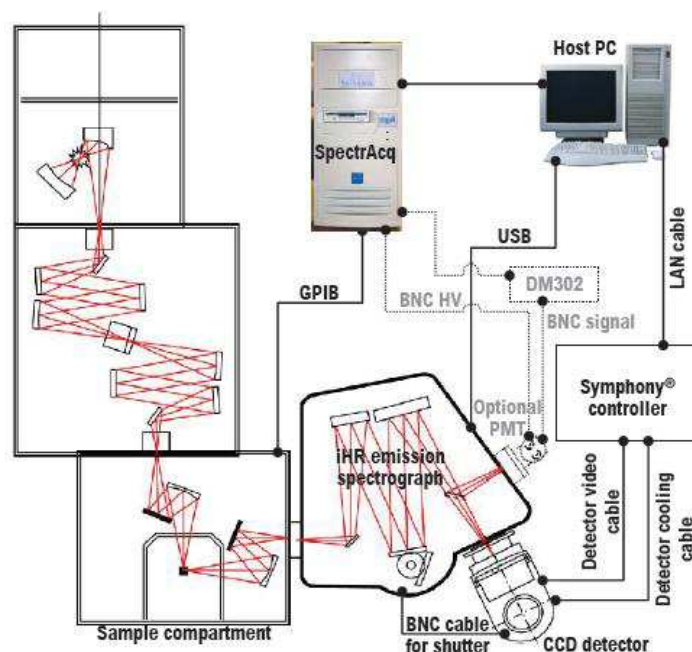
Figure 2.2 Sketch of the cable connections among an iHR spectrometer, a CCD detector, and the rest of the system. A photomultiplier tube detector with its connections is shown in dotted lines. Figure from http://www.horiba.com/fileadmin/uploads/Scientific/Downloads/UserArea/Fluorescence/Manuals/Nanolog_Manual.pdf

## 2.1.4 ARL X'TRA X-ray diffractometer

An ARL X'TRA X-ray diffractometer with Cu-Kα radiation (λ = 0.15405 nm) which composed with an MC 61- 04× 12 (0.4мм× 12мм) C X-ray tube (60 kV, 2200Wt), Ni- filter and a Peltier detector with a thermo-electric cooling system. A Windows XP based software WinXRD is fully integrated for data collection and analysis.
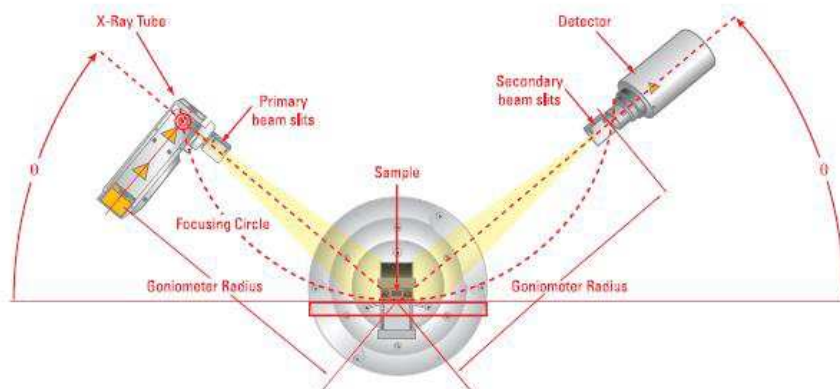


Figure 2.3 Scheme of the geometry of the theta-theta goniometer of the ARL X'TRA X-ray diffractometer. Figure from http://www.thermo.com.cn/Resources/200802/productPDF_10442.pdf

## 2.1.5 EDS/SEM/TEM

FEI XL30 (Philips) ESEM (Environmental scanning electron microscope) installed with an EDAX micro-analytical system. Morgagni 268D (FEI-Philips) equipped with MegaView2 CCD camera.

## 2.1.6 Raman spectrometer

A Raman spectra measurement setup of He-Ne laser (632.8 nm) and LabRam HR spectrometer (Horiba-Jobin Yvon), mounting a 600 lines/mm grating and equipped with a multichannel detector (a CCD with 256x1024 pixels) cooled by liquid nitrogen.

## 2.1.7 Microwave synthesis reactor

Monowave 400 microwave synthesis reactor (Anton Paar, Italia S.r.l.).

## 2.1.8 Scanning probe microscope

Solver P47H, Program version 845, NT-MDT, Zelenograd, Moscow, Russia

## 2.1.9 Dynamic light scanning spectrophotometer

Malvern zeta sizer Nano Series, Model (ZEN 3600), Malvern Instruments Limited, UK.

## 2.2 Spectroscopy

Spectroscopy refers to the study of the interaction between electromagnetic radiation and matter as a function of wavelength in the X ray, ultra-violet (UV), visible and near infra-red (IR) regions of the electromagnetic spectrum. A variety of materials, from atom, organic molecules to inorganic crystals such as quantum dots and up converting nanoparticles, undergo electronic transitions at these energies, therefore, spectroscopy technique is widely used to characterize the spectral properties of absorption, excitation, and emission. Furthermore, the application of pulsed laser diode and LED technology enables the studying of temporal dynamics of these processes in the order of femtosecond to picosecond time scale. Spectroscopy technique in general is therefore highly useful to study both the ultra-fast and long lived excited state dynamics of luminescent materials. More details about specific spectroscopic techniques relevant to this thesis are described in the following sections.

## 2.2.1 Absorption/transmittance Spectroscopy

Absorption/transmittance spectra of a sample in solution are recorded by a UV/VIS spectrometer. The incident light beam passes through a monochromator, usually a prism or a grating, which splits it into different wavelengths. The monochromatic beam is then split into two. One beam passes through a reference solution without sample, the other through the sample. The intensities of the two radiation beams are measured by photomultiplier tubes (PMT), and then the absorbance spectrum of the sample relative to the reference is derived.

The transmittance through the sample is expressed as:

$$T(\lambda) = \frac{I_t(\lambda)}{I_0(\lambda)}$$ (2.1)

The absorbance, A, equal to the logarithm of transmittance reciprocal, is defined by:

$$A(\lambda) = log \frac{I_0(\lambda)}{I_t(\lambda)} = log \frac{1}{T}$$ (2.2)

where $I_0$ and $I_t$ are the intensities of the light passes through the reference and the sample respectively.

Beer-Lambert's law states that the absorbance of monochromatic light through a homogenous, isotropic solution is proportional to the concentration $c$ of absorbing

molecules, and the optical path length $l$, See figure 2.4.

$$A(\lambda) = \varepsilon_\lambda \cdot c \cdot l \tag{2.3}$$

$$I_t = I_0 e^{-kcl} \tag{2.4}$$

where $\varepsilon_\lambda$ is the molar absorption coefficient, usually given in units of $cm^{-1}M^{-1}$. $k = \varepsilon ln10$ is the extinction coefficient. The optical path length in all absorption measurements is 1 cm.
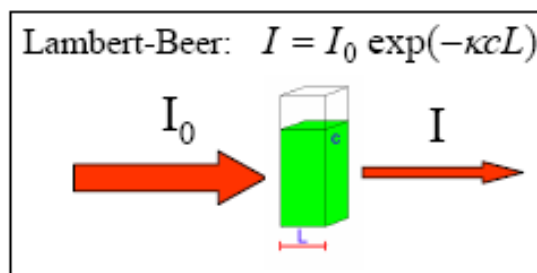


Figure 2.4 Beer-Lambert law, where κ=εln10.

## 2.2.2 Fluorescence Spectroscopy

Fluorescence spectroscopy enables quantification of the spectral properties of excitation and emission of the fluorophore sample and provides the information of the fluorescence.

In practice, high intensity light from an excitation source is directed into a sample solution in a cuvette. The interaction between the incident photon and the fluorophore result in the excitation of an electron from the valence band/HOMO into the conduction band/LOMO, left a hole in the valence band/HOMO. Subsequently, the electron and the hole recombine, and emit a photon in a mechanism of fluorescence or phosphorescence. The orientation of emission is 90°C compare to the excitation beam in order to minimize the detection of the excitation photon as shown in figure 2.5. The energy intensity of the emitted photon respect to the wavelength is recorded by a photon detector; results in an excitation/emission spectrum.

In fluorescence emission spectroscopy, the excitation wavelength ($\lambda_{ex}$) is kept constant by fixing excitation monochromator and the emissions at different wavelengths are measured by sweeping the emission monochromator over the desired spectral range. For fluorescence excitation spectroscopy, the emission wavelength ($\lambda_{em}$) is kept constant by fixing emission monochromator and the excitations at different wavelengths are measured by sweeping the excitation monochromator over the desired spectral range.

Each monochromator includes an adjustable slit with the width range in 2.5, 5, 10 and 20 nm in the case of FP-8200 spectrofluorometer. The slit width influences the intensity of impinging light both on the sample and the detector, and thus the signal to noise ratio

(SNR) of the sample. The transmitted light intensity is proportional to the square of the slit width and the SNR decreases as the slit width is reduced. In practice, the system can be adjusted by addition of neutral density filters in the same end to give more quantifiable data.
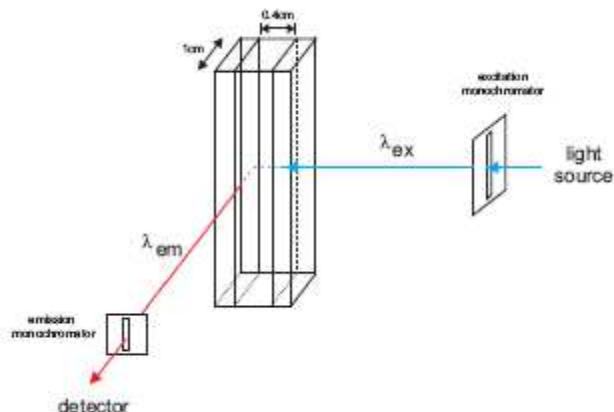


Figure 2.5 Schematic illustration of fluorescence spectroscopy.

## 2.2.3 X-ray diffraction crystallography

Crystals are regular arrays of atoms that can scatter impinging X-ray waves primarily through the atoms' electrons. A regular array of scatters produces a regular array of spherical waves that cancel one another out in most directions through destructive interference and add constructively in a few specific directions, determined by Bragg's law:

$$n\lambda = 2d\sin\theta \qquad (2.5)$$

Where d is the distance between diffracting planes, $\theta$ is the incident angle, n is any integer, and $\lambda$ is the wavelength of the beam. These specific directions appear as reflection spots and form the characteristic diffraction peaks on the diffraction pattern. The width of the diffraction peaks carries the information about the crystalline grain size and the strain in the crystal structure.

The Scherrer equation is a formula that relates the size of the crystallites in a solid to the broadening of a peak in a diffraction pattern in X-ray diffraction and crystallography. It is used in the determination of the size of crystal powder. The Scherrer equation can be given as: [37]

$$D = \frac{K\lambda}{\beta\cos\theta} \qquad (2.6)$$

where D is coherent diffraction domain size, $\lambda$ is the wavelength of the X-ray source, $\beta$ is the reflection width ($2\theta$), $\theta$ is the Bragg angle and K is the shape factor (around 0.9).

## 2.2.4 Energy dispersive X-ray spectroscopy

Energy dispersive X-ray spectroscopy (EDS, EDX) is an analytical technique used to determine the elemental composition of a sample. Its characterization capability relies on an interaction of the excitation from a beam of charged particles such as electrons or X-ray and a sample, since each element has a unique atomic structure to form a unique set of peaks on its electromagnetic emission spectrum.

At rest state, the ground state electrons in discrete energy levels or shells bound to the nucleus of the atom within a sample. When a high-energy beam of charged particles such as electrons, protons, or a beam of X-rays, is focused on the sample, the incident beam may excite and eject an electron in an inner shell, leaving behind a hole where the electron was. An electron with higher-energy from an outer shell then fills the hole, emitting an X-ray with the energy equal to the energy difference between the higher-energy shell and the lower energy shell. The number and energy of the X-rays photons emitted from a specimen can be measured by an energy dispersive spectrometer. For example, $K_\alpha$ X rays are emitted when an electron drops from a L orbital to the innermost K shell, see figure 2.6. Because each element has a unique atomic structure, the energies of the X-rays are characteristic of the difference in energy between the two shells and of the atomic structure of the element, therefor the EDS spectrum can provide the composition information of the specimen to be measured. EDS can be used to identify the chemical elements presented in a sample and to estimate their relative abundance. EDS is often operated in conjunction with TEM/SEM.
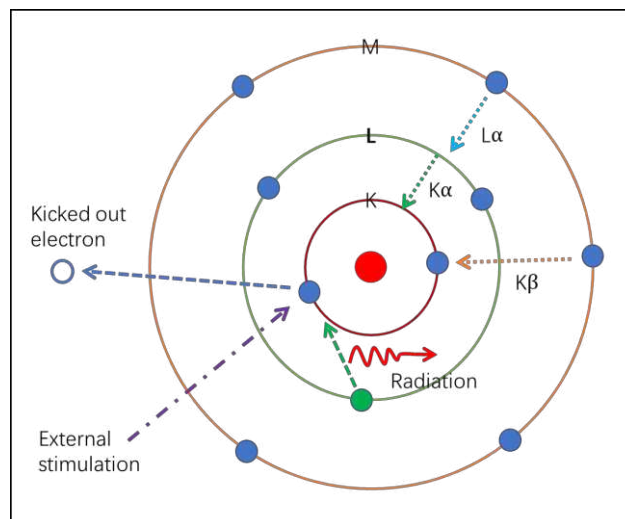


Figure 2.6 Illustration of the EDS principle.

## 2.2.5 Raman spectroscopy

Raman spectroscopy is a spectroscopic technique used to observe vibrational, rotational, and other low frequency modes in a chemical compound to provide a structural fingerprint of the molecules. It relies on inelastic scattering of a monochromatic light, usually a laser by sample. When illuminated with a laser beam, the laser light interacts with molecular vibrations in the sample, creates an induced dipole moment within the molecule based on its polarizability and resulting in the shifted energy of the laser photons, which gives information about the vibrational modes in the sample.

Raman scattering is typically very weak, and the magnitude of the Raman effect correlates with a change of electric dipole-electric dipole polarizability in a molecule. The intensity of the Raman scattering is proportional to this polarizability change. The laser beam puts the molecule into a virtual energy state for a short time and a scattering photon is emitted. After that, the sample is in a different rotational or vibrational state. The scattered photon shifts to a different energy to remain the total energy of the system constant after the molecule moves to a new rotational or vibrational state. If the final energy state is higher than the initial state, the scattered photon will undergo a Stokes shift so that the total energy remains the same, and vice versa. The Raman scattering spectrum shifts as a function of the frequency. Raman shifts are typically reported in wavenumbers with units of inverse length.

$$\Delta\omega(cm^{-1}) = \left(\frac{1}{\lambda_0(nm)} - \frac{1}{\lambda_1(nm)}\right) \times 10^7 \tag{2.7}$$

where $\Delta\omega$ is the Raman shift expressed in wavenumber, $\lambda_0$ is the excitation wavelength and $\lambda_1$ is the Raman scattering wavelength.

## 2.2.6 Dynamic Light Scattering (DLS) and Zeta Potential

Dynamic light scattering (DLS) is a spectroscopic method for measuring the size distribution profile of a colloidal suspension of small particles or polymers in solution. A monochromatic and coherent light source, usually a laser, is directed through the suspension, and scatters in all directions when light hits small particles. The scattering intensity fluctuates over time due to Brownian motion which is constantly changing the distance between the scatters in the solution with time. The scattered light then undergoes either constructive or destructive interference by the small particles. This intensity fluctuation contains information about the temporal movement of the scatters and an autocorrelation function (ACF) is derived to analyze this temporal fluctuation. The ACF usually decays exponentially due to diffusion of the particles. For monodisperse samples the decay follows a single exponential with a decay rate proportional to the translational diffusion coefficient D. The random reorientation of the particles is size dependent and the spectral profile of the hydrodynamic radius of particles in solution can be determined by the Stokes-Einstein equation. The analysis is simplified by the initial assumption of a

monodisperse suspension of spherical particles, and the measured hydrodynamic radius for samples with other shapes must be treated as an approximation. If the particle is not spherical, rotational motion must be considered as well since the scattering of light is orientation dependent. For example, for a rod-shaped scatter, a rotational diffusion coefficient must be considered in addition to a translational diffusion coefficient. The obtained size also includes any other molecules that move with the particle, as a result, DLS size is usually bigger than the real size of the particle being studied. The accuracy of the DLS measurement can be enhanced by lower nanoparticle concentrations and neutral pH.

Zeta potential ($\zeta$) is an electrokinetic potential in colloidal dispersions. Zeta potential is the electric potential difference between the stationary layer of fluid attached to the dispersed particle and the dispersion medium. It is caused by the net electrical charge contained within the region that bounded to the slipping plane, and is widely used to quantify the magnitude of the charged particle. Zeta potential is a key indicator of the stability of colloidal dispersions which indicate the degree of electrostatic repulsion between adjacent and similarly charged particles in dispersion. Therefore, colloids with high zeta potential are electrically more stable while colloids with low zeta potentials tend to coagulate.
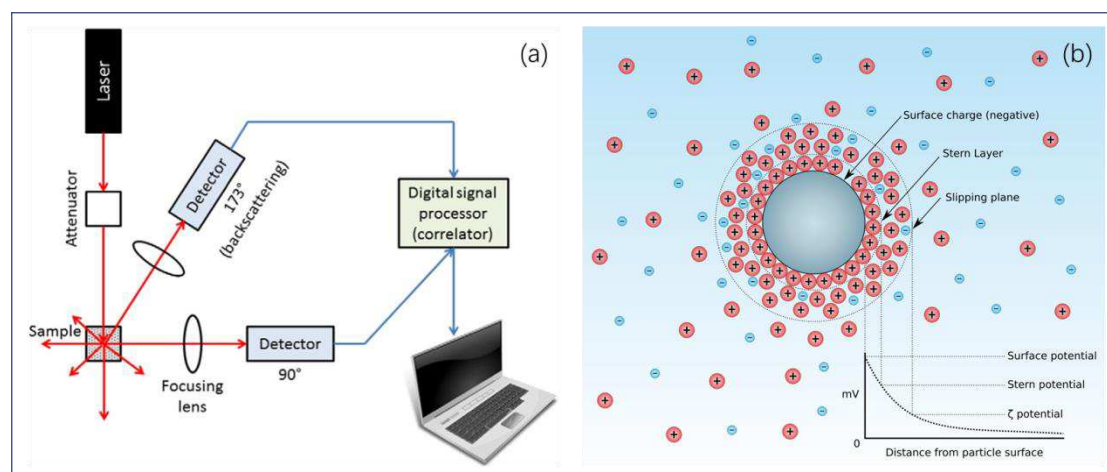


Figure 2.7 Schematic showing of DLS instrumentation (a) [38] and the zeta potential as a function of the distance from the surface of a particle. Figure (b) from https://en.wikipedia.org

## 2.2.7 Electron microscopy

When observe an object with the size small enough to the scale of light wavelength, the image's resolution can be limited by diffraction that causing blurring of the image. Diffraction comes from the wave nature of light and is determined by the finite aperture of the optical system. Light beam passing through the lens interferes with itself and forms a ring shaped diffraction pattern. The angular resolution of an optical system can be estimated by the Rayleigh criterion which states that two points like objects are just resolved when the principal diffraction maximum of one image coincides with the first

minimum of the other. The two points are well resolved if the distance is greater and not resolved if it is smaller. The resolution depends on the wavelength of the illumination source:

$$\theta = 1.22\frac{\lambda}{D} \tag{2.8}$$

where $\theta$ is the angular resolution, $\lambda$ is the wavelength of light, and $D$ is the diameter of the lens' aperture. The numerical factor 1.22 is derived from the Airy disc of the diffraction pattern. A more rigorous formula was provided by Abbe, considering the numerical aperture of the microscope ($NA = nsin\theta$):

$$d = 0.61\frac{\lambda}{nsin\theta} \approx \frac{\lambda}{2NA} \tag{2.9}$$

The resolution achieved with normal light microscopy is limited by the wavelength of the visible light source used. Electron microscope benefits from the much shorter de Broglie wavelength of electrons compare to normal light (100,000 times shorter than that of visible light) and are theoretically able to achieve resolution on the pm scale (10,000,000x whereas most light microscopes are limited below 2000x by diffraction). This property makes it an extremely powerful tool for imaging the structure of biological and inorganic materials at the nanoscale. Due to the nature of electrons, the lenses used in electron microscopy are electromagnetic lenses and are designed to behave like optical lenses.

The electron microscope can be sort into transmission electron microscope (TEM) and scanning electron microscope (SEM). The TEM uses a high voltage electron beam produced by an electron gun of tungsten filament cathode to illuminate the specimen. The beam is accelerated by an anode and focused by electrostatic and electromagnetic lenses, finally transmit through the specimen that is partly transparent to electrons and scatters part of them out. When emerges from the specimen, the electron beam carries information about the structure of the specimen and is magnified by the "objective lens" of the microscope. The magnified electron image is detected by the digital camera and can be displayed on a monitor or computer. The SEM produces images by scanning across the surface of the specimen with a focused electron beam. The electron beam loses energy by a variety of mechanisms when it interacts with the specimen. The lost energy result in light or X-ray emission, emission of low energy secondary electrons or high energy back scattered electrons, which provide signals that carry information about the topography and composition properties of the specimen surface. The electrons do not have to travel through the sample in SEM because it probes the surface of a sample rather than its interior. Usually, the image resolution of an SEM is lower than that of a TEM.
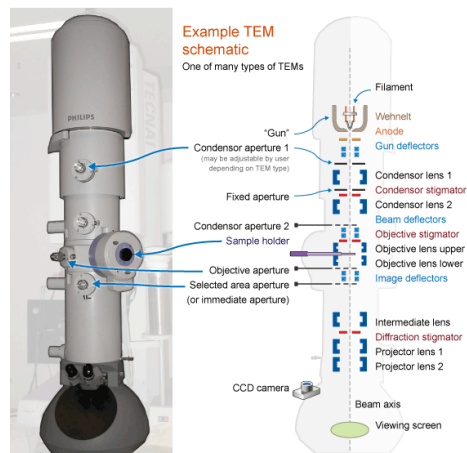
Figure 2.8 Schematic diagram of transmission electron microscopy (TEM). Figure from http://www.google.it/search? TEM diagram

## 2.2.8 Scanning probe microscopy (SPM)/Atomic force microscopy (AFM)

Scanning probe microscopy (SPM) is a microscopy technology to form surface image of samples using a physical probe that scans the specimen. SPM was founded in 1981, with the invention of the scanning tunneling microscope by Binnig and Rohrer, an instrument for imaging surfaces at the atomic level. When scanning probe microscopes raster scan the tip over the surface of sample, a value is recorded at discrete points in the raster scan. These recorded values are displayed as a heat map to produce the SPM images using a black and white or an orange color scale. Atomic force microscopy (AFM) is a high-resolution type of scanning probe microscopy, with demonstrated resolution on the order of nanometers, more than 1000 times better than the optical diffraction limit.

The AFM can be used to measure the force between the probe and the sample as a function of their mutual separation and thus to study the mechanical properties of the sample, such as Young's modulus of the sample. On the other hand, the reaction of the probe to the forces from the sample imposes can be used to form a three-dimensional image of a sample surface at a high resolution. This is achieved by raster scanning the surface of sample with a mechanical probe and recording the height of the probe corresponds to the probe-sample interaction. Specifically, a sharp tip is fixed to the free end of a small cantilever carried by the support. When perform the raster scanning, a ceramic piezoelectric oscillates the cantilever and the detector records the deflection and motion of the cantilever. The sample is mounted on the sample stage with a drive to move the sample and the sample stage in x, y, and z directions. The surface topography is usually displayed as a pseudo color plot.
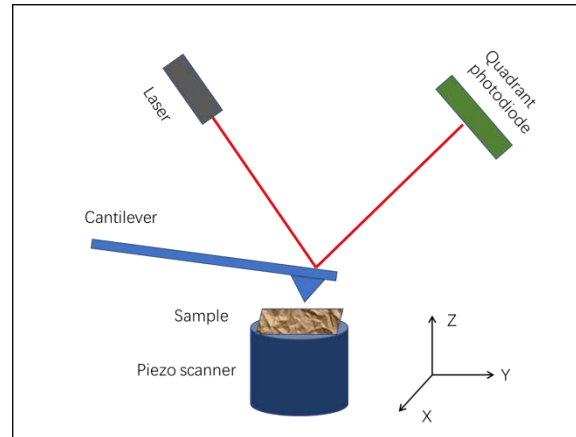
Figure 2.9 Schematic diagram of atomic force microscopy (AFM).

## 2.2.9 Magnetic resonance imaging (MRI)

Magnetic resonance imaging (MRI) is a form of nuclear magnetic resonance (NMR), a medical imaging technique used in radiology to obtain pictures of the anatomy and the physiological processes. Rather than X rays, MRI use strong magnetic fields, radio waves, and field gradients to generate images.

Isotopes that contain an odd number of protons or neutrons, such as $^1$H, have an intrinsic magnetic moment and angular moment with nonzero spin. If placed in an external magnetic field B, the external magnetic field exerts a torque $\tau$ on the magnetic moment $\mu$ ($\tau = \mu \times B = \gamma J \times B$), J is angular momentum vector. Then the angular momentum vector J precesses about the external field axis with Larmor frequency ($\varpi = -\gamma B$). When apply a radio frequency pulse to the patient at the Larmor frequency. The hydrogen atoms absorb the energy and the magnetic moment is perturbed to the XY plane in a non-equilibrium sate, the excited hydrogen atoms emit a radio frequency signal called free induction decay (FID), which is measured by a receiving coil. The radio signal can be made to encode position information by varying the main magnetic field by gradient coils, which is rapidly switched on and off for creating the characteristic MRI signal and image. Diseased tissue can be detected because the protons in different tissues have different relaxation times and thus return to the equilibrium state at different rates.

After excitation, each tissue returns to its equilibrium state by the independent T1 (spin-lattice) and T2 (spin-spin) relaxation processes. T1 characterizes the longitudinal magnetization vector that recovers exponentially to its thermodynamic equilibrium. It is the time for the longitudinal magnetization recovers approximately 63% of its initial value after being flipped into the magnetic transverse plane by a 90° radiofrequency pulse:

$$Mz(t) = Mz(0)(1 - e^{-t/T1}) \tag{2.10}$$

T2 characterizes the transverse magnetization vector that decays to its equilibrium value exponentially. It is the time it takes for the transverse magnetization decay to 37% of its

initial value after tipping to the magnetic transverse plane according to:

$$\text{Mxy(t)} = \text{Mxy(0)}e^{-\frac{t}{T_2}}$$ (2.11)

To create a T1-weighted image, magnetic moment is allowed to recover before measuring the MR signal by relatively a shorter repetition time (TR) and echo time (TE). To create a T2-weighted image, magnetic moment is allowed to decay before measuring the MR signal by relatively a longer repetition time (TR) and echo time (TE). In the brain, $T_1$ weighting causes the white matter to appear white, the gray matter to appear gray, and cerebrospinal fluid (CSF) appears dark. While $T_2$ weighting reverses the contrast of white matter, gray matter and cerebrospinal fluid.

Sometimes it is not possible to generate enough image contrast by adjusting the imaging parameters alone. In this case, administering the contrast agent such as gadolinium compound can enhance the image contrast significantly. Because of its unique electronic structure of 7 unpaired electrons in its 4f subshell, Gd is strongly paramagnetic. In its ionized state, $Gd^{+3}$ donates its $6s^2$ and $5d^1$ electrons for bonding, leaving its 4f electron shell intact, the powerful magnetic moment is therefore largely maintained even when chelated to a ligand such as DTPA. Because electrons have the same spin (½) but a much smaller size than protons, their gyromagnetic ratios are 657 times larger than protons and manifests its presence indirectly by facilitating the relaxation of nearby hydrogen protons. Gd preferentially shortens T1 values, makes the tissues and fluids extremely bright on T1-weighted images. This provides high sensitivity for detection of vascular tumors and brain stroke because of perfusion.

# Chapter 3 Photovoltaic material CZTS

## 3.1 Introduction

Copper zinc tin sulfide (CZTS) is a $I_2$-II-IV-$VI_4$ quaternary semiconductor compound. The class of related materials includes other $I_2$-II-IV-$VI_4$ compounds such as copper zinc tin selenide ($Cu_2ZnSnSe_4$, CZTSe) and copper zinc tin sulfur/selenium alloy $Cu_2ZnSn(S,Se)_4$ (CZTSSe). Like CIGS (copper indium gallium sulfide/selenide) and cadmium telluride (CdTe), CZTS provides favorable optical and electronic properties such as suitable band gaps of 1.54eV and high absorption coefficient ($10^4$ cm$^{-1}$) [39], but unlike CIGS and CdTe which involve the use of expensive rare earth or toxic elements indium, tellurium and cadmium, CZTS is composed of only earth abundant and non-toxic elements with low material cost and environmental benign characters and thus makes it well suited for absorber layer in thin film solar cell.

CZTS exists often as a kesterite, stannite or wurtzite structure, see figure 3.1. With a formula $Cu_2(Zn,Fe)SnS_4$, kesterinte is the Zn rich variety whereas the Zn poor form is stannite, and wurtzite is a less frequently encountered structure derived from ZnS wurtzite structure. The name kesterite is sometimes extended to include CZTSe, which contains selenium instead of sulfur [40].
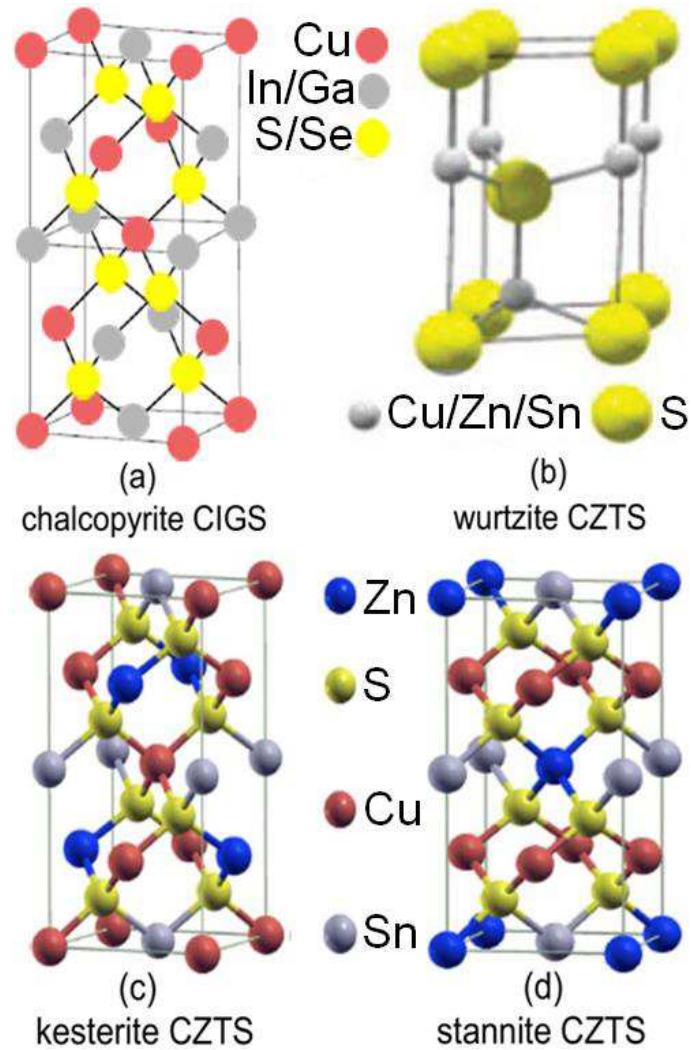
Figure 3.1 Crystal structure of CZTS kesterite (c), stannite (d), wurtzite (b), and a comparison with chalcopyrite CIGS (a) [41].

Although silicon, CdTe and CIGS technology has been commercialized, they involve rare earth elements used. Perovskite solar cell technology develops fast but toxic lead components and stability issues still remain consideration [42–44]. As a result, CZTS solar cell technology is worth investigation. Furthermore, studies indicate that by improving CZTSe crystalline quality, a record efficiency value of 17% can be achieved [45]. And it further could be in principle enhanced to 18.05% by optimization of device parameters [46].

Various methods were reported to fabricate CZTS solar cells, including electro-deposition [47–49], sputtering [50–52], thermal molten technique with Cu, Zn, Sn, and S powders [53], RF sputtering, thermal evaporation [54,55], spin coating or doctor blading, spray pyrolysis [56], CZTS powders by the method of solid-phase synthesis [50]， and so on. Among them, solution based low cost and fast processing method provides a very competitive strategy in fabricating low cost CZTS solar cells. With a variety of solution

been used, typical solution methods include: hydrazine based pure solution approach by IBM that has achieved a power conversion efficiency of 12.6% for CZTSSe solar cells [57]; metal salts/thiourea in methanol, dimethylformamide and dimethyl sulfoxide solution based approaches [58–60]; Ethanol−water solutions with dissolved metal salts and sulphur powder (Wangen Zhao et al. got 6.52% of efficiency with this method) [61]; Organic solution-based thermolysis approaches include dodecanethiol (DDT) or oleylamine (OLA) [62,63]；Successive ionic adsorption and reaction (SILAR) method [64]; Chemical bath deposition (CBD) [65,66]; Solution of thiol and amine and dissolved elemental powders or metal chalcogenides and oxides [67–70]. And a number of metal salts were employed include sulphate ($CuSO_4$, $ZnSO_4$, $SnSO_4$) [49][64], chlorides ($CuCl_2$, $ZnCl_2$, $SnCl_2$) [58][60][62], nitrades and acetate [59][71], and so on. It is also possible to use different salts (such as $Cu(NO_3)_2$, $Zn(CH_3COO)_2$, $SnCl_2$, with thiourea in dimethyl sulfoxide) in a single synthesis [72].

In this thesis study, we synthesized CZTS nanoparticles with two parallel solution methods, first one with the aqueous solution using copper and zinc nitrate, tin complex that synthesized from tin and iodine powders; second one with Cu, Zn, Sn and S powders dissolved in the mixture solution of thioglycolic acid and ethanolamine. Analysis by energy dispersive spectroscopy (EDS), Raman and X-ray diffraction (XRD) show that the kesterite phase of the CZTS nanoparticle were formed by the first method, and both kesterite and wurtzite phase formed with the second method.

# 3.2 Experimental

## 3.2.1 Chemicals

- Ammonium sulphide, $(NH_4)_2S$, MW = 68.14, 40-48% in water, Sigma-Aldrich

- Thiourea (TU), CH4N2S, MW = 76.11 g/mol, Merck Schuchardt OHG, ≥98%

- Thioglycolic acid, $HSCH_2COOH$, MW = 92,12 g/mol, d = 1.326 g/mL, Aldrich ≥99%

- Ethanolamine, $C_2H_7NO$, MW = 61.08 g/mol, d = 1.015 g/mL, Sigma-Aldrich, >98%

- Iodine powder, $I_2$, MW = 253.81 g/mol, Riedel de Haen, 99.8%

- Copper nitrate semipentahydrate, $Cu (NO_3)_2 \cdot 2.5H_2O$, MW = 232.59 g/mol, Sigma-Aldrich, 99.999%

- Zinc nitrate hexahydrate, $Zn (NO_3)_2 \cdot 6H_2O$, MW = 297.49 g/mol, Aldrich, ≥99.0%

- Tin powder, Sn, MW = 118.71 g/mol, Aldrich, 99.0%

- Copper powder, Cu, MW = 63.55 g/mol, Alfa Aesar, 99.9%

- Zinc powder, Zn, MW = 65.38 g/mol, Alfa Aesar, 97.5%

- Sulphur powder, S, MW = 32.07 g/mol, Sigma-Aldrich, 99.98%

## 3.2.2 CZTS synthesis

## 3.2.2.1 Synthesis in aqueous solution

### 3.2.2.1.1 Sn precursor solution preparation

Sn precursor solution was prepared with tin powder and solid iodine in ethanol, and adding $(NH_4)_2S$ to form Sn complex colloidal solution. Specifically, 5 mmol Sn powders (0.594g) and 10 mmol iodine ($I_2$) (2.54g) were stirred and heated in 20 ml ethanol at 50°C for overnight. After Sn and $I_2$ dissolved in ethanol, 1.5 ml $(NH_4)_2S$ (48%) was added to the reaction in a drop wise way. The brown precipitate from reaction was formed immediately and solution became transparent. The precipitates were collected by centrifuge and dissolved by adding more amount of $(NH_4)_2S$ (4ml) and brown coloured Sn precursor solution was obtained (Fig. 3.2 c).

### 3.2.2.1.2 CZTS Synthesis

In a typical synthesis of CZTS nanoparticle in aqueous solution, Sn, Cu, and Zn precursor aqueous solutions were prepared in separated vessels and then mixed together to obtain CZTS aqueous solution. Target ratios of Zn/Sn = 1.2 and Cu/ (Zn + Sn) = 0.8 were designed, specifically, 8.8 mmol (2.046g) Cu $(NO_3)_2 \cdot 2.5H_2O$ was dissolved in 2 ml deionized water (Fig. 3.2 a), 6 mmol (1.7844g) Zn $(NO_3)_2 \cdot 6H_2O$ was dissolved in mixture of 2 ml water and 6 ml ammonium solution (Fig. 3.2 b).

Together with previously prepared Sn precursor solution, the three precursor solutions were mixed and stirred vigorously and finally delivered the CZTS precursor solution (Fig. 3.2 d). The as-formed CZTS precursor solution shows dark brown colour, stable for several months and ready for film deposition.

## 3.2.2.2 Synthesis in organic solution

For this method, we used organic solvent and metal powders, with the same target elemental ratios of Zn/Sn = 1.2 and Cu/ (Zn + Sn) = 0.8 and the stoichiometry ratio of 2:1:1:4 among Cu, Zn, Sn and S. First, 1.0 mmol (0.1187g) Sn powders were added in the mixture solution of 2 ml thioglycolic acid and 4 ml ethanolamine, keep heating and stirring on a hot plate at around 60°C for 48 hours until Sn powders completely dissolved. When Sn dissolved, add 1.76 mmol (0.11185g) Cu and 1.2 mmol (0.0.0785g) Zn powders, continue to stir and heat at the same condition for around 24 hours until all the metal powders dissolved, the solution appears transparent yellow colour (Fig. 3.2 e). Finally, 4.0 mmol (0.128g) S powders were added in this solution, heat and stir over night. When sulfur powder is dissolved, the solution changes to transparent wine colour and the CZTS

precursor solution is ready (Fig. 3.2 f).

This organic precursor solution can be used to synthesize CZTS in two ways. First way is to deposit this precursor solution (Fig. 3.2 f) on glass substrate by spin coating or doctor blading method and then heat at higher temperature to form CZTS layer. Second way is to heat and stir the organic precursor solution further at around 120°C to synthesize CZTS nanoparticles in solution (Fig. 3.2 g), and then it can be used to deposit the layer. Alternatively, heating at around 200°C in microwave synthesis reactor for a few minutes, the CZTS nanoparticles can be synthesized faster.

## 3.2.3 Layer deposition

CZTS aqueous precursor solution (Fig. 3.2 d) can be deposited on glass by spin coating or doctor blade method, followed by high temperature annealing under argon atmosphere. With a single deposition, the layer appears inhomogeneous with quite a lot empty space left upon the solution evaporation. The process need to be repeated several times to obtain the desired homogeneous layer that covered by CZTS nanoparticles without empty space. Then the as prepared film was further annealed together with sulfur powder in argon atmosphere up to 450-500°C to obtain CZTS crystals.

The organic precursor solution (Fig. 3.2 f) can also be deposited directly on glass by spin coating or doctor blading method. The solution is very viscous and it can be diluted by water before deposition since both thioglycolic acid and ethanolamine are miscible with water. The CZTS nanoparticles are formed in the film after high temperature treating. If use the CZTS nanoparticles that are already formed in precursor solution by high temperature heating (120°C) (Fig.3.2 g), the nanoparticles can be collected by centrifuging and then deposited by doctor blade method. The as formed layer can be further annealed at higher temperature (450-500°C) to promote the further crystallization.

## 3.2.4 Characterization

The surface morphologies of CZTS films were observed by using a scanning probe microscope (Solver P47H, Program version 845, NT-MDT, Zelenograd, Moscow, Russia). The XRD patterns of nanoparticles were obtained with an ARL X'TRA X-ray diffractometer with Cu-Kα radiation ($\lambda$ = 0.15405 nm). The elemental composition of the CZTS nanoparticles was measured by EDS with XL30 ESEM (FEI-Philips) installed with an EDAX micro-analytical system. Raman spectra of CZTS were collected by the 632.8 nm line of a He-Ne laser and carried out in backscattering geometry by means of a LabRam HR spectrometer (Horiba-Jobin Yvon), mounting a 600 lines/mm grating and equipped with a multichannel detector (a CCD with 256x1024 pixels) cooled by liquid nitrogen. To minimize the laser irradiation damage of the investigated samples, these spectra were recorded under an optical density filter OD1 (0.6mW), OD2 (0.06mW), OD3 (0.006mW) using an 80X objective having a NA close to 1, during an integration time of 100s ,600 s, 900s.

## 3.3 Results and discussion

The $Cu_2ZnSnS_4$ (CZTS) nanoparticles were synthesized with two methods in this work. For the first method in aqueous solution, we used copper and zinc nitrates (Cu $(NO_3)_2 \cdot 2.5H_2O$ and Zn $(NO_3)_2 \cdot 6H_2O$) and tin precursor complex solution which was prepared from Sn powder and iodine solid in ethanol by stirring and heating, and diluted in $(NH_4)_2S$ to form metal chalcogenide complexes (MCCs) [73]. When the three solutions of Cu (Fig. 3.2 a), Zn (Fig. 3.2 b) and Sn (Fig. 3.2 c) were mixed, an exothermic reaction takes place immediately, and the black coloured CZTS aqueous precursor solution was formed (Fig. 3.2 d). The as prepared CZTS aqueous solution was stable for several months without precipitation and aggregation due to the ligand protection from MCCs. After deposition and high temperature treating, the CZTS crystal forms. The other elements and ligand molecules can thermally decompose into volatile species during annealing and be removed completely [74].

In the second method with organic solution, the metal powders were directly dissolved in mixture solution of thioglycolic acid and ethanolamine. The solution changed to clear and transparent yellowish colour when the metal powders dissolved (Fig. 3.2 e). The solution changed further to wine colour when sulfur powder was added and dissolved (Fig. 3.2 f). After heating and stirring at high temperature (120°C), the solution changed to black due to the CZTS nanoparticles formed in solution which can be used to deposit CZTS film (Fig. 3.2 g). Alternatively, the precursor solution (Fig. 3.2 f) can be directly used to deposit and then annealed in sulphur and argon atmosphere known as sulfurization, the CZTS nanoparticle forms in deposited layer after annealing.



Figure 3.2 CZTS precursor in aqueous solution (a-d) and organic solution (e-g). (a) Copper nitrate in deionized water. (b) Zn nitrate in deionized water. (c) Sn precursor complex solution in $(NH_4)_2S$. (d) CZTS aqueous solution after mixture of a, b and c. (e) The dissolved Cu, Zn and Sn powders in thioglycolic acid and ethanol amine. (f) The dissolved Cu, Zn, Sn and S powders in thioglycolic acid and ethanol amine. (g) The as formed CZTS nanoparticles in organic solution.

## 3.3.1 X-ray diffraction analysis

X-ray diffraction (XRD) measurements were carried both for the samples before and after

high temperature annealing. Figure 3.3 shows the XRD patterns (along with corresponding ICDD patterns) of $Cu_2ZnSnS_4$ prepared in aqueous solution. Before annealing, the XRD patterns of the CZTS powders from aqueous precursor solution (Fig. 3.2 d) show that the desired phase was not formed (Fig. 3.3 a). After high temperature annealing (up to 500°C), the as formed CZTS crystals show major peaks at 28.4°, 47.3°, and 56.2° (2θ°values), which can be attributed to the diffraction of (112), (220) and (312) planes, corresponding to the kesterite structure (JCPDS 26-0575) (Fig. 3.3 b). The high temperature annealing is essential for the forming of kesterite phase. The size of nanoparticle is calculated from the widths of the (112) and (220) diffraction peaks (at 28.4° and 47.3°) using Scherrer analysis:

$$D = \frac{K\lambda}{\beta cos\theta}$$
(3.1)

Where $\lambda$ is the X ray wavelength of 1.54nm and K is constant of 0.89, $\theta$ is the Bragg diffraction angle and $\beta$ is the FWHM of the diffraction peak.

The binary and ternary sulphides such as ZnS, $Cu_2S$, CuS and $Cu_2SnS_3$ have similar XRD patterns with kesterite/stannite CZTS [75]. To identify if there are binary or ternary sulphide impurities, the Raman spectroscopy test was carried out and the result was shown in figure 3.8. Raman test confirm that after annealing, the binary or ternary sulphide impurities were not presented in CZTS crystals.
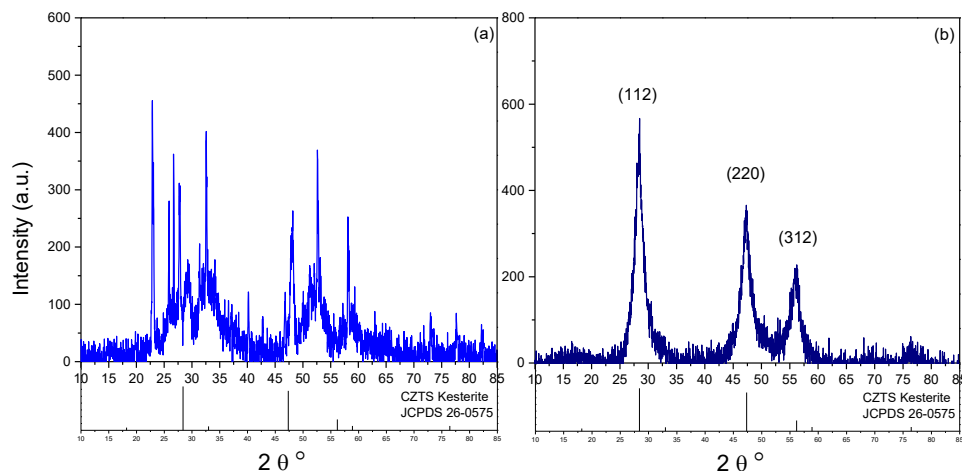


Figure 3.3 XRD diffraction spectrum of CZTS nanoparticles synthesized from aqueous solution. The reference of kesterite structure of CZTS was shown in below (JCPDS 26-0575). Upper solid line is for the before annealing (a) and after annealing (b) (up to 500°C)

In order to have more structural information, the observed XRD pattern was fitted by MAUD software based on the Rietveld refinement method. The accuracy of the profile fitting was judged by the goodness of fit (GOF) and the reliability parameters, include Rw (weighted profile factor), Rexp (expected weighted profile factor) and Rb (the Bragg factor) which are defined as:[76]

$$R_w = \left[ \frac{\Sigma w_i (I_{io} - I_{ic})^2}{\Sigma w_i I_{io}^2} \right]^{1/2}$$
(3.2)

$$R_b = \frac{\Sigma|I_{ko}-I_{kc}|}{\Sigma I_{ko}} \qquad\qquad (3.3)$$

$$R_{exp} = \frac{N-P}{\Sigma w_i I_{io}^2} \qquad\qquad (3.4)$$

$$GOF = \frac{R_w}{R_{exp}} \qquad\qquad (3.5)$$

Where $I_{io}$ and $I_{ic}$ are the observed and calculated intensities at the ith step, $I_{ko}$ and $I_{kc}$ are the intensities assigned to the kth Bragg reflection at the end of the refinement cycles; $w_i = (1/I_{io})$ is the weight factor, N is the number of data points and P denotes the number of parameters refined. This result is shown in figure 3.4.



Figure 3.4 The XRD refinement and the experimental pattern of CZTS nanoparticles synthesized from aqueous solution (dot: experimental data, upper red solid line: calculated pattern, lower blue solid line: subtracted pattern).

For the CZTS nanoparticles synthesized in organic solution by heating (Fig. 3.2 g), the diffraction spectrum from which is analyzed by MAUD and the result is shown in figure 3.5. The major XRD diffraction peaks appear at 2θ degree of 26.99°, 28.4°, 30.11°, 39.68°, 47.48°, 51.56° and 56.3° are attributed to the (100), (002), (101), (102), (110), (103) and (112) planes respectively, matching well with the theoretical simulation value of wurtzite CZTS [77]. These peaks are clearly resolved which indicate the unambiguous presence of wurtzite phase. They are absent and very weak in ZnS blende and tetragonal $Cu_2SnS_3$, respectively, which possess the similar diffraction patterns to CZTS [78]. The wurtzite CZTS XRD pattern was also refined using MAUD software with the same XRD peaks positions of Zn(II) replaced by Cu(I), Zn(II), and Sn(IV) in the wurtzite ZnS crystal structure [77]. No characteristic peaks for other impurities, such as CuS, $Cu_2S$, or $Sn_xS_y$, are observed in the XRD pattern. The wurtzite phase of CZTS nanocrystals have also been synthesized in other approaches [79]. The size of the nanocrystals formed in organic solution is around 14.28 nm as calculated from the widths of the (112) and (220) peaks (at 28.4° and 47.4°) using Scherrer equation.
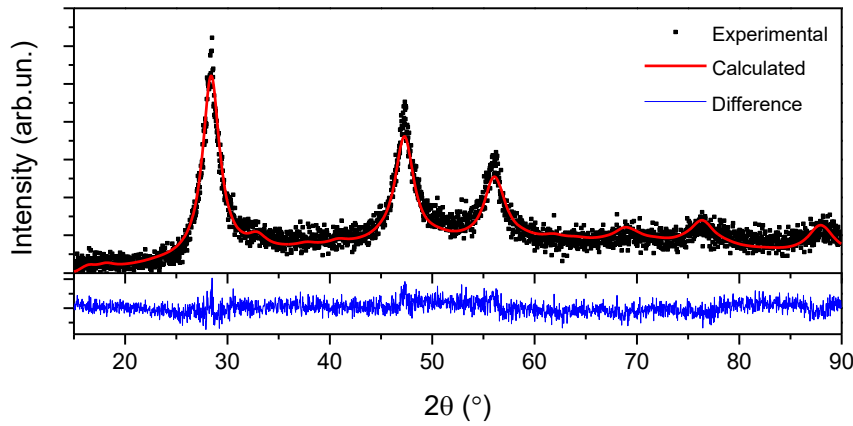
Figure 3.5 The XRD calculated and experimental patterns of CZTS nanoparticles synthesized from organic solution (dot: experimental data, upper red solid line: calculated pattern, lower blue solid line: subtracted pattern).

We also used microwave machine to obtain CZTS nanoparticle with the organic precursor solution. Microwave assisted method is a fast way to produce nanoparticles in solution. The machine offered a safe way to conduct reaction at high temperature and pressure. Typically, the solution (Fig. 3.2 f) was heated in microwave machine at 190°C-230°C for 5-15 minutes and followed by washing with deionized water. The obtained powder was analysed by x ray diffraction. The XRD pattern indicates that the NPs formed kesterite phase with trace amount of wurtzite mixed (Fig. 3.6). The CZTS nanoparticles synthesized at 230°C for 15 minutes was further refined by MAUD and the result is shown in figure 3.7.
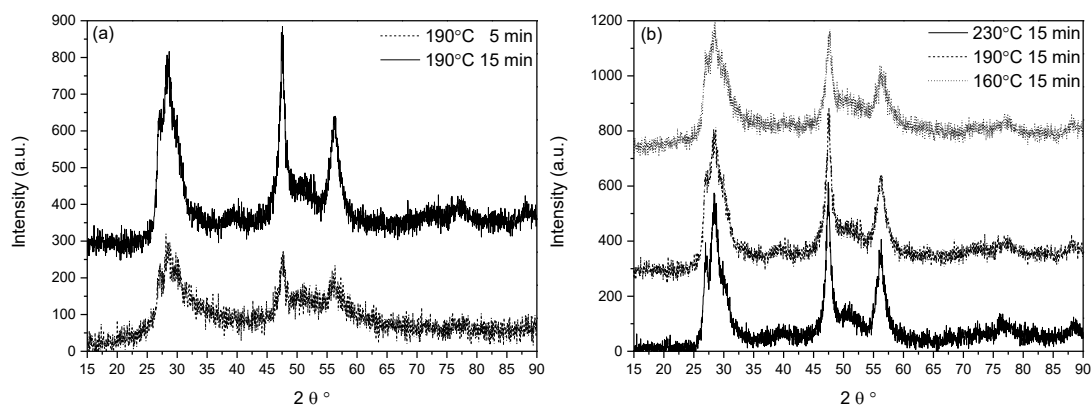


Figure 3.6 XRD pattern for the CZTS nanoparticles synthesized by microwave synthesizer machine from organic solution at different temperature and reaction time.
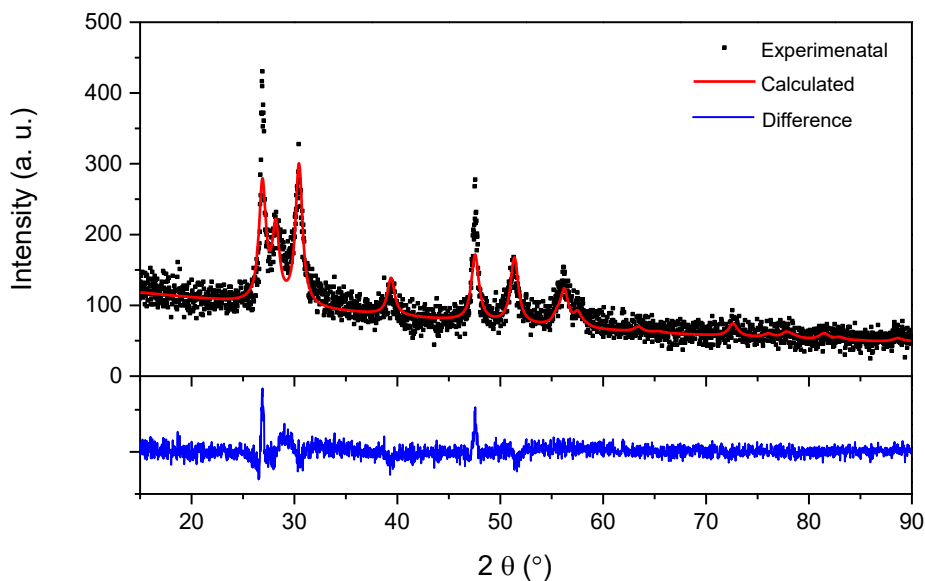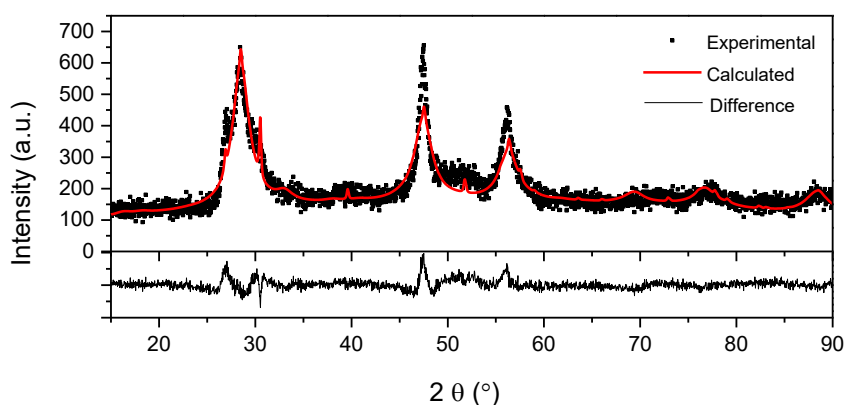
Figure 3.7 The XRD calculated and experimental patterns of CZTS nanoparticles synthesized from organic solution (dot: experimental data, upper red solid line: calculated pattern, lower blue solid line: subtracted pattern). The reaction was performed by microwave machine at 230°C for 15 minutes.

The crystallite size, root mean square microstrain and lattice parameters were extracted and the results are listed in table 3.1. The crystallite sizes obtained by MAUD software are in good agreement with the calculated values using the Scherrer's formula. The values of GOF indicate a good fitting of the observed XRD pattern by the derived pattern.

Table 3.1 Results from Rietveld analysis of the CZTS samples

|  | CZTS aqueous | CZTS organic Heating | CZTS organic Microwave |
|---|---|---|---|
| Lattice parameter (Å) a | 5.495±0.005 | 3.822±0.001 | 5.415±0.030 |
| Lattice parameter (Å) c | 10.777±0.021 | 6.323±0.003 | 10.841±0.123 |
| Size Scherrer (nm) | 4.125 | 14.28 | 4.589 |
| Size MAUD (nm) | 5.224±0.083 | 13.568±0.367 | 4.990±0.102 |
| rs-microstrain | $3.373\pm0.154\ e^{-7}$ | $4.886\pm0.618\ e^{-7}$ | $5.531\pm0.276\ e^{-8}$ |
| Rw (%) | 9.776 | 14.744 | 12.992 |
| Rb (%) | 7.740 | 11.607 | 10.446 |
| Rexp (%) | 6.786 | 10.387 | 7.082 |
| sig | 1.440 | 1.419 | 1.834 |
| GOF | 1.440 | 1.419 | 1.835 |
| Volume fraction | Kesterite 100% | Wurtzite 100% | Kesterite 98.2%; Wurtzite 1.8% |

## 3.3.2 Raman analysis

Raman spectroscopy analysis was performed for further analysis of the synthesized sample and the result is shown in figure 3.8. After annealing, the Raman spectrum exhibits a broad Raman band centered around 340 cm$^{-1}$, typical of kesterite phase. The band is broad due to phonon confinement in small nanocrystals [80].
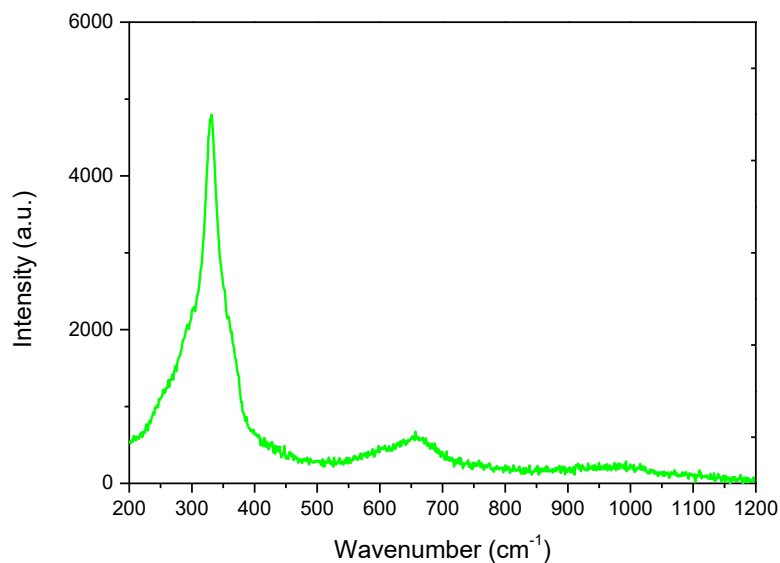
Figure 3.8 Raman spectrum of CZTS nanoparticles synthesized in aqueous precursor solution after annealing at 500 °C.

## 3.3.3 EDS analysis

EDS was used to analyse the elemental composition of the nanocrystals (Fig. 6). The precursor concentrations of Cu/Zn/Sn/S were set to 2:1:1:4 according to the stoichiometry of $Cu_2ZnSnS_4$. The stoichiometry can be easily tuned (e.g., slightly Cu poor or Zn rich) by varying the molar ratios of precursor metal salts used in the synthesis. In this study, the elemental ratios were set as Cu/(Zn+Sn) = 0.8 and Zn/Sn = 1.2. EDS was performed for the samples synthesized from aqueous and organic solution. The result indicates that the final elemental ratio among the cations was Cu/(Zn+Sn) = 0.74 and Zn/Sn = 1.3 for the samples from aqueous precursor solution (Fig. 3.9 a), and Cu/(Zn+Sn) = 0.52 and Zn/Sn=2.47 for the samples synthesized from organic precursor solution (Fig. 3.9 b). Since tin and copper atoms replace the zinc site partly in wurtzite ZnS to form wurtzite CZTS, compare to zinc, less amount of tin and copper may present in CZTS nanoparticles. And this few amount of off stoichiometry may favour the formation of wurtzite phase which possess higher tolerance for cation disorder in compound [81,82].

39
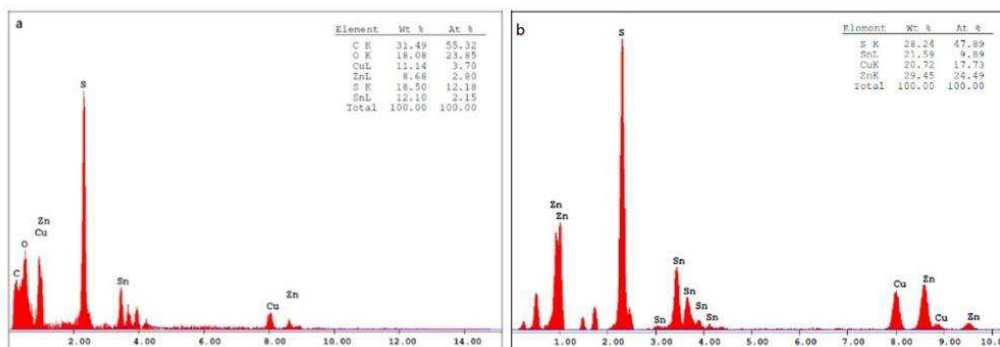
Figure 3.9 EDS analysis for the CZTS nanoparticles. (a) Sample synthesized from aqueous precursor solution; (b) Sample synthesized from organic precursor solution.

## 3.3.4 Film deposition

CZTS films can be obtained by suitable coating methods (e.g., spin coating, or doctor blading) and then annealed in argon and sulfur atmosphere to form polycrystalline layer with up to micron sized grains. The annealing process is needed to promote grain growth. Figure 3.10 shows SEM image of CZTS nanocrystal film that was doctor bladed with the CZTS sample synthesized from organic solution. The CZTS nanoparticles sintered into micrometer sized grains after annealing, which might lead electrical shorts or high shunt currents between solar cell device layers. The grain formation during drying process from a dispersion is complex and depends on many variables, such as film thickness, solvent evaporation rate, nanocrystal size, ligand molecules and the substrate property [83–85]. In order to prepare better films the coating and drying process can be repeating several times.
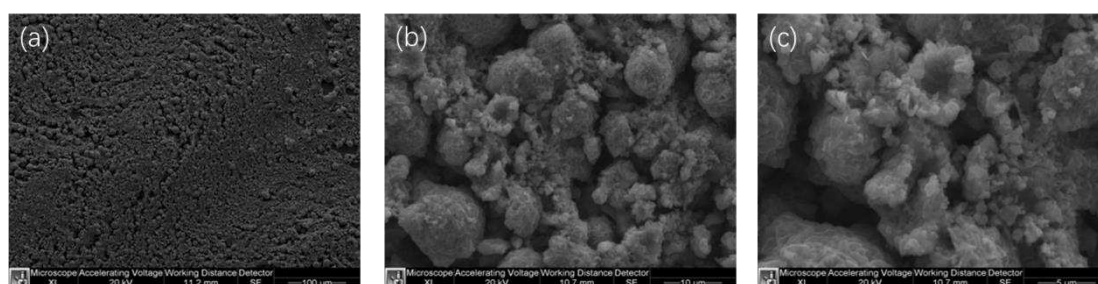


Figure 3.10 SEM images of the single CZTS layer from the CZTS nanoparticles synthesized from organic solution.

The CZTS layer deposited by spin coating with the organic precursor solution was also observed by AFM scanning scope and the AFM images was shown in figure 3.11. Further studies are in progress to optimize the deposition conditions for a high performance solar cell device.
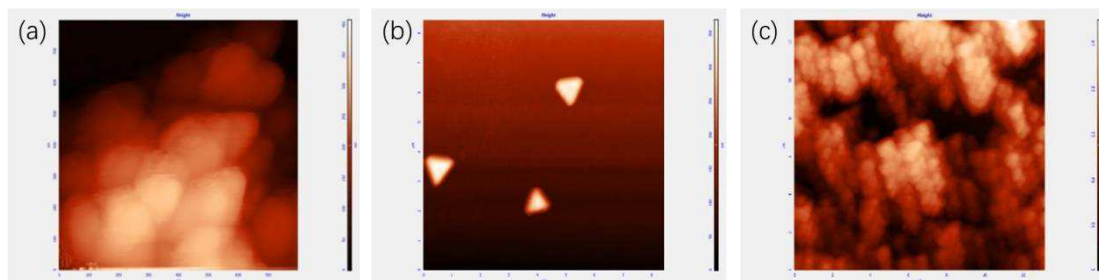
Figure 3.11 AFM images of the single CZTS layer of the CZTS nanoparticles synthesized from aqueous solution (a, b) and organic solution (c).

## 3.4 Conclusions

In summary, we used two methods for rapid and easy synthesis of semiconductor CZTS nanocrystals, one by using copper and zinc nitrates and tin precursor in thiourea and ammonia sulfide aqueous solution, and another one by dissolving copper, zinc, tin and sulfur powders in mixture solution of thioglycolic acid and ethanolamine. X-ray diffraction and Raman spectroscopy measurements confirm that kesterite phase CZTS nanoparticles were formed by the synthesis in water after annealing, while both wurtzite and kesterite phases were obtained by the synthesis in organic solvents. The high temperature and longer reaction time promote the crystallization of CZTS nanoparticle.

# Chapter 4 Zinc sulfide

## 4.1 Introduction

ZnS mainly occurs in nature as the mineral sphalerite or zinc blende with zinc and sulfur atoms tetrahedrally coordinated and takes a stable cubic crystalline form, while the hexagonal analog is known as the mineral wurtzite, see figure 4.1. The lattice constant for zinc sulfide in the zinc blende crystal structure is a = 0.54 nm, while for wurtzite, a = b = 0.382 nm and c = 3.12 nm. The refractive index of sphalerite is 2.37 (measured via sodium light 589.3 nm) [86,87]. Both sphalerite and wurtzite are intrinsic, wide band gap II-VI semiconductors. The sphalerite ZnS has a band gap of about 3.54 eV at 300 kelvins while wurtzite has a band gap of about 3.91 eV. ZnS can be doped as either an n-type semiconductor or a p-type semiconductor.
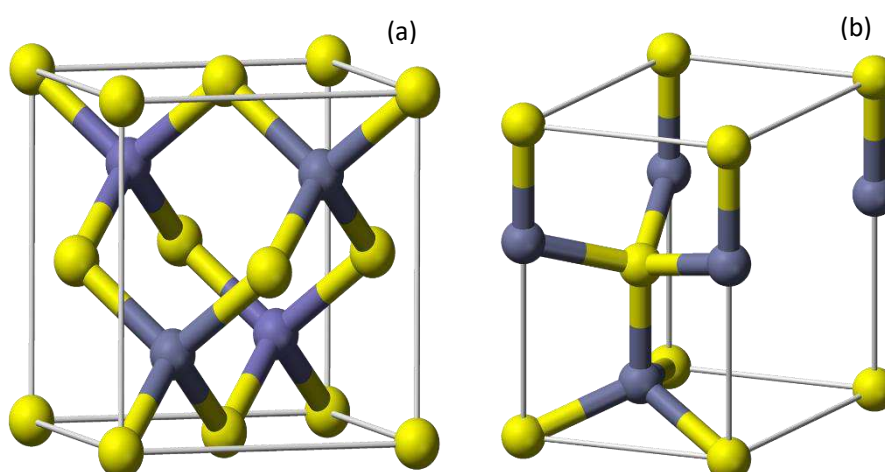


Figure 4.1 Crystalline structure of ZnS with sphalerite form (a) and wurtzite form (b). The grey balls represent metal atoms and yellow balls Sulphur or selenium atoms. Figure from https://en.wikipedia.org/wiki/Zinc_sulfide

With addition of few amount of suitable activator, zinc sulfide exhibits photoluminescence, and is currently used in many applications such as cathode ray tubes and glow in the dark products [88]. Copper gives long time greenish glow in the dark [89] and green phosphorescence also results from the presence of elemental sulfur species and sodium impurities [90]. Manganese doping yields an orange red color at around 585 nm [91]. The emitting color is bright blue when activated by silver [28]. ZnS powder is an efficient photo catalyst which produces hydrogen from water upon illumination. Sulfur vacancies can be introduced in ZnS during its synthesis and boosts the photocatalytic activity through enhanced light absorption [92]. Moreover, as a semiconductor material, ZnS can also be used in CZTS and CIGS solar cells as the buffer layer to collect electrons

[93][94][95], and in field effect transistors as biological and chemical sensors [96]. ZnS is also the most common quantum dot shell material since it has a wide band gap and is relatively inert chemically. In addition, ZnS has a small lattice mismatch (<5%) with common QDs such as CdS, CdSe and CIS to forming the shell without stress and strain at the core shell interface.

ZnS can be synthesized in various methods, such as one pot synthesis [97], sol-gel formation [98], hydrothermal synthesis [99], solid state synthesis [100]. and chemical bath deposition method [101,102].

In this study, we prepared ZnS film with chemical bath deposition (CBD) method. The x ray diffraction indicated that single phase ZnS crystal was formed. The film displayed high transparence in visible and infra-red-light region. The aim of this study is to prepare ZnS buffer layer for future solar cell application, and understand the optical property of ZnS for potential application in photoluminescence.

## 4.2 Experimental

### 4.2.1 Chemicals

- Zinc sulphate monohydrate, $ZnSO_4 \cdot H_2O$, MW = 179.45, Carlo Erba Reagents,97.5%

- Tri-Sodium citrate dehydrate, $C_6H_5Na_3O_7 \cdot 2H_2O$, MW = 294.1 g/mol, Aldrich, ≥99.0%

- Ammonium solution, $NH_4 \cdot OH$, 28-30% in water, Carlo Erba Reagents

- Thiourea (TU), $CH_4N_2S$, MW = 76.11 g/mol, Merck Schuchardt OHG, ≥98%

### 4.2.2 Synthesis

We used soda lime glass substrate to deposit ZnS thin film with the CBD method. Before CBD the substrate was pretreated in following steps: (1) Cleaning in water with soap and rinsing with deionized water. (2) Cleaning in acetone with ultrasonic vibration for 10 min, and then rinsing with deionized water. (3) Cleaning in ethanol with ultrasonic vibration for 10 min, and rinsing with deionized water. (4) Cleaning in deionized water and then drying in room temperature. Zinc sulfate ($ZnSO_4$) was used as the source of zinc ions ($Zn^{2+}$), thiourea ($SC(NH_2)_2$) as the source of sulfur ions ($S^{2-}$), tri-sodium citrate ($Na_3C_6H_5O_7$) as the complex agent, the pH value was adjusted with 30% ammonia water $NH_3 \cdot H_2O$. To prepare the chemical bath reaction, tri-sodium citrate 0.08M (1.1764g in 50mL water), zinc sulfate 0.03M (0.2692g in 50 mL water) and thiourea 0.06M (0.2284g in 50mL water) were in turn added into 50mL deionized water and mixed up thoroughly, the bath pH value was adjusted with around 3mL ammonia water to 11. The bath temperature and deposition time determines the thickness of the film, herein we set at 80°C and 20-40 min to get desired thickness. Once the reaction finished, the ZnS film was cleaned with deionized

water and dried with a $N_2$ gas stream.

## 4.2.3 Characterization

The surface morphologies of ZnS films were observed by using a scanning probe microscope (Solver P47H, Program version 845, NT-MDT, Zelenograd, Moscow, Russia), an X-ray diffractometer (ARL X'TRA X-ray diffractometer with Cu-Kα radiation, λ = 0.15405 nm) was used to determine the crystal structure of the ZnS films, an EDS set up with XL30 ESEM (FEI-Philips) installed the EDAX micro-analytical system was used to determine the elemental composition of the ZnS nanocrystals, an ultraviolet–visible spectrometer was used to measure the transmittance of the ZnS thin films.

## 4.3 Results and discussion

ZnS thin film was synthesized by CBD method. The obtained thin film was analyzed by XRD diffraction. As seeing from figure 4.2, the three main diffraction peaks that represent the typical sphalerite or zinc blende are seen at 28.64°, 47.51°, and 56.36°, which identified as 111, 220 and 311 planes of the tetragonal structure of the zinc blend phase.
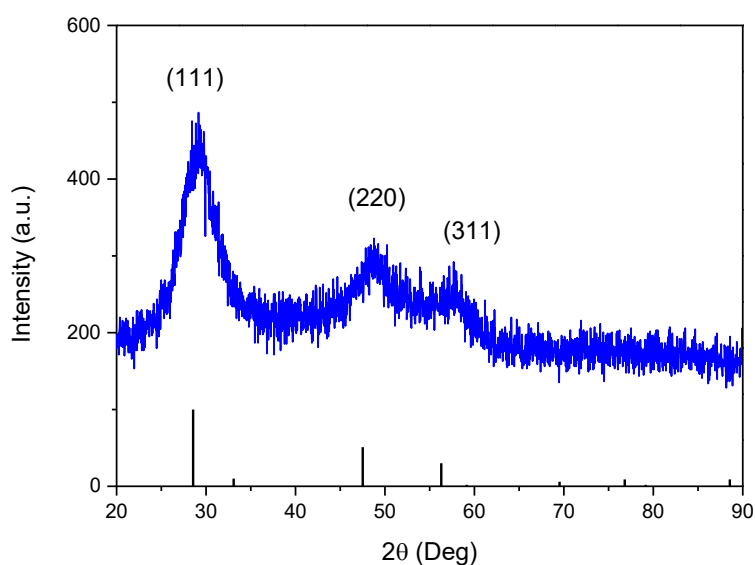


Figure 4.2 XRD diffraction pattern of ZnS synthesized by CBD method.

The film was also observed by AFM scanning scope, and the result is shown in figure 4.3. The AFM image shows that the ZnS film is homogeneously crystalized without apparent pin holes or cracks formed.
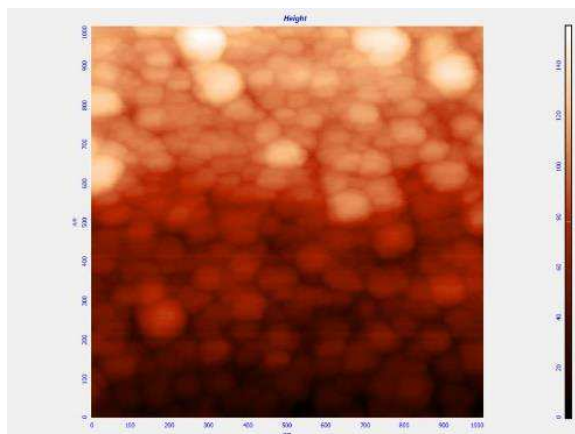
Figure 4.3 AFM image of ZnS synthesized by CBD.

The elements were analyzed by EDS, as shown in figure 4.4, the atomic ratio between Zn and S is 50.72:49.28, close to the stoichiometry of ZnS sphalerite.



```
EDAX ZAF Quantification (Standardless)
Element Normalized
SEC Table : Default

Element    Wt %     At %    K-Ratio     Z         A         F
  S K     32.27    49.28    0.2262    1.0969    0.6389    1.0000
  ZnK     67.73    50.72    0.6411    0.9498    0.9966    1.0000
  Total  100.00   100.00
```
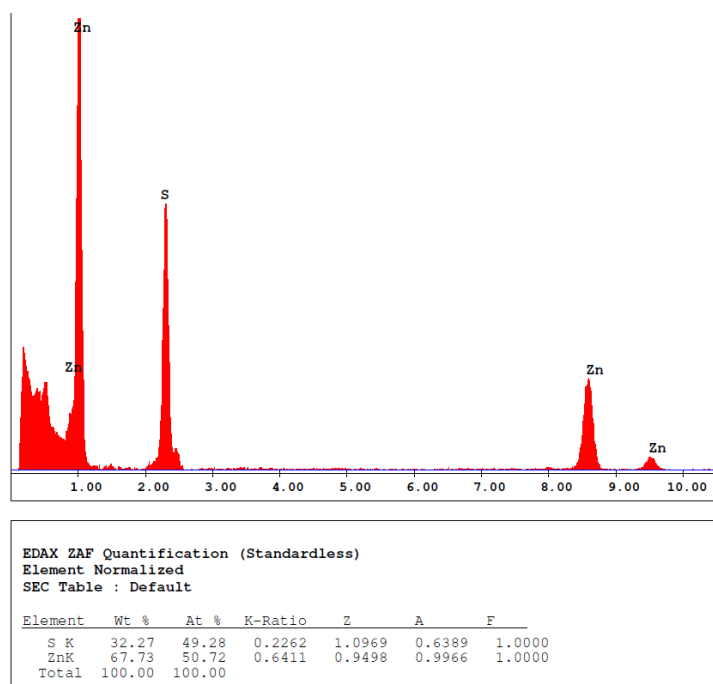
Figure 4.4 EDS spectrum of ZnS synthesized by CBD.

The transmittance was studied by UV-vis spectrometer. As shown in figure 4.5 for the ZnS synthesized for 20 min, the obtained ZnS film has good transmittance for visible light, which indicate that it is might suitable as the buffer layer for solar cell application.
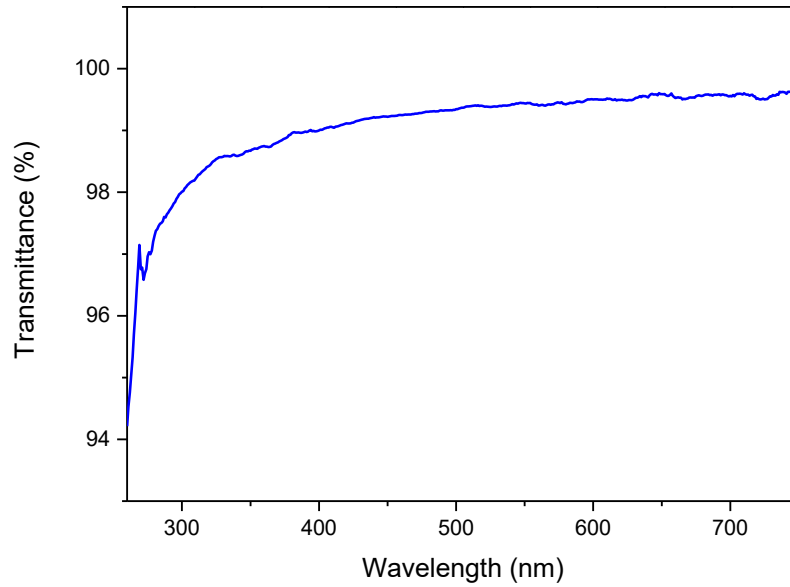
Figure 4.5 Transmittance spectrum of ZnS synthesized by CBD.

## 4.4 Conclusions

Chemical bath deposition offered an effective method to synthesize high quality ZnS film for potential application in photovoltaic and photoluminescence area. The as synthesized ZnS film possess single crystal phase of sphalerite, uniformly crystalized without any pinholes and cracks. It has high transmittance to visible and infra-red light, which might be suitable as the buffer layer for solar cell application.

# Chapter 5 Perovskite compounds

## 5.1 Introduction

Perovskites are a crystallographic family with the general chemical formula $ABX_3$ (A = Cs, $CH_3NH_3$, or $CH_2NH=CH$; B = Pb or Sn; X = I, Br, or Cl), consists of organic components in cuboctahedral A site and inorganic components in octahedral B site, where the B atom is a metal cation (typically $Pb^{2+}$ or $Sn^{2+}$) and X is monovalent halide anion $Cl^-$, $Br^-$, or $I^-$. The A cation is selected to balance the total charge, and it can be $Cs^+$, $Rb^+$, $K^+$, or a small organic molecule [103,104], see figure 5.1. Due to the cheap and simple producing process, low cost, and superior optoelectronic properties, it emerged as a new class of semiconductors with great potential for a variety of applications, such as high-efficiency photovoltaic cells, light-emitting diodes, lasers, and photodetectors [105–109]. Perovskite solar cells (PSCs) have experienced the fastest efficiency increase in reported ever obtained in photovoltaic technology since it was reported as a variant of the dye-sensitized solar cell configuration [110]. It has undergone a rapid expansion in third generation photovoltaic devices over the past few years [111,112] and recent progress has pushed the power conversion efficiency (PCE) up to 21% [17].
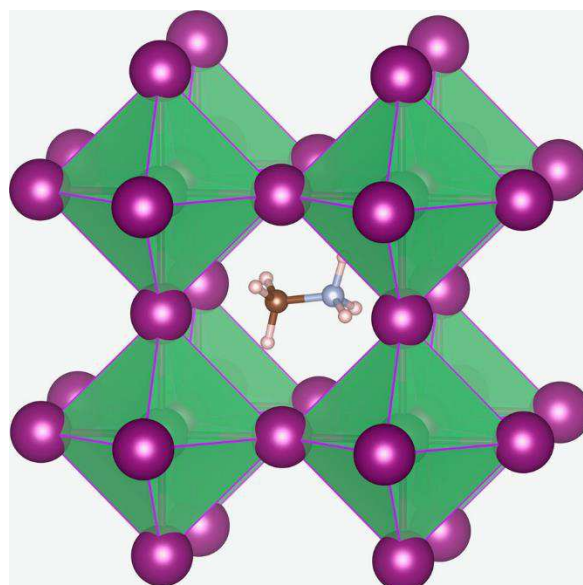


Figure 5.1 Crystal structure of $CH_3NH_3PbX_3$ perovskites (X=I, Br and/or Cl) [113].

The common single junction PSC architecture can be catalogued into mesoscopic and planar heterojunction structures (Fig. 5.2). In the mesoscopic structure, a mesoporous metal oxide scaffold, such as titanium oxide ($TiO_2$) or aluminum oxide ($Al_2O_3$) is used to reside the perovskite. Meantime, PSCs can also afford a planar heterojunction configuration to avoid the harsh processing of mesoporous $TiO_2$. The planar devices include regular (n–i–p) and inverted (p–i–n) types (Fig. 5.2 b,c) [114].
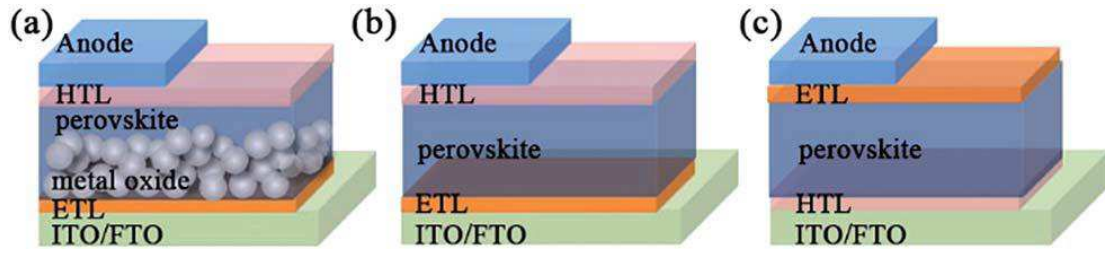
Figure 5.2 PVSCs device architectures of mesoporous, regular (n–i–p) and inverted (p–i–n) type [114].

With remark electronic conductivity, carbon materials have been identified as the good electron or hole transport materials in PSCs. They also provide flexibility and long-term stability to the devices. In recent years, numerous efforts were focused on the application of carbon materials in PSCs. It can work as charge transport layers to improve charge transfer, additives to perovskite layers to enhance the performance of devices, and counter electrode to collect holes.

The stability issue is a big challenge for developing PSCs, since perovskite degrades under humidity following the process: [115].

$$CH_3NH_3PbI_3 \rightarrow CH_3NH_2 + HI + PbI_2 \tag{5.1}$$

It was found that carbon counter electrodes can block moisture effectively to protect perovskite and ensure long-term stability. By using carbon counter electrodes, the stability of this device showed excellent over 1300 h [116]. Perovskite is also unstable at high temperature [117]. It was found that carbon counter electrode based PSCs showed good stability at high temperature as well. When suffering the temperature of 60°C, the device showed only a modest efficiency loss and Au counter electrode based solar cells experienced a dramatic efficiency loss [118]. Moreover, the PSCs using carbon fibers as back contact degrade slower than that with Au counter electrode at high temperature up to 85°C [119]. These facts indicate that carbon counter electrode based PSCs are more stable.

Despite the significant developments in lead halide perovskite, the consideration of high toxicity of lead and bioaccumulation in the ecosystem has stimulated the search for other materials with environmentally benign and comparable optical and optoelectronic performance. There have been efforts to replace lead with nontoxic elements, such as Sb, Ge, Bi, and Sn [44,120–122]. Among them, cesium tin halides (CsSnX$_3$, X=Cl, Br, I) perovskites are promising candidates due to the similar semiconductor properties [123–125]. However, the instability of CsSnX$_3$ perovskites due to its intrinsic unstable Sn$^{2+}$ ions requires the fabrication and testing process in nitrogen filled glove box and thus has prevented the fabrication of devices that can withstand sustained operation under ambient air conditions.

In contrast to unstable CsSnX$_3$ nanocrystals, which needs to be handled under an inert atmosphere, the perovskite variant Cs$_2$SnI$_6$, made from tetravalent tin (Sn$^{4+}$) instead of divalent tin (Sn$^{2+}$) precursors, were found to be more stable against oxidation under ambient conditions [126]. The cubic Cs$_2$SnX$_6$ (X = Cl, Br, I) structure is a defect variant of the perovskite in which half of the B sites are void, creating isolated [SnX$_6$] octahedra. The

sites between the [SnX$_6$] octahedra are filled with Cs atoms in a regular 12-fold coordination [127]. This compound formula gives the semiconducting perovskite Cs$_2$SnI$_6$ a band gap of 1.48eV and high absorption coefficient (over 10$^5$ cm$^{-1}$) [128]. The use of Sn$^{4+}$ defect perovskites as hole transporters in dye-sensitized solar cells with an efficiency of nearly 8% has been recently reported [129]. The Cs$_2$SnI$_6$ nanocrystals were synthesized with a hot injection method at 220 °C and a field effect transistors (FETs) that displayed a p-type semiconductor behavior with high hole mobility (>20 cm$^2$/(V s)) was fabricated [130].

It was also synthesized using a mixture of aqueous HI and H$_3$PO$_2$ with SnI$_2$ and CsI dissolved at 120 °C, the solar cell device with an efficiency of 0.86% was fabricated using ZnO as scaffold [131]. It was reported to obtain the Cs$_2$SnI$_6$ by reaction of SnI$_4$ and CsI in fused silica tubes that heated to 400 °C for 5 h and subsequently annealed at 200 °C for 5 days [127]. The CsSnI$_3$ that formed by vapor deposition followed by solid-state reaction at 190–330°C for 1800 second can undergo a phase transformation to form Cs$_2$SnI$_6$ in air [128].

In this work, not only produced the methylammonium lead trihalide solar cell device in an easy and simple method, we also synthesized lead free and stable perovskite derivative Cs$_2$SnI$_6$ with a facile one pot synthesis method in ambient air and low temperature condition by reacting Cs$_2$CO$_3$ and SnI$_4$ that formed with Sn powers and iodine in ethanol solution.

# 5.2 Experimental

## 5.2.1 Chemicals

- Caesium carbonate anhydrous, Cs$_2$CO$_3$, MW = 325.82 g/mol, BDH Laboratory Supplies Poole, BH15 1TD, England, 99.5%

- Tin powder, Sn, MW = 118.71 g/mol, Aldrich, 99.0%

- Iodine powder, I$_2$, MW = 253.81 g/mol, Riedel de Haen, 99.8%

## 5.2.2 Perovskite CH$_3$NH$_3$PbI$_3$ synthesis

(CH$_3$NH$_3$)PbI$_3$ was formed on TiO$_2$ surface from the γ-butyrolactone (GBL) solution containing equimolar mixture of CH$_3$NH$_3$I and PbI$_2$. CH$_3$NH$_3$I was synthesized by reacting 27.86ml methylamine (40% in methanol) and 30 mL of HI (hydroiodic acid) (57 wt% in water) in 250 mL round bottomed flask at 0°C for 2 h with stirring. The precipitate was collected by evaporation at 50°C for 1 h. The obtained methyl ammonium iodide (MAI: CH$_3$NH$_3$I) was washed with diethyl ether three times by stirring for 30 min, and then dried at 60°C in vacuum oven for 24 h. The synthesized CH$_3$NH$_3$I powder was mixed with PbI$_2$ at 1:1mol ratio in γ-butyrolactone at 60°C for 12 h, followed by filtering twice using a 13mm

diameter and 0.45mm pore PVDF syringe filter. The obtained solution is used for the spin coating on $TiO_2$ surface and for in situ formation of $(CH_3NH_3)PbI_3$. The concentration of the equimolar mixture of $CH_3NH_3I$ and $PbI_2$ was varied from 10.05 to 41.22 wt% (10.05, 20.13, 30.18, 40.26 and 41.22 wt%). For instance, 40.26 wt% solution contains 0.0123 mol $CH_3NH_3I$ (1.955g) and 0.0123 mol $PbI_2$ (5.728 g) in 10 mL γ-butyrolactone (with the density of 1.14 g $mL^{-1}$).

## 5.2.3 $TiO_2$ paste preparation

### 5.2.3.1 $TiO_2$ paste preparation method A

(1)   0.33 M $TiOCl_2$ solution is from hydrolysis of $TiCl_4$.

(2)   $NH_4OH$ (28%) solution adding dropwise into $TiOCl_2$ solution, when pH=9, stop.

(3)   Heating at 90°C for 3 hours, filtrate the solution.

(4)   Purify the resulting $TiO(OH)_2$ wet cake by repeated deionized water washing until no Cl ion presented in solution (test by adding $AgNO_3$ in the discarded supernatant solution, see if AgCl precipitate).

(5)   Add D water and stir 10 min get 300ml 2wt% $TiO(OH)_2$ solution.

(6)   Add 200ml 35% hydrogen peroxide such that $H_2O_2/Ti^{4+}$ ratio is around 40.

(7)   Stir the solution constantly in ice bath, once finish the adding of $H_2O_2$, the colour of precipitate change from white to yellowish, and finally light orange or reddish-coloured transparent solution formed within 1 hour.

(8)   Hydrothermal treat the solution at 250°C for 12h.

(9)   Add several drops of concentrated nitric acid ($HNO_3$), and stir for 1h.

(10)   Add ethanol, treat with ultrasonic irradiation, centrifuge and re-disperse for three times.

(11)   Disperse the collected $TiO_2$ nanoparticles (around 50nm) in 100ml ethanol, mix with 4.5g (per 1g of $TiO_2$) of 10wt% ethanol solution of ethyl cellulose (EC) (equal amount of the two kinds: 9-11mPa.S, 5% methylbenzene/toluene, isopropanol 80:20 and 45-55mPa.S, 5% methylbenzene/toluene, isopropanol 80:20) and 4.4g (per 1g of $TiO_2$) terpineol. And then stir 10 min and homogenize by ultrasonic irradiation.

(12)   Produce the paste with mill grinder and rotary evaporator.

### 5.2.3.2 $TiO_2$ paste preparation method B

(1)   Mix 10.1g titanium (IV) isopropoxide (TTIP) solution and 2.069g acetic acid (HAC)

solution, stir 20 min at room temperature.

(2)   Pour the mixture into 50ml D water quickly (stir during pouring), stir vigorously 1 h.

(3)   Add 0.68 ml $HNO_3$, heat in water bath at 80°C, stir 3 hours.

(4)   When cooling down, filter by pump.

(5)   Adjust the volume to 63 ml together with the washing water, heat in autoclave at 220°C for 12 hours.

(6)   Take out the reaction solution and pour into a beaker, add 0.4ml $HNO_3$, treat with ultrasonic irradiation for 30 min, then stir 2 hours.

(7)   Filter with pumping filter, wash with ethanol, add more ethanol, and centrifuge under 9000 rpm 15 min.

(8)   Take the precipitate, mix with ethyl cellulose and terpineol in the following ratio: $TiO_2$ (2.845g), ethyl cellulose (EC) (0.7112g+0.7112g) in 14.23g ethanol, terpineol (11.54g).

(9)   After mixing, ball milling 10 h + ultrasonic treatment 30 min three times.

(10) Evaporate the excessive ethanol with rotary evaporator for 20 hours.

## 5.2.4 Carbon paste preparation

The carbon paste can be prepared by mixing the carbon nanoparticle (around 18 nm) and flaky graphite (approximately 5μm) and adhesive resin. We use carbon ink which was first dried, then dissolved in chlorobenzene and milled in mill grinder overnight.

## 5.2.5 Perovskite solar cell fabrication

### 5.2.5.1 Carbon back electrodes solar cell device

1) Etch the Fluorine tin oxide (FTO) glass: Put the scotch tape on the glass to protect the area needed from etching, put the Zn powders on the area need to be etched, drop diluted HCl twice on Zn powders, the FTO layer is etched at once. Then clean with tissue and ethanol, ultrasonic treat the glass in acetone and ethanol three times, see figure 4.2

2) Deposit the compact layer of $TiO_2$: Drop the solution of 0.15 M titanium diisopropoxide bis (acetylacetonate) in 1-butanol on the glass uniformly and then do spin coating at 3000 rpm for 20 second. After this, heat the glass in oven at 500°C for 30 minutes.

3) Deposit the mesoporous layer of $TiO_2$ which is from hydrolysis of $TiCl_4$ with spin coating at 3000rpm for 20 min. and heat treat the glass again at 500°C for 30 minutes.

4) $TiCl_4$ treatment for the glass in 0.02-0.03 M $TiCl_4$ solution: Specifically, put 500 ml D water in fridge for 1h to cool down the temperature, add 10-15ml $TiCl_4$ by drop wise in to

the D-water to get 0.02-0.03 M $TiCl_4$ solution, put the glass in a dish and add the $TiCl_4$ solution, cover with plastic film and heat at 70°C for 30 min. After that, wash with D-water two times and then with ethanol. Finally, anneal at 500°C for 30 min again. The reaction is: $TiCl_4 + H_2O/O_2 \rightarrow TiO_2 + HCl \uparrow$

5) Deposit perovskite layer (sequential deposition):

(1) Cut the glass in to a few pieces of squared shape, then fix the square glass on spin coater. Make a solution of 1M $PbI_2$ in N,N-dimethylformamide (DMF), and mix with a little 0.15M methylammonium iodide (MAI). Drop the solution on the glass and spin with low speed at 1000rpm for 5 s and then high speed at 6000 rpm for 20s. After that, heat the glass at 100°C for around 20 minutes.

(2) Fix the glass on the spin coater; drop the methylammonium iodide (MAI) propanol solution or Formamidinium iodide (FAI) propanol solution at low speed 500 rpm for 30s and then high speed at 2000 rpm for 20s. After that, heat the glass at 100°C for around 20 minutes. The reaction with $PbI_2$ in N,N-dimethylformamide (DMF) and MAI (0.038 M: 6 mg of $CH_3NH_3I$ in 1 ml 2-propanol) or FAI in propanol take place immediately, the black colored $MAPbI_3$ perovskite layer is formed and the $FAPbI_3$ displays yellowish color (see figure 4.3).

6) Deposit Carbon layer: Fix all the obtained glasses on a paper, doctor blade the MAI mixed carbon paste on them, heat at 100°C for 20 min. Then doctor blade the second layer of pure carbon paste, heat at 100°C for 30 min.

## 5.2.5.2 Silver counter electrode p-i-n solar cell device

1) Prepare the etched ITO glass (3*3cm$^2$) by ultrasonic wash with Na (OH) (3-5%) for 20 min, followed by ultrasonic wash with soap for 20 min, and then ultrasonic wash with ethanol and acetone 20 min.

2) Deposit PEDOT: PSS layer by spin coating at 500 rpm for 10 seconds, then at 4000 rpm 30 sec, the obtained PEDOT: PSS layer is around 40nm thick.

3) Deposit $CH_3NH_3PbI_3$ layer by dropping 200μl $CH_3NH_3PbI_3$ on the glass and spin coating at 5000 rpm for 30 seconds, add 150 μl chlorobenzene at 5 seconds, anneal at 80℃ for 10 min. The obtained $CH_3NH_3PbI_3$ layer is around 300nm thick.

4) Deposit fullerene $C_{60}$ layer with thermal evaporation at 400℃ for 20 min (A/S0.3, power 6.5%, $10^{-6}$mba), the obtained fullerene $C_{60}$ layer is around 40 nm thick.

5) Deposit 2,9-dimethyl-4,7-diphenyl-1,10-phenanthroline (BCP) hole blocking layer with thermal evaporation at 400℃ for 10 min (A/S0.1, power 6.5%, $10^{-6}$mba), the obtained BCP layer is around 8nm thick.

6) Deposit Ag layer at 400℃ for 40-50 min (A/S0.3, power 13-14%, $10^{-6}$mba), the obtained Ag layer is around 100nm thick.

### 5.2.5.3 Gold counter electrode n-i-p solar cell device

1) Prepare the etched ITO glass ($3*3cm^2$) by ultrasonic wash with Na (OH) (3-5%) for 20 min and ultrasonic wash with soap for 20 min, then ultrasonic wash with ethanol and acetone for 20 min.

2) Deposit $TiO_2$ compact layer by spin coating at 3000 rpm for 30 sec, then anneal at 200℃ for 1h, the obtained $TiO_2$ compact layer is around 40-50nm thick.

3) Deposit $CH_3NH_3PbI_3$ layer by dropping 200μl $CH_3NH_3PbI_3$ on the glass and spin coating at 5000 rpm for 30 sec, add 150 μl chlorobenzene at 5 sec, anneal at 80℃ for 10 min. The obtained $CH_3NH_3PbI_3$ layer is around 300nm thick.

4) Deposit Spiro-OMeTAD layer of dissolve 80mg Spiro-OMeTAD in 1mL chlorobenzene, spin coating at 3000 rpm for 30 sec. The obtained Spiro-OMeTAD layer is around 100nm thick.

5) Deposit Au layer for 40-50 min (A/S0.33, 11.9V, power 19.8%, $10^{-6}$mba), the obtained Au layer is around 80nm thick.

## 5.2.6 $Cs_2SnI_6$ synthesis

In a typical synthesis of $Cs_2SnI_6$ perovskite derivative nanoparticles, Sn (0.5mmol) and iodine (1.5mmol) powders were dissolved in 10 mL ethanol solution, stirred and heated in low temperature (around 50°C) over night, then $Cs_2CO_3$ (0.5mmol) were mixed into the as prepared solution and kept stirring and heating at the same conditions for 5-6 hours, the white $Cs_2CO_3$ powder was changed into black $Cs_2SnI_6$ directly in solution. The product was washed with ethanol twice and collected for further characterization.

## 5.2.7 Characterization

The XRD patterns of nanoparticles were obtained with an ARL X'TRA X-ray diffractometer with Cu-Kα radiation (λ = 0.15405 nm).

## 5.3 Results and discussion

The generation of electrons and holes by light irradiation, separation and transmission of electrons and holes to the corresponding electrodes are the fundamental the process in solar cells. In perovskite solar cells (PSCs), electrons are transported through an electron transport layer (ETL) and holes are transferred though hole transport layer (HTL). The usual ETL materials include $TiO_2$, $SnO_2$, ZnO, [6,6]-phenyl-C61-butyric acid methyl ester (PCBM), etc. and the common HTL materials include 2,20,7,7'-tetrakis(N,N-di-p-methoxy-phenylamine)-9,9'-spirobifluorene (spiro-OMeTAD),

polymers, poly(3-hexylthiophene) (P$_3$HT), poly(triarlyamin) (PTAA) and Poly(3,4-ethylenedioxythiophene):poly(styrenesulfonate) (PEDOT:PSS) [132–135]. The conductivity is the key factor to the charge transfer in application of these materials. It is always a hot topic to employ a low-cost and effective charge transfer material in PSCs. Due to the high electric conductivity, chemical stability, extensive sources, low-cost and environmental kindness properties, carbon materials have attracted the great attention in solar cell application. There are several carbon allotropes according to the different bonded ways of carbon atoms in carbon materials, such as the usual diamond, graphite, graphene, fullerenes and carbon nanotubes. These allotropes display different physical and chemical properties due to the different structures. Conductive carbon black (paracrystalline carbons) is formed if the carbon atoms bond random. Conductive carbon materials mainly include fullerenes (i.e., C60), carbon nanotubes, graphene, graphdiyne, and graphite. Fullerenes are considered as ideal electron transport materials in PSCs that has been demonstrate by some researches [136,137]. The high electron affinity and mobility endow fullerene with high conductivity [138]. In addition, fullerenes are soluble, which is beneficial to apply in devices. C60 and PCBM have been used to form the ETL in perovskite solar cells since they are known to reduce the density of trap states and passivate the grain boundaries of methylammonium lead iodide layer [139].

## 5.3.1 Carbon counter electrode based PSCs

In PSCs, counter electrodes (CEs) transport holes (n-i-p type PSCs) or electrons (p-i-n type PSCs) to the external circuit. Carbon materials are low-cost and easily available industrial materials. The approximate 5.0 eV work function makes carbon the ideal CE material for PSCs. Carbon materials were first applied in PSCs as counter electrode by Hongwei Han's group with graphite and carbon black as the main components of the carbon paste [140]. According to the fabrication technology, carbon counter electrode should have high conductivity and uniformity. It is found that spheroidal graphite with better conductivity and favorable uniform loose morphology for the higher efficiency than flaky graphite. Thus, the fill factor (FF) and short circuit current density (Jsc) of the devices with spheroidal graphite CEs is higher than that with flaky ones. As a main component in carbon paste, carbon black is poor conductive and with small particle size about tens of nanometers. A small amount of carbon black (20%) mixed with graphite was in favor of improving the photovoltaic performances of PSCs. Excess carbon black increased the electric resistance and decreased Jsc and FF.

Usually, the carbon pastes consist of graphite, carbon black and binders. Tingli Ma's group developed a low-temperature conductive carbon ink that was doctor bladed on perovskite surface directly [141]. The carbon paste was prepared by replacing commercial conductive carbon ink solvent with chlorobenzene which is the common solvent for HTL and would not damage the perovskite. The doctor bladed carbon layer showed high capacity as counter electrode to different perovskites with various solvents such as γ-butyrolactone (GBL), dimethyl sulfoxide (DMSO), chlorobenzene (CB) and toluene (TO) [142]. Sumei Huang's and Licheng Sun's groups directly made CE using commercial

carbon paste by doctor-blade and it showed high performance and stability in air as well [142,143]. It was found that poor contact between perovskite and CE was caused by the large size of the graphite flakes. Guanglan Liao's group modified the common flaky graphite (10 $\mu$m) and carbon black powder (40 nm) with the addition of nano-graphite powder (400 nm) to improve the interfacial contact. Through providing more contact sites, the introduction of nano-graphite powders improved the interfacial contact by making the carbon film more compact. As a result, the stability of the device prolonged over 1300 h [116]. Furthermore, they use polydimethylsiloxane (PDMS) to fill in the gaps of carbon layer and perovskite. The efficiency reached 10.8% and the stability prolonged to 3000 h after encapsulating the device by PDMS [144].

By using the carbon paste as the counter electrode, we fabricated methylammonium lead trihalide $(CH_3NH_3)PbI_3$ solar cell with good stability and modest performance. The performance of the cells fabricated is summed in table 5.1.

**Table 5.1 $(CH_3NH_3)PbI_3$ with carbon paste as the counter electrode solar cell performance**

|   | Voc (mV) | Jsc (mA/cm$^2$) | FF (%) | PCE (%) |
|---|---|---|---|---|
| 1 | 887 | 2.17 | 32.70 | 0.63 |
| 2 | 900 | 2.07 | 37.57 | 0.7 |
| 3 | 880 | 2.79 | 39.90 | 0.98 |
| 4 | 430 | 10.5 | 29.81 | 1.35 |
| 5 | 750 | 5.75 | 34.78 | 1.50 |
| 6 | 792 | 5.92 | 38.2 | 1.79 |
| 7 | 810 | 6.69 | 41.95 | 2.27 |
| 8 | 845 | 8.14 | 42.74 | 2.94 |
| 9 | 900 | 13.06 | 51.64 | 6.07 |

In these devices, the best performance reaches to a Voc of 900Mv, Jsc of 13.06 mA/cm2, FF of 51.64%, and PEC of 6.07%, as seeing in figure 5.3.
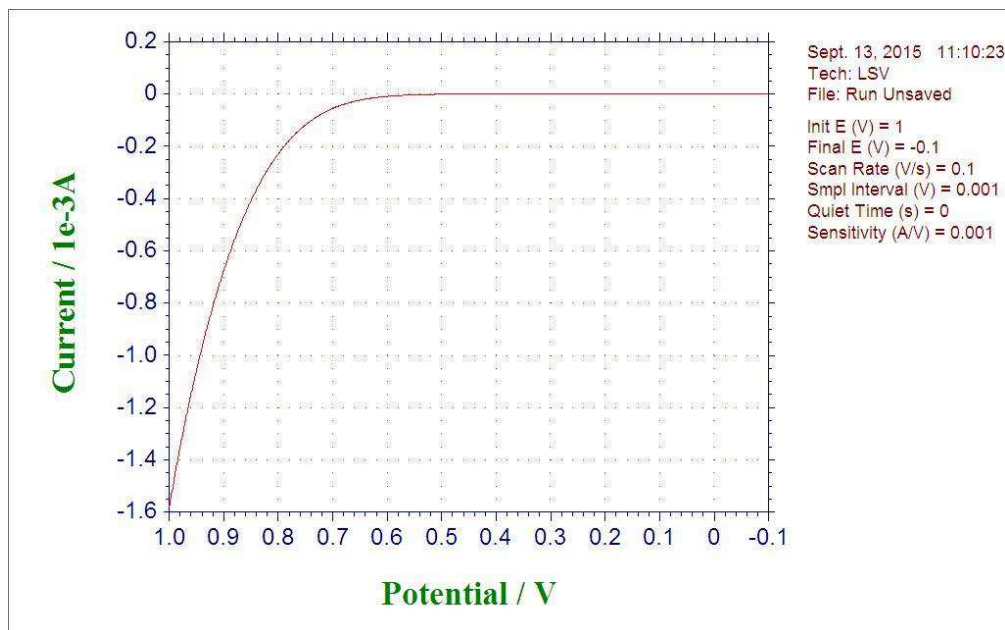
Figure 5.3 I-V curve of the one of the perovskite solar cell that reached to 6.07% efficiency.

## 5.3.2 Gold and Silver counter electrode based PSCs

Novel metals, such as gold and silver, are the most efficient and widely used CE materials in PSCs reported, although they are expensive and thus increased the overall manufacturing cost of the PSCs. These metal electrodes are usually deposited by vacuum evaporation. The preparation of this kinds of CEs needs to be simplified to cater for large scale industrial fabrication of PSCs. Metal counter electrode, especially Ag, suffered less stability when contact with the perovskite layer directly. Moreover, it was reported that a crucial instability factor is related to the migration of Au from the counter electrode to interact with the perovskite when operate at elevated temperatures, causing dramatic loss of solar cell performance [145]. Nevertheless, by using Au and Ag, we fabricated a typical n-i-p and p-i-n type PSCs.

In the n-i-p type PSCs, the most popular hole transport materials (HTM) are small molecular, spiro-OMeTAD, P$_3$HT and PTAA [132–134], etc. To be an ideal HTM in n-i-p type PSCs, the HOMO energy level of the material should be approach and lower than the maximum valence band of perovskite to effectively transport the hole from perovskite to HTL. Moreover, it should be highly conductive with high mobility, which has low series resistance and high fill factor. In addition, it should protect perovskite from atmospheric moisture and prevent the thermally induced loss of the organic molecules. With a low electrical conductivity of $10^{-8}$ S cm$^{-1}$, spiro-OMeTAD makes an ideal HTL material [146]. Carbon quantum dot synthesized by polymerization carbonization hydrothermal approach is an alternative competitor for spiro-OMeTAD [147]. The HOMO (-5.12 eV) and LUMO (-2.07 eV) of carbon quantum dot are appropriate to ensure both efficient hole transfer and electron blocking capability from perovskite to HTL.

By spin coating $TiO_2$ compact layer as the ETL layer, spiro-OMeTAD as the HTL layer, and evaporating Au as the counter electrode, we fabricated a typical n-i-p type PSCs with a structure of ITO/$TiO_2$/$CH_3NH_3PbI_3$/Spiro-OMeTAD/Au. The result is shown in figure 5.4. The performance of the device is satisfactory, with Voc of 970mV, Jsc of 21.4 mA/$cm^2$, FF of 66.9%, and PEC of 13.9%. This device degraded very fast, for the possible reason of the migration of Au through HTL to perovskite [118,119].
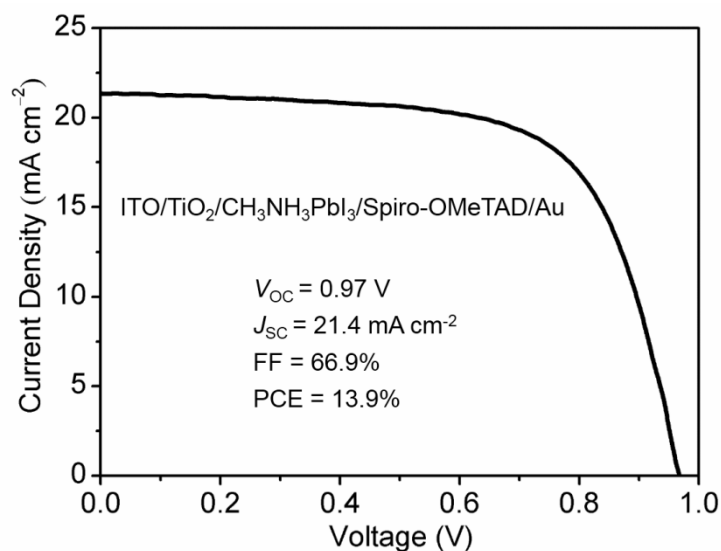


Figure 5.4 J-V characteristic of the n-i-p typed planar perovskite solar cell with Au as counter electrode.

In the typical p-i-n type PSCs, which are inherited from organic photovoltaics (OPV), holes are collected by the TCO anode and electrons are collected by the metal cathode. In this case, HTL is commonly deposited through solution process to make the cell low temperature and flexible. Highly conductive PEDOT:PSS is a commonly used HTL material. The work function of PEDOT:PSS (-5.0 eV) and the VB of MAPbI3 (-5.4 eV) are stepped with small distances. The drawbacks of PEDOT:PSS is acidity and hygroscopicity.

By spin coating PEDOT:PSS layer as the HTL layer, evaporating fullerene $C_{60}$ as the ETL layer [136,137], BCP as hole blocking layer, and Ag as the counter electrode, we fabricated a typical p-i-n typed planar PSCs with a structure of ITO/PEDOT:PSS/$CH_3NH_3PbI_3$/$C_{60}$/BCP/Ag. The result is shown in figure 5.5. The performance of the device is encouraging, with Voc of 880mV, Jsc of 21.7 mA/$cm^2$, FF of 73.4%, and PEC of 14.0%. However, the stability of this device is poor. It depredated very fast, in a possible process in which diffusing iodine react with Ag layer and produce AgI [148].
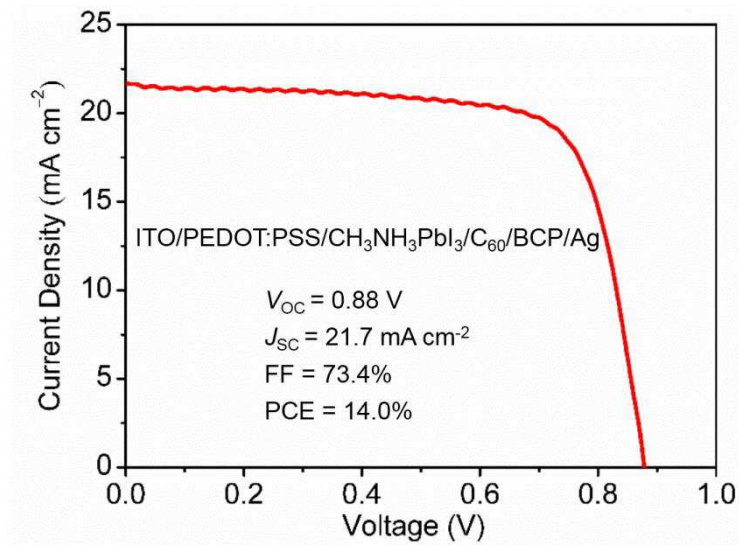
Figure 5.5 J-V characteristic of the p-i-n typed planar perovskite solar cell with Ag as counter electrode.

## 5.3.3 $Cs_2SnI_6$ based PSCs

$Cs_2SnI_6$ is environmental benign and longtime stable compare to common methyl ammonium lead halide perovskite. Yet the development of this material is still in its infant state. The reported performance of $Cs_2SnI_6$ solar cell is very poor. We are trying to make the solar cell device with the structure of FTO/$TiO_2$/ $Cs_2SnI_6$/Carbon CE, this work is ongoing.

The XRD pattern of the cubic $Cs_2SnI_6$ crystal together with MAUD software fit were shown in figure 5.6. The crystallite size (d), root mean square microstrain and lattice parameters (a) and the fitting parameters are listed in table 5.2.

**Table 5.2 Results from Rietveld analysis of the $Cs_2SnI_6$ crystals**

| Rw (%) | Rexp (%) | Rb (%) | sig | a (Å) | d (nm) | Rs-strain |
|--------|----------|--------|-----|-------|--------|-----------|
| 24.126 | 12.871 | 18.018 | 1.874 | $11.644 \pm 2.259e^{-4}$ | $301.614 \pm 18.548$ | $7.466e^{-4} \pm 4.023e^{-5}$ |
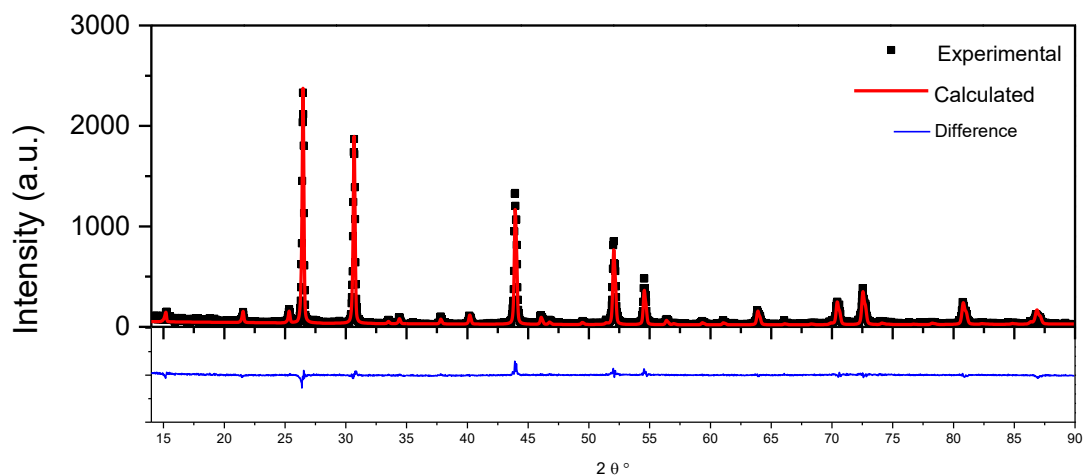
Figure 5.6 The XRD calculated and experimental spectrum of $Cs_2SnI_6$ crystals (dot: experimental data, upper red solid line: calculated pattern, lower blue solid line: subtracted pattern).

## 5.4 Conclusion

Carbon materials can be used in counter electrode to transport holes to outer circuit effectively. It offered a low cost and straightforward approach to form electrode in PVSCs. Furthermore, carbon materials ensured the photovoltaic performance and long-term stability. Carbon materials, such as C60 can be used in electron transporting layer to accelerate electron transport and block holes. Comparatively, Au and Ag combined with HTL materials such as spiro-OMeTAD and PEDOT:PSS and hole blocking materials such as C60 and BCP offered a higher performance for PSCs, but suffered low stability. $Cs_2SnI_6$ cubic nanoparticle has been synthesized by simply react tin and iodine powders in ethanol, and then with cesium carbonate.

# Chapter 6 CIS@ZnS Quantum dots

## 6.1 Introduction

Quantum dots are crystalline particles that exhibit size dependent optical and electronic properties. With typical dimensions in the range of several nanometers (2-10 nm), these nanocrystals display discrete electric transition and bridge the gap between small molecules and large crystals. Their optoelectronic properties change as a function of size and shape. Smaller QDs emit shorter wavelengths with colors in blue and green, larger QDs emit longer wavelengths with colors in orange or red and the specific colors and sizes vary depending on the exact composition of the QD [149]。

When the size of the semiconductor crystallite is smaller than twice the size of its exciton Bohr radius, the excitons will be squeezed and leading to quantum confinement. The Exciton Bohr radius can be expressed as: [150,151]

$$a_b = \frac{\varepsilon \hbar^2}{e^2}\left(\frac{1}{m_e^*} + \frac{1}{m_h^*}\right) = \varepsilon \left(\frac{m_e}{\mu_{eh}}\right) a_0 \qquad (6.1)$$

where $a_0$ is the Bohr radius (0.053 nm), $m_e$ is the electron mass, $\mu_{eh}$ is the reduced electron-hole mass ($\mu_{eh}^{-1} = m_e^{*-1} + m_h^{*-1}$), and $\varepsilon$ is the dielectric constant (permittivity).

When the size of a semiconducting particle shrinks and approaches to the size of the electron-hole distance known as the Bohr radius, the quantum confinement effects take over. For the 3D spherical nanoparticle, as we think of particle in a box or infinite potential well, the energy of particle can only have discrete values which can be expressed by:[152]

$$E_n = \frac{h^2 n^2}{8 m_c R^2} \qquad (6.2)$$

where n is energy level, h is Planck's constant, $m_c$ is the effective mass of the point charge and R is the radius of box (the size of the particle). We see from this that as the size of the nanocrystal increases, the absorption energy (thus band gap energy) decreases. Therefore, as nanoparticles (i.e. QDs) size varies, the energy changes since the exciton in the particles behaves like a "particle in a box."

The first excited electronic transition energy (i.e., band gap of a particle in a box) is the sum of the fundamental bulk band gap ($E_g^0$) and the confinement energy ($E_{conf}$) of both electrons and holes, if the Coulomb interaction is also taken into account, the band gap of a QDs with radius R can be described as: [150,153]

$$E_g = E_g^0 + \frac{\hbar^2 \pi^2}{2R^2}\left(\frac{1}{m_e^*} + \frac{1}{m_h^*}\right) - \frac{1.786 e^2}{\varepsilon R} + E_e^{POL} + E_h^{POL} - 0.248 E_{R_Y}^* \qquad (6.3)$$

Where $E_g^0$ is the band gap of the corresponding bulk material, $J_{e-h}$ represents the effective Coulomb interaction between the electron and the hole, which is equal to $1.786e^2/\varepsilon R$ ($\varepsilon$ is the dielectric constant). The smaller terms $E_e^{pol}$ and $E_h^{pol}$ are the self-polarization energies

of the electron and hole, respectively, which depend on $e^2/R$ and the dielectric constant of the NP or QDs and the surrounding medium. The smaller term exciton Rydberg energy $E_{Ry}$ accounts for spatial correlation between the electron and the hole.

Equation 6.3 clearly describes the two most important consequences of quantum confinement. The first consequence is that the band gap of a semiconductor NP or QDs becomes larger when size decrease which means that the optical band gap of QDs can be tuned by simply changing their size. The second consequence is that discrete energy levels arise at the band-edges of both the conduction band and valence band with decreasing size. These size dependent effects are schematically depicted in Figure 6.1.
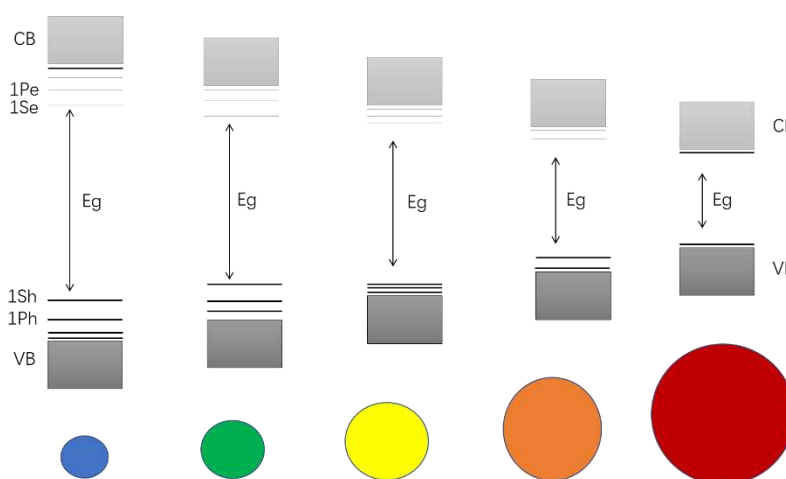


Figure 6.1 Schematic illustration of the quantum confinement effect: the band gap of the NP or QDs increases with decreasing size, and discrete energy levels arise at the band edges.

Quantum dots (QD) are an very interesting material with tunable emission range from blue to near-infrared region due to the quantum confinement effect [154]. Quantum dots nanomaterials can be divided into four classes: II−VI, IV, III−V, and I−III−VI QDs [155–158]. II−VI quantum dots, especially heavy metal Cd, Hg and Pb based QDs have received much interest in optical application. However, heavy metal based QDs are potentially toxic to humans and the environment. The Cd free ternary I−III−VI compounds that are less toxic have been considered as replacement to conventional Cd-based QDs. I−III−VI ternary QDs comprised of two cations (I: $Cu^+$ or $Ag^+$, III: $Al^{3+}$, $Ga^{3+}$ and $In^{3+}$) and one anion (VI: $S^{2-}$, $Se^{2-}$, and $Te^{2-}$). In recent years, ternary compositional nanoparticles have gained increased attention due to their wide range of potential applications in solar cell [159]. lighting emitting diodes and displaying devices [160], biosensors [161], drug delivery, biolabeling [162] and biological imaging [163,164]. The syntheses and optical properties of ternary I−III−VI compounds, such as $CuInS_2$ (CIS) [165,166], $CuInSe_2$ (CISe) [167], $CuGaS_2$ (CGS) [168,169], $AgInS/Se_2$ (AIS/Se) [170–172] and $AgGaS_2$ (AGS) [173] have been extensively investigated.

Ternary I–III–VI semiconductors $CuInS_2$ QD is a director band gap semiconductor. As a typical ternary quantum dot material, $CuInS_2$ (CIS) quantum dot possess unique

properties, including large Stokes shift, high absorption coefficient ($\alpha = 5 \cdot 10^5 \text{cm}^{-1}$) and long fluorescence lifetime [174], ideal direct adjustable band gap of 1.45-1.5 eV that covers a large color window [159,175,176], narrow full width at half-maximum, and high photostability. CIS and its heavier congener CISe with band gap of 1.05eV are well suited for application in photovoltaics. The Bohr exciton radius of CIS is 4.1 nm; thus, quantum confinement effects can be observed in CIS nanocrystals up to a size of about 8nm. By changing the sizes of CIS nanoparticles, their absorption and emission can be tuned almost in the whole visible part of the solar spectrum, up to the near infrared [177].

CIS QDs are synthesized by solvothermal synthesis [178], thermolysis [169,179], photochemical decomposition [180] and hot injection method [166,181], etc. The major relaxation process in CIS QDs is the donor and acceptor pair recombination within the band gap. The band gap of the CIS QDs relies on the amount ratio of Copper and Indium. The more deficient of copper creates a wider band gap in CIS QDs. The PL in the CIS@ZnS QDs could be attributed to the host defect state emission [182].

ZnS shell passivates the surface of CIS QDs and improves the fluorescence quantum yield (QY) significantly. It was reported that 68%-78% of quantum yield were reached by ZnS shell covered CIS QDs [183] and 65% with a cation exchange reaction method [184]. It is also reported that CIS quantum dot with CdS passivation layer has higher PL efficiency of 86% than ZnS (29%) due to the smaller lattice mismatch of 2% between CIS and ZnS (2%) compare to 5.2% between CIS and CdS [185,186].

Noninvasive imaging is widely used in hospital for disease diagnosis and treatment. Among the variety of imaging technologies, magnetic resonance imaging (MRI) becomes a powerful diagnostic method due to its less harmful radiation advantage and high spatiotemporal resolution with deep tissue penetration and exquisite image contrast. The contrast of MR image depends on the T1 (spin-lattice) and T2 (spin-spin) relaxation in external magnetic field triggered by a radio frequency. T1-weighted image is created by changing the repetition time (TR) before measuring the MR signal when the longitudinal magnetic moment is recovering and T2-weighted image is created by changing the echo time (TE) when transverse magnetization is decaying before measuring the MR signal. T1 weighted image contrast agents can enhance brightness contrast and thus have been widely used clinically in the diagnosis of brain tumors and vascular diseases [187]. As a typical paramagnetic metal ion with seven unpaired electrons in its 4f orbital, gadolinium is widely used as a T1 weighted MRI contrast agent. Gadolinium ion is toxic but its ionic complexes ($Gd^{3+}$) are relative safe and they can produce bright signal enhancement on T1 weighted images [188]. There are also strategies to incorporate gadolinium complex and nanoparticles such as gold and silica [189,190], but complicated structure limited their deep tissue and intracellular signal collection. Therefore, the multimodality imaging techniques with a single nanoprobe have gained high attention due to the complementary imaging capabilities. Both ferromagnetic and paramagnetic materials as contrast agents have been investigated. For instance, iron oxide nanoparticle $Fe_3O_4$ and its effect on positron emission tomography (PET), near-infrared fluorescence (NIRF) and magnetic resonance imaging (MRI) tri-modality imaging [191], gadolinium doped GdZCIS@ZnS quantum dot and its effect on MRI and fluorescence dual modal imaging [192], transit

element manganese doped CMIS and CMIS@ZnS nanoparticle that display paramagnetic properties [193–195]. However, the Mn doping in the core of CIS@ZnS QDs results in the significant decrease of the photoluminescence intensity in these nanoparticles [194]. The doping of Mn in the ZnS shell with only 2.25mol% (Mn/Zn+Cu+In) leads to the photoluminescence red shifted from 557nm to 610nm due to the 4T1–6A1 transition of the $Mn^{2+}$ impurity, which is excited by the energy transfer from the host CIS-ZnS [196]. The introduction of Gd in the ZCIS core creates more defects and leads to decrease of QYs [192].

In the present thesis, the lanthanide element $Gd^{3+}$ doped $CuInS_2$@ZnS QDs were synthesized using zinc, indium, manganese and gadolinium acetate, copper iodide and 1-dodecanethiol (DDT) as S precursors. A poly (ethylene glycol) (PEG) based hydrophilic ligand was used for enable the resultant nanoparticles water soluble through ligand exchange. This $Gd^{3+}$ doped multi-shell QDs distinguished in: (1) The doped amount of $Gd^{3+}$ can be tuned high enough without any change of CIS@ZnS QDs luminescence property; (2) By incorporate high concentration of $Gd^{3+}$ ion in a single NP composition with $Gd^{3+}$ close to the nanoparticle surface, the strategy simplified the probe structure with a high r1 relaxivity; (3) $Gd^{3+}$ doped $CuInS_2$@ZnS QDs are capable of simultaneous visible fluorescence and MRI imaging in vivo. With an excellent fluorescent property and high relaxation rate, the $Gd^{3+}$ doped QDs are verified to be a qualified dual-modal contrast agent.

It is well known that certain metal elements (e.g., Fe, Cu, Zn, and Mn) are nutritionally essential for a healthy life, while other heavy metals (e.g., Hg, Pb, Cd, and Cr) are toxic in organism. These metals show a trend to form complexes, with biological ligands that containing oxygen, sulfur, and nitrogen. As a result, changes in the molecular structure of proteins, breaking of hydrogen bonds, inhibition of enzymes, or even cell apoptosis can occur by uptake excessive amount of trace elements needed [197,198]. Copper is a transition element essential to organism, it is required as a catalytic cofactor for biological processes such as respiration, connective tissue formation, iron transport and metabolism, oxidative stress protection, peptide hormone production, pigmentation, blood clotting and normal cell growth and development [199,200]. However, copper also participates in redox reactions to generate the hydroxyl radical that causes damage to lipids, proteins and DNA [201]. Unregulated presence of excess copper can disturb the cellular homeostasis which will cause different neurodegenerative diseases, such as Wilson's, Parkinson's, and Alzheimer's disease and obstruct many other biological activities [202,203] In recent years, as the growing of industry, some amount of copper leak into the environment through various routes and become an abundant pollutant of drinking water. Its potential toxic effect on human beings makes it a challenging problem throughout the world due to the widespread use of copper in industry. The U.S. Environmental Protection Agency (EPA) has set the maximum level of copper in drinking water at 1.3 ppm (~20 μM) [204]. It is therefore essential and challenging to develop highly sensitive and selective probes for copper ion detection.

Quite a few fluorescent-based sensors have been developed in the past decade for the selective detection of $Cu^{2+}$ ions with their distinct advantages of high sensitivity, specificity,

and ease of operation [205–207]. However, most of them are fluorescent organic moieties that covalently bind to the $Cu^{2+}$ ions, and thus suffered from drawbacks in practical applications, such as complicated organic synthesis, low solubility in water due to the presence of hydrophobic moieties, harmful systems, and cross-sensitivity toward other metal ions. They are thus not appropriate for the detection of $Cu^{2+}$ ions in biological systems. There is an increasing interest recently of using nanoparticles with ligand functionalized silver, gold nanoparticles, quantum dots and polymer dots for sensing of varieties of metal ions (e.g., $Cu^{2+}$, $Zn^{2+}$, $Hg^{2+}$, $Cd^{2+}$) due to their high selectivity, sensitivity, and rapid response time [208–219]. Among these nanoparticle sensors, quantum dots present considerable advantages. They have unique optical and electronic properties due to the quantum confinement and are currently under intensive studies for potential use in biosensing and biolabeling [220–222]. However, most of these quantum dots are based on the cadmium sulfide/selenide/telluride in which cadmium is even more toxic than copper in organism and tellurium is a rare and expensive element. Comparatively, ternary quantum dot $CuInS_2$ (CIS) is composed of earth abundant elements and possesses unique properties, including large Stokes shift and narrow full width at half-maximum, high photostability and long fluorescence lifetime [174],

In this work, we use low cost and easy operation material $Gd^{3+}$ doped $CuInS_2@ZnS$ quantum dot as selective copper (II) ion probe. Doped with gadolinium, a typical T1 weighted MRI contrast agent, this material can not only enhance MRI contrast signal significantly, but also can detect $Cu^{2+}$ ion with high sensitivity and selectivity. The limit of detection calculated could reach as low as 0.1 ppb (1.5 nM).

# 6.2 Experimental

## 6.2.1 Chemicals

- 1-dodecanethiol (DDT), $CH_3(CH_2)_{11}SH$, MW = 202.40 g/mol, d = 0.845 g/mL, Sigma-Aldrich, 98%

- 1-octadecene (ODE), $CH_3(CH_2)_{15}CH=CH_2$, MW = 252.48 g/mol, d = 0.789 g/mL, Aldrich, 90%

- Oleic acid (OA), $CH_3(CH_2)_7CH=CH(CH_2)_7COOH$, MW = 282.46 g/mol, Aldrich, 90%

- Copper (I) iodide, CuI, MW = 190.45 g/mol, Riedel de Haen, 99%

- Indium (III) acetate, $In(C_2H_3O_2)_3$, MW = 291.95 g/mol, Aldrich, 99.99%

- Zinc acetate dihydrate, $Zn(CH_3COO)_2 \cdot 2H_2O$, MW = 219.51 g/mol, Aldrich, ≥99%

- Gadolinium Acetate hydrate, $Gd(C_2H_3O_2)_3 \cdot 4.54H_2O$, MW = 416.04 g/mol Aldrich, 99.9%

- Copper (II) chloride dihydrate, $CuCl_2 \cdot 2H_2O$, MW = 170.48 g/mol, J. T. Baker, 99.0%

- Aluminum nitrate nonahydrate, $Al(NO_3)_3 \cdot 9H_2O$, MW = 375.14 g/mol, J. T. Sigma-Aldrich, 98.0%

- Iron (II) chloride tetrahydrate, $FeCl_2 \cdot 4H_2O$, MW = 198.81 g/mol, Sigma-Aldrich, 99.0%

- Tin (II) chloride, $SnCl_2$, MW = 189.62 g/mol, Sigma-Aldrich, 98%

- Manganese (II) chloride tetrahydrate, $MnCl_2 \cdot 4H_2O$, MW = 197.91 g/mol, Sigma-Aldrich, ≥99.0%

- Sodium chloride, NaCl, MW = 58.44 g/mol, Sigma-Aldrich, 99.5%

- Calcium nitrate tetrahydrate, $Ca(NO_3)_2 \cdot 4H_2O$, MW = 236.15 g/mol, J. T. Baker, 99.0%

## 6.2.2 Synthesis of CuInS2@ZnS:Gd$^{3+}$ QDs

In a solvothermal synthesis of CIS core nanoparticles, indium acetate (0.0876g, 0.3 mmol) and copper(I) iodide (0.0571g, 0.3 mmol) are mixed with 1-dodecanethiol (DDT, 3 mL) and 1-octadecene (ODE, 6mL) in a three neck round flask. The reaction mixture is keep purged with argon. The flask is heated in silicon oil bath to 120°C for 30 min until a clear solution is formed. The temperature is then gradually raised to 230°C. When the temperature increases, the color of the reaction solution progressively changes from colorless to yellow, red, and finally black, indicating nucleation and subsequent growth of CIS nanoparticles. In this synthesis, DDT acts simultaneously as the stabilizing ligand and the solvent together with ODE. It further acts as sulfur precursor by forming thiolates with metal and decomposes to form metal sulfides during heating.

Shell coating of CIS QDs with ZnS was carried out in situ without purification of the core. Specifically, 1,2 mmol zinc acetate dihydrate was dissolved in the mixture solution of 1.5mL oleic acid, 1.5mL ODE and 0.3mL DDT under stirring and heating at 110°C in argon atmosphere. It was kept stirring and heating during the core synthesis. When the core synthesis completed, it was added into the CIS core synthesis solution in a drop wise manner at 230°C.

When the above ZnS precursor solution finished, start to add the Gd$^{3+}$ doped ZnS precursor solution in the same way. The Gd$^{3+}$ doped ZnS shell precursor solution was prepared by dissolving 0.3 mmol zinc acetate dihydrate and 0.9 mmol gadolinium acetate hydrate in the mixture solution of 1.5mL oleic acid, 1.5mL ODE and 0.3mL DDT under stirring and heating at 110°C in argon atmosphere. It was also kept stirring and heating during the core synthesis. This solution was added drop wise into the three neck round flask at 230°C after the pure ZnS shell capping.

After that, the reaction was quenched by immersing the flask in an ice or water bath. The nanoparticles can be collected by precipitating with addition of ethanol, centrifuging, and decanting the supernatant. After washing with ethanol and acetone three times for the purification steps, the obtained CuInS2@ZnS:Gd$^{3+}$ QDs were dried at room temperature. These QDs are easily dispersed in chloroform or toluene. The dried sample was conserved at room temperature.

**Table 6.1 Reagents quantities in the reaction**

| | Reagents | Quantity | Moles |
|---|---|---|---|
| Core | DDT | 3 mL | |
| | ODE | 6 mL | |
| | CuI | 0.0571g, | 0.3 mmol |
| | In(ac)₃ | 0.0876g, | 0.3 mmol |
| Inner Shell | DDT | 0.3 mL | |
| | ODE | 1.5 mL | |
| | OA | 1.5 mL | |
| | Zn(ac)₂ · 2H₂O | 0.2634g | 1.2 mmol |
| Outer Shell | DDT | 0.3 mL | |
| | ODE | 1.5 mL | |
| | OA | 1.5 mL | |
| | Zn(ac)₂ · 2H₂O | 0.0659g | 0.3 mmol |
| | Gd(ac)₃ ·4.54H₂O | 0.3744g | 0.9 mmol |

# 6.2.3 Phase transfer of QDs to the aqueous phase

The surface of the as synthesized CuInS2@ZnS:Gd$^{3+}$ nanoparticles is hydrophobic and can be dispersed in chloroform and toluene. The phase transfer was achieved by polyethylene glycol (PEG) cover strategy. Typically, 150 mg PEG with a molecular structure of $CH_3$-$(OCH_2CH_2)_n$-O-O-SH was dissolved in 10 ml toluene by stirring, 10 mg QDs were dissolved in 10 ml toluene. After PEG dissolved, the solution was added into QD solution drop wise and stirring in argon atmosphere at 70°C for 1-2 hours. The PEG coated QDs can be precipitated and washed with diethyl ether. After washing with diethyl ether three times, the final products can be easily dissolved in water.

Except for PEG, bovine serum albumin (BSA) was also used to transfer the phase into aqueous state. Specifically, 20 mg BSA and 2.5 mg QDs were dissolved in 10mL deionized water and 0.5 mL chloroform, respectively. Then QD solution was slowly injected into BSA solution and performed ultrasonification for 10 minutes. When an emulsion solution formed, the chloroform was evaporated by stirring at room temperature for around 2-3 hours.

Bovine serum albumin (BSA) is a serum albumin protein derived from cows. It contains 583 amino acid residues with a molecular weight of 66.5 kD and the size of 14 × 4 × 4 nm.

BSA is made up of three homologous domains (I, II, and III) with nine loops (L1–L9) (Fig. 6.2) [223]. It is often used as a protein concentration standard, a nutrient in cell and microbial culture, a stabilizer of some enzyme and a blocker in immunohistochemistry in lab experiments.
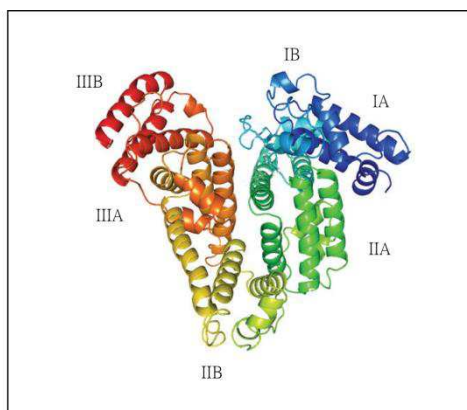


Figure 6.2 BSA protein structure [224].

## 6.2.4 Cell Viability Test

Cell Counting Kit-8 (CCK-8) (Dojindo, Japan) was applied to evaluate the cytotoxicity of the obtained QDs with tumor HeLa cell lines. Cells growing in log phase were seeded into a 96-well cell-culture plate with 3000 cells per well. After cultured at 37°C in a 5% $CO_2$ atmosphere for 12 h, the culture medium was removed and replaced with the complete medium with a series of QDs concentrations (up to 0.4mg/mL per well) and cultured for another 12 h and 24 h. A blank group without QDs was set as the control. After exposure, 100 µL of media containing CCK-8 (10%) was added and incubated at 37 °C, the absorbance at 450 nm was measured using a multifunctional microplate reader (Infinite 200, TECAN). The cytotoxicity was expressed as the percentage of cell viability of the treated group relative to the control group.

## 6.2.5 *In vitro* Relaxivity measurements and Optic/NMR images

The T1 and T2 relaxation of QDs were measured and MR images were acquired using a Bruker Tomograph (Bruker,Germany) equipped with 4.7T, 33-cm bore horizontal magnet (Oxford,Uk). The relaxivity values (r1 and r2) were obtained from the slope of the linear fitting plot between reciprocal of the relaxation time and the $Gd^{3+}$ ion concentration. The in vitro T1 weighted image of QDs at various $Gd^{3+}$ concentrations were obtained on a 7.0 T small animal MRI instrument. Parameters set as: TR = 120 ms, TE = 1.8 ms, field of view = 35 mm×35 mm, matrix size = 256×256, number of slices = 15, slice thickness = 1 mm, and NEX = 5. The laser confocal scanning microscopy was used to in vitro acquire

fluorescence images. Briefly, Hela cells pre-seeded on glass-bottom dishes were incubated with DMEM (10% FBS) containing 400 µg/mL QDs. At 12 h post treatment, cells were rinsed twice with PBS; photographs of cells were obtained immediately by the confocal microscopy. The excitation wavelengths were 405 nm for QDs.

## 6.2.6 *In vivo* MR imaging

The animal experiments were conducted on BALB/c nude mice (4-6 weeks, 20 g of body weight). In vivo MR imaging was performed on a 7.0 T small animal MRI instrument. The mice were anesthetized with isoflurane (1.5%) at 1 L/min airflow throughout the experiment. Prior to imaging, QDs (dosage of 0.05 mmol $Gd^{3+}$ per kg of body weight) were administrated by intravenous injection. MRI images were acquired using T1_RARE sequence with parameters set as follows: TR = 120 ms, TE = 1.8 ms, field of view (FOV) = 35 mm×35 mm, matrix size = 256×256, number of slices = 15, slice thickness = 1 mm, and number of excitation (NEX) = 5.

## 6.2.7 Characterization

Transmission electron microscopy (TEM) images were taken on Morgagni 268D (FEI-Philips) equipped with MegaView2 CCD camera. The QDs were drop-cast from a diluted dispersion in toluene solution onto a thin holely carbon film supported by a copper grid. X-ray powder diffraction (XRD) patterns were obtained using an ARL X'TRA X-ray diffractometer produced by Thermo Fisher. UV–vis spectra were recorded on an Evolution 201 UV–visible spectrophotometer. PL spectra were recorded using a FP-8200 cspectrofluorometer (Japan).
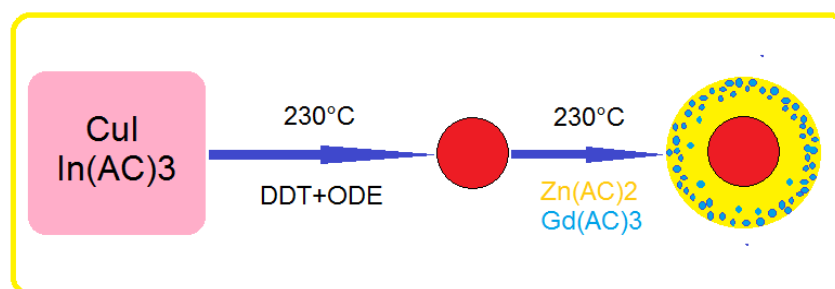
## 6.3 Results and discussion



Figure 6.3 Schematic illustration of the synthesis of CuInS2@ZnS:$Gd^{3+}$ QDs.

As shown in Figure 6.3, the hydrophobic $CuInS_2$@ZnS core shell QDs were synthesized by decomposition of copper iodide and indium acetate as starting materials in 1-dodecanethiol solvent at 230°C. The high temperature could promote the rapid

decomposition of the starting metal materials and $CuInS_2$ seeds generation and nanocrystal formation in which DDT served as the solvent and sulfur source. With a wide direct band gap to confine electrons and holes in core, the ZnS shell around the single-core CIS nanoparticle was deposited to passivate the core surface and enhance the fluorescence intensity. The Gd doped ZnS shell was formed at the outmost position to serve as MR imaging agent. Since the resulting core/shell QDs are hydrophobic, the phase transfer is essential for biological applications. Serum albumin is most abundant natural biomacromolecule in plasma. Bovine serum albumin (BSA) has one free sulfhydryl and eight pairs of disulfide bonds which can replace hydrophobic surfactants and bind to nanoparticle surface and thus can be used for phase transferring as the emulsifier between the organic and aqueous phase [225,226]. As an amphiphilic polymer, polyethylene glycol (PEG) is low toxic, flexible and water soluble and thus both BSA and PEG were adopted to wrap quantum dots in this study.

## 6.3.1 Crystal structure and composition

The crystal structure and composition were studied by x-ray diffraction (XRD), EDS and ICP-MS. Figure 6.4 (a) shows a typical TEM image of Gd doped $CuInS_2$@ZnS QDs. The average size of these QDs is 3.14±0.44nm, as determined from the TEM images by Image 3J and OriginPro 9 software (Fig. 6.4 b). The size distribution in solution was also measured by dynamic light scattering (DLS) method. The result show that the average size of $CuInS_2$@ZnS@BSA QDs in aqueous solution is 52.21±19.32nm (Fig. 6.5 a). The DLS size of QDs capped with BSA appears twice bigger than that capped with PEG in water due to the complex protein structure (Fig. 6.5 b).
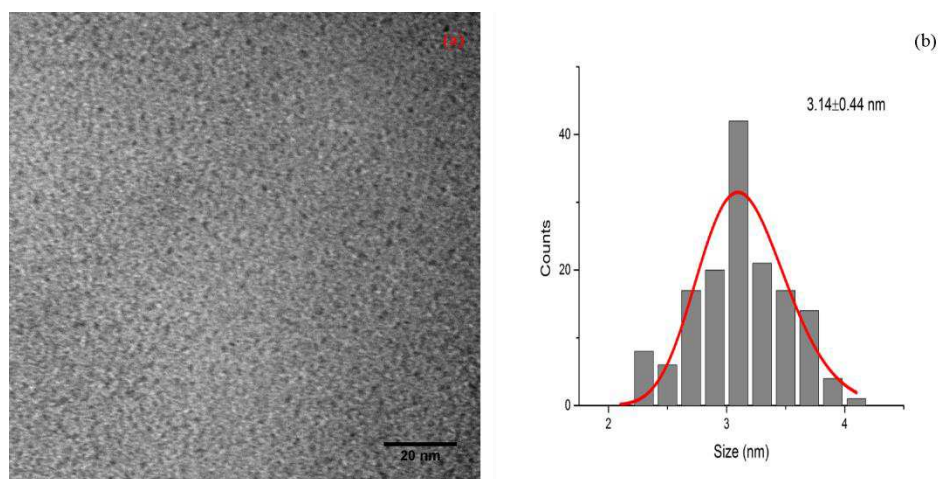


Figure 6.4 (a) TEM image of as synthesized Gd doped CuInS2/ZnS QDs. (b) Particle size distribution and log-normal fit of the distribution (solid line).
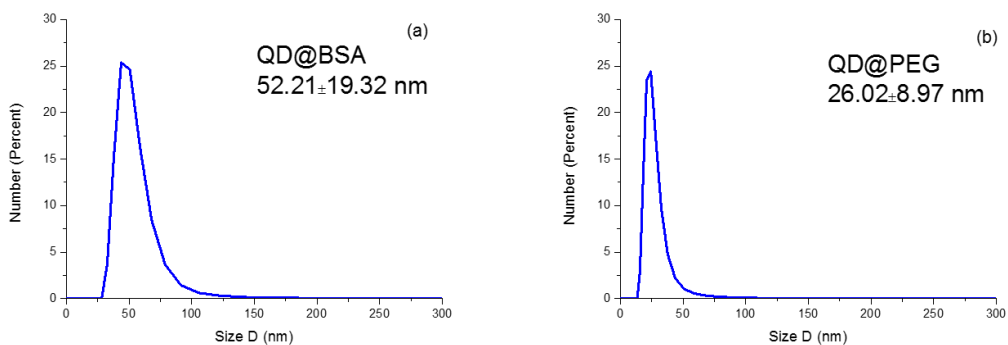
Figure 6.5 Dynamic light scattering (DLS) measurement of CIS@ZnS:Gd$^{3+}$ quantum dots. (a) Qds@BSA with an average size distribution of 52.21±19.32 nm. (b) Qds@PEG with an average size distribution of 26.02±8.965nm.

Figure 6.6 shows the representative X-ray diffraction (XRD) patterns of the CuInS2@ZnS:Gd$^{3+}$ QDs. The peaks are broad, implying the tiny size of the resultant QDs. Three major peaks at 28.3°, 46.4°, and 55.7° were found in XRD patterns. All the diffraction peaks are compatible with those of CuInS$_2$ (JCPDS Card No. 47-1372) and ZnS (JCPDS Card No. 05-0566). Except for these typical XRD peaks, a peak at around 21° is present attributed the organic caps [227]. According to the above XRD diffraction result, the Gd$^{3+}$ ions incorporated into CuInS$_2$@ZnS QDs do not induce any appreciable change in crystal structure.



Figure 6.6 XRD pattern of CuInS2@ZnS:Gd3+QD powders, inserted below is the JCPDS card of ZnS (05 0566) and CIS (47 1372).

| Element | Wt % | At % |
|---------|------|------|
| S K | 36.71 | 66.40 |
| InL | 16.84 | 8.51 |
| GdL | 31.26 | 11.53 |
| CuK | 3.33 | 3.04 |
| ZnK | 11.86 | 10.53 |
| Total | 100.00 | 100.00 |

Figure 6.7 EDS spectrum of Gd$^{3+}$ doped CIS@ZnS quantum dots.

## 6.3.2 Fluorescence Properties

The UV–visible absorption and PL spectra of CuInS2@ZnS:Gd$^{3+}$ QDs are shown in Fig. 6.8. The absorption spectra of the QDs exhibit a broad shoulder with a long tail at the low energy side with a typical absorption spect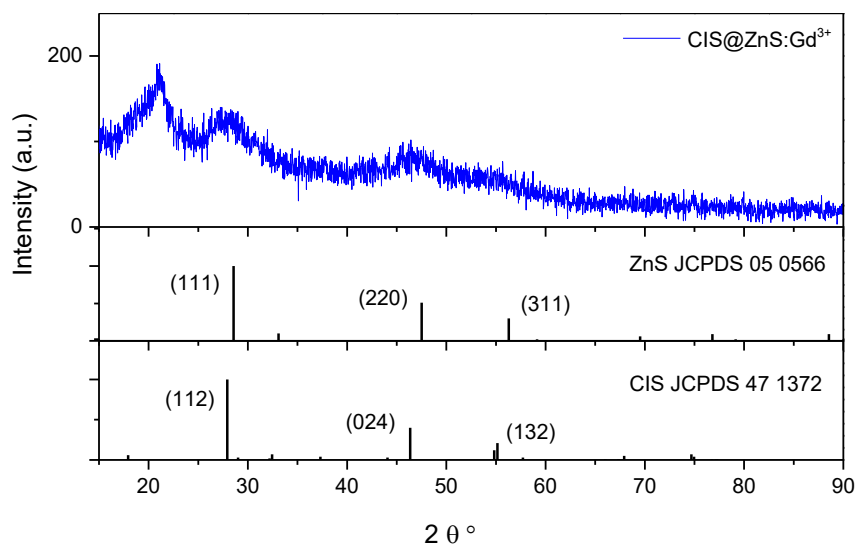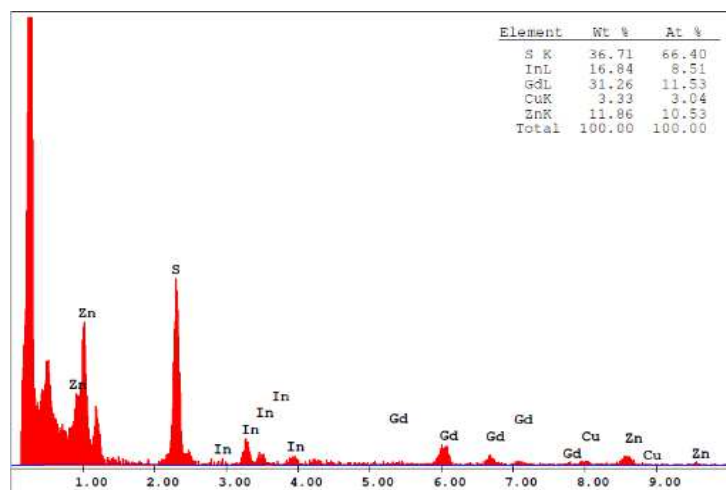rum of QDs [228]. The QDs have a broad absorption below 600 nm, indicating a wild range of excitation wavelength. Considering the similar crystal structure, cation exchange of Cu$^{+}$ or In$^{3+}$ ions in CIS core (Eg bulk = 1.53 eV) by the Zn$^{2+}$ ion could form an alloyed interface, resulting in band gap widening and absorption spectrum shifting [174,183,186].

The emission peak centers at 590 nm. The full width at half-maximum (FWHM) of PL emissions of CuInS$_2$@ZnS QDs is approximately 86 nm. As typical nanoparticle, the quantum dots have significantly high surface-to-volume ratio, resulting in lots of defects on the QD surface. In CIS quantum dot, a commonly accepted transition mechanism is so-called donor−acceptor pair (DAP) recombination [97]. The dominant DAP recombination route is $V_S$−$V_{Cu}$ in CIS QDs where $In_{Cu}$ (In substituted at the Cu site) or $V_S$ (S vacancy) possibly act as donor states and $V_{Cu}$ (Cu vacancy) as acceptor state [160]. The PL decay of the nanoparticle was also studied and the decay curve was shown in figure 6.9. The decay fit with biexponential decay profile $I(t)=A_1exp(-t/\tau_1)+A_2exp(-t/\tau_2)$, and the average life time was determined by the expression $\tau=(A_1\tau_1^2+A_2\tau_2^2)/(A_1\tau_1+A_2\tau_2)$. The calculated average life time is around 54.4 ns, significantly longer than most organic fluorophores [229,230].

When the ZnS shell was deposited on the CIS QD surface, the PL intensity was significantly enhanced and blue-shifted, which indicates an effective surface passivation. The significant enhancement of PL emission by ZnS shell implies that the nonradiative recombination pathways can be effectively suppressed with surface trap passivation. Additionally, covering of ZnS shell may also lead to delocalization of the CIS core electron wave function into the shell area and reduce the electron/hole wave function overlap. This

process will lower the electron–hole recombination probability and prolong slightly both the nonradiative and radiative processes, slightly [231]. When $Gd^{3+}$ is doped into ZnS shell, the QDs structure and the PL emission remains the same, supporting the strategy to develop $Gd^{3+}$ doped QDs as a dual modality imaging nanoparticle probe for MRI contrast.
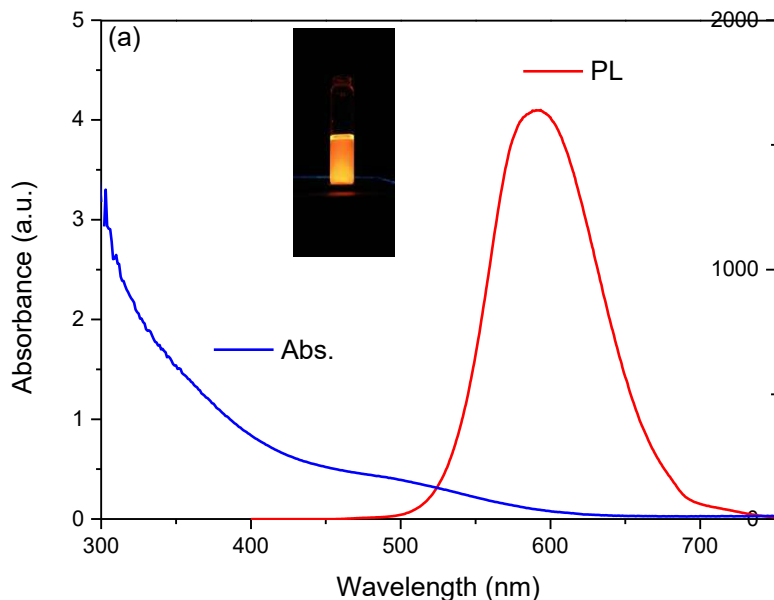


Figure 6.8 Absorption and photoluminescence spectrum of CuInS2@ZnS:$Gd^{3+}$ QDs ($\lambda_{ex} = 365$ nm).
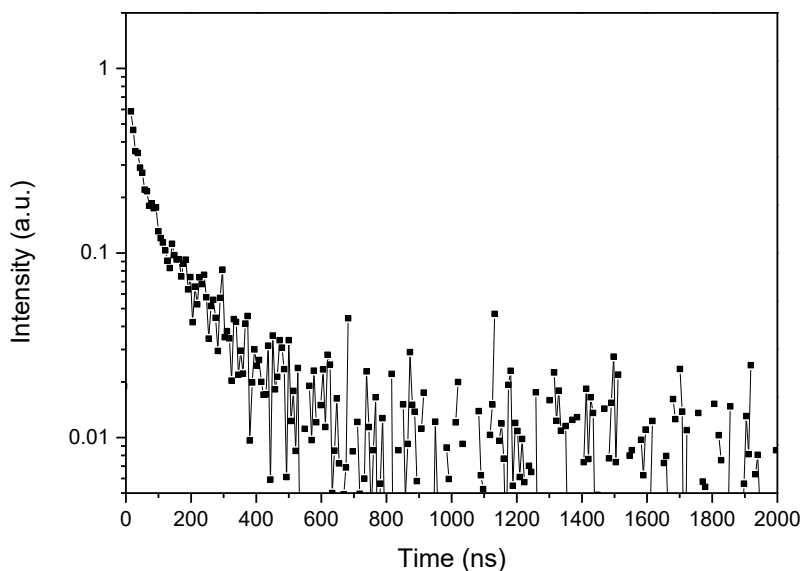


Figure 6.9 PL decay curve of CuInS2@ZnS:$Gd^{3+}$ QDs ($\lambda_{ex} = 365$ nm).

The PL of the $Gd^{3+}$ doped QDs capped with PEG and BSA quenches in aqueous solution over time. This was investigated by measuring the PL emission at different time and

temperature. As shown in figure 6.10, PEG and BSA showed different abilities in protecting the QDs from quenching. At room temperature, the QDs capped with BSA remain 73% of PL intensity after 5 days and the QDs capped with PEG remain 13% of PL intensity. For the QDs without $Gd^{3+}$ doping, it only remains 10% in 48 hours. In the 37°C environment, the PL lose intensity even faster.
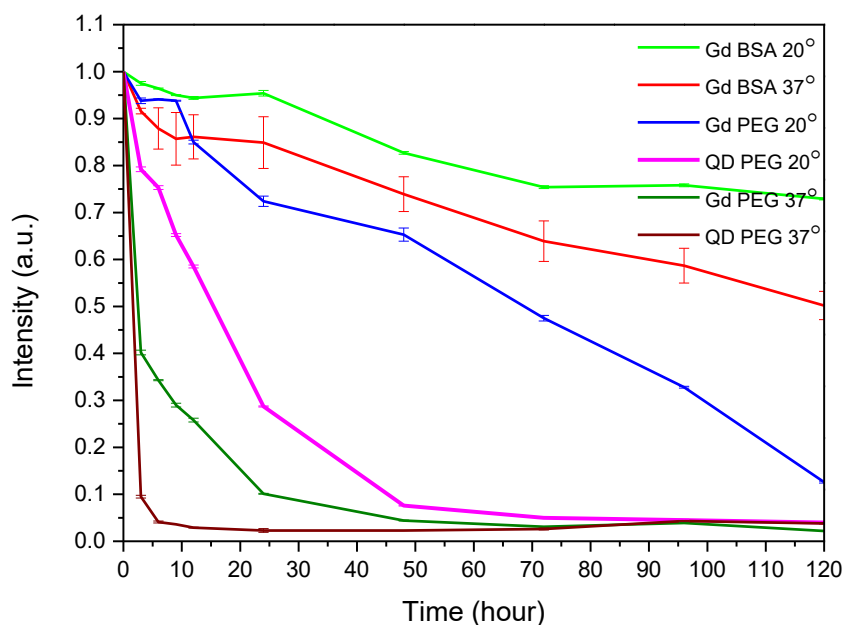


Figure 6.10 Time resolved PL decay curve of CuInS2@ZnS:$Gd^{3+}$ QDs ($\lambda_{ex} = 365$ nm).

## 6.3.3 Fluorescence and MRI Imaging In vitro and In vivo

$Gd^{3+}$ doped $CuInS_2$@ZnS@PEG QDs suspended in water were tested for the relaxivity value. Relaxivity (r1 and r2) is a measurement of the effectiveness of a paramagnetic material that derives from the slope of linear fit of the plot of inverse relaxation time (1/T1 and 1/T2) versus $Gd^{3+}$ concentration. Figure 6.11 (a) shows the relaxation profile of QDs. The QDs prepared at the initial Gd/Cu ratio of 3/1 showed r1 and r2 values of 33.81 $mM^{-1} \cdot s^{-1}$ and 45.61 $mM^{-1} \cdot s^{-1}$, respectively. The ratio of r2/r1 is 1.35, a value that much lower than other studies [192,232]. r2/r1 ratio is an important parameter to estimate the efficiency of T1 contrast agents and contrast agents with lower r2/r1 ratios show a stronger T1 positive effect [233,234]. The remarkably low r2/r1 ratio of 1.35 suggests that the CuInS2@ZnS:$Gd^{3+}$ QD is an efficient T1 contrast agents. In order to confirm that $Gd^{3+}$ content was sufficient to produce contrast in an MR image at the concentration used for optical imaging, CuInS2@ZnS:$Gd^{3+}$ QDs prepared with Gd/Cu feeding ratios at 3/1 with fluorescence emission at 590 nm were tested by MRI imaging (Fig. 6.11 b). Due to the much higher r1 value, QDs produced better T1 contrast. The above results suggest that CuInS2@ZnS:$Gd^{3+}$ QDs are qualified as bimodal imaging probes for excellent fluorescence and MR enhancement application.
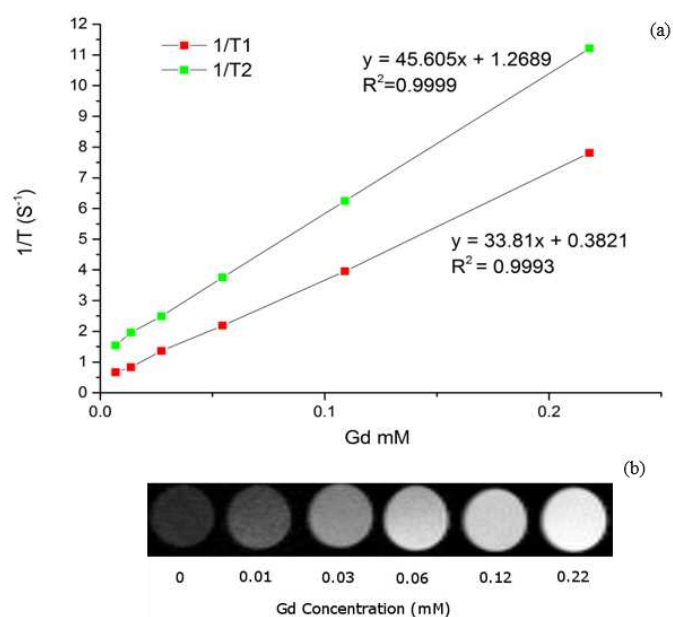
Figure 6.11 The comparison of linear relationship of the longitudinal and transverse relaxation rate versus the $Gd^{3+}$ concentration of $CuInS_2@ZnS:Gd^{3+}$ QDs. (b) $T_1$ weighted MR images at various $Gd^{3+}$ concentrations.

The cytotoxicity of the obtained BSA capped QDs was tested on Hela cell lines, and small cell viability loss was found after incubation with QDs at various concentration for 12-24 h. In the cytotoxicity assay, the cell viability is more than 80% when the QD concentration ranged from 25 to 400 μg/mL, which is nontoxic to HeLa cell (Fig. 6.12).
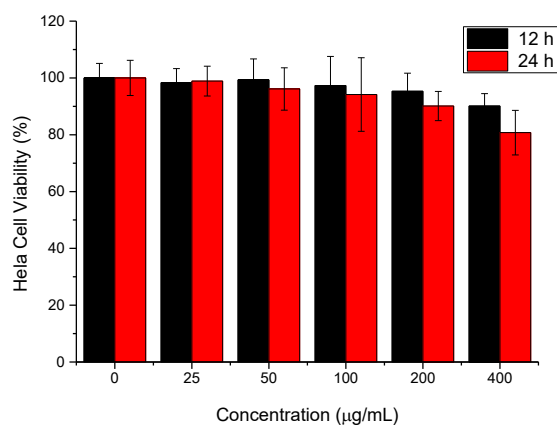


Figure 6.12 Cytotoxicity of $CuInS_2@ZnS:Gd^{3+}@BSA$ QDs on Hela cells at different QD concentration for 12h and 24h.

For the quantum dots capped with PEG, the cell viability is more than 90% on Hela and MDA-MB-231 cells at different QD concentration for 24h and 48h as shown in Fig. 6.13.
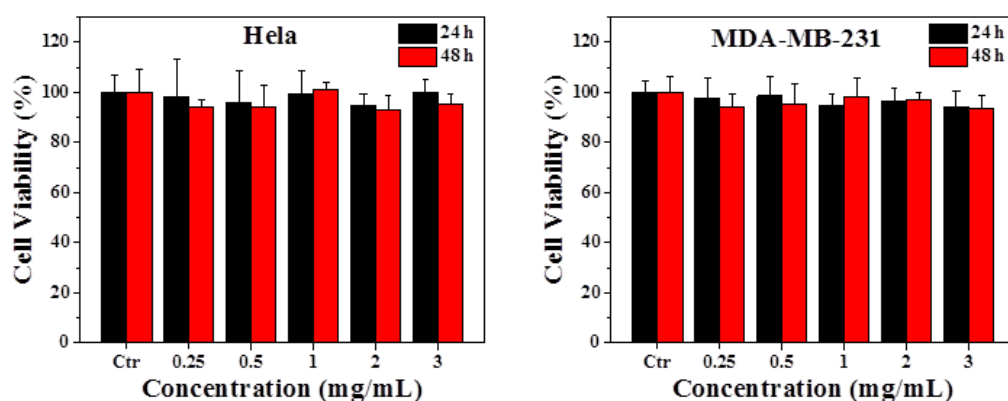
Figure 6.13 Cytotoxicity of CIS@ZnS:Gd$^{3+}$@PEG QDs on Hela and MDA-MB-231 cells at different QD concentration for 24h and 48h.

In vitro cellular dual-modal imaging was performed to confirm the utility of the Gd$^{3+}$ doped QDs for biological applications. HeLa cells were incubated with CuInS$_2$@ZnS:Gd$^{3+}$@BSA QDs at a concentration of 400 µg/mL for 12 hours. As shown in Fig. 6.14 a-c, the fluorescence images could clearly outline the whole cell with the nucleus region shown in dark. The MRI image shows that after incubated with QDs, the precipitated cells are clearly distinguishing from upper phosphate buffer saline (PBS) solution indicating that the MR signals is apparently enhanced (Fig. 6.14 d).
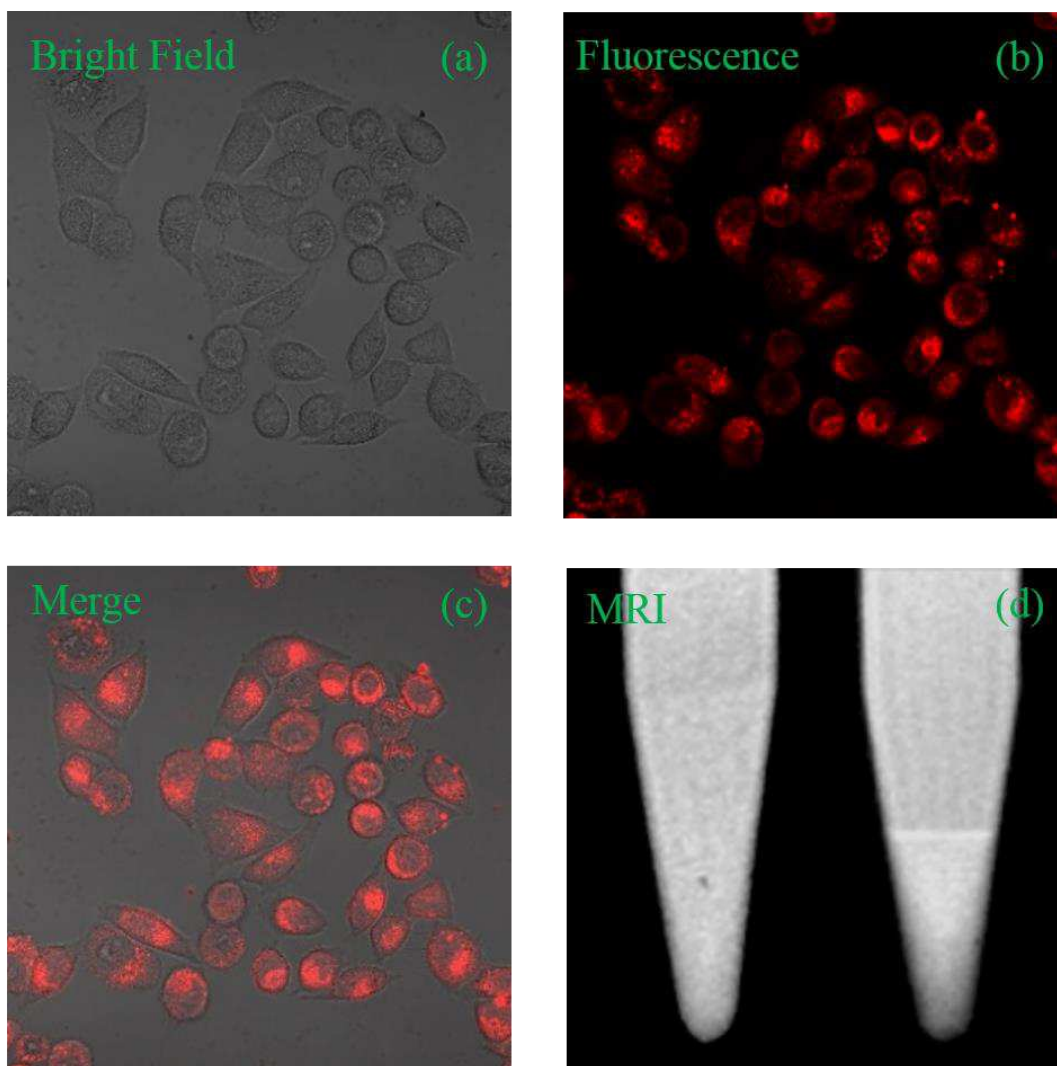
Figure 6.14 The confocal fluorescence and MRI images of Hela cells that incubated with $CuInS_2$@ZnS:$Gd^{3+}$@BSA QDs for 12h at a concentration of 400 μg/mL. (a) Bright field image. (b) Fluorescent image. (c) Merged image. (d) MRI image with control cell group (left tube) and cells incubated in $Gd^{3+}$ doped QDs (right tube).

The *in vivo* MR image was conducted with $CuInS2$@ZnS:$Gd^{3+}$ QDs on a 7.0 T MRI scanner. As shown in Fig. 6.15, we acquired the T1-weighted MR images at various time points after intravenous injection of the bimodal QDs, with a dose of 200 μL which is around 0.05 mmol Gd/kg of mouse body weight. Due to the high reticuloendothelial system (RES) accumulation of the nanoparticles, T1-weighted MR images at liver area exhibited a significantly enhanced signal even after 10 minutes comparing to that before QD injection. This T1-weighted MR signal continually increases and remains strong after 2 hours and even to 5 hours when we stopped the signal recording. Based on the above animal experiments, it can be concluded that the as fabricated QDs are a potential dual modal contrast agent which can simultaneously generate strong MR contrast enhancement as well as fluorescence imaging, and eventually provide more comprehensive imaging information and contribute to higher diagnostic accuracy, particularly in the detection and diagnosis of liver lesions.
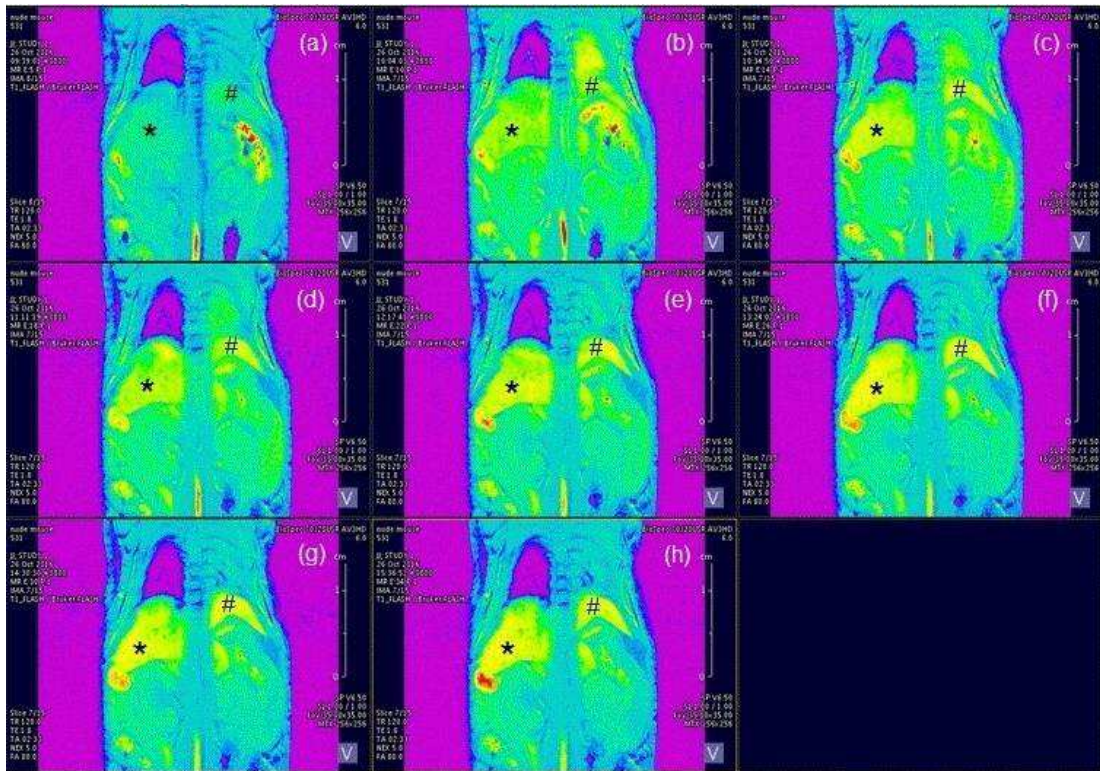
Figure 6.15 In vivo T1-weighted MR images of nude mouse before and various time points post injection of QDs. The right and left lobe of liver were marked with * and #. (a) control; (b) 10 min; (c) 20 min; (d) 1h; (e) 2h; (f) 3h; (g) 4h; (h) 5h.

In order to check the leaking of the $Cu^{2+}$, $In^{3+}$ and $Gd^{3+}$ ions, main organs (heart, liver, spleen, lung and kidney) were collected after 21 days from injection and treated with haematoxylin and eosin stain (H&E stain). The mice without QDs treatment were used as control. As shown in figure 6.16, except for a few hemorrhages in kidney, other distinct changes and lesions such as edema, inflammation and necrosis are not seen in main organs. Compare to Cd containing QDs, $Gd^{3+}$ doped CIS@ZnS QDs present much lower toxicity *in vivo*. All these result exhibits a good biocompatibility of the as obtained QDs as dual-modal contrast agent.
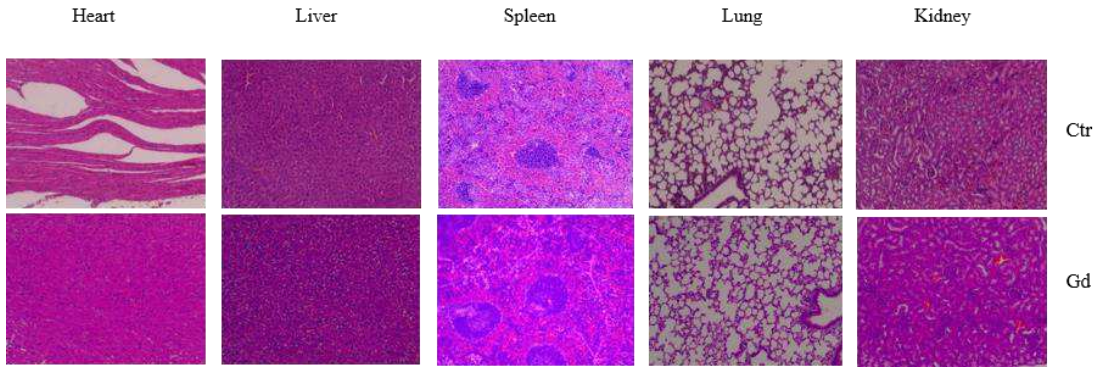


Figure 6.16 H&E stained pictures of main organs collected from control and QDs injected mice after 21 days post injection.

## 6.3.4 Investigation on detection of metal ions using QDs

Various concentrations of $Cu^{2+}$ ions were prepared in deionized water. An aliquot of the given metal ion solutions (1uL) was added into 1 mL CIS@ZnS:$Gd^{3+}$ QDs solutions. After equilibration for 1 minute, the fluorescence spectrum of $Gd^{3+}$-CIS@ZnS QDs solutions was measured at excitation wavelength of 365 nm. The fluorescence properties of the CIS@ZnS:$Gd^{3+}$ QDs were studied in response to various metal ions, i.e., $Cu^{2+}$, $Al^{3+}$, $Sn^{2+}$, $Zn^{2+}$, $Fe^{2+}$, $Mn^{2+}$, $Ca^{2+}$, $Na^+$, and $Gd^{3+}$.

The fluorescence of the CIS@ZnS:$Gd^{3+}$ QDs can respond to the addition of $Cu^{2+}$ as fast as 30 seconds. However, in the following measurements, the fluorescence spectra of the CIS@ZnS:$Gd^{3+}$ QDs were recorded after adding the metal ions for 1 min. The fluorescence quenching of QDs was investigated in response to $Cu^{2+}$ with various concentrations. Fig. 6.17 (a) and (b) indicate that the fluorescence intensity of QDs decreased with increasing the concentration of $Cu^{2+}$ ions in the solution. Fig. 6.18 (a) plots the fluorescence-intensity ratios $(I_0-I_{Cu})/I_0$ at 600 nm versus the concentration of $Cu^{2+}$ ions in logarithm scale. $I_0$ and $I_{Cu}$ were the maximum fluorescence intensities of the QDs at 600nm in the absence and presence of $Cu^{2+}$ ions, respectively. The fluorescence property of QDs is sensitive to the surface state. $Cu^{2+}$ can interact with QDs and change the surface property, leading to the formation of CuS layers on the surface. CuS is not soluble in water and thus induced the aggregation and precipitation of the QDs which lead to quenching of the fluorescence. The lowest concentration of $Cu^{2+}$ detected in the present work can be as low as 0.5 ppb (7.5 nM), which is $1.3 \times 10^4$ times lower than the maximum level of $Cu^{2+}$ (i.e., 1.3 ppm or ~20 uM) in drinking water permitted by the U.S. Environmental Protection Agency (EPA).
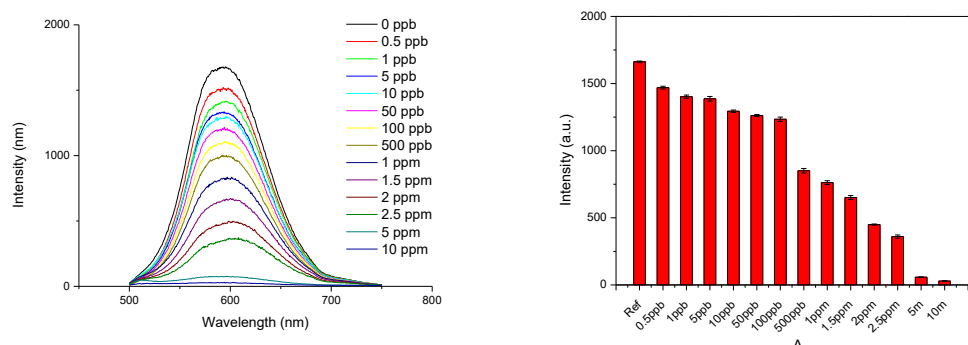


Figure 6.17 Fluorescence response of CIS@ZnS:$Gd^{3+}$ QDs upon the addition of different concentrations of $Cu^{2+}$ ions (0.5, 1, 5, 10, 50, 100, 500, 1000, 1500, 2000, 2500, 5000 and 10,000 ppb). The excitation wavelength was 365 nm.

The effects of other metal ions on the selectivity of the CIS@ZnS:$Gd^{3+}$ QDs were further studied by adding various metal ions into the QD solution. Fig. 6.18 b shows the fluorescence intensities of QDs when add other metal ions. The concentration of each metal ion was set at 5 ppm (blue bars). The chosen metal ions were $Al^{3+}$, $Sn^{2+}$, $Zn^{2+}$, $Fe^{2+}$,

Mn$^{2+}$, Ca$^{2+}$, Na$^+$, and Gd$^{3+}$. It can be clearly seen from Fig. 6.18 b that the QDs are not selectively sensitive to these metal ions. Interestingly, the successive addition of the same concentration of Cu$^{2+}$ leads to the significant quenching of the QDs (red bars). As a result, CIS@ZnS:Gd$^{3+}$ QDs exhibited a good selectivity for Cu$^{2+}$ ions even in the presence of other metal ions.
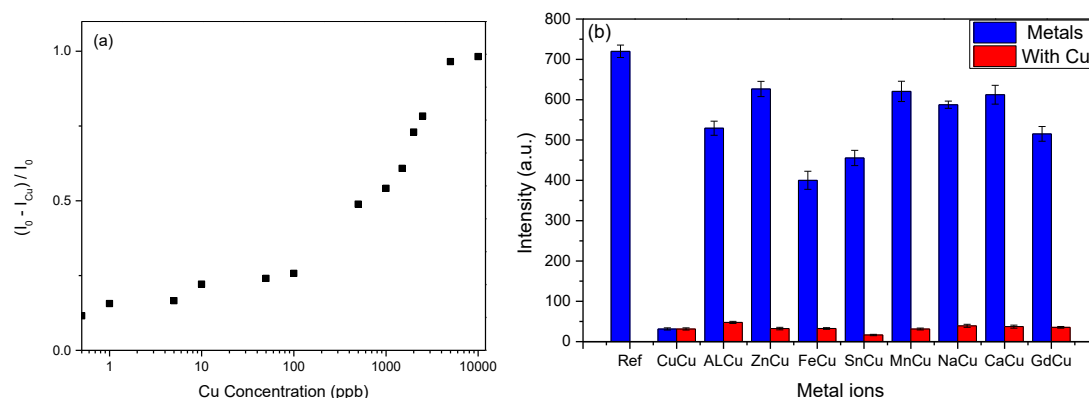


Figure 6.18 (a) Plot of fluorescence-intensity ratios $(I_0 - I_{Cu})/I_0$ of QDs at 600 nm versus different concentration of Cu$^{2+}$ ions added in logarithm scale. $I_0$ and $I_{Cu}$ were the maximum fluorescence intensities of the QDs at 600nm in the absence and presence of Cu$^{2+}$ ions, respectively. (b) Fluorescence-intensities of QDs at 600 nm after sequential addition of various metal ions (blue bars). The tested of metal ions were Al$^{3+}$, Sn$^{2+}$, Zn$^{2+}$, Fe$^{2+}$, Mn$^{2+}$, Ca$^{2+}$, Na$^+$, and Gd$^{3+}$. The concentration of each metal ion in the solution was 5 ppm. When the same concentration of Cu$^{2+}$ ion was added, the fluorescence was quenched significantly (red bars).

# 6.4 Conclusion

In this work, an efficient bimodal MR/fluorescence imaging nanoprobe is presented. We demonstrate a facile strategy to fabricate novel Gd$^{3+}$ doped CIS@ZnS quantum dots that allows incorporation of high levels of Gd$^{3+}$ into the quantum dots to afford superior MR enhancement with sufficient red fluorescent emission. This dual-modality nanoprobe shows low toxicity on HeLa cells and good colloidal stability. The bimodal nanoprobes have a high longitudinal relaxivity (r1 = 33.81 mM$^{-1}$s$^{-1}$) and an apparently increasing contrast enhancement ability of magnetic resonance image. The highly-qualified MR and fluorescence imaging properties in vitro and in vivo paved a new way to take advantage of this nontoxic I−III−VI quantum dot for biomedical applications.

For Cu$^{2+}$ detection, the QDs exhibited fast fluorescence response, high sensitivity and selectivity toward Cu$^{2+}$ ions over other metal ions in aqueous solution. The detection limit could reach as low as 0.5 ppb (7.5 nM). The presence of other metal ions did not affect the selectivety of the QDs toward Cu$^{2+}$. The sensing mechanism was mainly attributed to Cu$^{2+}$ induced aggregation and precipitation of CuInS$_2$@ZnS QDs that lead to the significant fluorescence quench.

# Chapter 7 Luminescent Cu based compounds

## 7.1 Introduction

In recent years, stimulus-responsive luminescent materials have emerged as a new class of smart functional materials with potential recording and sensor applications [235][236]. Various external stimuli can induce a change in the colors of the luminophore compounds, which generally can be classified by thermochromism, mechanochromism, solvatochromism, vapochromism, photochromism, electrochromism and acidochromism. In most cases, these chromism may be based on a change in the electron state of the molecules, the coordination geometry, the band gap, the crystal field strength, the mechanical deformation and the molecular rearrangement [237–239].

Among them, mechanochromic and thermochromism luminescent materials research have attracted much intention due to their potential application in optical recording devices, pressure sensing and security system, and damage detectors [240–243]. A number of pressure and temperature sensitive luminescent materials have been developed in recent years with examples on organic dyes and transition-metal complexes [244–246]. Nanomaterials, especially noble metal nanomaterials have been recognized as the most popular research topics in the past decades. With interesting size-dependent electrical, optical, magnetic, chemical properties and many technological applications, they are intensively investigated [247–253]. In this family, metal nanoclusters (NCs) have received much attention for their unique physical, chemical, electrical, optical and molecule-like properties with promising application in catalysis, chemical sensors, electronic devices, and biological imaging [36,254–257]. A few strategies have been developed to synthesize copper nanoclusters such as Cu-S and Cu-I based Cu clusters [258–265].

In most luminescence materials, the concentration quenching (CQ) or aggregation caused quenching (ACQ), is a harmful photophysical phenomenon in which the emission from a solution of luminophore is quenched with an increase in concentration or aggregation of luminophore. Interestingly, some other materials exhibit the opposite effect, the emission can be enhanced by the aggregation of chromogen and thus called aggregation induced emission (AIE) [266]. As a constructive effect, AIE makes it possible to actively utilize the aggregation process, instead of passively working against it as in the case of ACQ effect. It was reported that metal complex or nanocluster luminescence can be enhanced by controlling NCs aggregation structures of NCs surface ligands configuration [267–269]. The aggregation of NCs is capable to induce the ligand-to-metal charge transfer (LMCT) or ligand-to-metal-metal charge transfer (LMMCT) and subsequent radiative relaxation via a metal centered triplet state [267,270]. Aggregation restrains the intramolecular vibration and rotation of ligands and increases the rates of radiative energy transfer by suppressing ligand-related non-radiative relaxation of excited states [271]. According this analysis, the aggregation involves a high ordered molecular assembly of chromophore among nanocluster and ligands.

Self-assembly has emerged as an efficient strategy for optimizing the performance of fluorescent nanomaterials. By directing the spatial distribution of building blocks, self-assembly process can spontaneously build hierarchically structured nanosheets, chain-like clusters and spherical supraparticles in solution via high valence interactions in combination with interfacial adsorption and compression. Dipole moment, small positive charge, and directional hydrophobic attraction are the driving forces for the self-organization process [272–274]. Through transforming the disordered aggregates into regular and uniform self-assembly architectures, self-assembly can enhance nanoparticle luminescence performance.

Except for metal nanoclusters (NCs), layered organic-inorganic (O/I) hybrid materials have attracted great attention due to their ability to combine the unique properties of pure organic and inorganic materials [275–277]. Extensive research for several decades has produced many classes of such hybrid materials with a molecular leveled control of structure and properties [278], particularly in nonlinear optical behavior [279], electrical conductivity [280], superconductivity [281], and ferromagnetism [282]. The majority of these layered O/I materials are prepared by intercalation of organic moieties between inorganic layers [283]. Among these, layered organic-inorganic hybrid silver thiolates were synthesized by simply adding $Ag^+$ ions into thiol, triethylamine and acetonitrile and the properties were studied [284]. According to the X-ray diffraction measurements, the authors suggest that the precipitated products are periodically layered bimolecular assemblies of Ag O/I hybrid thiolates (AgSRs). Ag and S atoms occur in regularly stacked layers with a large interlayer lattice distance, and the intralayer two-dimensional lattice possesses relatively small repeat distances.

The pioneering study of Dance et al suggested that three SR moieties are projected in either direction coordinated to the Ag atom in center plane to make layered silver thiolates. They proposed that the structure of silver thiolates is comprised of a trigonal-planar layered, inorganic Ag-S lattice in a quasi-hexagonal symmetry with the SR moieties on either side perpendicularly extended. After that, the structure of the long chain organic analogues has been explored in detail by Parikh et al [285]. They found that the long chain homologues of AgSRs exhibit conformationally all-trans order, perpendicular orientation with respect to the inorganic Ag-S slab and slight overlap between the hydrogen atoms of methyl groups. They proposed a two-step, hierarchical self-assembly mechanism involving primary self-assembly of the inorganic core in 2D dimension and subsequent self-assemblely in the third dimension to produce the pillared silver thiolates.

Because of the similarity in the alkyl chain assembly of thiolates and monolayers in silver thiolates (AgSRs), the methodologies and model system of silver analogues can be used for the study of copper thiolates. Moreover, due to the similarity in the optical properties, the methods and mechanisms in metal clusters can also be used to study the luminescent property of copper thiolates. Copper possess the same chemical properties and it is comparatively much cheaper, but the investigation on copper thiolates is relatively few. Sandhyarani et al prepared copper alkane thiolates with octadecane, octane, pentane and butane thiols. They report that copper thiolates possess a bilayer structure in the solid state and undergo a transition to a columnar mesophase upon increasing the temperature

[286].

In this work, we describe a one-step facile preparation method for synthesis of Cu thiolates (CuSRs) in colloidal solution. With 1-dodecanethiol (DDT) as reductant and coordinate ligand, the layered organic-inorganic (O/I) hybrid Cu thiolates were obtained in 1-octadecene (ODE) colloidal solution by controlling the reaction and synthesis condition. The as synthesized Cu thiolates can emit light that cover in a broad spectrum from blue, green, yellow to red, the emission intensity among these colours varies in different synthesis temperature, and thus we obtained the green, yellow and near white light emitting copper thiolate multi-layer material. Except for the unique light emission character, it exhibits both mechano- and thermochromic luminescent properties. It reveals that strong emission can be generated by transforming the disordered aggregates to ordered assemblies and thus improved DDT-related radiative LMCT and/or LMMCT energy transfer.

# 7.2. Experimental

## 7.2.1. Chemicals

- 1-dodecanethiol (DDT), $CH_3(CH_2)_{11}SH$, MW = 202.40 g/mol, d = 0.845 g/mL, Sigma-Aldrich, 98%

- 1-octadecene (ODE), $CH_3(CH_2)_{15}CH=CH_2$, MW = 252.48 g/mol, d = 0.789 g/mL, Sigma-Aldrich, 90%

- Copper (I) chloride, CuCl, MW = 99.0 g/mol, Sigma-Aldrich, 97%

## 7.2.2. Preparation of CuSRs

0.5 mmol (0.05mg) of CuCl was mixed in 6 mL of ODE in a glass bottle purged with argon atmosphere at room temperature and stirred for 10 min. Set another glass bottle beside with water and metal thermometer inside to control the temperature. 12 mmol (3mL) DDT was then added into the mixture and stirred at room temperature (20°C) for 10 min to produce DDT-capped CuSRs. When DDT was added, the solution become milky immediately and the yellow emission was saw under 365 nm UV lamp. To improve the self-assembly, the temperature was increased at a rate of around 2-4 °C/min and stirring speed set at 300-500 rpm. Take out the fraction of the solution at different temperatures, 20°C, 30°C, 40°C, 50°C, 60°C, 70°C, 80°C, 90°C, 100°C, 110°C, 120°C, 130°C, 140°C, 150°C, centrifuge and discard the solvents, then wash with diethyl ether to obtain the copper thiolate crystals. The changing of emission colour at different temperature can be seen in figure 7.6. Alternatively, the reaction can be conducted in an argon connected three neck glass which was heated in silicon oil. In this way, the emission changing over temperature appears different, see figure 7.7. When the temperature is close to around

140°C-150°C, the milky product in solution disappears and the solution is transparent. The transparent solution above 150°C emits red light under 365 nm UV light and the emission disappears when the sample cools down. Upon putting back into the reaction and heating, it reemits, and emission disappears again when it cools, see figure 7.8.

## 7.2.3. Purification and dispersion in water solution

At room temperature, the self-assembled CuSRs were washed twice and precipitated through the addition of diethyl ether. Separated by centrifugation, the precipitates were collected and dried at room temperature. The powders of samples dispersed well in toluene and chloroform. In order to disperse in water, the CuSRs powders and Dioctyl Sulfosuccinate Sodium Salt, or potassium oleate, or BSA were mixed in deionized water under ultrasonification for a few minutes and CuSRs dispersed in water homogeneously. Both the powder and solution of CuSRs are stable in air for several months without obvious reduction of emission colour.

## 7.2.4. Characterization

Transmission electron microscopy (TEM) images were taken on Morgagni 268D (FEI-Philips) equipped with MegaView2 CCD camera. The CuSRs were drop-cast from a diluted dispersion in water solution onto a thin carbon film supported by a copper grid. X-ray powder diffraction (XRD) patterns were obtained using an ARL X'TRA X-ray diffractometer produced by Thermo Fisher. UV– vis spectra were recorded on an Evolution 201 UV–visible spectrophotometer. PL spectra were recorded using a FP-8200 spectrofluorometer (Japan) and NanoLog® spectrofluorometer system (Horiba Scientific, New Jersey, USA). Fourier transform infrared (FTIR) spectra of the samples were recorded in the 5000-400 cm-1 range using a Jasco FT/IR-660 plus spectrometer

## 7.3. Results and discussion

## 7.3.1 TEM and XRD analysis

A schematic illustration of the layered copper (I) thiolate structure by self-assembly is shown in Fig. 7.1. Copper atoms are arranged in center plane and the sulfur atoms are attached either side of the Cu plane. The initial strong bonding of the thiolate to copper and the three-dimensional stacking of these two-dimensional organic–inorganic hybrid layers leading to a self-assembled multi-layered structure through the van der Waals' interactions between the alkyl chains [286]. This structure can be compared and correlated with the two dimensional self-assembled monolayers (2D-SAMs) and silver thiolates [287,288]. In addition, this structure is very similar to the lipid bilayer of the cell membrane, which is composed of lipid hydrophilic head and hydrophobic tails.
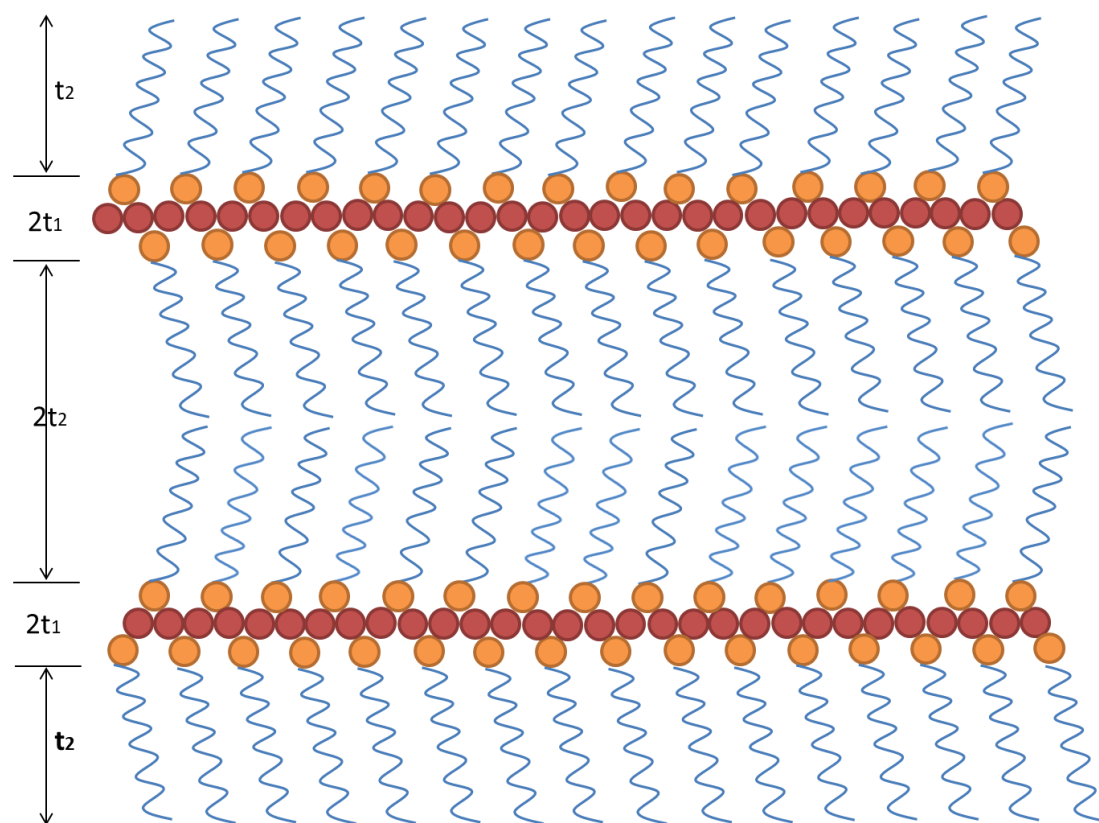
Figure 7.1 Cross-sectional scheme of the layered structure of copper (I) thiolate crystal structure. The yellow circles show the sulfur atoms, which are arranged alternately in two planes. Copper atoms are represented by the red spheres arranged in one plane. Horizontal lines define the thickness. 2t1 represents the central Cu,S. The vertical lines represent the chains extending from sulfur to the distal atom $CH_3$ include the van der Waals radii of the molecule $CH_3$ at which the layers are in contact. The total thickness of one layer is $2t_1 + 2t_2$. The possible interpenetration of layers at their interface is neglected in the model.

The CuSRs employed to investigate assembly induced luminescence enhancement were initially synthesized in ODE with DDT as ligand and reductant at various temperature (20-150°C). Then the products that emit yellow and green light synthesized at 20°C and 40°C were chosen to be studied. TEM image show that the CuSRs are composed of stacking layers (Figure 7.2 a-d). The average layer distance was determined as 3.18 nm by Image J program.
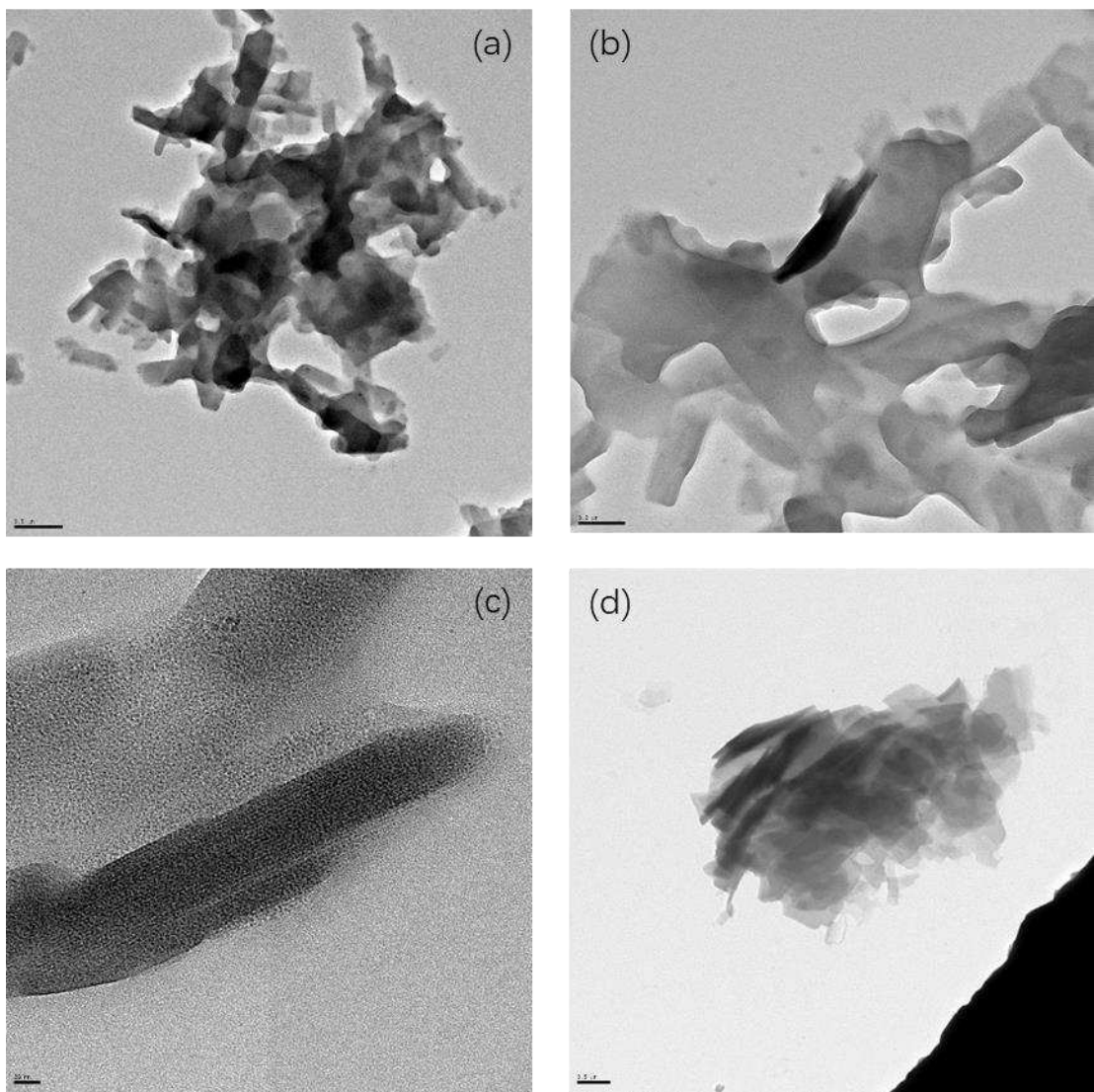
Figure 7.2 TEM images of CuSRs

The high ordered stacking features are further proved by XRD analysis. It is seen from the powder XRD pattern that there are distinct diffraction peaks at 5.16°, 7.76°, 10.4°, 13.01°, 15.27°, 17.3°, 18.41°, 19.52°, 20.91°, 23.57°, 24.41°, 26.27°, 27.83°, 28.46°, 30.53°, 32.75°, 35.12°, 37.1°, 39.86°, 42.35°, 44.3° and 47.36°. Figure 7.2 shows the XRD pattern. In the powder XRD, the sample shows a well-defined progression of intense reflections, which are successive orders of diffraction from a layered structure with a single large d spacing (d > 4.5 Å). There is a significantly large d spacing reflection in small angle XRD pattern at 0.56°. The weak reflections at higher $2\theta$ corresponding to d < 4.5 Å are assigned to the intralayer Cu-S lattice structure and periodicities [285]. All these reflections are indexed as (0k0) and a detailed summary of the X-ray peak structure and their crystallographic assignments is provided in Table 7.1. The intense diffraction patterns with large d spacing can be interpreted in terms of a crystal structure in regularly stacked layers of Cu and S atoms with a large interlayer lattice dimension. Each layer of Cu-S slab is separated from the other by twice the length of the alkyl chain. The average derived interlayer space a is 31 Å. The data is derived from the model in which parallel slabs of Cu

and S atoms are not coplanar, see figure 7.1. The slabs contribute a small thickness $2t_1$, which is the perpendicular separation of the planes of S atoms to the layer [284]. The principal thickness of the layer is due to the length L of the DDT chain, from S to the distal molecule $CH_3$. Together with $r_w(CH_3)$ as the van der Waals radius, each DDT substituent contributes $t_2 = L + r_w(CH_3)$ to the thickness of the layer. The calculated thickness of the layer (*Tcal*) is then $2t_1 + 2t_2$, where $t_2 = L + r_w(CH_3) \times \cos\theta$, L is the length of the alkyl chain, $rw(CH_3)$ is the van der Waals' radius of the $CH_3$ group (2.0 Å) and $\theta$ is the tilt angle. The tilt angle is assumed as 13°, which is the same as that of a 2D-SAM on copper and the relatively low $t_1$ is neglected [286][287]. In case of all-trans conformation, the chain length of 1.253 Å per $CH_2$ group was calculated [285], the observed and calculated thickness (*Tobs* and *Tcal*) of the layer are 31.03 Å and 31.4 Å, respectively. There is excellent agreement between the values of $k \times d$ and the interlayer repeat distance (*a*) for reflections with *k* up to 11 (*Tobs=a=$k \times d$*, where *k* is the order of diffraction), see table 7.1.
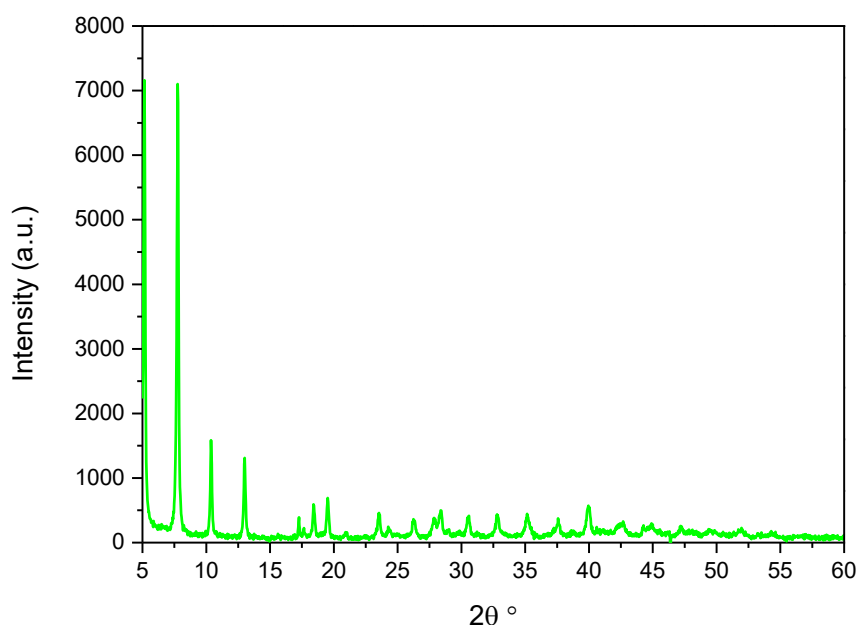


Figure 7.3 XRD patterns of CuSRs synthesized at 20 and 40°C with yellow and green emission color.

## Table 7.1 Summary of the interlayer XRD peaks and their Assignments

| 2 Theta | 0.56 | 2.53 | 5.16 | 7.76 | 10.4 | 13.01 | 15.27 | 18.39 | 20.91 | 23.54 | 26.32 | 28.32 |
|---|---|---|---|---|---|---|---|---|---|---|---|---|
| hkl | 010 | 010 | 020 | 030 | 040 | 050 | 060 | 070 | 080 | 090 | 0100 | 0110 |
| d (Å) | 157.56 | 34.86 | 17.11 | 11.39 | 8.5 | 6.80 | 5.8 | 4.82 | 4.25 | 3.78 | 3.38 | 3,15 |
| a (Å) | 157.56 | 34.86 | 34.22 | 34.17 | 34.00 | 33.99 | 34.8 | 33.73 | 33.96 | 33.98 | 33.83 | 34.63 |

The small angle XRD was also performed and the CuSRs appears some distinctive peaks at small angle area. As shown in figure 7.4, for the sample synthesized at 20°C, an

intense peak at 0.56° is seen, the second high peak appears at 2.5°, with a shoulder at 2.1°. After grind, this peak decrease clearly, and the shoulder disappeared. The following peaks towards the higher angles are decreasing as well. The high peak at the near zero angle (0.56°) moved to 0.96°. For the sample synthesized at 40°C, a high peak at 0.52° is seen and it moved to 0.92° after grinding; the second-high peak appears at 2.52°, without shoulder. After grind, this peak remains the same. The following peaks towards the higher angles remain the same as well after grinding.
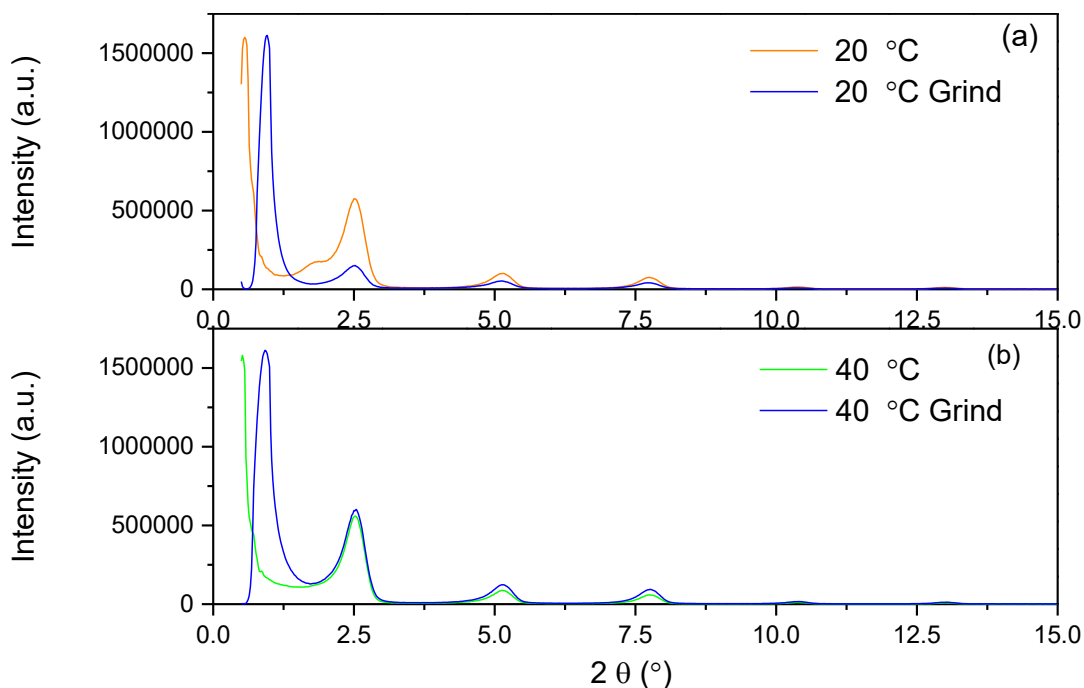


Figure 7.4 Small angle XRD pattern of CuSRs synthesized at 20 and 40°C with yellow and green emission color.

The chemical properties of the CuSRs were examined by FTIR measurements and the infrared spectra are shown in Fig. 7.5. In the IR spectra, disappearance of S-H band around 2500-2600 cm-1 indicates that the S-H bond in DDT has been replaced by the S-Cu bond in thiolates, showing high affinity of S to Cu(I). DDT exhibits a number of characteristic IR bands. The characteristic peaks observed in high frequency region are assigned to the C-H stretching modes of the polymethylene [$-(CH_2)_n$-] sequence and methyl [$-CH_3$] groups (Fig. 7.5 a). The two strongest bands with peak maxima at 2850 and 2918 $cm^{-1}$ are assigned to methylene $CH_2$ C-H symmetric ($d^+$) and antisymmetric ($d^-$) stretching modes, respectively. The weak peak observed at 2873 and 2956 $cm^{-1}$ are assigned to methyl C-H symmetric ($r^+$) and antisymmetric ($r^-$) stretch. The position of methylene symmetric ($d^+$) and antisymmetric ($d^-$) peaks is known to be an indicator of chain conformation and the observed location of these peaks in this case strongly indicate that the dominant structure of the polymethylene sequences in DDT is all trans compare to the crystalline n-alkanes [289]. When the alkyl chains are in disordered state, in which the gauche conformation appears, the methylene symmetric ($d^+$) and antisymmetric ($d^-$) peaks display higher values (2856 and 2926 $cm^{-1}$, respectively) [290].

In the low frequency region of the IR spectra as shown in figure 7.5 b, the series of uniformly spaced peaks of moderate intensities with alternating weak shoulders between 1150 and 1300 cm$^{-1}$ are assigned to the progression series formed by the delocalized wagging (Wx) and twisting (Tx) vibrations of the polymethylene sequences [290][291]. The wag–twist progression series in the range of 1150 cm$^{-1}$ to 1300 cm$^{-1}$ shows the presence of an all-trans arrangement and these progression bands will smear into a broad envelope in disordered state [290]. The peak observed between 1000 cm$^{-1}$ and 1150 cm$^{-1}$ is assigned to the C–C–C vibrational modes and those between 715 cm$^{-1}$ and 1027 cm$^{-1}$ are assigned to the rocking modes [285]. The prominent peaks in the low frequency region are the scissoring and rocking modes centered at 1469 cm$^{-1}$ and 715 cm$^{-1}$ [285]. The intense asymmetric band observed at 715 cm$^{-1}$ is assigned to the head-band of the progression series in the rocking modes [285].The $\nu$(C–S)$_t$ stretch mode also appears at around 720 cm$^{-1}$ [286]. The peak at 1425 cm$^{-1}$ is assigned as the deformation of the methylene adjacent to sulfur. The typical band at 650 cm$^{-1}$ for the $\nu$(C–S)$_g$ structure is absent [286].. All of the peaks can be straightforwardly assigned (see Table 7.2), include the bands from CH$_2$ twisting, wagging and rocking modes.

**Table 7.2 Identification and Fundamental Vibrational Assignment to the Observed Infrared Peak Maxima in Wavenumbers, cm-1 for the Cu thiolates**

| Bands | 2956 | 2918 | 2850 | 2873 | 1471 | 1427 | 1382 | 1346 w | 1323 w |
|---|---|---|---|---|---|---|---|---|---|
| Modes | CH3 r- | CH2 d- | CH2 d+ | CH3 r+ | CH2 def. | CH2 sci. | CH3 def. | CH2 Tx | CH2 Wx |
| Bands | 1298 | 1270 | 1242 | 1215 | 1188 | 1126 w | 1068 | 1029 w | 931 |
| Modes | CH2 Wx | CH2 Wx | CH2 Wx | CH2 Wx | CH2 Wx | C-C-C | C-C-C | CH2 Px | CH2 Px |
| Bands | 890w | 827 w | 752 | 735 | 715 | | | | |
| Modes | CH2 Px | CH2 Px | CH2 Px | CH2 Px | CH2 Px | | | | |

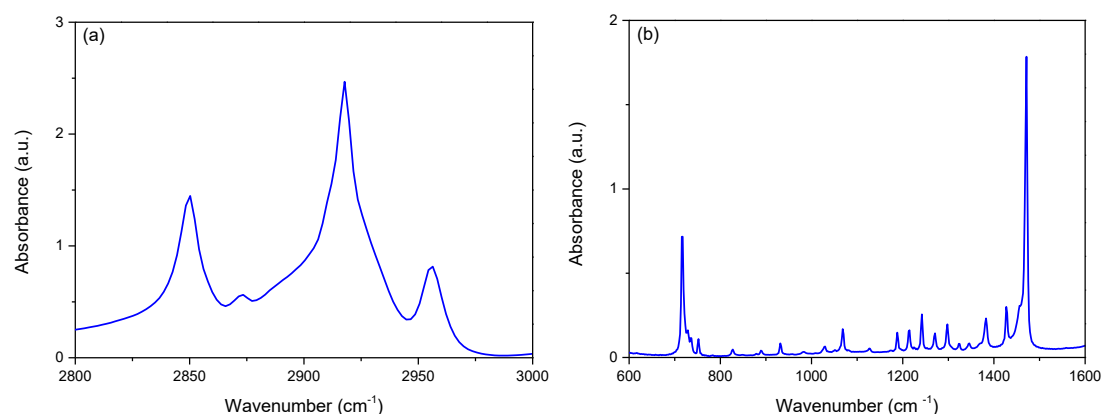$^*$ Tx, twisting; Wx, wagging; Px, rocking; def, deformation; sci, scissoring; w, weak



Figure 7.5 FTIR patterns of CuSRs at higher (a) and lower (b) frequency region.

## 7.3.2 Optical properties

The self-assembly of Cu CuSRs was controlled by changing temperature in ODE solution from around 20°C to 150°C. The higher solution temperature and stirring speed facilitates the dynamic mobility of DDT alkyl chain on CuSRs, thus permitting the two-dimensional self-assembly of CuSRs via dipole induced van der Waals attraction [292]. Thus, a dramatic intensity increase of emission was found when the temperature was increased. The CuSRs assemblies exhibit a broad emission ranged from blue, green, yellow to red. As the reaction temperature increased gradually, the emission intensity ratio among blue, green, yellow and red fluctuated and thus the colour of emission changed correspondingly. With a 0.3 mmol of CuCl in 6 mL of ODE and 3 mL DDT, stirring speed of around 400rpm and heating speed of 4°C/min, the emission peak centered at 550 nm with a full width at half-maximum (fwhm) around 100 nm at room temperature (20°C), corresponding to yellow emission (Fig. 7.6). When the temperature increased to 40°C, the emission peak that centered at 510 nm increased dramatically with a full width at half-maximum around 90 nm, corresponding to green emission. Further increase the temperature causes the emission intensity decreased. The emission colour changes over temperature and this changing rate relates to stirring speed, starting temperature and temperature increasing rate (Fig. 7.7).
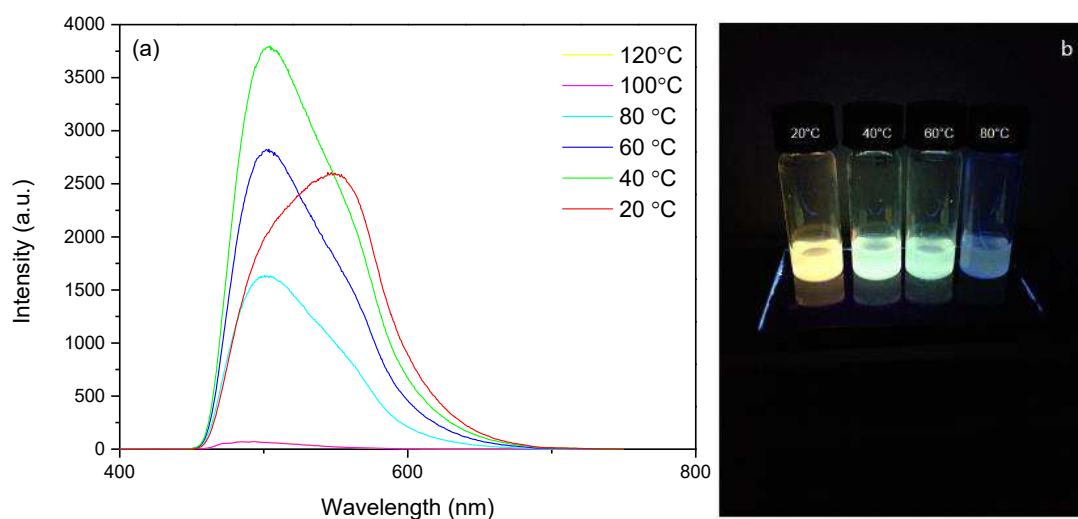


Figure 7.6 Room temperature steady-state emission spectra of CuSRs assemblies prepared at 20, 40, 60, 80, 100, and 120°C in a glass bottle (a) and the fluorescent images in water with 365 nm excitation (b). The glass container with reaction solution was heated on the heating board; the synthesis stirring and heating speed are set as around 350 rpm and 4°C/min, respectively.
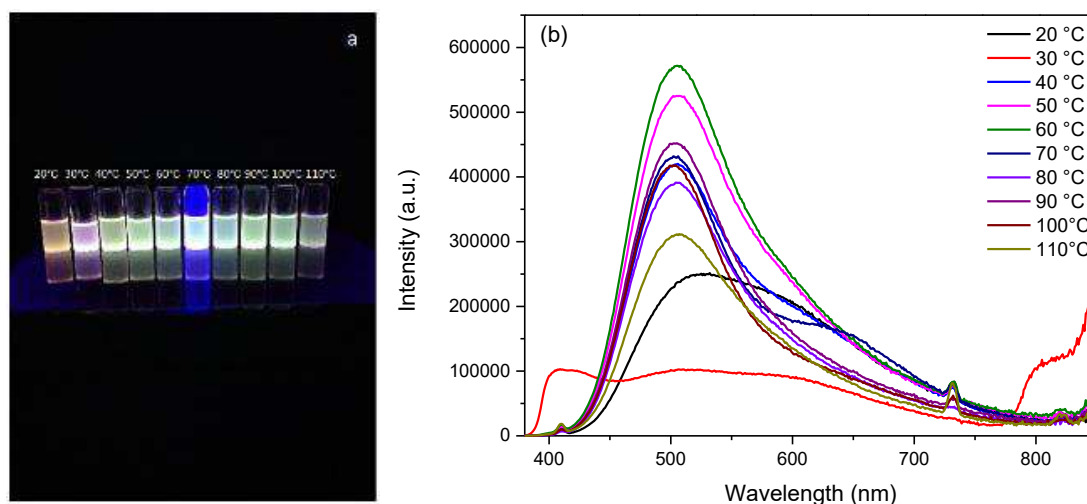
Figure 7.7 Luminescent images from 20-110 °C with 365 nm excitation in toluene (a) and steady-state emission spectra of CuSRs assemblies prepared at 20, 30, 40, 50, 60, 70, 80, 90, 100 and 110°C (b). The reaction is conducted in three neck glass which was heated in silicon oil; the synthesis stirring and heating speed are set as around 600 rpm and 2°C/min.

As shown in figure 7.8, the disappearing of milky product in solution at higher temperature (>150°C) that accompanying with red emission and the recovering of the milky product along with disappearing of the red emission when temperature goes down might be due to the copper thiolate crystal structure changing versus temperature. The alkyl chains in the layers might have the similar properties as the hydrophobic tails of lipid layer in the biological membranes. The biological membrane undergoes the conformation changes between liquid crystal at higher temperature and gel at lower temperature. This gives more information about the structure of Cu thiolates.



Figure 7.8 Red emissions of transparent CuSRs solution at higher temperature (>150°C). This emission disappears and transparent solution becomes milky when it cools down.

The excitation spectra of yellow and green colour emission CuSRs is shown in figure 7.9.

There appears two excitation peaks, the higher one at 370 nm and 377 nm, the lower one at 315 nm and 322 nm for yellow and green emission Cu cluster, respectively.
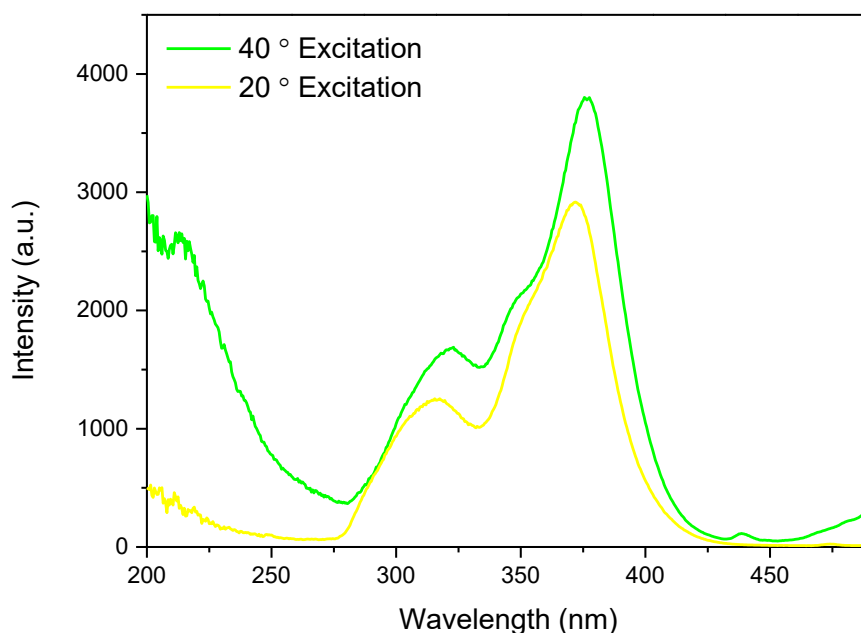


Figure 7.9 Excitation of CuSRs for the yellow and green emissions.

The PL decay at green (510 nm) and yellow (550nm) were expressed with the biexponential profile $I(t)=A_1exp(-t/\tau_1)+A_2exp(-t/\tau_2)$, the average lifetime was estimated by the expression $\tau=(A_1\tau_1^2+A_2\tau_2^2)/(A_1\tau_1+A_2\tau_2)$. The average lifetime was calculated as 1.2 μs for yellow and 0.7μs for green emission compounds by integrating two individual lifetimes (Figure 7.10). Take into account with the long excited-state lifetime and large Stokes shift (>200 nm), the emission intensity increasing with the Cu NCs self-assembly could be attributed to the coordination of metal with the DDT ligand by the mechanism of charge transfer through LMCT and/or LMMCT. The DDT ligand facilitates to generate subsequent radiative relaxation via a metal centered triplet state [267,268,293]. The process of disordered aggregation and ordered self-assembly of CuSRs mainly involves the structure building of DDT chains and the changing of cuprophilic Cu(I)···Cu(I) interaction [294].

Since we regard that the shifting of emission spectrum is attributed to the alteration of average Cu(I)···Cu(I) distance [294], increasing of Cu(I)···Cu(I) distance leads to the blue shift of luminescence, while Cu(I)···Cu(I) distance decreasing causes red shift. We can classify the cuprophilic interactions into cuprophilic interaction within the intra-layer and inter-layer which influence the average Cu(I)···Cu(I) distances and thus the emission color. Cuprophilic interaction between inter-layer involves longer distances and is generated by forming more compact CuSRs layers. The improved compactness of CuSRs from disordered aggregation to ordered self-assembly induces additional coprophilic interaction through longer Cu(I)···Cu(I) distance. As a result, green emission is generated. In addition, the alkyl chains of CuSRs rearrange during CuSRs self-assembly process through the

van der Waals attraction and thus forms the cuprophilic interaction in a same mechanism to Au cluster [292]. When increasing the reaction temperature, the apparent emission turns from yellow to green with the enhancement of emission intensity. Higher temperature facilitates the further stacking of compact layers which change the property of CuSRs and induce the cuprophilic interaction between the inter layer through a longer Cu(I)···Cu(I) distance. As a result, the emission intensity enhances with spectral blue shift. In contrast, lower reaction temperature favours to produce less layered assemblies with short Cu(I)···Cu(I) distances and lead to nonradiative relaxation of excited states and lower emission energy. According to this, we assign the assembly induced emission enhancement into two aspects. First, the enhanced cuprophilic intra and interactions greatly facilitate the excited state relaxation via radiative pathway [295,296]. Second, the restriction or prohibition of intramolecular vibration and rotation of DDT chains reduces the nonradiative relaxations [266,267,297]. These two effects greatly enhance the emission intensity of CuSRs after self-assembly into compact layers.
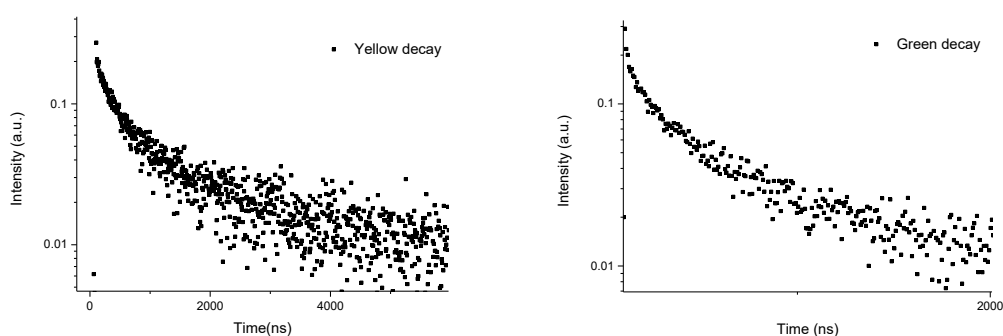


Fig. 7.10 Luminescence life time of the yellow and green light emitting CuSRs at 550 nm (a) and at 510 nm (b). The excitation is set at 365 nm.

## 7.3.3 Mechano- and Thermochromic Luminescence

The relationship between the architecture of CuSRs self-assemblies and the emission properties is further revealed by mechanochromic luminescence property of as synthesized CuSRs, which is often observed in organic and organometallic complexes [298,299]. As shown in Fig. 7.11 and Fig 7.12, the grinding treatment does not alter the composition of CuSRs, but dramatically change the emission color and intensity. For the yellow emission CuSRs, a red emission at around 650nm appears and the emission colour changes to white (Fig. 7.11 a, b and e). The fwhm increases from 137.26 nm to 220.6 nm. For the green NCs, as the emission color changes from green to yellow (Fig. 7.11 c, d), the emission at 510 nm decreases and a red emission at around 650-700nm grows (Fig. 7.11 f). The fwhm increases from 122.7nm to 219.8nm. The spectral shift implying the transformation of CuSRs assemblies from higher ordered layer to disordered state after grinding. Specifically, grinding treatment rearranged the compactness of CuSRs layers and alters the interactions between DDT and metal slab.
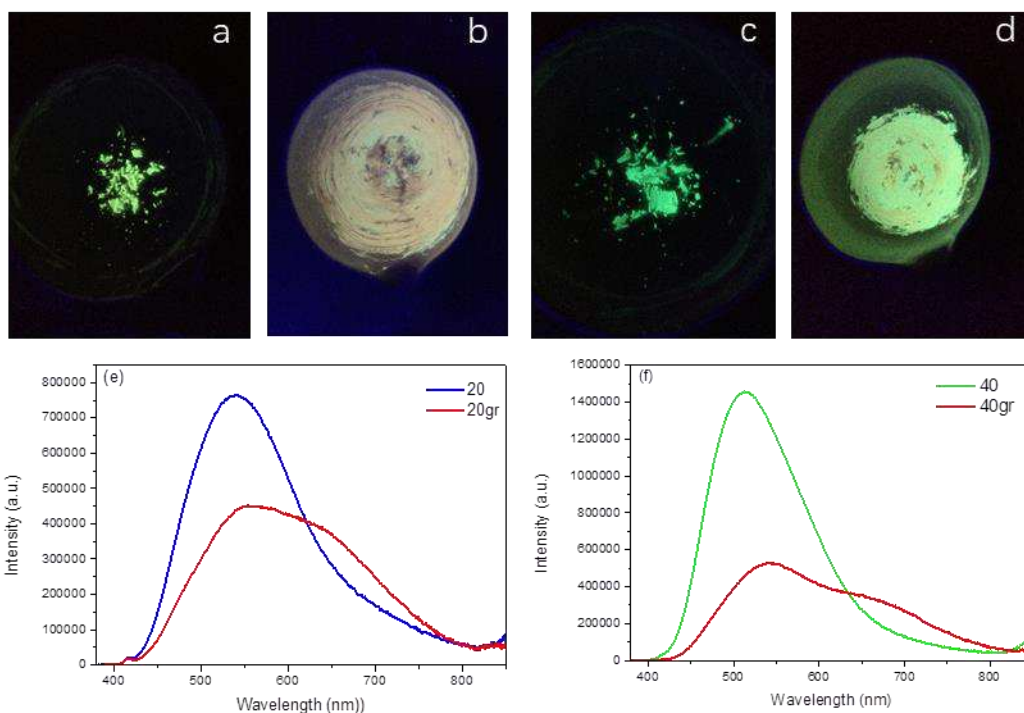
Figure 7.11 Luminescent images of yellow and green light emitting CuSRs under 365 nm excitation before and after grinding (a-d). The lower graphs are emission spectra of yellow and green light emitting CuSRs under 365 nm excitation before and after grinding (e-f).
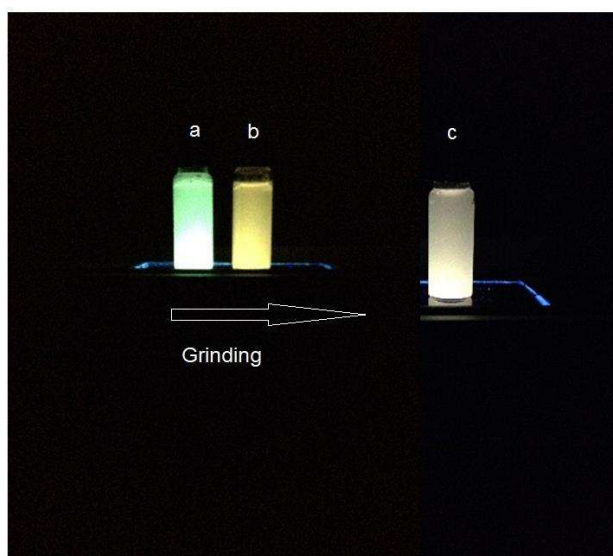


Figure 7.12 Fluorescent images of green light emitting CuSRs in water with 365 nm excitation. (a) before grinding, (b) after grinding, (c) further grinding.

The CuSRs assemblies also exhibit the thermochromic luminescence property. With 365 nm excitation, when the temperature increase from 20°C to 70°C, the original yellow emission CuSRs peaked at 550 nm blue shifts until to 510 nm and emission intensity decrease; the green emission CuSRs centered at 510 nm blue shifts to 500 nm

accompany with the emission intensity decrease (Fig. 7.13 and 7.14). This thermochromic luminescence is reversible when cycling the temperature from 70°C back to 20°C. The ligand coordinated excited state and the interactions between NCs and DDT in the assemblies are extremely sensitive to the surrounding temperature [294]. At low temperature, the molecular vibration and rotation of DDT are greatly restricted and both intra and inter coprophilic interactions are reinforced, which favor radiative relaxation of excited states and lead to stronger emission. When the temperature increase, both inter and intra Cu(I)···Cu(I) distances enlarge and thus lead to the spectra blue shift and decreased intensity.
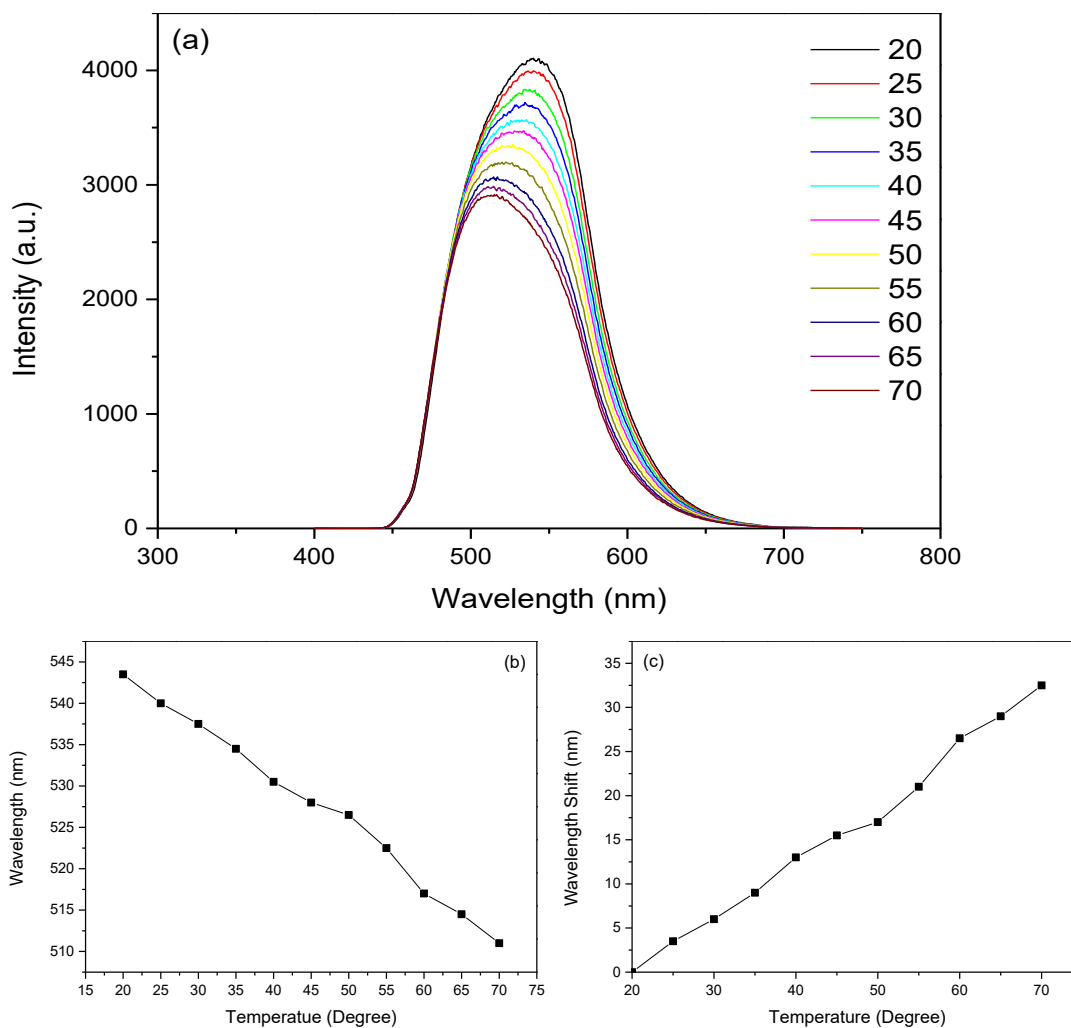


Figure 7.13 Thermosensitivity as function of wavelength versus temperature for yellow colour emitting CuSRs. Luminescent spectra at different temperature when excited by 365 nm (a). The blue shifting luminescent peak versus temperature for yellow colour emitting CuSRs (b, c)
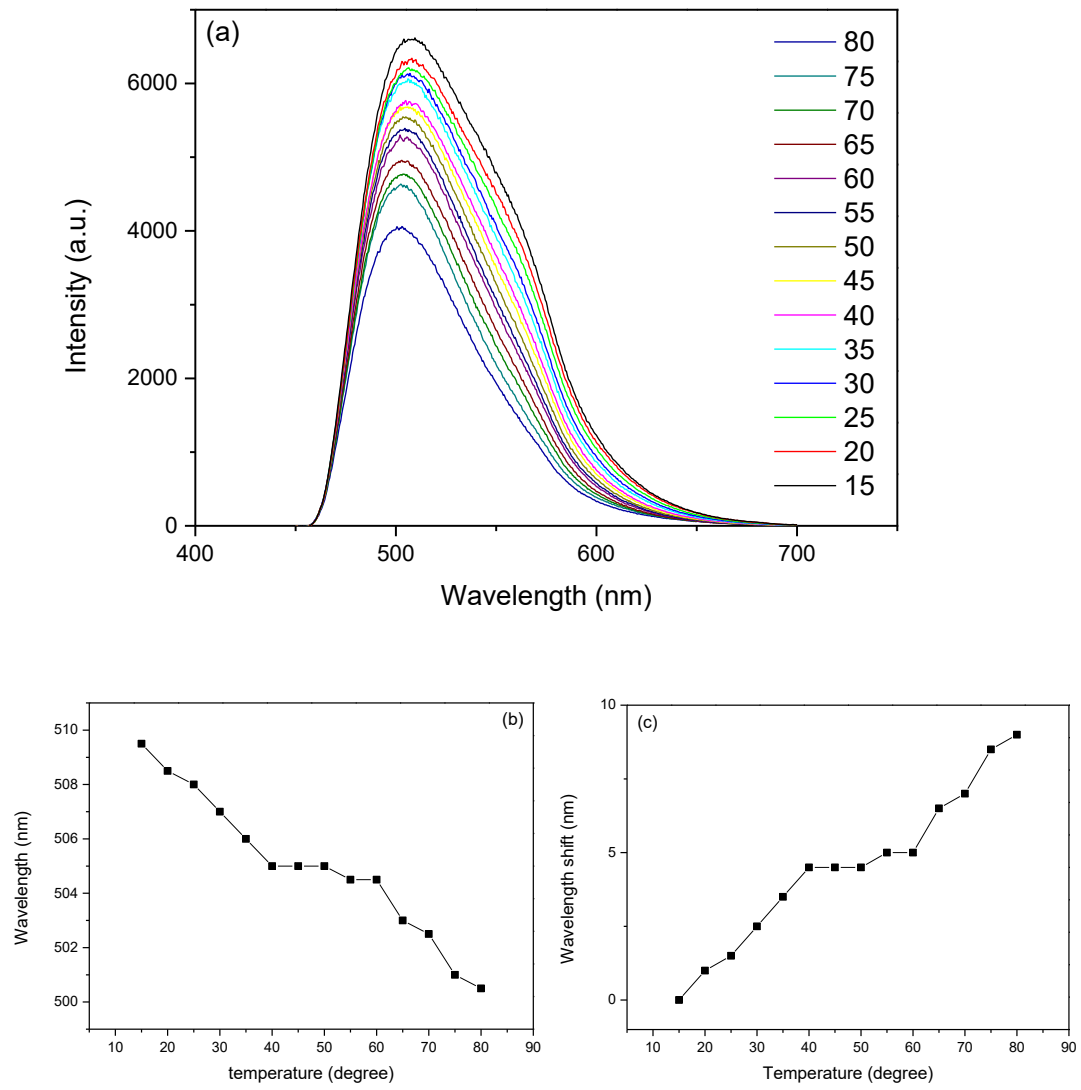
Figure 7.14 Thermosensitivity as function of wavelength versus temperature for green colour emitting CuSRs. Fluorescent spectra at different temperature when excited by 365 nm (a). The blue shifting fluorescent peak versus temperature for green colour emitting CuSRs (b, c)

If define the thermosensitivity as the wavelength shifting respect to temperature variation, we found that the thermosensitivity for both yellow and green is linear in the temperature range from 20°C up to 70°C. The thermosensitivity between 20 and 70 °C is determined as 0.65 nm/°C for the yellow CuSRs and 0.125 nm/°C for the green CuSRs. If we evaluate the thermosensitivity performance use the concepts of "Fluorescence Intensity Ratio" (FIR) of the emission intensity normalized to the maximum and the absolute thermal sensitivity (S), which defined as [300–303]:

$$FIR = \frac{I}{Imax} \tag{7.1}$$

$$S = \left| \frac{\partial FIR}{\partial T} \right| \tag{7.2}$$

where I is the intensity of the emission at the chosen temperature and $I_{max}$ is the maximum intensity at room temperature. The FIR values calculated from the emission spectra at various temperatures decrease with a linear behavior when increase the temperature and the variations of the FIR upon changing the temperature were shown in fig. 7.15. From a linear fit of the FIR values vs temperature, a thermal sensitivity of $(-0.013 \pm 0.0002)$ $K^{-1}$ and $(-0.007 \pm 0.00027)$ $K^{-1}$ have been evaluated for the yellow and green emission CuSRs, respectively.
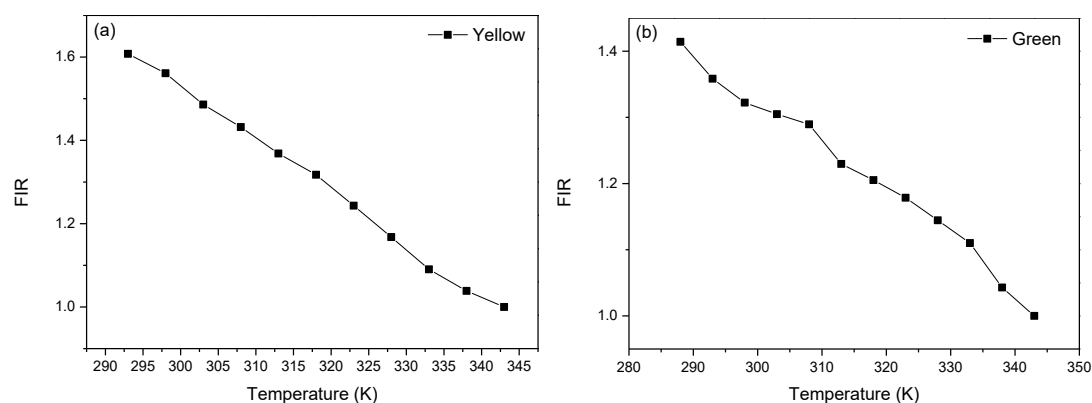


Figure 7.15 FIR behavior of the yellow (a) and green colour (b) emitting CuSRs.

## 7.3.4 Green, yellow and white light source from CuSRs

Due to the bright and tunable emission, the CuSRs could be employed as ordinary green, yellow and white light source in LEDs. In details, the light devices can be fabricated by mixing CuSRs with Ethylene-vinyl acetate (EVA) polymers in chloroform, depositing on commercially available GaN LED chip or a piece of glass substrate illuminated by UV lamp with the emission center at 365 nm. Upon chloroform evaporated, the CuSRs form desired light emitting film. Owing to broad emission spectra of CuSRs, and tunable colour ratio at different synthesis temperature, white light can be obtained directly from single CuSRs without the need to mix with other phosphors. With a synthesis condition of 0.5mmol CuCl, 3mL DDT and 6mL ODE, under stirring speed of around 350 rpm and heating speed of 4°C/min, a yellow colour with CIE color coordinate at (0.385, 0.454) is obtained at 20°C, and a green colour with CIE color coordinate at (0.288, 0.448) is obtained at 40°C (Fig. 7.16). Especially, an ideal white light with CIE color coordinate at (0.324, 0.334) is obtained at 30°C with around 2°C/min of heating speed, while as synthesized CuSRs at other temperatures have a CIE x axis range of 0.28-0.38 and y axis range of 0.44-0.46 (Table 7.3), all close to white light source (Fig. 7.17). To our best knowledge, this is the first trial that employs single CuSRs to produce white light source. Samples of yellow light in water, green light in film, and white light emission in chloroform, together with corresponding emission spectra and CIE coordinates are shown in figure 7.16.
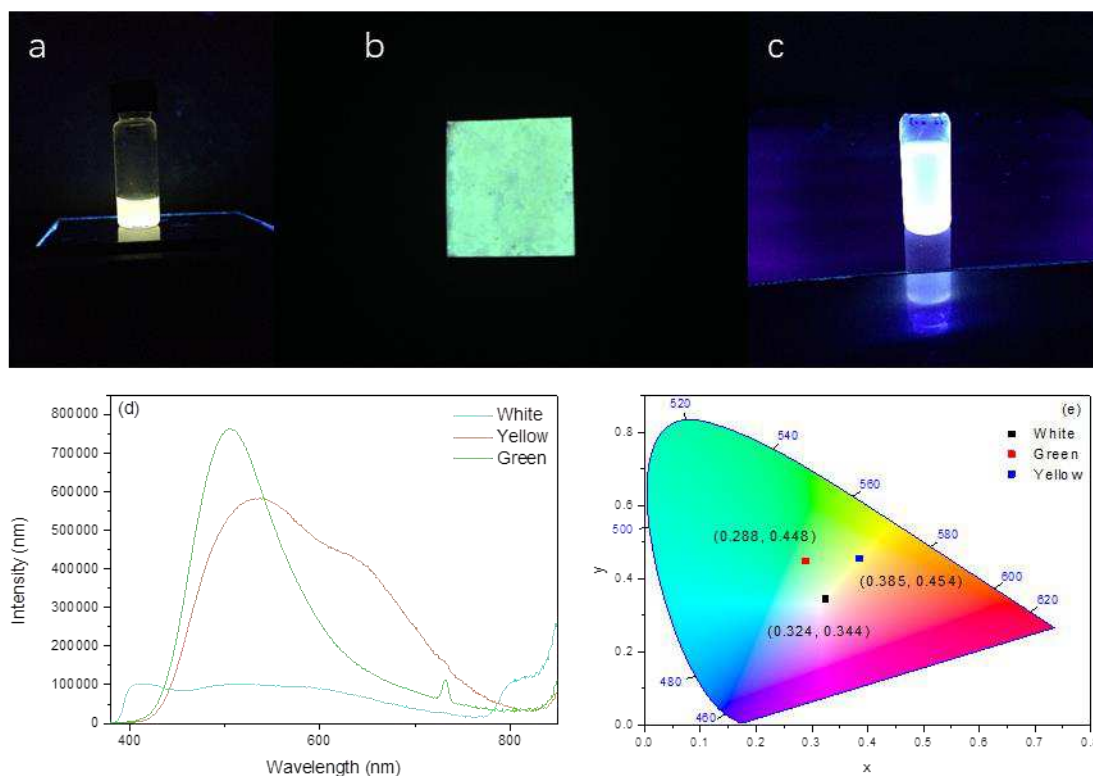
Figure 7.16 The typical yellow (in water), green (in film) and white light (in chloroform) emittinmg CuSRs and corresponding emission spectra (d). CIE color coordinates of typical yellow, green and white light from CuSRs (e).

**Table 7.3 Calculated CIE x, y and z coordinates that represent red, green and blue components from wide emitting spectra of CuSRs synthesized under 4 apm stirring speed and around 2°C/min heating speed**

|       | 20°C  | 30°C  | 40°C  | 50°C  | 60°C  | 70°C  | 80°C  | 90°C  | 100°C | 110°C |
|-------|-------|-------|-------|-------|-------|-------|-------|-------|-------|-------|
| Red   | 0.383 | 0.324 | 0.321 | 0.314 | 0.308 | 0.309 | 0.298 | 0.291 | 0.280 | 0.311 |
| Green | 0.461 | 0.344 | 0.444 | 0.448 | 0.446 | 0.437 | 0.446 | 0.444 | 0.438 | 0.450 |
| Blue  | 0.156 | 0.332 | 0.235 | 0.238 | 0.245 | 0.254 | 0.256 | 0.265 | 0.282 | 0.238 |

**CIE 1931**
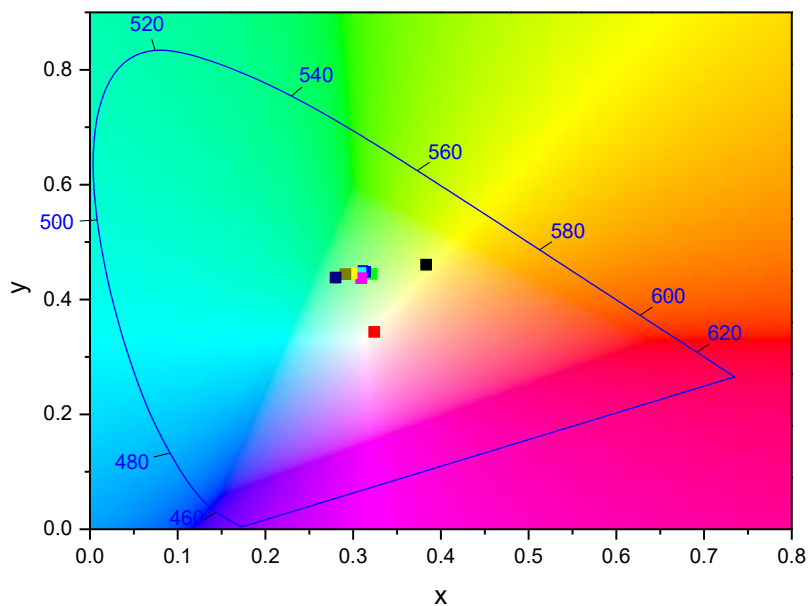
Figure 7.17 CIE color coordinates of CuSRs synthesized with stirring speed of 600 rpm and heating rate of around 2°C/min at various temperature from 20-110°C. At 20°C, it clearly located in yellow area (black point) and perfectly in white area at 30°C (red point). Others appear with greenish white.

## 7.4 Conclusion

In summary, we investigated the emission enhancement of CuSRs by self-assembly process that form compact and ordered multilayers. The self-assembly process reinforces the cuprophilic interaction of CuSRs, suppresses intramolecular vibration and rotation of the ligands, and improves the radiative relaxation of excited states. By adjusting the synthesis conditions such as temperature and stirring speed, various emission colors can be tuned. The structure changing by grinding leads to mechanochromic luminescence of CuSRs assemblies. The delicate DDT coordinated CuSRs exhibits thermochromic property as well. Owning to the bright and colour tunable emission from CuSRs with great potential in practical applications, green, yellow and white light can be obtained from single CuSRs as the phosphors that possibly be used in daily life such as LEDs, aquarium，advertising board and route signs.

# Chapter 8 Lanthanide doped fluoride based luminescent materials

## 8.1 Introduction

Due to the use in early stage disease detection, screening, and image-guided therapy, photoluminescence (PL) optical imaging attracted great attention in biomedical research. In practice, PL materials for in vivo deep tissue imaging should meet the following requirements: (1) nontoxic; (2) It can minimize the light scattering and tissue autofluorescence by adopting the excitation light and PL emission in the spectral range that is able to penetrate through the thick tissues, and (3) efficient and stable PL emission signal. Commonly used Stokes shifted nanoprobes, such as organic fluorophores and semiconductor quantum dots absorb and produce emission in the UV and visible range [304,305]. Despite their high PL efficiency, the *in vivo* PL imaging application of these probes are limited due to poor photostability of organic dyes, light scattering, strong autofluorescence background and low tissue penetration in the visible range [306]. Hence, to develop biocompatible and efficient anti-Stokes nanoprobes with excitation and PL in the NIR window is of great interest for both high contrast in vitro and in vivo optical imaging of cells and deep tissues.

An attractive alternative nanomaterial for bioimaging and even imaging guided drug delivery and therapy applications is lanthanide doped up converting nanoparticles (UCNPs)[307,308]. By utilization of the "optical transmission window" for biological tissues in the near infra-red (NIR) range (~750-1000 nm), UCNPs allow the deep light penetration with lower autofluorescence and light scattering [309,310]. Due to the peculiar electronic configuration of $Ln^{3+}$ ions, trivalent lanthanide ($Ln^{3+}$) doped nanoparticles (NPs) display this interesting up conversion (UC) phenomena, which the NPs convert the longer NIR wavelength excitation light into emission at a shorter wavelength in ultraviolet, visible, or relatively shorter NIR, using a ladder like system of energy levels of lanthanide ions [311,312]. This process involves a stepwise photon mechanism, allowing excitation with low cost continuous wave laser diodes at a relatively low energy density of $10^{-1}$-$10^2$ W/cm$^2$. Lanthanide doped UCNPs have shown high photostability and low toxicity, making them suitable contrast agents for *in vitro* and *in vivo* optical imaging applications [313].

Among the UCNP materials, $AREF_4$ (A = alkali, RE = rare earth ions and Y) NPs have been regarded as excellent host matrix materials for various optically active $Ln^{3+}$ ions both in up conversion and down conversion luminescence, because of its high refractive indexes, low phonon frequencies and non-radiative decay rates [314,315]. Hexagonal $NaYF_4$ NPs are well investigated and the 45 nm hexagonal ($NaYF_4$:$Yb^{3+}$/$Tm^{3+}$)/$NaYF_4$ core/shell nanocrystals excited at 980 nm with a power density of ~78 W/cm$^2$ exhibited ~3.5% [316]. Various methods have been proposed to improve the UCNP efficiency [317,318]. It was reported that by elevating the concentration of the sensitizer ($Yb^{3+}$), the

quantum yield of NIR up converting photoluminescence (UCPL) was enhanced 8.6 folds per $Yb^{3+}$ concentration and 3.6 times higher per nanoparticle than the 25-30 nm nanocrystals of $NaYF_4$:20% $Yb^{3+}$/2% $Tm^{3+}$ [319]. When encapsulated in a hetero-shell of $CaF_2$, the PL of $NaYbF_4$:$Tm^{3+}$ UCNPs was enhanced 35 times, yielding a QY of 0.1% under excitation with a low power density of ~0.3 W/cm$^2$ [320]. Through increasing sensitizer and activator concentration to a high level and suppressing dissipating process, $NaYbF_4$:Tb nanoparticles were synthesized by thermal decomposition method, efficient cooperative sensitization up conversion emission from $Tb^{3+}$ ions was obtained and the emission increased 690 fold by $CaF_2$ shell shielding [33]. $Er^{3+}$, $Tm^{3+}$, and $Ho^{3}$+ ions codoped $NaYbF_4$ UCNPs were synthesized in the water-ethanol-oleic acid system with a multicolour emission, the higher temperature and extended reaction time favours the phase transition from cubic to hexagonal phase. After surface amino-functionalizing, and linking to the rabbit anti-CEA8 antibody, the UCNPs were used for the immunolabeling and imaging of live HeLa cells and immunolabeling of HeLa cells was specific [321].

Due to both the magnetic and upconverting luminescent properties, the multifunctional lanthanide doped $NaGdF_4$ and $KGdF_4$ have been studied [12], such as water dispersible ultra small multifunctional $KGdF_4$:$Tm^{3+}$, $Yb^{3+}$ [13], color-tunable luminescence properties of hydrophilic $Ln^{3+}$ doped $KGdF_4$ [14]. The energy transfer from $Ce^{3+}$ to $Gd^{3+}$, $Ce^{3+}$ to $Tb^{3+}$ and $Gd^{3+}$ to $Tb^{3+}$ has been demonstrated in $KGdF_4$ [322]. These NPs possess some unique physical properties originated from $Gd^{3+}$ ions. Owing to the lowest excited state $^6P_{7/2}$ of $Gd^{3+}$ in the ultraviolet region, it can not only act as an efficient light sensitizer to absorb UV excitation light and subsequently transfer the energy to its neighboring $Ln^{3+}$ ions which activate and emit various colours [323], but also serve as an intermediate ion to pass the energy from sensitizers such as $Ce^{3+}$ and $Yb^{3+}$/$Tm^{3+}$ to activators ions such as $Tb^{3+}$ and $Eu^{3+}$, thus consequently facilitate the energy transfer process [324]. In addition, $Gd^{3+}$ is an ideal paramagnetic element because of its seven unpaired electrons and find its extensive use as a contrast agents for magnetic resonance imaging (MRI) [325] $Ln^{3+}$ ion doped $NaGdF_4$ NPs have versatile applications, such as multimodal imaging in high sensitivity fluorescence and MRI [326], in vivo image-guided surgery [327], therapeutics [328], enhanced X-ray excited optical imaging [329].

In this Part of study, we will synthesize $NaGdF_4$, $KYb_2F_7$ and $KGdF_4$ core-shell nanoparticle doped with lanthanide ions as $Yb^{3+}$, $Tm^{3+}$, $Ce^{3+}$, $Eu^{3+}$ and $Tb^{3+}$ ions and we will investigate the spectroscopic properties.

# 8.2 Experimental

## 8.2.1 Chemicals

- Gadolinium chloride hexahydrate, $GdCl_3 \cdot 6H_2O$, MW = 371.61 g/mol, Aldrich, 99%

- Ytterbium chloride hexahydrate, $YbCl_3 \cdot 6H_2O$, MW = 387.49 g/mol, Aldrich, 99.9%

- Thulium chloride hexahydrate, $TmCl_3 \cdot 6H_2O$, MW = 383.38 g/mol, Aldrich, 99.9%

- Terbium chloride hexahydrate, $TbCl_3 \cdot 6H_2O$, MW = 373.38 g/mol, Aldrich, 99.9%

- Europium chloride hexahydrate, $EuCl_3 \cdot 6H_2O$, MW = 366.41 g/mol, Aldrich, 99.9%

- Cerium nitate hexahydrate, $Ce(NO_3)_3 \cdot 6H_2O$, MW = 434.22 g/mol, Aldrich, 99.99%

- Sodium citrate tribasic dihydrate, $C_6H_5Na_3O_7 \cdot 2H_2O$, MW = 294.1 g/mol, Sigma–Aldrich, ≥99.0%

- Potassium citrate tribasic monohydrate, $C_6H_5K_3O_7 \cdot H_2O$, MW = 324.41 g/mol, Sigma–Aldrich, ≥99.0%

- Ammonium fluoride, $NH_4F$, MW = 37.04 g/mol, Sigma–Aldrich, ≥98.0%

## 8.2.2 Synthesis of NPs

The synthetic process was conducted using a microwave synthesis reactor (Anton Paar Monowave 400 and Auto sampler MAS 24) operating at 1600W output power. The temperature and reaction time is main synthetic condition. Specifically, Gadolinium chloride hexahydrate, ytterbium chloride hexahydrate, terbium chloride hexahydrate, europium chloride hexahydrate and cerium nitate hexahydrate were dissolved in deionized water to make 1 M stock solution, with exception for thulium chloride hexahydrate and ammonium fluoride, which are 0.428M and 3.5M, respectively. Then the precursor solutions were added according to the molar ratio of the elements in compounds. For $NaGdF_4$:Yb,Tm and $KGdF_4$:Yb,Tm, 0.5 ml Gd 1 M stock solution, 0.49 ml Yb 1 M stock solution and 0.023 ml Tm 0.428 M stock solution were mixed in 30G glass vial, 2 g sodium citrate tribasic dehydrate or potassium citrate tribasic monohydrate were dissolved in 10 ml deionized water, stir both solutions for 5 minutes, then add the sodium citrate solution into the lanthanide solution, keep stirring, add 1.5 ml ammonium fluoride 3.5M stock solution, stir for another 10 minutes. After all reagents mixed well, mount the glass vial into microwave reactor, keep reaction at 190°C for 3 minutes. When the reaction finished, wash the obtained NPs with acetone and water for three times, then go on the shell covering reaction at the same reaction conditions. The quantities of reagents are summarized in the following tables.

**Table 8.1 $KYb_2F_7$:Tm NPs reagents quantities**

| NPs | Reagents | Quantity | Moles |
|---|---|---|---|
| $KYb_2F_7$:Tm0.5% | $C_6H_5K_3O_7 \cdot H_2O$ | 2 g | 6.2mmol |
| | $NH_4F$ | 1.5 mL, 3.5 M | 5.25mmol |
| | $YbCl_3 \cdot 6H_2O$ | 0.995 mL, 1 M | 0.995 mmol |
| | $TmCl_3 \cdot 6H_2O$ | 0.012 mL, 0.428 M | 0.005 mmol |

**Table 8.2 $NaYbF_4$:Eu,Tb NPs reagents quantities**

| NPs | Reagents | Quantity | Moles |
|---|---|---|---|
| NaYbF$_4$:Eu 20%<br><br>NaYbF$_4$:Tb 20% | C$_6$H$_5$Na$_3$O$_7 \cdot$ 2H$_2$O | 2 g | 6.8mmol |
| | NH$_4$F | 1.5 mL, 3.5 M | 5.25mmol |
| | YbCl$_3 \cdot$ 6H$_2$O | 0.8 mL, 1 M | 0.8 mmol |
| | EuCl$_3 \cdot$ 6H$_2$O | 0.2 mL, 1 M | 0.2 mmol |
| | TbCl$_3 \cdot$ 6H$_2$O | 0.2 mL, 1 M | 0.2 mmol |

**Table 8.3 NaGdF$_4$:Yb,Tm and KGdF$_4$:Yb,Tm**

| NPs | Reagents | Quantity | Moles |
|---|---|---|---|
| NaGdF$_4$:Yb49%,Tm1%<br><br>KGdF$_4$:Yb49%,Tm1% | C$_6$H$_5$Na$_3$O$_7 \cdot$ 2H$_2$O | 2 g | 6.8mmol |
| | C$_6$H$_5$K$_3$O$_7 \cdot$ H$_2$O | 2 g | 6.2mmol |
| | NH$_4$F | 1.5 mL, 3.5 M | 5.25mmol |
| | GdCl$_3 \cdot$ 6H$_2$O | 0.5 mL, 1 M | 0.5 mmol |
| | YbCl$_3 \cdot$ 6H$_2$O | 0.49 mL, 1 M | 0.49 mmol |
| | TmCl$_3 \cdot$ 6H$_2$O | 0.0234 mL, 0.428 M | 0.01 mmol |

**Table 8.4 NaGdF$_4$:Eu,Tb and KGdF$_4$:Eu,Tb**

| NPs | Reagents | Quantity | Moles |
|---|---|---|---|
| NaGdF$_4$:Eu20%<br><br>NaGdF$_4$:Tb20%<br><br>KGdF$_4$:Eu20%<br><br>KGdF$_4$:Tb20% | C$_6$H$_5$Na$_3$O$_7 \cdot$ 2H$_2$O | 2 g | 6.8mmol |
| | C$_6$H$_5$K$_3$O$_7 \cdot$ H$_2$O | 2 g | 6.2mmol |
| | NH$_4$F | 1.5 mL, 3.5 M | 5.25mmol |
| | GdCl$_3 \cdot$ 6H$_2$O | 0.8 mL, 1 M | 0.8 mmol |
| | EuCl$_3 \cdot$ 6H$_2$O | 0.2 mL, 1 M | 0.2 mmol |
| | TbCl$_3 \cdot$ 6H$_2$O | 0.2 mL, 1M | 0.2 mmol |

**Table 8.5 NaGdF$_4$:Ce and KGdF$_4$:Ce**

| NPs | Reagents | Quantity | Moles |
|---|---|---|---|
| NaGdF$_4$:Ce20%<br><br>KGdF$_4$:Ce20% | C$_6$H$_5$Na$_3$O$_7$ $\cdot$ 2H$_2$O | 2 g | 6.8mmol |
| | C$_6$H$_5$K$_3$O$_7$ $\cdot$ H$_2$O | 2 g | 6.2mmol |
| | NH$_4$F | 1.5 mL, 3.5 M | 5.25mmol |
| | GdCl$_3$ $\cdot$ 6H$_2$O | 0.8 mL, 1 M | 0.8 mmol |
| | CeCl$_3$ $\cdot$ 6H$_2$O | 0.2 mL, 1 M | 0.2 mmol |

## 8.2.3 Characterization

The XRD diffraction was measured by an ARL X'TRA X-ray diffractometer with Cu-Kα radiation (λ = 0.15405 nm). The down converting luminescent spectra were measured in a FP-8200 spectrofluorometer (Japan). The up converting luminescent spectra were measured in an Andor Shamrock SR-500i-B1-R imaging spectrometer equipped with a CCD (DU420A-BVF) and photomultiplier tube TE177TSRF. The laser is a 980 nm MDL (1W) with a power supply LD-WL206.

## 8.3 Results and discussion

## 8.3.1 Crystal structure and composition

The phases of the synthesized NaYbF$_4$, NaGdF$_4$, NaGdF$_4$:(Yb49%,Tm1%), KYb$_2$F$_7$:Tm0.5%, KGdF$_4$ and KGdF$_4$:(Yb49%,Tm1%) were determined by the XRD technique (Figure 8.1-8.5). The XRD pattern of NaYbF$_4$ agrees well with the standard cubic NaYbF$_4$ pattern of JCPDS 77-2043, indicating a pure cubic phase formed (Fig. 8.1 a). The NaGdF$_4$ exhibits hexagonal phase, as analyzed by MAUD software (Fig. 8.2). The NaGdF$_4$:(Yb49%,Tm1%) sample also exhibits hexagonal β-phase (Fig. 8.3) [330]. The XRD pattern of KYb$_2$F$_7$ agrees well with JCPDS card 27 0459 and exhibits orthorhombic phase (Fig. 8.1 b) [331]. MAUD fit results of the XRPD patterns are reported in Table 8.6 [332]. Both of the potassium containing NPs exhibit cubic phase, see Fig 8.4 and 8.5.
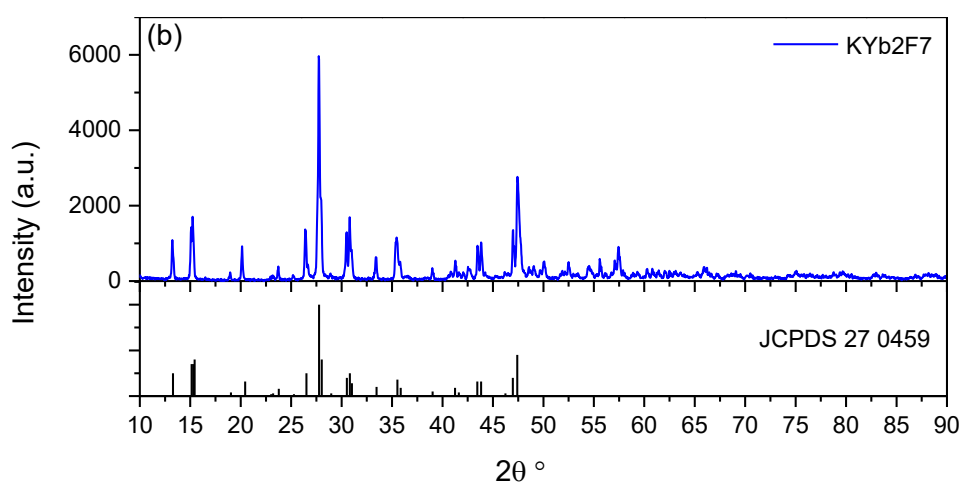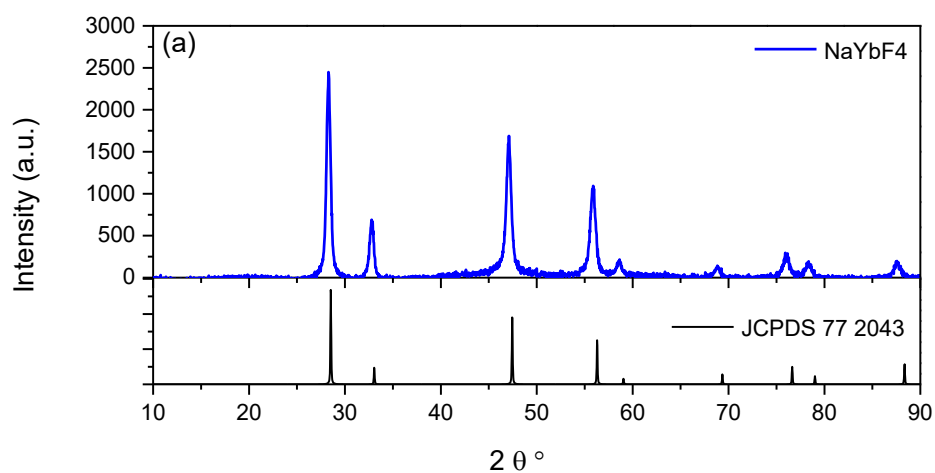
Figure 8.1 XRD pattern of cubic NaYbF$_4$(a) and orthorhombic KYb$_2$F$_7$ (b).
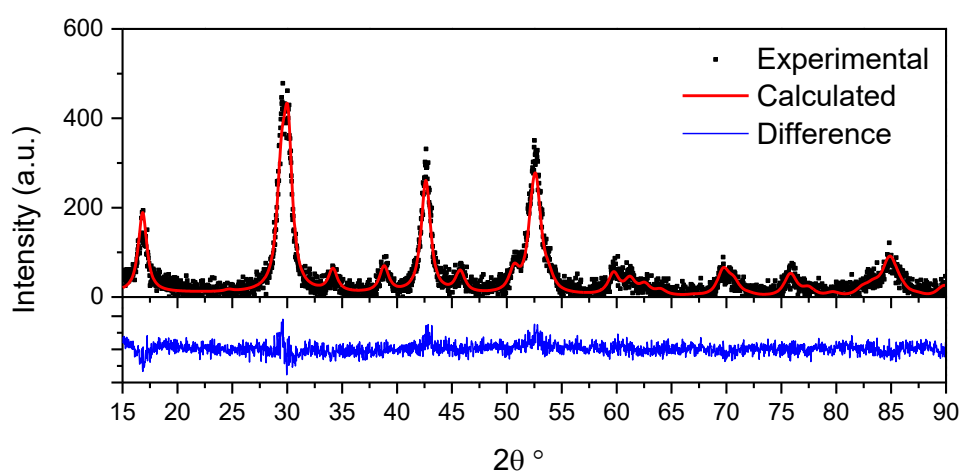


Figure 8.2 XRD diffraction pattern and the refinement of hexagonal NaGdF$_4$ NPs using MAUD software (dot: experimental data, upper red solid line: calculated pattern, lower blue solid line: subtracted pattern).
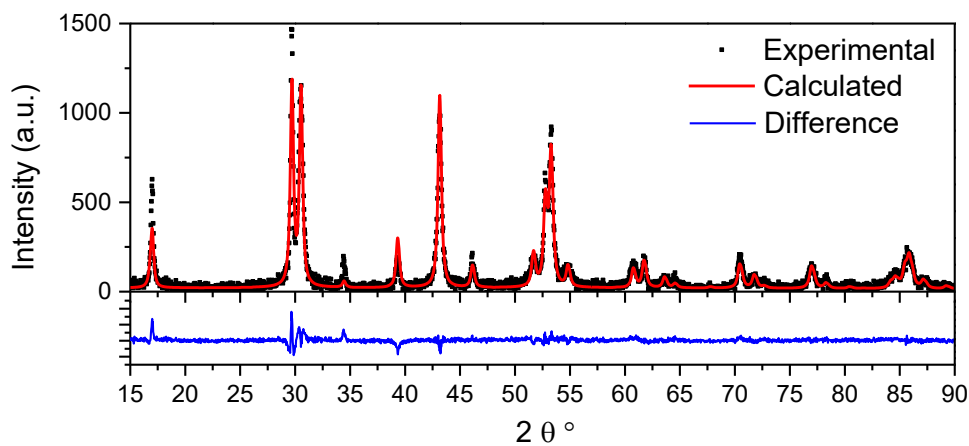
Figure 8.3 XRD diffraction pattern and the refinement of hexagonal $NaGdF_4$:(Yb49%,Tm1%) NPs using the MAUD software (dot: experimental data, upper red solid line: calculated pattern, lower blue solid line: subtracted pattern).



Figure 8.4 XRD diffraction pattern and the refinement of cubic $KGdF_4$ NPs using the MAUD software (dot: experimental data, upper red solid line: calculated pattern, lower blue solid line: subtracted pattern).



Figure 8.5 XRD diffraction pattern and the refinement of cubic $KGdF_4$:(Yb49%,Tm1%) NPs using the MAUD software (dot: experimental data, upper red solid line: calculated pattern, lower blue solid line: subtracted pattern).

**Table 8.6 Results from Rietveld analysis of the NP samples**

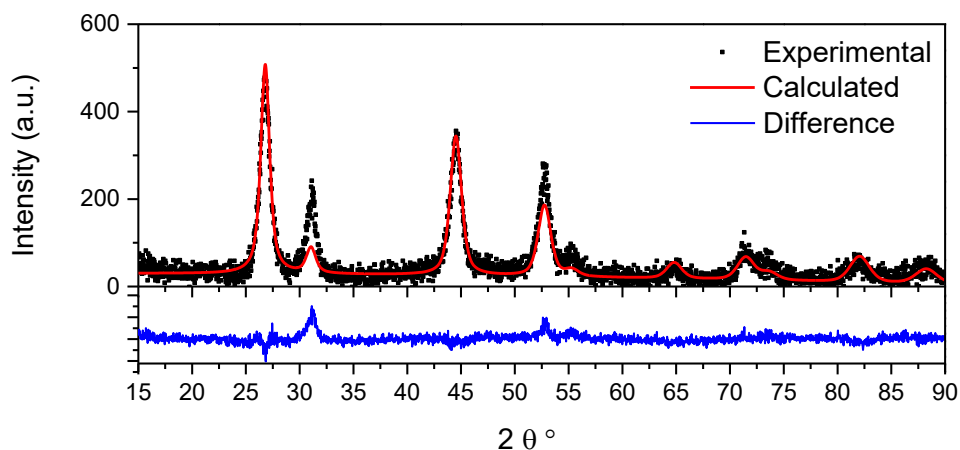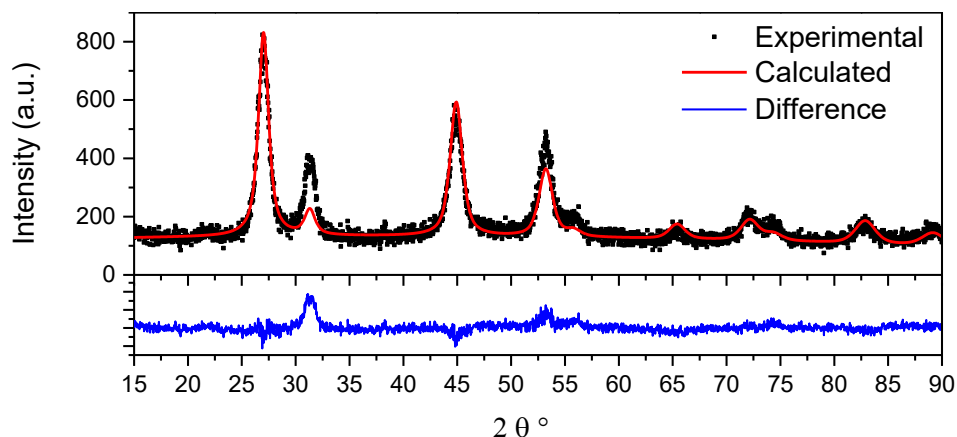|                          | NaGdF$_4$ (β)         | NaGdYbF$_4$ (β)              | KGdF$_4$ (α)           | KGdYbF$_4$ (α)         |
| ------------------------ | --------------------- | --------------------------- | ---------------------- | ---------------------- |
| Lattice parameter (Å) a  | 6.06±9.89 e$^{-4}$    | 6.01±3.35 e$^{-4}$          | 5.75±8.85 e$^{-4}$     | 5.71±8.78 e$^{-4}$     |
| Lattice parameter (Å) c  | 3.60±1.00 e$^{-4}$    | 3.54±3.65 e$^{-4}$          |                        |                        |
| Size MAUD (nm)           | 11.83±0.13            | 39.18±0.54                  | 13.57±0.41             | 10.88±0.27             |
| rs-microstrain           | 0.002±1.76 e$^{-4}$   | 6.373 e$^{-4}$±1.755 e$^{-3}$ | 0.006±3.417 e$^{-4}$  | 0.006±3.798 e$^{-4}$   |
| Rw (%)                   | 12.04                 | 13.13                       | 14.47                  | 13.91                  |
| Rb (%)                   | 9.67                  | 10.13                       | 11.16                  | 10.53                  |
| Rexp (%)                 | 8.87                  | 7,57                        | 9.02                   | 7.62                   |
| sig                      | 1.36                  | 1.74                        | 1.6                    | 1.82                   |
| GOF                      | 1.36                  | 1.74                        | 1.6                    | 1.83                   |

# 8.3.2 Luminescent property of Tm$^{3+}$, Eu$^{3+}$ and Tb$^{3+}$ doped NaYbF$_4$ and KYb$_2$F$_7$ NPs

Eu$^{3+}$ and Tb$^{3+}$ doped NaYbF$_4$ NPs show red and green light under 365nm UV excitation, see figure 8.6. Increasing the doping amounts of Eu$^{3+}$ and Tb$^{3+}$ enhances the luminescent emission.
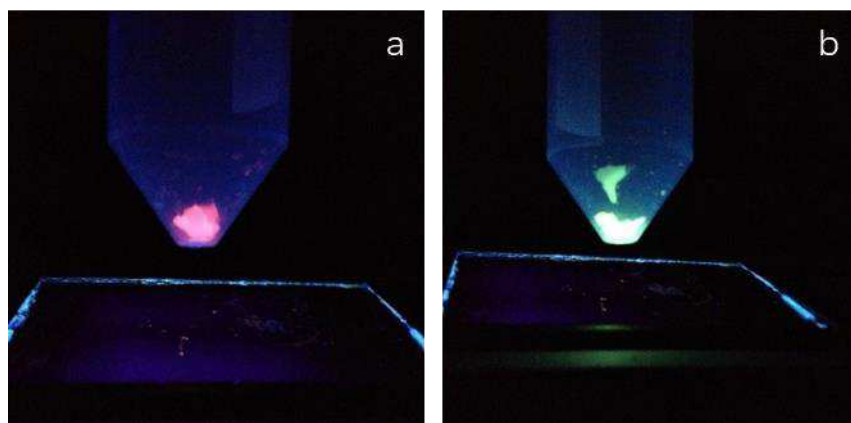


Figure 8.6 Eu$^{3+}$(a) and Tb$^{3+}$ (b) NaYbF$_4$ NPs under 365 nm UV light illumination.

The luminescence spectra of Eu$^{3+}$ and Tb$^{3+}$ were measured. As seen from figure 8.7, the two dominant bands at 592 (5D0 → 7F1 transition) and 613 nm (5D0 → 7F2 transition), along with two weak bands at 650 (5D0 → 7F3) and 700 nm (5D0 → 7F4) confer on the Eu$^{3+}$ luminescence upon excitation with 365 nm light. For the Tb$^{3+}$ doped NaYbF4 NPs, under 365 nm excitation, a group of 5D3 → 7FJ (J=3,4,5,6) transition were presented: 489 nm (5D4 → 7F6), 543 nm (5D4 → 7F5), 584 nm (5D4 → 7F4), and 621 nm (5D4 → 7F3) [333].
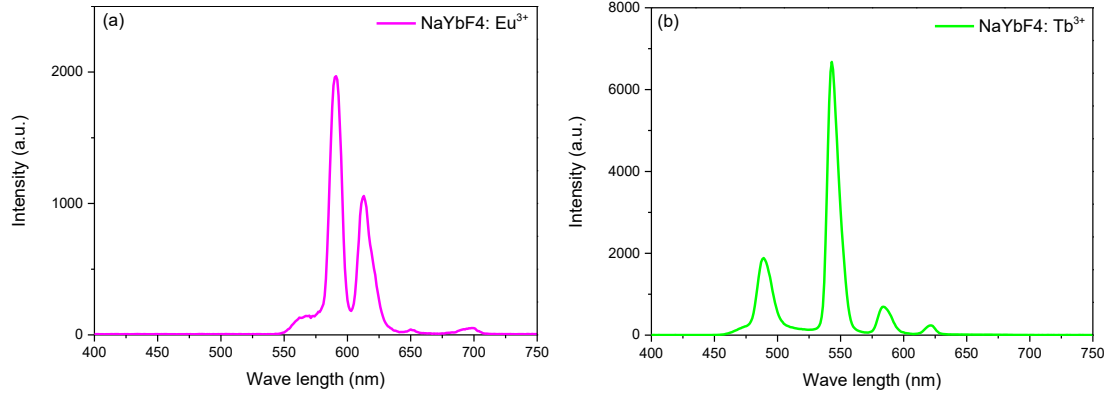
Figure 8.7 Photoluminescence (DCPL) spectrum of Eu^{3+} (a) and Tb[3+] (b) doped NaYbF4 NPs under 365nm UV light excitation.

When doped with $Tm^{3+}$, the $NaYbF_4$ and $KYb_2F_7$ NPs exhibit the typical blue and NIR upconversion luminescence under 980 nm excitation. As seen from figure 8.8, bands with maxima at 350, 450, 480, 513, 650, 700 and 800 nm can be clearly observed, corresponding to the 1I6 → 3F4, 1D2 → 3F4, 1G4 → 3H6, 1D2 → 3H5, 1G4 → 3F4, 3F2,3 → 3H6, and 3H4 → 3H6 transitions of the $Tm^{3+}$ ions, respectively [320,330,334,335]. It is seen that for core-shell NPs, the blue emission at 450 nm is relatively enhanced, and it is much increased when covered with a $NaYbF_4$ shell, notice that the weak peak at 513 nm appears stronger when the $NaYbF_4$ shell is present.
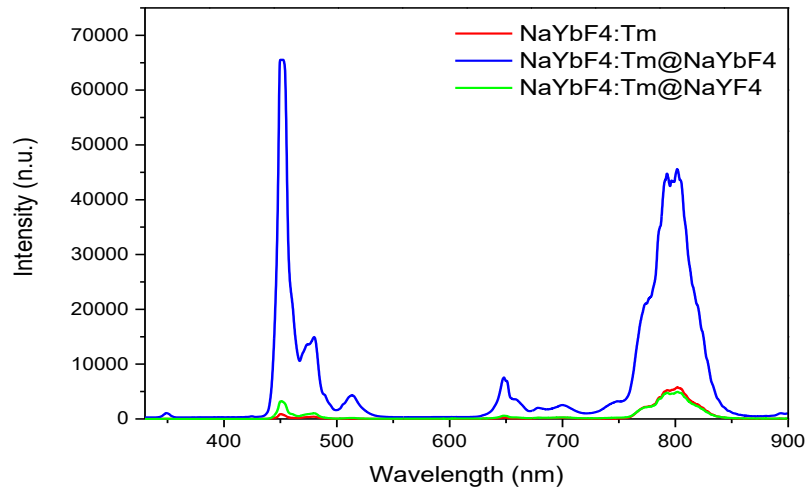


Figure 8.8 UCPL spectrum of $NaYbF_4$:Tm1%, $NaYbF_4$:Tm1%@$NaYbF_4$ and $NaYbF_4$:Tm1%@$NaYF_4$ ($\lambda_{ex} = 980\,nm$).

The weak red emission at 650 nm (1G4 → 3F4) and at 700 nm (3F3 → 3H6) and the intense NIR emission at 800 nm (3H4 → 3H6) are ascribed to upconversion processes [332]. The NIR excitation at 980 nm and the intense NIR emission at 800 nm are close or located in the biological window, which is beneficial for tissue penetration.

Figure 8.9 shows a comparison of $Tm^{3+}$ UC luminescence spectrum for $NaYbF_4$ (a) and $KYb_2F_7$ (b) NPs under 980 nm laser excitation. The transition at 480 nm (1G4 → 3H6) for $KYb_2F_7$ is stronger than the red one compared to $NaYbF_4$.
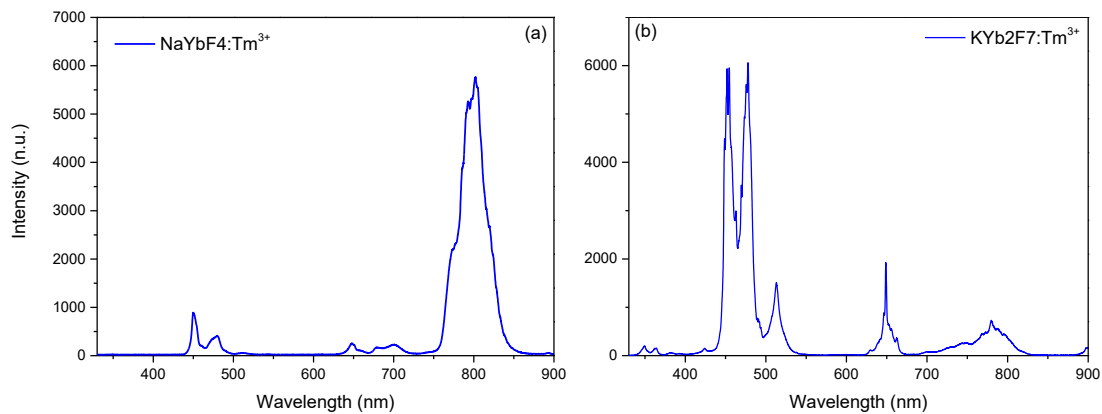
Figure 8.9 UCPL spectra of NaYbF$_4$:Tm1% (a) and KYb$_2$F$_7$:Tm0.5% (b) NPs ($\lambda_{ex} = 980\ nm$).

## 8.3.3 Luminescent property of Yb$^{3+}$, Tm$^{3+}$, Ce$^{3+}$, Eu$^{3+}$ and Tb$^{3+}$ doped NaGdF$_4$ and KGdF$_4$ NPs

We synthesized MGdF$_4$:(Yb49%,Tm1%)@MGdF$_4$:(Eu/Tb20%)@MGdF$_4$:Ce20% (M: Na or K) NPs that could incorporating the NIR to NIR luminescence of Tm$^{3+}$, Up and down converting luminescence of Eu$^{3+}$ and Tb$^{3+}$ by using the energy transfer process in Yb$^{3+}$ → Tm$^{3+}$→ Gd$^{3+}$ → Eu$^{3+}$/Tb$^{3+}$, or Ce$^{3+}$ → Gd$^{3+}$ → Eu$^{3+}$/Tb$^{3+}$. The as synthesized core-shell-shell NPs exhibit good Stokes and UC luminescence. The luminescence images are shown in figure 8.10 under 254 and 365 nm excitation, respectively.
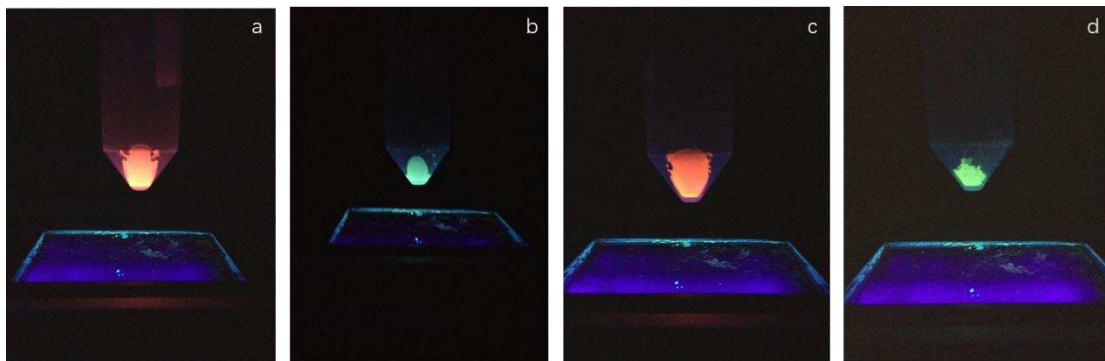


Figure 8.10 NaGdF$_4$:(Yb49%,Tm1%)@NaGdF$_4$:(Eu/Tb20%)@NaGdF$_4$:Ce20% NP Down converting luminescent images ($\lambda_{ex} = 254\ nm$, a, b) ($\lambda_{ex} = 365\ nm$ c, d).

Figure 8.11 shows the excitation and emission spectra of NaGdF$_4$:Yb,Tm@NaGdF$_4$:Eu@NaGdF$_4$:Ce NPs. Several sharp lines in the 360–480 nm range are observed (peak at about 297 nm due to Rayleigh scattering). These sharp bands correspond to the characteristic f → f transitions of Eu$^{3+}$ ions. They are ascribed to 7F0 → 5H6 (320 nm), 7F0 → 5D4 (364 nm), 7F0 → 5GJ, 5L7 (381 nm), 7F0 → 5L6 (396 nm), 7F0 → 5D3 (418 nm), and 7F0 → 5D2 (466 nm), 7F0,1 → 5D1 (527 nm, 537 nm) transitions of Eu$^{3+}$ ion, respectively [333,336,337]. As shown in figure 8.6 (b), when excited into the 7F0 → 5L6 transition by 395 nm UV light, it yields some characteristic emission lines from the 5D0 excited states to the 7FJ (J=1,2,3,4) ground states: 5D1

→7F1 (536 nm), 5D1→ 7F2 (556 nm), 5D0 → 7F1 (592 nm), 5D0 → 7F2 (617 nm), 5D0 → 7F3 (651 nm), and 5D0 → 7F4 (697 nm), respectively [333].
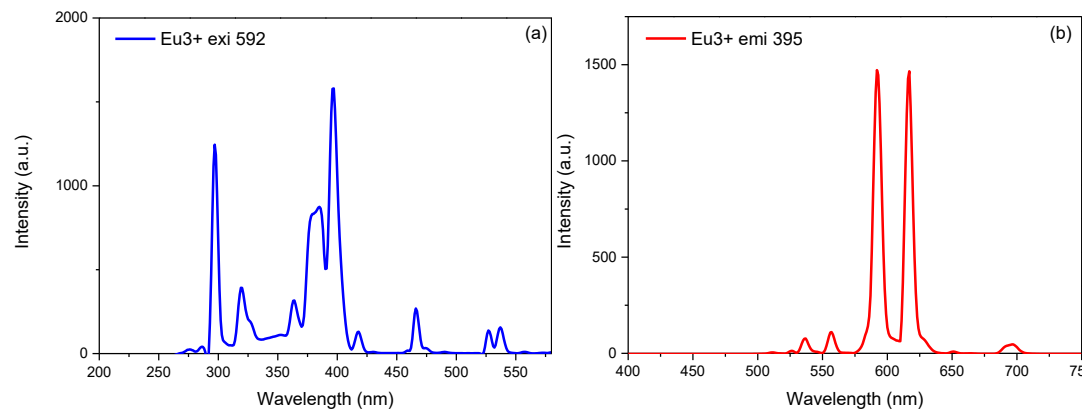


Figure 8.11 Excitation ($\lambda_{em} = 592\,nm$) (a) and DCPL spectrum of NaGdF$_4$:Yb,Tm@NaGdF$_4$:Eu@NaGdF$_4$:Ce NPs (b) ($\lambda_{ex} = 395\,nm$).

As shown in figure 8.12, the excitation spectrum of NaGdF$_4$:Yb,Tm@NaGdF$_4$:Tb@NaGdF$_4$:Ce NPs involves several sharp lines (Rayleigh scattering at 274 nm). The sharp 4f → 4f excitation lines at 305, 312, 320, 327,343, 354, 371, 380 and 490 nm are assigned to 7F6–5H6, 7F6–5H7, 7F6–5G2, 7F6–5D1, 7F6–5L6, 7F6–5D2, 7F6–5L10, 7F6–5G6 and 7F6–5D4, respectively [333,338]. Under 380 nm excitation, a group of 5D3 → 7FJ (J=3,4,5,6) transitions were presented: 489 nm (5D4 → 7F6), 544 nm (5D4 → 7F5), 584 nm (5D4 → 7F4), and 620 nm (5D4 → 7F3) [333].
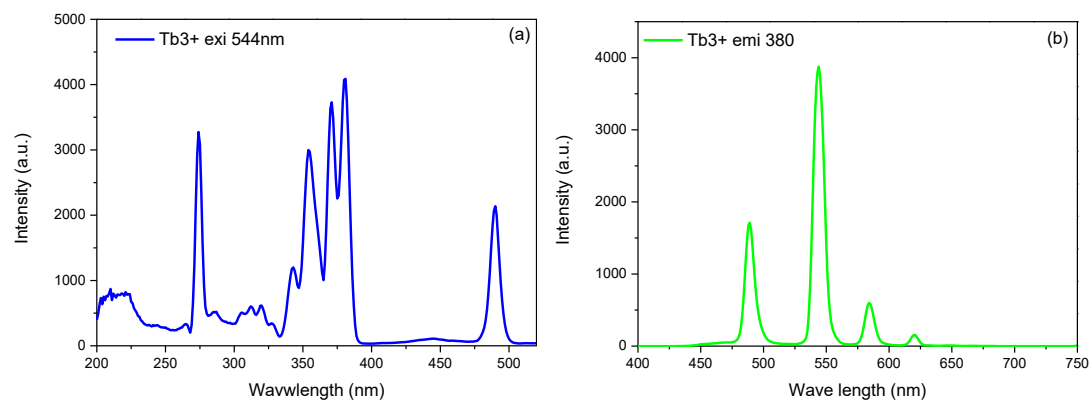


Figure 8.12 Excitation ($\lambda_{em} = 544\,nm$) (a) and DCPL (b) spectrum of NaGdF$_4$:Yb,Tm@NaGdF$_4$:Tb@NaGdF$_4$:Ce NPs ($\lambda_{ex} = 380\,nm$).

The as synthesized NPs exhibit UC luminescence of Tm$^{3+}$, Eu$^{3+}$ and Tb$^{3+}$ through an energy transfer process Yb$^{3+}$ → Tm$^{3+}$→ Gd$^{3+}$ → Eu$^{3+}$/Tb$^{3+}$. MGdF$_4$:Yb,Tm@MGdF$_4$:Eu/Tb@MGdF$_4$:Ce NPs exhibit the same UC as MGdF$_4$:Yb,Tm@MGdF$_4$:Eu/Tb core shell NPs (M: Na or K). Figure 8.13 shows the UC emission image of NaGdF$_4$:Yb,Tm@NaGdF$_4$:Eu/Tb (a, b) and KGdF$_4$:Yb,Tm@KGdF$_4$:Eu/Tb (c, d). In the same synthesis conditions and doping ratio, the UCPL from potassium based NPs appears brighter than that from Sodium NPs.

Figure 8.13 UC emission image for NaGdF$_4$:Yb,Tm@NaGdF$_4$:Eu/Tb NPs (a, b) and KGdF$_4$:Yb,Tm@KGdF$_4$:Eu/Tb NPs ($\lambda_{ex} = 980\ nm$).

For the NaGdF$_4$:Yb,Tm and KGdF$_4$:Yb,Tm core, as seen from figure 8.14, the typical UC bands with maxima at 449 nm (1D2 → 3F4), 476 nm (1G4 → 3H6), 646 nm (1G4 → 3F4), 695 nm (3F2,3 → 3H6) and 802 nm (3H4 → 3H6) can be clearly resolved. Contrary to the UC of Eu$^{3+}$/Tb$^{3+}$ in core shell shell NPs, the UC of Tm$^{3+}$ in NaGdF$_4$:Yb,Tm core is slightly stronger than for the KYb$_2$F$_7$ core.
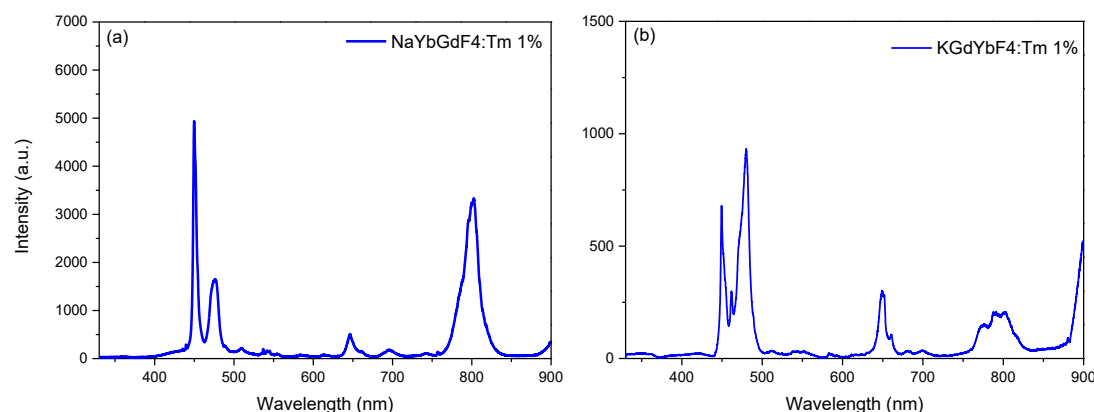


Figure 8.14 UCPL spectrum of NaGdF$_4$:Yb,Tm 1% (a) and KGdF$_4$:Yb,Tm 1% (b) excited by 980 nm laser.

After covering a shell of MGdF$_4$:Eu,Tb (M: Na or K), the UC spectra of Na and K core shell NPs were measured, and the results are shown in figure 8.15. The spectra confirm that the relative red and green UC of Eu$^{3+}$/Tb$^{3+}$ are more efficient in K based NPs than in Na based NPs, with comparison to the Tm$^{3+}$ emission. Stokes emission for KGdF$_4$:Yb,Tm@KGdF$_4$:Eu/Tb NPs under 254 nm UV lamp excitation is shown in figure 8.16.

The energy level diagrams of Yb$^{3+}$, Tm$^{3+}$, Gd$^{3+}$, Ce$^{3+}$, Eu$^{3+}$ and Tb$^{3+}$ with the schematic representations of Stokes and UC processes are shown in figure 8.17-8.19.
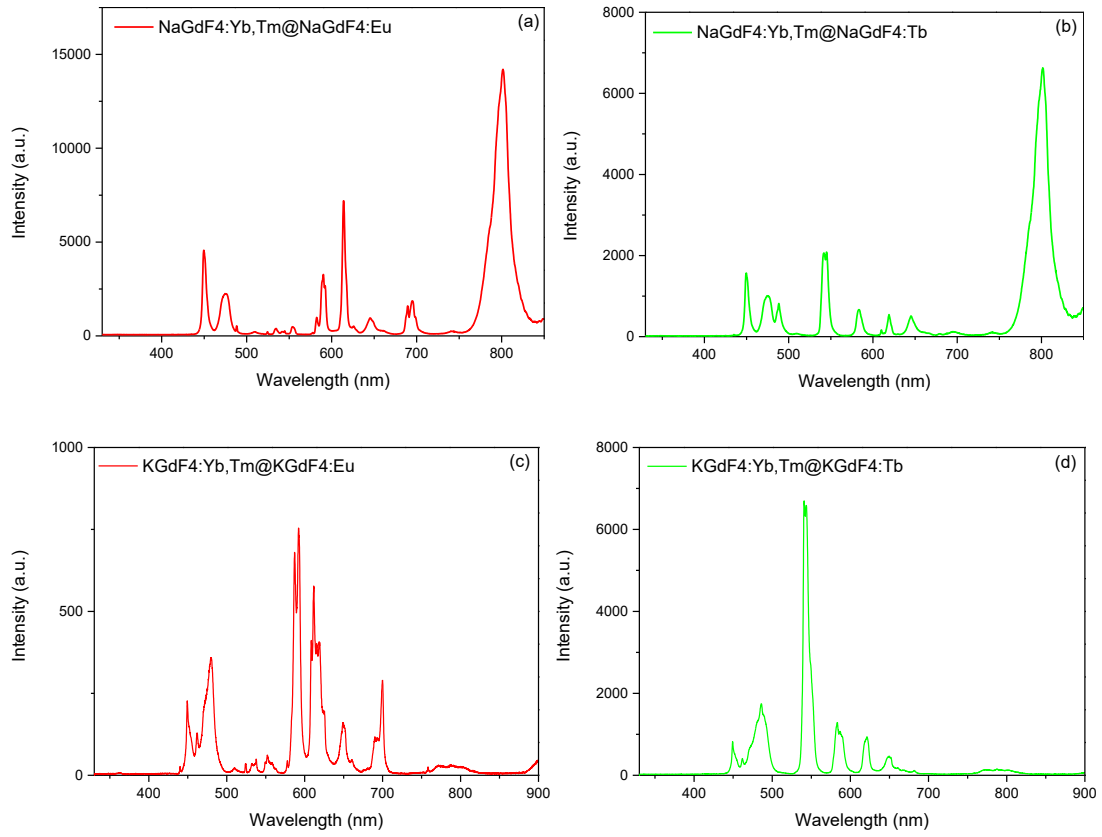
Figure 8.15 UCPL spectrum of NaGdF$_4$:Yb,Tm@NaGdF$_4$:Eu/Tb (a, b) and KGdF$_4$:Yb,Tm@KGdF$_4$:Eu/Tb (c, d) ($\lambda_{ex} = 980\ nm$).
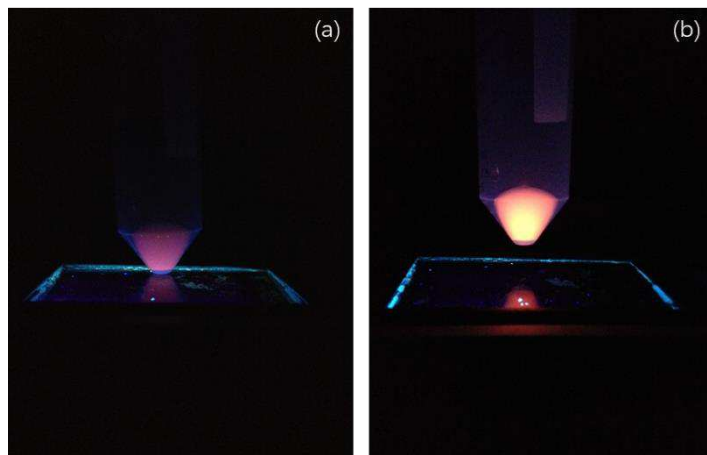


Figure 8.16 PL image of KGdF$_4$:(Yb49%,Tm1%)@KGdF$_4$:Eu20% excited by 254 nm (a) and 365 nm (b) UV lamp.
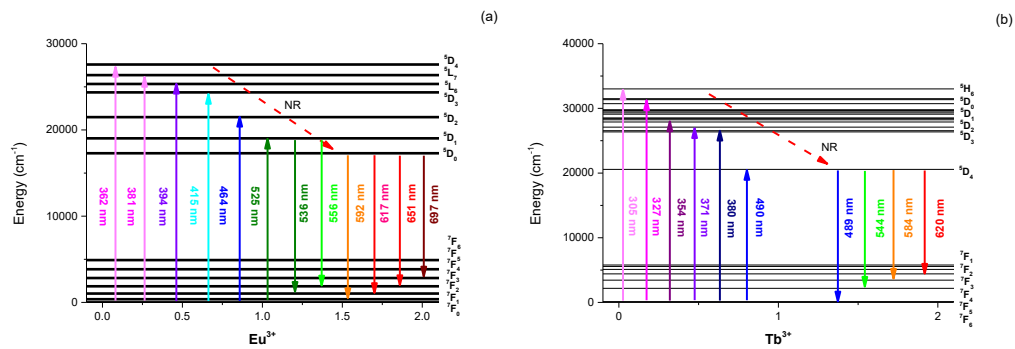
Figure 8.17 Energy level diagrams of $Eu^{3+}$ and $Tb^{3+}$ with the excitation and emission process.
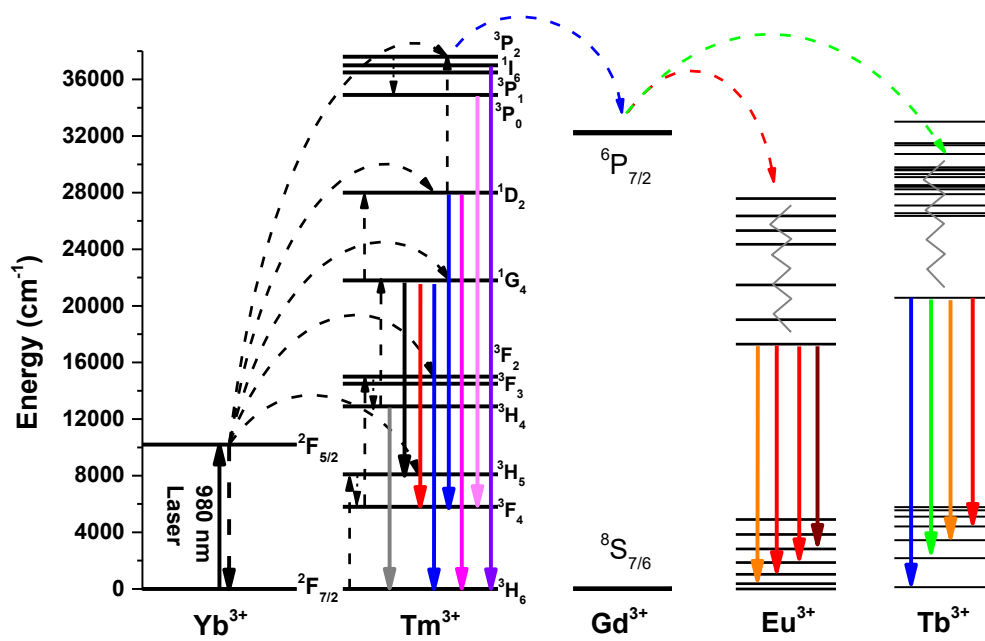


Figure 8.18 Energy level diagrams of $Yb^{3+}$, $Tm^{3+}$, $Gd^{3+}$, $Eu^{3+}$ and $Tb^{3+}$ with the schematic representation of up converting energy transfer processes.
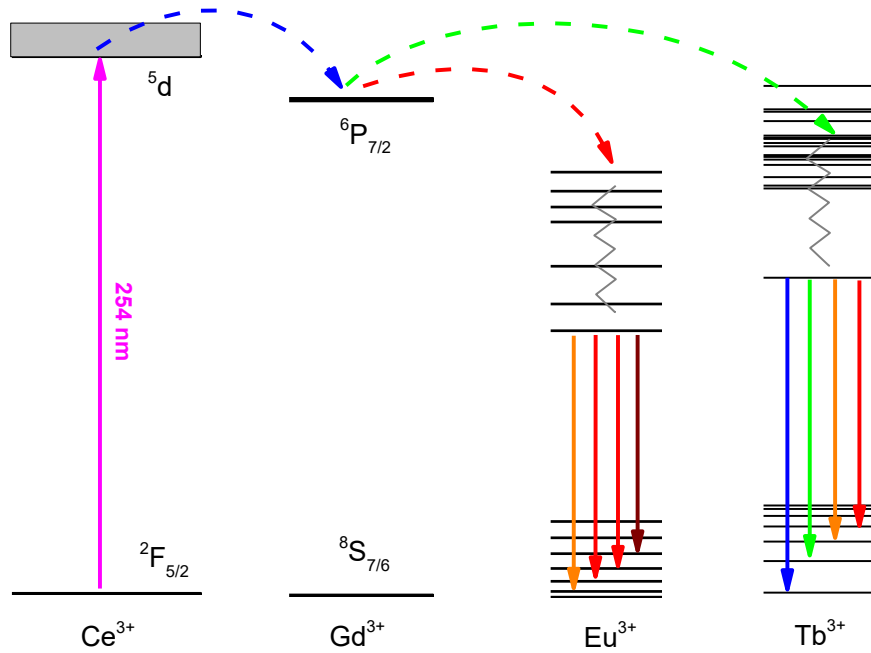
Figure 8.19 Energy level diagrams of Ce$^{3+}$, Gd$^{3+}$, Eu$^{3+}$ and Tb$^{3+}$ with the schematic representation of the down converting energy transfer processes. .

# 8.4 Conclusion

In conclusion, through a citrate and microwave assisted hydrothermal route, the α -NaYbF4, β -NaGdF$_4$, β -NaGdF$_4$:Yb,Tm, orthorhombic KYb$_2$F$_7$, α -KGdF$_4$, α-KGdF$_4$:Yb,Tm, MGdF$_4$:Ce@MGdF$_4$:Eu,Tb core shell, MGdF$_4$:Yb,Tm@MGdF$_4$:Eu,Tb core shell, MGdF$_4$:Yb,Tm@MGdF$_4$:Eu,Tb@MGdF$_4$:Ce (M: Na or K) core shell shell NPs have been synthesized.

Under UV excitation (365-400 nm), the Eu$^{3+}$/Tb$^{3+}$ doped NaYbF$_4$, NaGdF$_4$ and KGdF$_4$ samples emit red and green light, respectively. MGdF$_4$:Ce@MGdF$_4$:Eu$^{3+}$/Tb$^{3+}$ core-shell NPs and MGdF$_4$:Yb,Tm@MGdF$_4$:Eu$^{3+}$/Tb$^{3+}$@MGdF$_4$:Ce core-shell-shell NPs can also emit red and green light excited by UV light at 254 nm which is sensitized by Ce$^{3+}$ and Ce$^{3+}$→ Gd$^{3+}$ → Eu$^{3+}$/Tb$^{3+}$ processes. The KGdF$_4$:Yb,Tm@KGdF$_4$:Eu$^{3+}$/Tb$^{3+}$ NPs have a weak Stokes emission when excited by 254 nm UV light.

Under 980 nm NIR laser excitation, the MGdF$_4$:Yb,Tm@MGdF$_4$:Eu$^{3+}$/Tb$^{3+}$ core shell NPs and MGdF$_4$:Yb,Tm@MGdF$_4$:Eu$^{3+}$/Tb$^{3+}$@MGdF$_4$:Ce$^{3+}$ core-shell-shell NPs emit red and green UC luminescence by Yb$^{3+}$ → Tm$^{3+}$→ Gd$^{3+}$ → Eu$^{3+}$/Tb$^{3+}$ processes. The potassium based NPs exhibit brighter red and green UCPL than sodium based NPs. As a result of their unique luminescence properties, these nanoparticles may find potential applications in the fields of biomedicine, color displays, light-emitting diodes (LEDs), and solid-state lasers.

# Chapter 9 Final conclusions and future work

## 9.1 Photovoltaic material copper zinc tin sulfide

Composed with earth abundant and nontoxic elements, quaternary semiconductor compound copper zinc tin sulfide (CZTS) provides a photovoltaic ability with favorable optical and electronic properties. Solution based approaches play an important role in reducing the cost of solar cells manufacturing. By reacting copper and zinc nitrates and tin precursor in thiourea and ammonia sulphide solution, typical kesterite phase of $Cu_2ZnSnS_4$ nanoparticles without other binary or ternary impurity phases were formed from the aqueous solution after annealing at 500°C. The CZTS precursor solution can also be obtained by dissolving copper, zinc, tin and sulphur powders in mixture solution of organic solvents thioglycolic acid and ethanol amine. Crystal of wurtzite phase can be formed when heated at 120°C, and kesterite phase mixed with trace amount of wurtzite phase (1.8%) can be obtained when heating under microwave assisted process. The as synthesized CZTS nanoparticle represents potential application in photovoltaic device, IR light luminescent and water splitting fields. Future work will be aimed to produce stable and high efficient CZTS solar cell device.

## 9.2 Photovoltaic material perovskite

Methylammonium lead halide perovskite material $CH_3NH_3PbX_3$ (X=I, Br and Cl) can be produced in a cheap and simple process. With low cost and superior optoelectronic properties, it represents a great potential for high-efficiency photovoltaic cells and light-emitting diodes, but the use of toxic element and the unfavorable stability is a concerning issue. The efficiency can reach as high as 14% when use gold and silver counter electrode, but the device degrades very fast and performance low down. When use carbon paste as the counter electrode, the device performance is lower comparatively, but the stability is enhanced significantly. Nontoxic and very stable variety cesium tin halide derivative ($Cs_2SnX_6$, X=Cl, Br, I) is an alternative route to produce perovskite solar cell without concerning of the toxicity and stability, the fabrication technology for high performance device is needed to develop in future.

## 9.3 Fluorescent material CuInS$_2$@ZnS quantum dots

Zinc sulfide (ZnS) and ZnS covered ternary I–III–VI semiconductors $CuInS_2$ quantum dots possess unique optical properties with both excellent photovoltaic and fluorescent abilities.

The incorporation of $Gd^{3+}$ in the surface of the $CuInS_2$@ZnS quantum dot doesn't change

the optical property of the initial nanoparticle and makes it versatile. The covering of PEG or BSA on the surface of CuInS2@ZnS:Gd$^{3+}$ quantum dots allows phase transfer of hydrophobic quantum dots into aqueous phase. The MRI longitudinal relaxivity value for QDs@PEG reaches to as high as 33.81 mM$^{-1}$s$^{-1}$. The dual-modality nanoprobe exhibits negligible cytotoxicity with >80% cell viability in human cervical (HeLa) cells after 24 hours. The fluorescence and MR imaging study were performed *in vitro* and *in vivo* and both the clear, positive, and increasing contrast enhancement of magnetic resonance and fluorescent image were obtained. The results demonstrated that CuInS2@ZnS:Gd$^{3+}$ quantum dots could present great potential in simultaneously producing strong MR contrast enhancement and fluorescence imaging as dual-modal contrast agent. Future work might be aimed to the surface modification of the quantum dots to enable the nanoparticle to target the cancer cells specifically.

## 9.4 Luminescent copper thiolate compounds

As an interesting class of phosphors, copper thiolate compounds have attracted a great interest due to their unique structure and optical properties. In this work, we present a self-assembly strategy using 1-dodecanethiol (DDT) as ligand and reductant to produce the highly luminescence nanomaterial. In a simple synthesis process, the emission properties can be controlled. By forming compact and layered structure, the emission can be tuned so that green, yellow and even white emitting light can be obtained with single Cu thiolates. The Cu thiolates exhibit distinct mechano and thermochromic luminescent properties. The green, yellow and white light emitting source from single Cu thiolates could have interesting potential in LED applications.

## 9.5 Lanthanide doped fluoride luminescent materials

By the assisting of citrate and microwave, the $\alpha$-NaYbF4, $\beta$-NaGdF$_4$, $\beta$-NaGdF$_4$:Yb,Tm, orthorhombic KYb$_2$F$_7$, $\alpha$ -KGdF$_4$, $\alpha$ -KGdF$_4$:Yb,Tm, MGdF$_4$:Ce@MGdF$_4$:Eu,Tb, MGdF$_4$:Yb,Tm@MGdF$_4$:Eu,Tb, MGdF$_4$:Yb,Tm@MGdF$_4$:Eu,Tb@MGdF$_4$:Ce (M: Na or K) NPs have been synthesized hydrothermally.

Under longer UV excitation (365-400 nm), the Eu$^{3+}$/Tb$^{3+}$ doped NaYbF$_4$, NaGdF$_4$ and KGdF$_4$ samples emit the red and green light, respectively. Not only under longer UV excitation, MGdF$_4$:Ce@MGdF$_4$:Eu$^{3+}$/Tb$^{3+}$ core shell NPs and MGdF$_4$:Yb,Tm@MGdF$_4$:Eu$^{3+}$/Tb$^{3+}$@MGdF$_4$:Ce core shell shell NPs can also emit the red and green light under 254 nm UV light excitation by Ce$^{3+}$→ Gd$^{3+}$ → Eu$^{3+}$/Tb$^{3+}$ energy transfer processes. Under 980 nm NIR laser excitation, the MGdF$_4$:Yb,Tm@MGdF$_4$:Eu$^{3+}$/Tb$^{3+}$ core shell NPs and MGdF$_4$:Yb,Tm@MGdF$_4$:Eu$^{3+}$/Tb$^{3+}$@MGdF$_4$:Ce$^{3+}$ core shell shell NPs emit red and green UC luminescence by an energy transfer process of Yb$^{3+}$ → Tm$^{3+}$→ Gd$^{3+}$ → Eu$^{3+}$/Tb$^{3+}$. The potassium based NPs exhibit brighter red and green UC than sodium based NPs. More investigation about the luminescent properties is under progressing.

# Acknowledgments

# Bibliography

[1]    S. Mikulovic, S. Pupe, H.M. Peixoto, G.C. Do Nascimento, K. Kullander, A.B.L. Tort, R.N. Leão, On the photovoltaic effect in local field potential recordings, Neurophotonics. 3 (2016) 15002. doi:10.1117/1.NPh.3.1.015002.

[2]    D.A. Neamen, Semiconductor Physics and Devices Basic Principles, 3rd ed., Elizabeth A. Jones, 2002. doi:10.1016/S1369-7021(06)71498-5.

[3]    A. Al-Azzawi, Light Production, in: Light Opt. Pract., CRC press, 2006. https://books.google.it/books?id=Iw7NBQAAQBAJ&dq=In+certain+semiconductors,+e xcited+electrons+can+relax+by+emitting+light+instead+of+producing+heat.%5C&sour ce=gbs_navlinks_s.

[4]    J.-L. Bredas, Mind the gap!, Mater. Horiz. 1 (2014) 17–19. doi:10.1039/C3MH00098B.

[5]    J.D. Jordan Hanania, Kailyn Stenhouse, Energy Education, (2017). http://energyeducation.ca/encyclopedia/Band_gap (accessed March 11, 2017).

[6]    A. Zunger, Solid State Physics, 39 (1986) 275. doi:citeulike-article-id:495035.

[7]    Principles of Semiconductor Devices, (2017). http://ecee.colorado.edu/~bart/book/book/chapter2/ch2_3.htm (accessed May 11, 2017).

[8]    Direct and Indirect Semiconductors, (2017). https://www.doitpoms.ac.uk/tlplib/semiconductors/direct.php (accessed March 11, 2017).

[9]    K. Jager, O. Isabella, A.H.M. Smets, R.A.C.M.M. van Swaaij, M. Zeman, Solar Energy Fundamentals, Technology and Systems, Delf Univ. Technol. (2014) 1–420. doi:10.1007/SpringerReference_29746.

[10]   S.D. Stranks, S.D. Stranks, G.E. Eperon, G. Grancini, C. Menelaou, M.J.P. Alcocer, T. Leijtens, L.M. Herz, A. Petrozza, H.J. Snaith, Electron-Hole Diffusion Lengths Exceeding, Science. 342 (2014) 341–344. doi:10.1126/science.1243982.

[11]   G. Hodes, P. V. Kamat, Understanding the Implication of Carrier Diffusion Length in Photovoltaic Cells, J. Phys. Chem. Lett. 6 (2015) 4090–4092. doi:10.1021/acs.jpclett.5b02052.

[12]   A.G. Alexandru Micu, Elena Motivans, Dragos Mitrica, Henry Conrad, Record-breaking silicon solar cell efficiency of 26.6% demonstrated by Japanese researchers, very close to the theoretical limit, (n.d.). https://www.zmescience.com/ecology/renewable-energy-ecology/solar-cell-close-ideal -limit/ (accessed November 24, 2017).

[13]   K. Rui, Y. Takeshi, A. Shunsuke, H. Atsushi, F.T. Kong, K. Takuya, S. Hiroki, New World Record Cu(In,Ga)(Se,S)2 Thin Film Solar Cell Efficiency Beyond 22%, 2016

IEEE 43th Photovolt. Spec. Conf. PVSC 2016 Portland(OR) USA, June 2016. (2016) 3–7. doi:10.1109/PVSC.2016.7749822.

[14]    S. Krum, S. Haymore, First Solar Achieves Yet Another Cell Conversion Efficiency World Record, First Sol. (2016). http://investor.firstsolar.com/releasedetail.cfm?ReleaseID=956479.

[15]    L. Kranz, C. Gretener, J. Perrenoud, R. Schmitt, F. Pianezzi, F. La Mattina, P.B. ouml Sch, E. Cheah, A.C. Abreve, C.M. Fella, H. Hagendorfer, T.J. auml Ger, S. Nishiwaki, A.R. Uhl, S. Buecheler, A.N. Tiwari, Doping of polycrystalline CdTe for high-efficiency solar cells on flexible metal foil, Nat. Commun. 4 (1AD) 1–7. doi:10.1038/ncomms3306.

[16]    S. Mathew, A. Yella, P. Gao, R. Humphry-Baker, B.F.E. Curchod, N. Ashari-Astani, I. Tavernelli, U. Rothlisberger, M.K. Nazeeruddin, M. Grätzel, Dye-sensitized solar cells with 13% efficiency achieved through the molecular engineering of porphyrin sensitizers, Nat. Chem. 6 (2014) 242–247. doi:10.1038/nchem.1861.

[17]    R. Fang, W.J. Zhang, S.S. Zhang, W. Chen, The rising star in photovoltaics-perovskite solar cells: The past, present and future, Sci. China Technol. Sci. 59 (2016) 989–1006. doi:10.1007/s11431-016-6056-8.

[18]    Steven S. Hegedus; Antonio Luque; et. al., Handbook of Photovoltaic Science and Engineering, John Wiley & Sons Ltd, The Atrium, Southern Gate, Chichester, West Sussex PO19 8SQ, England, 2002. doi:10.1002/9780470974704.

[19]    B.S. Keith McIntosh, Malcolm Abbott, PV Lighthouse:, (n.d.). https://www2.pvlighthouse.com.au/resources/courses/altermatt/The PV Principle/The solar cell under illumination.aspx (accessed November 30, 2017).

[20]    B. Valeur, M.N. Berberan-Santos, A brief history of fluorescence and phosphorescence before the emergence of quantum theory, J. Chem. Educ. 88 (2011) 731–738. doi:10.1021/ed100182h.

[21]    J.R. Lakowicz, Principles of Fluorescence Spectroscopy, 3rd ed., Springer Science+Business Media, LLC, 233 Spring Street, New York, NY 10013, USA), 2006. doi:10.1007/978-0-387-46312-4.

[22]    R.Y. Tsien, The green fluorescent protein, Annu. Rev. Biochem. 67 (1998) 509–544. doi:10.1146/annurev.biochem.67.1.509.

[23]    R.H. Douglas, C.W. Mullineaux, J.C. Partridge, Long-wave sensitivity in deep-sea stomiid dragonfish with far-red bioluminescence: evidence for a dietary origin of the chlorophyll-derived retinal photosensitizer of Malacosteus niger, Philos. Trans. R. Soc. B Biol. Sci. 355 (2000) 1269–1272. doi:10.1098/rstb.2000.0681.

[24]    P. Vukusic, Directionally Controlled Fluorescence Emission in Butterflies, Science (80-. ). 310 (2005) 1151–1151. doi:10.1126/science.1116612.

[25]    A. Salih, A. Larkum, G. Cox, M. Kühl, O. Hoegh-Guldberg, Fluorescent pigments in corals are photoprotective., Nature. 408 (2000) 850–853. doi:10.1038/35048564.

[26] Fluorescent Minerals Learn about the minerals and rocks that "glow" under ultraviolet light, (2017). http://geology.com/articles/fluorescent-minerals/ (accessed November 11, 2017).

[27] H. Song, Y.M. Leem, B.G. Kim, Y.T. Yu, Synthesis and fluorescence properties of pure and metal-doped spherical ZnS particles from EDTA-metal complexes, J. Phys. Chem. Solids. 69 (2008) 153–160. doi:10.1016/j.jpcs.2007.08.011.

[28] K.B. Lin, Y.H. Su, Photoluminescence of Cu:ZnS, Ag:ZnS, and Au:ZnS nanoparticles applied in Bio-LED, Appl. Phys. B Lasers Opt. 113 (2013) 351–359. doi:10.1007/s00340-013-5497-z.

[29] Database of luminescent Minerals, (2017). https://www.fluomin.org/uk/fiche.php?id=157 (accessed November 11, 2017).

[30] Y. Liu, T. Lu, T. Mu, H. Chen, J. Ke, Color measurement of a ruby, Color Res. Appl. 38 (2013) 328–333. doi:10.1002/col.21743.

[31] H. Search, C. Journals, A. Contact, M. Iopscience, I.P. Address, The lifetime of EuZ + fluorescence in CaF ,: Eu * + crystals, 1. Phys. Condens. Matter. 9163 (1991) 9162–9167.

[32] Q. Zhan, J. Qian, H. Liang, G. Somesfalean, D. Wang, S. He, Z. Zhang, S. Andersson-Engels, Using 915-nm Laser Excited Tm3+/Er3+/Ho3+ Doped NaYbF4 Upconversion Nanoparticles for In Vitro and Deeper In Vivo Bioimaging Without Overheating Irradiation, ACS Nano. 5 (2011) 3744–3757. doi:10.1021/nn200110j.

[33] M. Xue, X. Zhu, X. Qiu, Y. Gu, W. Feng, F. Li, Highly Enhanced Cooperative Upconversion Luminescence through Energy Transfer Optimization and Quenching Protection, ACS Appl. Mater. Interfaces. 8 (2016) 17894–17901. doi:10.1021/acsami.6b05609.

[34] C. Li, W. Chen, D. Wu, D. Quan, Z. Zhou, J. Hao, J. Qin, Y. Li, Z. He, K. Wang, Large Stokes Shift and High Efficiency Luminescent Solar Concentrator Incorporated with CuInS2/ZnS Quantum Dots, Sci. Rep. 5 (2016) 17777. doi:10.1038/srep17777.

[35] L. Zhang, E. Wang, Metal nanoclusters: New fluorescent probes for sensors and bioimaging, Nano Today. 9 (2014) 132–157. doi:10.1016/j.nantod.2014.02.010.

[36] L. Shang, S. Dong, G.U. Nienhaus, Ultra-small fluorescent metal nanoclusters: Synthesis and biological applications, Nano Today. 6 (2011) 401–418. doi:10.1016/j.nantod.2011.06.004.

[37] J.S.J. Hargreaves, Some considerations related to the use of the Scherrer equation in powder X-ray diffraction as applied to heterogeneous catalysts, Catal. Struct. React. 2 (2016) 33–37. doi:10.1080/2055074X.2016.1252548.

[38] S. Bhattacharjee, DLS and zeta potential - What they are and what they are not?, J. Control. Release. 235 (2016) 337–351. doi:10.1016/j.jconrel.2016.06.017.

[39] J. Henry, K. Mohanraj, G. Sivakumar, Electrical and optical properties of CZTS thin

films prepared by SILAR method, J. Asian Ceram. Soc. 4 (2016) 81–84. doi:10.1016/j.jascer.2015.12.003.

[40]   I. Repins, N. Vora, C. Beall, S.-H. Wei, Y. Yan, M. Romero, G. Teeter, H. Du, B. To, M. Young, R. Noufi, Kesterites and Chalcopyrites: A Comparison of Close Cousins, MRS Proc. 1324 (2011) mrss11-1324-d17-01. doi:10.1557/opl.2011.844.

[41]   M. Jiang, Cu2ZnSnS4 Thin Film Solar Cells: Present Status and Future Prospects, in: A. Morales-Acevedo (Ed.), Sol. Cells - Res. Appl. Perspect., INTECH, 2013. doi:10.5772/50702.

[42]   M. Leng, Z. Chen, Y. Yang, Z. Li, K. Zeng, K. Li, G. Niu, Y. He, Q. Zhou, J. Tang, Lead-Free, Blue Emitting Bismuth Halide Perovskite Quantum Dots, Angew. Chemie - Int. Ed. 55 (2016) 15012–15016. doi:10.1002/anie.201608160.

[43]   S. Gupta, T. Bendikov, G. Hodes, D. Cahen, CsSnBr 3 , A Lead-free Halide Perovskite for Long-term Solar Cell Application: Insights on SnF 2 Addition, ACS Energy Lett. (2016) acsenergylett.6b00402. doi:10.1021/acsenergylett.6b00402.

[44]   I. Chung, J.H. Song, J. Im, J. Androulakis, C.D. Malliakas, H. Li, A.J. Freeman, J.T. Kenney, M.G. Kanatzidis, CsSnI 3: Semiconductor or metal? High electrical conductivity and strong near-infrared photoluminescence from a single material. High hole mobility and phase-transitions, J. Am. Chem. Soc. 134 (2012) 8579–8587. doi:10.1021/ja301539s.

[45]   M. Courel, J.A. Andrade-Arvizu, O. Vigil-Galán, The role of buffer/kesterite interface recombination and minority carrier lifetime on kesterite thin film solar cells, Mater. Res. Express. 3 (2016) 95501. doi:10.1088/2053-1591/3/9/095501.

[46]   A.D. Adewoyin, M.A. Olopade, M. Chendo, Enhancement of the conversion efficiency of Cu2ZnSnS4 thin film solar cell through the optimization of some device parameters, Optik (Stuttg). 133 (2017) 122–131. doi:10.1016/j.ijleo.2017.01.008.

[47]   Y. Yeh, H. Chen, S. Liu, FABRICATION OF Cu 2 ZnSnS 4 ( CZTS ) FILMS BY ONE-STEP ELECTROCHEMICAL DEPOSITION AND ANNEALING, 10 (2013) 565–571.

[48]   L. Yao, J. Ao, M.-J. Jeng, J. Bi, S. Gao, Q. He, Z. Zhou, G. Sun, Y. Sun, L.-B. Chang, J.-W. Chen, CZTSe solar cells prepared by electrodeposition of Cu/Sn/Zn stack layer followed by selenization at low Se pressure, Nanoscale Res. Lett. 9 (2014) 678. doi:10.1186/1556-276X-9-678.

[49]   Y. Li, T. Yuan, L. Jiang, F. Liu, Y. Liu, Y. Lai, Cu2ZnSnS4 thin film solar cell fabricated by co-electrodeposited metallic precursor, J. Mater. Sci. Mater. Electron. 26 (2014) 204–210. doi:10.1007/s10854-014-2384-2.

[50]   F. Yang, R. Ma, W. Zhao, X. Zhang, X. Li, Fabrication of Cu2ZnSnS4 (CZTS) absorber films based on different compound targets, J. Alloys Compd. 689 (2016) 849–856. doi:10.1016/j.jallcom.2016.08.053.

[51] Z.S. Li, S.R. Wang, Z. Jiang, M. Yang, Y.L. Lu, S.J. Liu, Q.C. Zhao, R.T. Hao, Cu2ZnSnS4 solar cells prepared by sulfurization of sputtered ZnS/Sn/CuS precursors, Phys. B Condens. Matter. 502 (2016) 56–60. doi:10.1016/j.physb.2016.08.014.

[52] M.A. Olgar, J. Klaer, R. Mainz, S. Levcenco, J. Just, E. Bacaksiz, T. Unold, Effect of precursor stacking order and sulfurization temperature on compositional homogeneity of CZTS thin films, Thin Solid Films. 615 (2016) 402–408. doi:10.1016/j.tsf.2016.07.058.

[53] C. Sripan, R. Ganesan, E.M. Vinod, A.K. Viswanath, The effect of sulfur on the phase formation of Cu2ZnSnS4 solar cell material, Mater. Lett. 180 (2016) 295–297. doi:10.1016/j.matlet.2016.05.027.

[54] T.G. Sánchez, X. Mathew, N.R. Mathews, Obtaining phase-pure CZTS thin films by annealing vacuum evaporated CuS/SnS/ZnS stack, J. Cryst. Growth. 445 (2016) 15–23. doi:10.1016/j.jcrysgro.2016.03.039.

[55] R. Touati, M. Ben Rabeh, M. Kanzari, Effect of post-sulfurization on the structural and optical properties of Cu2ZnSnS4 thin films deposited by vacuum evaporation method, Thin Solid Films. 582 (2014) 2–6. doi:10.1016/j.tsf.2014.12.032.

[56] R.J. Deokate, A.D. Adsool, N.S. Shinde, S.M. Pawar, C.D. Lokhande, Structural and Optical Properties of Spray-deposited Cu2ZnSnS4 thin Films, Energy Procedia. 54 (2014) 627–633. doi:10.1016/j.egypro.2014.07.304.

[57] W. Wang, M.T. Winkler, O. Gunawan, T. Gokmen, T.K. Todorov, Y. Zhu, D.B. Mitzi, Device characteristics of CZTSSe thin-film solar cells with 12.6% efficiency, Adv. Energy Mater. 4 (2014) 1–5. doi:10.1002/aenm.201301465.

[58] K. Patel, V. Kheraj, D. V. Shah, C.J. Panchal, N.G. Dhere, Cu2ZnSnS4 thin-films grown by dip-coating: Effects of annealing, J. Alloys Compd. 663 (2016) 842–847. doi:10.1016/j.jallcom.2015.11.233.

[59] F. Liu, S. Shen, F. Zhou, N. Song, X. Wen, J.A. Stride, K. Sun, C. Yan, X. Hao, Kesterite Cu2ZnSnS4 thin film solar cells by a facile DMF-based solution coating process, J. Mater. Chem. C. 3 (2015) 10783–10792. doi:10.1039/C5TC01750E.

[60] C.M. Sutter-Fella, A.R. Uhl, Y.E. Romanyuk, A.N. Tiwari, Large-grained Cu2ZnSnS4 layers sintered from Sn-rich solution-deposited precursors, Phys. Status Solidi Appl. Mater. Sci. 212 (2015) 121–125. doi:10.1002/pssa.201431147.

[61] W. Zhao, G. Wang, Q. Tian, Y. Yang, L. Huang, D. Pan, Fabrication of Cu2ZnSn(S,Se)4 Solar Cells via an Ethanol-Based Sol-Gel Route Using SnS2 as Sn Source., ACS Appl. Mater. Interfaces. (2014). doi:10.1021/am5026006.

[62] B.D. Chernomordik, a. E. Béland, N.D. Trejo, a. a. Gunawan, D.D. Deng, K. a. Mkhoyan, E.S. Aydil, Rapid facile synthesis of Cu2ZnSnS4 nanocrystals, J. Mater. Chem. A. 2 (2014) 10389. doi:10.1039/c4ta01658k.

[63] B. Ananthoju, J. Mohapatra, M.K. Jangid, D. Bahadur, N. V. Medhekar, M. Aslam,

Cation/Anion Substitution in Cu2ZnSnS4 for Improved Photovoltaic Performance, Sci. Rep. 6 (2016) 35369. doi:10.1038/srep35369.

[64] M.P. Suryawanshi, S.W. Shin, U. V. Ghorpade, K. V. Gurav, C.W. Hong, P.S. Patil, A. V. Moholkar, J.H. Kim, Improved solar cell performance of Cu2ZnSnS4 (CZTS) thin films prepared by sulfurizing stacked precursor thin films via SILAR method, J. Alloys Compd. 671 (2016) 509–516. doi:10.1016/j.jallcom.2016.02.015.

[65] S. Gupta, T.J. Whittles, Y. Batra, V. Satsangi, S. Krishnamurthy, V.R. Dhanak, B.R. Mehta, A low-cost, sulfurization free approach to control optical and electronic properties of Cu2ZnSnS4 via precursor variation, Sol. Energy Mater. Sol. Cells. 157 (2016) 820–830. doi:10.1016/j.solmat.2016.08.004.

[66] C. Xue, J. Li, Y. Wang, G. Jiang, L. Weifeng, C. Zhu, Fabrication of Cu2ZnSn(SxSe1−x)4 solar cells by ethanol-ammonium solution process, Appl. Surf. Sci. 383 (2016) 90–97. doi:10.1016/j.apsusc.2016.04.192.

[67] D.H. Webber, R.L. Brutchey, Alkahest for V2VI3 chalcogenides: Dissolution of nine bulk semiconductors in a diamine-dithiol solvent mixture, J. Am. Chem. Soc. 135 (2013) 15722–15725. doi:10.1021/ja4084336.

[68] G. Wang, W. Zhao, Y. Cui, Q. Tian, S. Gao, L. Huang, D. Pan, Fabrication of a Cu2ZnSn(S,Se)4 photovoltaic device by a low-toxicity ethanol solution process, ACS Appl. Mater. Interfaces. 5 (2013) 10042–10047. doi:10.1021/am402558a.

[69] Y. Liu, D. Yao, L. Shen, H. Zhang, X. Zhang, B. Yang, Alkylthiol-enabled se powder dissolution in oleylamine at room temperature for the phosphine-free synthesis of copper-based quaternary selenide nanocrystals, J. Am. Chem. Soc. 134 (2012) 7207–7210. doi:10.1021/ja300064t.

[70] Y. Yang, G. Wang, W. Zhao, Q. Tian, L. Huang, D. Pan, Solution-Processed Highly E ffi cient Cu 2 ZnSnSe 4 Thin Film Solar Cells by Dissolution of Elemental Cu , Zn , Sn , and Se Powders, (2015).

[71] F. Aslan, A. Tumbul, Non-vacuum processed Cu2ZnSnS4 thin films: Influence of copper precursor on structural, optical and morphological properties, J. Alloys Compd. 612 (2014) 1–4. doi:10.1016/j.jallcom.2014.05.140.

[72] K.D. Zhang, Z.R. Tian, J.B. Wang, B. Li, X.L. Zhong, D.Y. Guo, S.M. He, Preparation of Cu2ZnSnS4 thin films using spin-coating method with thermolysis and annealing, J. Sol-Gel Sci. Technol. 73 (2014) 452–459. doi:10.1007/s10971-014-3561-8.

[73] C. Jiang, J. Lee, D. V Talapin, Soluble Precursors for CuInSe 2 , CuIn 1 −, J. Am. Chem. Soc. 134 (2012) 5010–5013.

[74] J. Zhong, Z. Xia, C. Zhang, B. Li, X. Liu, Y. Cheng, J. Tang, One-Pot Synthesis of Self-Stabilized Aqueous Nanoinks for Cu 2 ZnSn(S,Se) 4 Solar Cells, Chem. Mater. 26 (2014) 3573–3578. doi:10.1021/cm501270j.

[75] S. Schorr, H.-J. Hoebler, M. Tovar, A neutron diffraction study of the stannite-kesterite

solid solution series, Eur. J. Mineral. 19 (2007) 65–73. doi:10.1127/0935-1221/2007/0019-0065.

[76] J. Mandal, M. Dalal, B.J. Sarkar, P.K. Chakrabarti, Room Temperature Antiferromagnetic Ordering of Nanocrystalline Tb1.90Ni0.10O3, J. Electron. Mater. 46 (2017) 1107–1113. doi:10.1007/s11664-016-5077-1.

[77] X. Lu, Z. Zhuang, Q. Peng, Y. Li, Wurtzite Cu2ZnSnS4 nanocrystals: a novel quaternary semiconductor, Chem. Commun. 47 (2011) 3141. doi:10.1039/c0cc05064d.

[78] A. Khare, B. Himmetoglu, M. Johnson, D.J. Norris, M. Cococcioni, E.S. Aydil, Calculation of the lattice dynamics and Raman spectra of copper zinc tin chalcogenides and comparison to experiments, J. Appl. Phys. 111 (2012) 2000–2002. doi:10.1063/1.4704191.

[79] H. Qing, Y. Zhu, Y. Hu, W. Hu, W. Zhou, J. Yi, T. Shen, A facile two-step-heating route to synthesize hierarchical metastable wurtzite Cu2ZnSnS4 microcrystals under the open-air condition, Mater. Lett. 176 (2016) 177–180. doi:10.1016/j.matlet.2016.04.084.

[80] C. Lejon, L. Österlund, Influence of phonon confinement, surface stress, and zirconium doping on the Raman vibrational properties of anatase TiO2 nanoparticles, J. Raman Spectrosc. 42 (2011) 2026–2035. doi:10.1002/jrs.2956.

[81] R. Mainz, A. Singh, S. Levcenko, M. Klaus, C. Genzel, K.M. Ryan, T. Unold, Phase-transition-driven growth of compound semiconductor crystals from ordered metastable nanorods, Nat. Commun. 5 (2014) 3133. doi:10.1038/ncomms4133.

[82] S. Chen, A. Walsh, Y. Luo, J.H. Yang, X.G. Gong, S.H. Wei, Wurtzite-derived polytypes of kesterite and stannite quaternary chalcogenide semiconductors, Phys. Rev. B - Condens. Matter Mater. Phys. 82 (2010) 1–8. doi:10.1103/PhysRevB.82.195203.

[83] J.Y. Kim, K. Cho, S. Ryu, S.Y. Kim, B.M. Weon, Crack formation and prevention in colloidal drops, Sci. Rep. (2015) 1–9. doi:10.1038/srep13166.

[84] H. Cao, D. Lan, Y.R. Wang, Crack and size-dependence of shear modulus in a drying particulate film, Sci. China Physics, Mech. Astron. 55 (2012) 1093–1097. doi:10.1007/s11433-012-4758-x.

[85] W.P. Lee, A.F. Routh, Temperature dependence of crack spacing in drying latex films, Ind. Eng. Chem. Res. 45 (2006) 6996–7001. doi:10.1021/ie051256m.

[86] Sphalerite Mineral Data, (n.d.). http://webmineral.com/data/Sphalerite.shtml#.WfYZsltSzIU (accessed October 29, 2017).

[87] mindat.org Wurtzite, (n.d.). https://www.mindat.org/min-4318.html (accessed October 29, 2017).

[88] L. Ozawa, M. Itoh, Cathode Ray Tube Phosphors, Chem. Rev. 103 (2003) 3835–3855. doi:10.1021/cr0203490.

[89]   G.C. Lisensky, M.N. Patel, M.L. Reich, Experiments with Glow-in-the-Dark Toys: Kinetics of Doped ZnS Phosphorescence, J. Chem. Educ. 73 (1996) 1048. doi:10.1021/ed073p1048.

[90]   Y. Li, L. Zhang, K. Kisslinger, Y. Wu, Y.J.M. Huang, S.H. Yang, B. Xue, S.Y. Yang, J.C. Liu, P. Shen, W. Chen, J.O. Malm, V. Zwiller, Y.N. Huang, S.M. Liu, R. Wallenberg, J.O. Bovin, L. Samuelson, 8 Y Li, S. Zhou, Z. Chen, Y. Yang, N. Chen, G.P. Du, 14 M W Wang, L.D. Sun, X.F. Fu, C.S. Liao, C.H. Yan, 16 P Yang, M. Lü, D. Xü, D. Yuan, J. Chang, G. Zhou, Green phosphorescence of zinc sulfide optical ceramics, Phys. B Cryst. Res. Technol. J. Phys. Soc. Jpn. Solid State Commun. 404 (2009) 3855–3858. doi:10.1364/OME.4.001140.

[91]   B. Pejjai, V.R. Minnam Reddy, K. Seku, T.R.R. Kotte, C. Park, Chemical bath deposition of Mn-doped ZnS thin films using greener complexing agents: Effect of Mn-doping on the optical properties, Optik (Stuttg). 130 (2017) 608–618. doi:10.1016/j.ijleo.2016.10.083.

[92]   G. Wang, B. Huang, Z. Li, Z. Lou, Z. Wang, Y. Dai, M.-H. Whangbo, Synthesis and characterization of ZnS with controlled amount of S vacancies for photocatalytic H2 production under visible light, Sci. Rep. 5 (2015) 8544. doi:10.1038/srep08544.

[93]   M. Nguyen, K. Ernits, K.F. Tai, C.F. Ng, S.S. Pramana, W.A. Sasangka, S.K. Batabyal, T. Holopainen, D. Meissner, A. Neisser, L. H.Wong, ZnS buffer layer for Cu2ZnSn(SSe)4 monograin layer solar cell, Sol. Energy. 111 (2015) 344–349. doi:10.1016/j.solener.2014.11.006.

[94]   J.Y. Park, R.B.V. Chalapathy, A.C. Lokhande, C.W. Hong, J.H. Kim, Fabrication of earth abundant Cu2ZnSnSSe4 (CZTSSe) thin film solar cells with cadmium free zinc sulfide (ZnS) buffer layers, J. Alloys Compd. 695 (2017) 2652–2660. doi:10.1016/j.jallcom.2016.11.178.

[95]   A. Ichiboshi, M. Hongo, T. Akamine, T. Dobashi, T. Nakada, Ultrasonic chemical bath deposition of ZnS(O,OH) buffer layers and its application to CIGS thin-film solar cells, Sol. Energy Mater. Sol. Cells. 90 (2006) 3130–3135. doi:10.1016/j.solmat.2006.06.032.

[96]   H. He, Y.Y. Zhang, J. Liu, D. Moore, G. Bao, Z.L. Wang, ZnS/silica nanocable field effect transistors as biological and chemical nanosensors, J. Phys. Chem. C. 111 (2007) 12152–12156. doi:10.1021/jp074772u.

[97]   D.E. Nam, W.S. Song, H. Yang, Noninjection, one-pot synthesis of Cu-deficient CuInS2/ZnS core/shell quantum dots and their fluorescent properties, J. Colloid Interface Sci. 361 (2011) 491–496. doi:10.1016/j.jcis.2011.05.058.

[98]   I.Y.Y. Bu, Sol-gel synthesis of ZnS (O,OH) thin films: Influence of precursor and process temperature on its optoelectronic properties, J. Lumin. 134 (2013) 423–428. doi:10.1016/j.jlumin.2012.08.008.

[99]   Z. Li, J. Wang, X. Xu, X. Ye, The evolution of optical properties during hydrothermal coarsening of ZnS nanoparticles, Mater. Lett. 62 (2008) 3862–3864.

doi:10.1016/j.matlet.2008.05.004.

[100] D.C. Onwudiwe, T.P.J. Krüger, C.A. Strydom, Laser assisted solid state reaction for the synthesis of ZnS and CdS nanoparticles from metal xanthate, Mater. Lett. 116 (2014) 154–159. doi:10.1016/j.matlet.2013.10.118.

[101] W.-L. Liu, C.-S. Yang, S.-H. Hsieh, W.-J. Chen, C.-L. Fern, Effect of deposition variables on properties of CBD ZnS thin films prepared in chemical bath of ZnSO4/SC(NH2)2/Na3C3H5O7/NH4OH, Appl. Surf. Sci. 264 (2013) 213–218. doi:10.1016/j.apsusc.2012.09.174.

[102] L. ZHOU, Y. XUE, J. LI, Study on ZnS thin films prepared by chemical bath deposition, J. Environ. Sci. 21 (2009) S76–S79. doi:10.1016/S1001-0742(09)60042-5.

[103] J.-H. Im, C.-R. Lee, J.-W. Lee, S.-W. Park, N.-G. Park, E.H. Sargent, K.-S. Cho, E.K. Lee, W.-J. Joo, E. Jang, T.-H. Kim, S.J. Lee, S.-J. Kwon, J.Y. Han, B.-K. Kim, B.L. Choi, J.M. Kim, A.L. Rogach, T. Franzl, T.A. Klar, J.N. Gaponik, V. Lesnyak, A. Shavel, A. Eychmüller, Y.P. Rakovich, J.F. Donegan, T. Takagahara, K. Takeda, S. Kan, T. Mokari, E. Rothenberg, U. Banin, C.A. Leatherdale, W.-K. Woo, F. V. Mikulec, M.G. Bawendi, W. Yu, L. Qu, W. Guo, X. Peng, A.J. Nozik, A.J. Nozik, B. O′Regan, M. Grätzel, R. Vogel, K. Pohl, H. Weller, D. Liu, P. V. Kamat, R. Vogel, P. Hoyer, H. Weller, A. Zaban, O.I. Micic, B.A. Gregg, A.J. Nozik, S. Rühle, M. Shalom, A. Zaban, H.J. Lee, J.-H. Yum, H.C. Leventis, S.M. Zakeeruddin, S.A. Haque, P. Chen, S.I. Seok, M. Grätzel, M.K. Nazeeruddin, Y.-L. Lee, Y.-S. Lo, V. Gonzalez-Pedro, X. Xu, I. Mora-Sero, J. Bisquert, J.A. Chang, J.H. Rhee, S.H. Im, Y.H. Lee, H.-J. Kim, S.I. Seok, M.K. Nazeeruddin, M. Grätzel, X.-Y. Yu, B.-X. Lei, D.-B. Kuang, C.-Y. Su, G. Hodes, A. Kojima, K. Teshima, Y. Shirai, T. Miyasaka, D.B. Mitzi, C.A. Feild, W.T.A. Harrison, A.M. Guloy, C.R. Kagan, D.B. Mitzi, C.D. Dimitrakopoulos, D.B. Mitzi, G.C. Papavassiliou, K. Tanaka, T. Takahashi, T. Ban, T. Kondo, K. Uchida, N. Miura, K. Yamada, H. Kawaguchi, T. Matsui, T. Okuda, S. Ichiba, M.-J. Kim, C.-R. Lee, W.-S. Jeong, J.-H. Im, T.I. Ryu, N.-G. Park, J.H. Park, H.-J. Koo, B.J. Yoo, K.C. Yoo, K.G. Kim, W.Y. Choi, N.-G. Park, G.-W. Lee, D.H. Kim, M.J. Ko, K.K. Kim, N.-G. Park, Y. Kawamura, H. Mashiyama, K. Hasebe, A.J. Frank, N. Kopidakis, J. van de Lagemaat, 6.5% Efficient Perovskite Quantum-Dot-Sensitized Solar Cell, Nanoscale. 3 (2011) 4088. doi:10.1039/c1nr10867k.

[104] F. Hao, C.C. Stoumpos, R.P.H. Chang, M.G. Kanatzidis, Anomalous band gap behavior in mixed Sn and Pb perovskites enables broadening of absorption spectrum in solar cells Anomalous band gap behavior in mixed Sn and Pb perovskites enables broadening of absorption spectrum in solar cells, J. Am. Chem. Soc. 136 (2014) 8094–8099. doi:10.1021/ja5033259.

[105] Y. Tian, A. Merdasa, E. Unger, M. Abdellah, K. Zheng, S. Mckibbin, A. Mikkelsen, T. Pullerits, A. Yartsev, V. Sundström, I.G. Scheblykin, Enhanced Organo-Metal Halide Perovskite Photoluminescence from Nanosized Defect-Free Crystallites and Emitting Sites, J. Phys. Chem. Lett. 6 (2015) 4171–4177. doi:10.1021/acs.jpclett.5b02033.

[106] Y. Park, S. Guo, N. Makarov, V.I. Klimov, Room Temperature Single-Photon Emission

from Individual Perovskite Quantum Dots Room Temperature Single-Photon Emission from Individual Perovskite Quantum Dots, (2015) 10386–10393. doi:10.1021/acsnano.5b04584.

[107] S. Yakunin, L. Protesescu, F. Krieg, M.I. Bodnarchuk, G. Nedelcu, M. Humer, G. De Luca, M. Fiebig, W. Heiss, M. V Kovalenko, Low-threshold amplified spontaneous emission and lasing from colloidal nanocrystals of caesium lead halide perovskites, Nat. Commun. 6 (2015) 8056. doi:10.1038/ncomms9056.

[108] J. Song, J. Li, X. Li, L. Xu, Y. Dong, H. Zeng, Quantum Dot Light-Emitting Diodes Based on Inorganic Perovskite Cesium Lead Halides (CsPbX3), Adv. Mater. 27 (2015) 7162–7167. doi:10.1002/adma.201502567.

[109] C.C. Stoumpos, M.G. Kanatzidis, The Renaissance of Halide Perovskites and Their Evolution as Emerging Semiconductors, Acc. Chem. Res. 48 (2015) 2791–2802. doi:10.1021/acs.accounts.5b00229.

[110] A. Kojima, K. Teshima, Y. Shirai, T. Miyasaka, Organometal halide perovskites as visible-light sensitizers for photovoltaic cells, J. Am. Chem. Soc. 131 (2009) 6050–6051. doi:10.1021/ja809598r.

[111] H.-S. Kim, C.-R. Lee, J.-H. Im, K.-B. Lee, T. Moehl, A. Marchioro, S.-J. Moon, R. Humphry-Baker, J.-H. Yum, J.E. Moser, M. Grätzel, N.-G. Park, Lead iodide perovskite sensitized all-solid-state submicron thin film mesoscopic solar cell with efficiency exceeding 9%., Sci. Rep. 2 (2012) 591. doi:110.1038/srep00591.

[112] A. Mei, X. Li, L. Liu, Z. Ku, T. Liu, Y. Rong, M.M. Xu, M. Hu, J. Chen, Y. Yang, M. Grätzel, H. Han, M. Gratzel, H. Han, A hole-conductor-free, fully printable mesoscopic perovskite solar cell with high stability, Science (80-. ). 345 (2014) 295–298. doi:10.1126/science.1254763.

[113] C. Eames, J.M. Frost, P.R.F. Barnes, B.C. O'Regan, A. Walsh, M.S. Islam, Ionic transport in hybrid lead iodide perovskite solar cells, Nat. Commun. 6 (2015) 7497. doi:10.1038/ncomms8497.

[114] S. Yang, W. Fu, Z. Zhang, H. Chen, C.-Z. Li, Recent advances in perovskite solar cells: efficiency, stability and lead-free perovskite, J. Mater. Chem. A. 5 (2017) 11462–11482. doi:10.1039/C7TA00366H.

[115] J.M. Frost, K.T. Butler, F. Brivio, C.H. Hendon, M. Van Schilfgaarde, A. Walsh, Atomistic origins of high-performance in hybrid halide perovskite solar cells, Nano Lett. 14 (2014) 2584–2590. doi:10.1021/nl500390f.

[116] Z. Liu, T. Shi, Z. Tang, B. Sun, G. Liao, Using a low-temperature carbon electrode for preparing hole-conductor-free perovskite heterojunction solar cells under high relative humidity, Nanoscale. 8 (2016) 7017–7023. doi:10.1039/C5NR07091K.

[117] J. Chen, X. Cai, D. Yang, D. Song, J. Wang, J. Jiang, A. Ma, S. Lv, M.Z. Hu, C. Ni, Recent progress in stabilizing hybrid perovskites for solar cell applications, J. Power Sources. 355 (2017) 98–133. doi:10.1016/j.jpowsour.2017.04.025.

[118] K. Aitola, K. Domanski, J.P. Correa-Baena, K. Sveinbjörnsson, M. Saliba, A. Abate, M. Grätzel, E. Kauppinen, E.M.J. Johansson, W. Tress, A. Hagfeldt, G. Boschloo, High Temperature-Stable Perovskite Solar Cell Based on Low-Cost Carbon Nanotube Hole Contact, Adv. Mater. 29 (2017). doi:10.1002/adma.201606398.

[119] S. Gholipour, J.-P. Correa-Baena, K. Domanski, T. Matsui, L. Steier, F. Giordano, F. Tajabadi, W. Tress, M. Saliba, A. Abate, A. Morteza Ali, N. Taghavinia, M. Grätzel, A. Hagfeldt, Highly Efficient and Stable Perovskite Solar Cells based on a Low-Cost Carbon Cloth, Adv. Energy Mater. 6 (2016) 1601116. doi:10.1002/aenm.201601116.

[120] W. Ming, H. Shi, M.H. Du, Large dielectric constant, high acceptor density, and deep electron traps in perovskite solar cell material CsGeI3, J. Mater. Chem. A. 0 (2016) 1–7. doi:10.1039/C6TA04685A.

[121] T. Oku, Y. Ohishi, A. Suzuki, Y. Miyazawa, Effects of Cl Addition to Sb-Doped Perovskite-Type CH3NH3PbI3 Photovoltaic Devices, Metals (Basel). 6 (2016) 147. doi:10.3390/met6070147.

[122] H.X. Zhu, J.-M. Liu, S. Kazim, M.K. Nazeeruddin, M. Grätzel, S. Ahmad, M.A. Loi, J.C. Hummelen, A. Kojima, K. Teshima, Y. Shirai, T. Miyasaka, H.S. Kim, J. Burschka, M.Z. Liu, M.B. Johnston, H.J. Snaith, C. Wehrenfennig, M. Liu, H.J. Snaith, M.B. Johnston, L.M. Herz, J. Feng, B. Xiao, E. Mosconi,   t A. Ama, M.K. Nazeeruddin, M. Gratzel, F.D. Angelis, G. Xing, S.D. Stranks, M. Grätzel, S. Sun, W.J. Yin, T. Shi, Y. Yan, J. Krüger, R. Plass, M. Grätzel, P. Cameron, L. Peter, B. Cai, Y. Xing, Z. Yang, W. Zhang, X. Zhu, H. Su, R.A. Marcus, M.E. Michel-Beyerle, G. Kresse, J. Hafner, G. Kresse, J. Furthmüller, L.G. Devi, B.N. Murthy, S.G. Kumar, P.E. Blöchl, H.J. Monkhorst, J.D. Pack, L.P.J. Even, J.-M. Jancu, C. Katan, E. Mosconi, A. Amat, M.K. Nazeeruddin, M. Gratzel, F.D. Angelis, Y. Kawamura, H. Mashiyama, K. Hasebe, A. Maalej, M. Khan, W.B. Cao, N. Chen, Asadullah, M. Iqbal, C.C. Parks, X. Yu, Y. Wang, F. Brivio, A.B. Walker, A. Walsh, D.B. Melrose, R.J. Stoneham, T. Baikie, W. Geng, L. Zhang, Y.N. Zhang, W.M. Lau, L.M. Liu, Electronic structure of organometal halide perovskite CH3NH3BiI3 and optical absorption extending to infrared region, Sci. Reports, Publ. Online 18 Novemb. 2016; | doi10.1038/srep37425. 6 (2016) 2812–2824. doi:10.1038/srep37425.

[123] Y. Zhou, H.F. Garces, B.S. Senturk, A.L. Ortiz, N.P. Padture, Room temperature "one-pot" solution synthesis of nanoscale CsSnI3 orthorhombic perovskite thin films and particles, Mater. Lett. 110 (2013) 127–129. doi:10.1016/j.matlet.2013.08.011.

[124] Z. Chen, C. Yu, K. Shum, J.J. Wang, W. Pfenninger, N. Vockic, J. Midgley, J.T. Kenney, Photoluminescence study of polycrystalline CsSnI3 thin films: Determination of exciton binding energy, J. Lumin. 132 (2012) 345–349. doi:10.1016/j.jlumin.2011.09.006.

[125] A.T. and L. Uzun, Long Minority-Carrier Diffusion Length and Low Surface-Recombination Velocity in Inorganic Lead-free CsSnI3 Perovskite Crystal for Solar Cells, Adv. Funct. Mater. (2015) 1–596. doi:10.1017/CBO9781107415324.004.

[126] Z. Xiao, H. Lei, X. Zhang, Y. Zhou, H. Hosono, T. Kamiya, Ligand-hole in [SnI6] unit

and origin of band gap in photovoltaic perovskite variant Cs2SnI6, Bull. Chem. Soc. Jpn. 88 (2015) 1250–1255. doi:10.1246/bcsj.20150110.

[127] A. Kaltzoglou, M. Antoniadou, A.G. Kontos, C.C. Stoumpos, D. Perganti, E. Siranidi, V. Raptis, K. Trohidou, V. Psycharis, M.G. Kanatzidis, P. Falaras, Optical-Vibrational Properties of the Cs2SnX6 (X = Cl, Br, I) Defect Perovskites and Hole-Transport Efficiency in Dye-Sensitized Solar Cells, J. Phys. Chem. C. 120 (2016) 11777–11785. doi:10.1021/acs.jpcc.6b02175.

[128] X. Qiu, B. Cao, S. Yuan, X. Chen, Z. Qiu, Y. Jiang, Q. Ye, H. Wang, H. Zeng, J. Liu, M.G. Kanatzidis, From unstable CsSnI3 to air-stable Cs2SnI6: A lead-free perovskite solar cell light absorber with bandgap of 1.48??eV and high absorption coefficient, Sol. Energy Mater. Sol. Cells. 159 (2017) 227–234. doi:10.1016/j.solmat.2016.09.022.

[129] B. Lee, C.C. Stoumpos, N. Zhou, F. Hao, C. Malliakas, C.-Y. Yeh, T.J. Marks, M.G. Kanatzidis, R.P.H. Chang, Air-Stable Molecular Semiconducting Iodosalts for Solar Cell Applications: Cs(2)SnI(6) as a Hole Conductor, J. Am. Chem. Soc. 136 (2014) 15379–15385. doi:10.1021/ja508464w.

[130] A. Wang, X. Yan, M. Zhang, S. Sun, M. Yang, W. Shen, X. Pan, P. Wang, Z. Deng, Controlled synthesis of lead-free and stable perovskite derivative Cs2SnI6 nanocrystals via a facile hot-injection process, Chem. Mater. 28 (2016) 8132–8140. doi:10.1021/acs.chemmater.6b01329.

[131] X. Qiu, Y. Jiang, H. Zhang, Z. Qiu, S. Yuan, P. Wang, B. Cao, Lead-free mesoscopic Cs 2 SnI 6 perovskite solar cells using different nanostructured ZnO nanorods as electron transport layers, Phys. Status Solidi - Rapid Res. Lett. 591 (2016) 587–591. doi:10.1002/pssr.201600166.

[132] E.J. Juarez-Perez, M. Wußler, F. Fabregat-Santiago, K. Lakus-Wollny, E. Mankel, T. Mayer, W. Jaegermann, I. Mora-Sero, Role of the selective contacts in the performance of lead halide perovskite solar cells, J. Phys. Chem. Lett. 5 (2014) 680–685. doi:10.1021/jz500059v.

[133] N.Y. Nia, F. Matteocci, L. Cina, A. Di Carlo, High-Efficiency Perovskite Solar Cell Based on Poly(3-Hexylthiophene): Influence of Molecular Weight and Mesoscopic Scaffold Layer, ChemSusChem. 10 (2017) 3854–3860. doi:10.1002/cssc.201700635.

[134] J. Kim, N. Park, J.S. Yun, S. Huang, M.A. Green, A.W.Y. Ho-Baillie, An effective method of predicting perovskite solar cell lifetime?Case study on planar CH3NH3PbI3 and HC(NH2)2PbI3 perovskite solar cells and hole transfer materials of spiro-OMeTAD and PTAA, Sol. Energy Mater. Sol. Cells. 162 (2017) 41–46. doi:10.1016/j.solmat.2016.12.043.

[135] X. Jiang, Z. Yu, Y. Zhang, J. Lai, J. Li, G.G. Gurzadyan, X. Yang, L. Sun, High-Performance Regular Perovskite Solar Cells Employing Low-Cost Poly(ethylenedioxythiophene) as a Hole-Transporting Material, Sci. Rep. 7 (2017) 1–9. doi:10.1038/srep42564.

[136]  L.-C. Chen, Z.-L. Tseng, J.-K. Huang, C.-C. Chen, S. Chang, Fullerene-Based Electron Transport Layers for Semi-Transparent MAPbBr3 Perovskite Films in Planar Perovskite Solar Cells, Coatings. 6 (2016) 53. doi:10.3390/coatings6040053.

[137]  Y. Li, D. Qi, P. Song, F. Ma, Fullerene-based photoactive layers for heterojunction solar cells: Structure, absorption spectra and charge transfer process, Materials (Basel). 8 (2015) 42–56. doi:10.3390/ma8010042.

[138]  P.M. Allemand, A. Koch, F. Wudl, Y. Rubin, F. Diederich, M.M. Alvarez, S.J. Anz, R.L. Whetten, Two Different Fullerenes Have the Same Cyclic Voltammetry, J. Am. Chem. Soc. 113 (1991) 1050–1051. doi:10.1021/ja00003a053.

[139]  Y. Shao, Z. Xiao, C. Bi, Y. Yuan, J. Huang, Origin and elimination of photocurrent hysteresis by fullerene passivation in CH3NH3PbI3 planar heterojunction solar cells, Nat. Commun. 5 (2014) 1–7. doi:10.1038/ncomms6784.

[140]  Z. Ku, Y. Rong, M. Xu, T. Liu, H. Han, Full printable processed mesoscopic CH3 NH3 PbI 3 /TiO2 heterojunction solar cells with carbon counter electrode, Sci. Rep. 3 (2013). doi:10.1038/srep03132.

[141]  H. Zhou, Y. Shi, Q. Dong, H. Zhang, Y. Xing, K. Wang, Y. Du, T. Ma, Hole-Conductor-Free, Metal-Electrode-Free TiO2/CH3NH3PbI3 Heterojunction Solar Cells Based on a Low-Temperature Carbon Electrode., J. Phys. Chem. Lett. 5 (2014) 3241–6. doi:10.1021/jz5017069.

[142]  C. Zhang, Y. Luo, X. Chen, Y. Chen, Z. Sun, S. Huang, Effective Improvement of the Photovoltaic Performance of Carbon-Based Perovskite Solar Cells by Additional Solvents, Nano-Micro Lett. 8 (2016) 347–357. doi:10.1007/s40820-016-0094-4.

[143]  F. Zhang, X. Yang, H. Wang, M. Cheng, J. Zhao, L. Sun, Structure engineering of hole-conductor free perovskite-based solar cells with low-temperature-processed commercial carbon paste as cathode, ACS Appl. Mater. Interfaces. 6 (2014) 16140–16146. doi:10.1021/am504175x.

[144]  Z. Liu, B. Sun, T. Shi, Z. Tang, G. Liao, Enhanced photovoltaic performance and stability of carbon counter electrode based perovskite solar cells encapsulated by PDMS, J. Mater. Chem. A. 4 (2016) 10700–10709. doi:10.1039/C6TA02851A.

[145]  K. Domanski, J.P. Correa-Baena, N. Mine, M.K. Nazeeruddin, A. Abate, M. Saliba, W. Tress, A. Hagfeldt, M. Grätzel, Not All That Glitters Is Gold: Metal-Migration-Induced Degradation in Perovskite Solar Cells, ACS Nano. 10 (2016) 6306–6314. doi:10.1021/acsnano.6b02613.

[146]  W.H. Nguyen, C.D. Bailie, E.L. Unger, M.D. McGehee, Enhancing the hole-conductivity of spiro-OMeTAD without oxygen or lithium salts by using spiro(TFSI)2 in perovskite and dye-sensitized solar cells, J. Am. Chem. Soc. 136 (2014) 10996–11001. doi:10.1021/ja504539w.

[147]  S. Paulo, G. Stoica, W. Cambarau, E. Martinez-Ferrero, E. Palomares, Carbon quantum dots as new hole transport material for perovskite solar cells, Synth. Met. 222

(2016) 17–22. doi:10.1016/j.synthmet.2016.04.025.

[148] F. Behrouznejad, S. Shahbazi, N. Taghavinia, H.-P. Wu, E. Wei-Guang Diau, A study on utilizing different metals as the back contact of CH 3 NH 3 PbI 3 perovskite solar cells, J. Mater. Chem. A. 4 (2016) 13488–13498. doi:10.1039/C6TA05938D.

[149] A.M. Smith, S. Nie, Semiconductor Nanocrystals: Structure, Properties, and Band Gap Engineering, Acc Chem Res. 43 (2010) 190–200. doi:10.1021/ar9001069.Semiconductor.

[150] C. De Mello Donegá, Nanoparticles: Workhorses of nanoscience, 2014. doi:10.1007/978-3-662-44823-6.

[151] S. V. Gaponenko, Introduction to Nanophotonics, Cambridge University Press, 2010. www.cambridge.org/9780521763752.

[152] T. Kippeny, L.A. Swafford, S.J. Rosenthal, Semiconductor Nanocrystals: A Powerful Visual Aid for Introducing the Particle in a Box, J. Chem. Educ. 79 (2002) 1094. doi:10.1021/ed079p1094.

[153] L. Brus, Electronic wave functions in semiconductor clusters: experiment and theory, J. Phys. Chem. 90 (1986) 2555–2560. doi:10.1021/j100403a003.

[154] D. V. Talapin, J.S. Lee, M. V. Kovalenko, E. V. Shevchenko, Prospects of colloidal nanocrystals for electronic and optoelectronic applications, Chem. Rev. 110 (2010) 389–458. doi:10.1021/cr900137k.

[155] J. Fan, P.K. Chu, Group IV nanoparticles: Synthesis, properties, and biological applications, Small. 6 (2010) 2080–2098. doi:10.1002/smll.201000543.

[156] O.I. Micic, C.J. Curtis, K.M. Jones, J.R. Sprague, A.J. Nozik, Synthesis and Characterization of InP Quantum Dots, J. Phys. Chem. 98 (1994) 4966–4969. doi:10.1021/j100070a004.

[157] R. Xie, M. Rutherford, X. Peng, Formation of High-Quality I # III # VI Semiconductor Nanocrystals by Tuning Relative Reactivity of Cationic Precursors Formation of High-Quality I - III - VI Semiconductor Nanocrystals by Tuning Relative Reactivity of Cationic Precursors, (2009) 5691–5697.

[158] W. Xiang, X. Ma, L. Luo, W. Cai, C. Xie, X. Liang, Facile synthesis and characterization of core/shell Cu-In-Zn-S/ZnS nanocrystals with high luminescence, Mater. Chem. Phys. 149 (2015) 437–444. doi:10.1016/j.matchemphys.2014.10.042.

[159] W.-C. Huang, C. Tseng, S. Chang, H. Tuan, C. Chiang, L. Lyu, M.H. Huang, Solvothermal synthesis of zincblende and wurtzite CuInS2 nanocrystals and their photovoltaic application., Langmuir. 28 (2012) 8496–501. doi:10.1021/la300742p.

[160] P.-H. Chuang, C.C. Lin, R.-S. Liu, Emission-Tunable CuInS2/ZnS Quantum Dots: Structure, Optical Properties, and Application in White Light-Emitting Diodes with High Color Rendering Index, ACS Appl. Mater. Interfaces. 6 (2014) 15379–15387. doi:10.1021/am503889z.

[161]  N. Hildebrandt, C.M. Spillmann, W.R. Algar, T. Pons, M.H. Stewart, E. Oh, K. Susumu, S.A. Díaz, J.B. Delehanty, I.L. Medintz, Energy Transfer with Semiconductor Quantum Dot Bioconjugates: A Versatile Platform for Biosensing, Energy Harvesting, and Other Developing Applications, Chem. Rev. (2016) acs.chemrev.6b00030. doi:10.1021/acs.chemrev.6b00030.

[162]  E.S. Speranskaya, N. V Beloglazova, S. Abé, T. Aubert, P. Smet, Hydrophilic , Bright CuInS 2 Quantum Dots as Cd-free Fluorescent Labels in Quantitative Immunoassay, (2014) 1–11.

[163]  M. Michalska, A. Florczak, H. Dams-Kozlowska, J. Gapinski, S. Jurga, R. Schneider, Peptide-functionalized ZCIS QDs as fluorescent nanoprobe for targeted HER2-positive breast cancer cells imaging., Acta Biomater. 35 (2016) 293–304. doi:10.1016/j.actbio.2016.02.002.

[164]  K. Yu, P. Ng, J. Ouyang, M.B. Zaman, A. Abulrob, T.N. Baral, D. Fatehi, Z.J. Jakubek, D. Kingston, X. Wu, X. Liu, C. Hebert, D.M. Leek, D.M. Whitfield, Low-Temperature approach to highly emissive copper indium sulfide colloidal nanocrystals and their bioimaging applications, ACS Appl. Mater. Interfaces. 5 (2013) 2870–2880. doi:10.1021/am302951k.

[165]  Q. Dai, X. Zhang, S. Wang, B. Huang, J. Zhang, Y. Cui, Superlattices and Microstructures Strong two-photon absorption of CuInS 2 / ZnS quantum dots with various Cu / In ratios, Superlattices Microstruct. 84 (2015) 126–131. doi:10.1016/j.spmi.2015.05.001.

[166]  J. Hua, Y. Du, Q. Wei, X. Yuan, J. Wang, J. Zhao, H. Li, Composition-dependent photoluminescence properties of CuInS2/ZnS core/shell quantum dots, Phys. B Condens. Matter. 491 (2016) 46–50. doi:10.1016/j.physb.2016.03.025.

[167]  M.G. Panthani, C.J. Stolle, D.K. Reid, D.J. Rhee, T.B. Harvey, V. a. Akhavan, Y. Yu, B. a. Korgel, CuInSe 2 Quantum Dot Solar Cells with High Open-Circuit Voltage, J. Phys. Chem. Lett. 4 (2013) 2030–2034. doi:10.1021/jz4010015.

[168]  Y. Vahidshad, S.M. Mirkazemi, M.N. Tahir, A.I. Zad, R. Ghasemzadeh, W. Tremel, Facile one-pot synthesis of polytypic (wurtzite–chalcopyrite) CuGaS2, Appl. Phys. A. 122 (2016) 187. doi:10.1007/s00339-016-9637-2.

[169]  Z. Liu, Q. Hao, R. Tang, L. Wang, K. Tang, Facile one-pot synthesis of polytypic CuGaS 2 nanoplates, Nanoscale Res. Lett. (2013) 2–7.

[170]  B. Mao, C. Chuang, C. McCleese, J. Zhu, C. Burda, Near-Infrared Emitting AgInS 2 /ZnS Nanocrystals, J. Phys. Chem. C. (2014) 140611152129000. doi:10.1021/jp500872w.

[171]  D. Deng, L. Qu, J. Zhang, Y. Ma, Y. Gu, Quaternary Zn − Ag − In − Se Quantum Dots for Biomedical Optical Imaging of RGD-Modi fi ed Micelles, (2013).

[172]  X. Kang, Y. Yang, L. Wang, S. Wei, D. Pan, Warm White Light Emitting Diodes with Gelatin-Coated AgInS 2 /ZnS Core/Shell Quantum Dots, ACS Appl. Mater. Interfaces.

7 (2015) 27713–27719. doi:10.1021/acsami.5b10870.

[173] T. Uematsu, T. Doi, T. Torimoto, S. Kuwabata, Preparation of Luminescent AgInS2-AgGaS2 solid solution nanoparticles and their optical properties, J. Phys. Chem. Lett. 1 (2010) 3283–3287. doi:10.1021/jz101295w.

[174] M. Michalska, A. Aboulaich, G. Medjahdi, R. Mahiou, S. Jurga, R. Schneider, Amine ligands control of the optical properties and the shape of thermally grown core/shell CuInS2/ZnS quantum dots, J. Alloys Compd. 645 (2015) 184–192. doi:10.1016/j.jallcom.2015.04.162.

[175] Y. Lai, Y. Li, F. Liu, Z. Zhang, Y. Liu, Characterization of CuInS<inf>2</inf> thin films prepared by one-step DC reactive sputtering, 2009 34th IEEE Photovolt. Spec. Conf. (2009) 002322–002325. doi:10.1109/PVSC.2009.5411338.

[176] N. Guezmir, J. Ouerfelli, S. Belgacem, Optical properties of sprayed CuInS2 thin layers, Mater. Chem. Phys. 96 (2006) 116–123. doi:10.1016/j.matchemphys.2005.06.059.

[177] J. Kolny-Olesiak, H. Weller, Synthesis and Application of Colloidal CuInS 2 Semiconductor Nanocrystals, ACS Appl. Mater. Interfaces. 5 (2013) 12221–12237. doi:10.1021/am404084d.

[178] B. Bin Li, Y. Xie, J. Huang, Y. Qian, Synthesis by a Solvothermal Route and Characterization of CuInSe$_{2}$ Nanowhiskers and Nanoparticles, Adv. Mater. 11 (1999) 1456–1459. doi:10.1002/(SICI)1521-4095(199912)11:17<1456::AID-ADMA1456>3.0.CO;2-3.

[179] N. Bao, X. Qiu, Y.-H. a Wang, Z. Zhou, X. Lu, C. a Grimes, A. Gupta, Facile thermolysis synthesis of CuInS(2) nanocrystals with tunable anisotropic shape and structure., Chem. Commun. (Camb). 47 (2011) 9441–9443. doi:10.1039/c1cc13314d.

[180] J.J. Nairn, P.J. Shapiro, B. Twamley, T. Pounds, R. Von Wandruszka, T. Rick Fletcher, M. Williams, C. Wang, M. Grant Norton, Preparation of ultrafine chalcopyrite nanoparticles via the photochemical decomposition of molecular single-source precursors, Nano Lett. 6 (2006) 1218–1223. doi:10.1021/nl060661f.

[181] Y. Vahidshad, R. Ghasemzadeh, A. Irajizad, S.M. Mirkazemi, C. Solvent, Synthesis and Characterization of Copper Indium Sulfide Chalcopyrite Structure with Hot Injection Method, 3 (2013) 145–154.

[182] D. Aldakov, A. Lefrancois, P. Reiss, Ternary and quaternary metal chalcogenide nanocrystals: synthesis, properties and applications, J. Mater. Chem. C. 1 (2013) 3756–3776. doi:10.1039/c3tc30273c.

[183] W.S. Song, H. Yang, Efficient white-light-emitting diodes fabricated from highly fluorescent copper indium sulfide core/shell quantum dots, Chem. Mater. 24 (2012) 1961–1967. doi:10.1021/cm300837z.

[184] J. Park, S.-W. Kim, CuInS2/ZnS core/shell quantum dots by cation exchange and their blue-shifted photoluminescence, J. Mater. Chem. 21 (2011) 3745–3750.

doi:10.1039/c0jm03194a.

[185] Y.-K. Kim, S.-H. Ahn, K. Chung, Y.-S. Cho, C.-J. Choi, The photoluminescence of CuInS2 nanocrystals: effect of non-stoichiometry and surface modification, J. Mater. Chem. 22 (2012) 1516. doi:10.1039/c1jm13170b.

[186] L. Li, A. Pandey, D.J. Werder, B.P. Khanal, J.M. Pietryga, V.I. Klimov, Efficient synthesis of highly luminescent copper indium sulfide-based core/shell nanocrystals with surprisingly long-lived emission, J. Am. Chem. Soc. 133 (2011) 1176–1179. doi:10.1021/ja108261h.

[187] S.H. Lee, B.H. Kim, H. Bin Na, T. Hyeon, Paramagnetic inorganic nanoparticles as T1 MRI contrast agents, Wiley Interdiscip. Rev. Nanomedicine Nanobiotechnology. 6 (2014) 196–209. doi:10.1002/wnan.1243.

[188] F. Hu, H.M. Joshi, V.P. Dravid, T.J. Meade, High-performance nanostructured MR contrast probes., Nanoscale. 2 (2010) 1884–91. doi:10.1039/c0nr00173b.

[189] L.M. Manus, D.J. Mastarone, E.A. Waters, X.Q. Zhang, E.A. Schultz-Sikma, K.W. MacRenaris, D. Ho, T.J. Meade, Gd(III)-nanodiamond conjugates for MRI contrast enhancement, Nano Lett. 10 (2010) 484–489. doi:10.1021/nl903264h.

[190] F. Carniato, L. Tei, W. Dastrù, L. Marchese, M. Botta, Relaxivity modulation in Gd-functionalised mesoporous silicas., Chem. Commun. (Camb). 15 (2009) 1246–8. doi:10.1039/b820591d.

[191] J. Xie, K. Chen, J. Huang, S. Lee, J. Wang, J. Gao, X. Li, X. Chen, PET/NIRF/MRI triple functional iron oxide nanoparticles, Biomaterials. 31 (2010) 3016–3022. doi:10.1016/j.biomaterials.2010.01.010.

[192] W. Guo, W. Yang, Y. Wang, X. Sun, Z. Liu, B. Zhang, J. Chang, X. Chen, Color-tunable Gd-Zn-Cu-In-S/ZnS quantum dots for dual modality magnetic resonance and fluorescence imaging, Nano Res. 7 (2014) 1581–1591. doi:10.1007/s12274-014-0518-8.

[193] J. Yao, B.W. Rudyk, C.D. Brunetta, K.B. Knorr, H.A. Figore, A. Mar, J.A. Aitken, Mn incorporation in CuInS 2 chalcopyrites: Structure, magnetism and optical properties, Mater. Chem. Phys. 136 (2012) 415–423. doi:10.1016/j.matchemphys.2012.06.066.

[194] J. Hua, Y. Zhang, X. Yuan, H. Cheng, X. Meng, J. Zhao, H. Li, Photoluminescence properties of Cu-Mn-In-S/ZnS core/shell quantum dots, Superlattices Microstruct. 73 (2014) 214–223. doi:10.1016/j.spmi.2014.05.027.

[195] K. Ding, L. Jing, C. Liu, Y. Hou, M. Gao, Magnetically engineered Cd-free quantum dots as dual-modality probes for fluorescence/magnetic resonance imaging of tumors, Biomaterials. 35 (2014) 1608–1617. doi:10.1016/j.biomaterials.2013.10.078.

[196] S. Cao, C. Li, L. Wang, M. Shang, G. Wei, J. Zheng, W. Yang, Long-lived and well-resolved $Mn^{2+}$ ion emissions in CuInS-ZnS quantum dots., Sci. Rep. 4 (2014) 7510. doi:10.1038/srep07510.

[197] J.W. Hamilton, R.C. Kaltreider, O. V. Bajenova, M.A. Ihnat, J. McCaffrey, B.W. Turpie, E.E. Rowell, J. Oh, M.J. Nemeth, C.A. Pesce, J.P. Lariviere, Molecular basis for effects of carcinogenic heavy metals on inducible gene expression, Environ. Health Perspect. 106 (1998) 1005–1015. doi:10.1289/ehp.98106s41005.

[198] T. Partanen, P. Heikkila, S. Hernberg, T. Kauppinen, G. Moneta, A. Ojajarvi, Renal cell cancer and occupational exposure to chemical agents., Scand. J. Work. Environ. Health. 17 (1991) 231–239. doi:10.5271/sjweh.1708.

[199] S. Lutsenko, Human copper homeostasis: a network of interconnected pathways, Curr. Opin. Chem. Biol. 14 (2010) 211–217. doi:10.1016/j.cbpa.2010.01.003.

[200] S. Puig, D.J. Thiele, Molecular mechanisms of copper uptake and distribution, Curr. Opin. Chem. Biol. 6 (2002) 171–180. doi:10.1016/S1367-5931(02)00298-3.

[201] B. Halliwell, J.M.C. Gutteridget, Oxygen toxicity, oxygen radicals, transition metals and disease, Biochem. J. 219 (1984) 1–14. doi:10.1016/j.siny.2010.04.003.

[202] E. J., E. M., B. F., Neurodegenerative diseases and oxidative stress, Biomed. Pharmacother. 58 (2004) 39–46. doi:10.1016/j.biopha.2003.11.004.

[203] J.C. Lee, H.B. Gray, J.R. Winkler, Copper ( II ) Binding to r -Synuclein , the Parkinson ' s Protein, (2008) 6898–6899.

[204] J. Liu, Y. Lu, A DNAzyme Catalytic Beacon Sensor for Paramagnetic Cu 2+ Ions in Aqueous Solution with High Sensitivity and Selectivity, J. Am. Chem. Soc. 129 (2007) 9838–9839. doi:10.1021/ja0717358.

[205] S. Khatua, S.H. Choi, J. Lee, J.O. Huh, Y. Do, D.G. Churchill, Highly Selective Fluorescence Detection of Cu 2 + in Water by Chiral Dimeric Zn 2 + Complexes through Direct Displacement, Communication. 48 (2009) 1799–1801. doi:10.1021/ic802314u.

[206] Y. Zhou, F. Wang, Y. Kim, S.J. Kim, J. Yoon, Cu2+-selective ratiometric and "off-on" sensor based on the rhodamine derivative bearing pyrene group, Org. Lett. 11 (2009) 4442–4445. doi:10.1021/ol901804n.

[207] W. Lin, L. Yuan, W. Tan, J. Feng, L. Long, Construction of fluorescent probes via protection/deprotection of functional groups: A ratiometric fluorescent probe for Cu2+, Chem. - A Eur. J. 15 (2009) 1030–1035. doi:10.1002/chem.200801501.

[208] R. Elghanian, Selective Colorimetric Detection of Polynucleotides Based on the Distance-Dependent Optical Properties of Gold Nanoparticles, Science (80-. ). 277 (2007) 1078–1081. doi:10.1126/science.277.5329.1078.

[209] Y. Kim, R.C. Johnson, J.T. Hupp, Gold Nanoparticle-Based Sensing of Spectroscopically Silent Heavy Metal Ions, Nano Lett. 1 (2001) 165–167. doi:10.1021/nl0100116.

[210] C.C. Huang, Z. Yang, K.H. Lee, H.T. Chang, Synthesis of highly fluorescent gold nanoparticles for sensing mercury(II), Angew. Chemie - Int. Ed. 46 (2007) 6824–6828.

doi:10.1002/anie.200700803.

[211] Y. Zhou, H. Zhao, Y. He, N. Ding, Q. Cao, Colorimetric detection of Cu2+ using 4-mercaptobenzoic acid modified silver nanoparticles, Colloids Surfaces A Physicochem. Eng. Asp. 391 (2011) 179–183. doi:10.1016/j.colsurfa.2011.07.026.

[212] F. Yang, Q. Ma, W. Yu, X. Su, Naked-eye colorimetric analysis of Hg2+ with bi-color CdTe quantum dots multilayer films, Talanta. 84 (2011) 411–415. doi:10.1016/j.talanta.2011.01.054.

[213] H.Y. Xie, J.G. Liang, Z.L. Zhang, Y. Liu, Z.K. He, D.W. Pang, Luminescent CdSe-ZnS quantum dots as selective Cu2+ probe, Spectrochim. Acta - Part A Mol. Biomol. Spectrosc. 60 (2004) 2527–2530. doi:10.1016/j.saa.2003.12.039.

[214] H. Xu, R. Miao, Z. Fang, X. Zhong, Quantum dot-based turn-on fluorescent probe for detection of zinc and cadmium ions in aqueous media, Anal. Chim. Acta. 687 (2011) 82–88. doi:10.1016/j.aca.2010.12.002.

[215] K.M. Gattás-Asfura, R.M. Leblanc, Peptide-coated CdS quantum dots for the optical detection of copper(II) and silver(I)., Chem. Commun. 2003 (2003) 2684–5. doi:10.1039/b308991f.

[216] M.T. Fernández-Argüelles, J.J. Wei, J.M. Costa-Fernández, R. Pereiro, A. Sanz-Medel, Surface-modified CdSe quantum dots for the sensitive and selective determination of Cu(II) in aqueous solutions by luminescent measurements, Anal. Chim. Acta. 549 (2005) 20–25. doi:10.1016/j.aca.2005.06.013.

[217] R. Freeman, T. Finder, I. Willner, Multiplexed analysis of Hg2+ and Ag+ ions by nucleic acid functionalized CdSe/ZnS quantum dots and their use for logic gate operations, Angew. Chemie - Int. Ed. 48 (2009) 7818–7821. doi:10.1002/anie.200902395.

[218] H. Li, Y. Zhang, X. Wang, l-Carnitine capped quantum dots as luminescent probes for cadmium ions, Sensors Actuators, B Chem. 127 (2007) 593–597. doi:10.1016/j.snb.2007.05.013.

[219] Y.-H. Chan, Y. Jin, C. Wu, D.T. Chiu, Copper(II) and iron(II) ion sensing with semiconducting polymer dots., Chem. Commun. (Camb). 47 (2011) 2820–2822. doi:10.1039/c0cc04929h.

[220] W.C.W. Chan, D.J. Maxwell, X. Gao, R.E. Bailey, M. Han, S. Nie, Luminescent quantum dots for multiplexed biological detection and imaging, Curr. Opin. Biotechnol. 13 (2002) 40–46. doi:10.1016/S0958-1669(02)00282-3.

[221] C.-A.J. Lin, T. Liedl, R.A. Sperling, M.T. Fernández-Argüelles, J.M. Costa-Fernández, R. Pereiro, A. Sanz-Medel, W.H. Chang, W.J. Parak, Bioanalytics and biolabeling with semiconductor nanoparticles (quantum dots), J. Mater. Chem. 17 (2007) 1343–1346. doi:10.1039/B618902D.

[222] M. Han, X. Gao, J.Z. Su, S. Nie, Quantum-dot-tagged microbeads for multiplexed optical coding of biomolecules., Nat. Biotechnol. 19 (2001) 631–635.

doi:10.1038/90228.

[223]  S. Patra, K. Santhosh, A. Pabbathi, A. Samanta, Diffusion of organic dyes in bovine serum albumin solution studied by fluorescence correlation spectroscopy, RSC Adv. 2 (2012) 6079. doi:10.1039/c2ra20633a.

[224]  S. Chinnathambi, S. Karthikeyan, D. Velmurugan, N. Hanagata, P. Aruna, S. Ganesan, Effect of Moderate UVC Irradiation on Bovine Serum Albumin and Complex with Antimetabolite 5-Fluorouracil: Fluorescence Spectroscopic and Molecular Modelling Studies, Int. J. Spectrocopy. 2015 (2015) 1–12. doi:10.1155/2015/315764.

[225]  B. Zhang, Q. Li, P. Yin, Y. Rui, Y. Qiu, Y. Wang, D. Shi, Ultrasound-triggered BSA/SPION hybrid nanoclusters for liver-specific magnetic resonance imaging, ACS Appl. Mater. Interfaces. 4 (2012) 6479–6486. doi:10.1021/am301301f.

[226]  B. Zhang, X. Wang, F. Liu, Y. Cheng, D. Shi, Effective reduction of nonspecific binding by surface engineering of quantum dots with bovine serum albumin for cell-targeted imaging, Langmuir. 28 (2012) 16605–16613. doi:10.1021/la302758g.

[227]  A. Pein, M. Baghbanzadeh, T. Rath, W. Haas, E. Maier, H. Amenitsch, F. Hofer, C.O. Kappe, G. Trimmel, Investigation of the formation of CuInS2 nanoparticles by the oleylamine route: Comparison of microwave-assisted and conventional syntheses, Inorg. Chem. 50 (2011) 193–200. doi:10.1021/ic101651p.

[228]  H. Zhong, S.S. Lo, T. Mirkovic, Y. Li, Y. Ding, Y. Li, G.D. Scholes, Noninjection gram-scale synthesis of monodisperse pyramidal CuInS 2 nanocrystals and their size-dependent properties, ACS Nano. 4 (2010) 5253–5262. doi:10.1021/nn1015538.

[229]  M. Heilemann, D.P. Herten, R. Heintzmann, C. Cremer, C. Müller, P. Tinnefeld, K.D. Weston, J. Wolfrum, M. Sauer, High-resolution colocalization of single dye molecules by fluorescence lifetime imaging microscopy, Anal. Chem. 74 (2002) 3511–3517. doi:10.1021/ac025576g.

[230]  J.-P. Knemeyer, N. Marmé, J.D. Hoheisel, Spectrally resolved fluorescence lifetime imaging microscopy (SFLIM)--an appropriate method for imaging single molecules in living cells., Anal. Bioanal. Chem. 387 (2007) 37–40. doi:10.1007/s00216-006-0762-1.

[231]  B. Zhang, Y. Wang, C. Yang, S. Hu, Y. Gao, Y. Zhang, Y. Wang, H.V. Demir, L. Liu, K.-T. Yong, The composition effect on the optical properties of aqueous synthesized Cu–In–S and Zn–Cu–In–S quantum dot nanocrystals, Phys. Chem. Chem. Phys. 17 (2015) 25133–25141. doi:10.1039/C5CP03312H.

[232]  J. Zhang, G. Hao, C. Yao, S. Hu, C. Hu, B. Zhang, Paramagnetic albumin decorated CuInS 2 /ZnS QDs for CD133 + glioma bimodal MR/fluorescence targeted imaging, J. Mater. Chem. B. 4 (2016) 4110–4118. doi:10.1039/C6TB00834H.

[233]  B.H. Kim, N. Lee, H. Kim, K. An, Y. Il Park, Y. Choi, K. Shin, Y. Lee, S.G. Kwon, H. Bin Na, J.-G. Park, T.-Y. Ahn, Y.-W. Kim, W.K. Moon, S.H. Choi, T. Hyeon, Large-scale synthesis of uniform and extremely small-sized iron oxide nanoparticles for high-resolution T1 magnetic resonance imaging contrast agents., J. Am. Chem. Soc.

133 (2011) 12624–12631. doi:10.1021/ja203340u.

[234] R. Di Corato, F. Gazeau, C. Le Visage, D. Fayol, P. Levitz, F. Lux, D. Letourneur, N. Luciani, O. Tillement, C. Wilhelm, High-resolution cellular MRI: Gadolinium and iron oxide nanoparticles for in-depth dual-cell imaging of engineered tissue constructs, ACS Nano. 7 (2013) 7500–7512. doi:10.1021/nn401095p.

[235] E. Kim, S.B. Park, Chemistry as a prism: A review of light-emitting materials having tunable emission wavelengths, Chem. - An Asian J. 4 (2009) 1646–1658. doi:10.1002/asia.200900102.

[236] S. Hirata, T. Watanabe, Reversible Thermoresponsive Recording of Fluorescent Images (TRF), Adv. Mater. 18 (2006) 2725–2729. doi:10.1002/adma.200600209.

[237] B. Huitorel, Q. Benito, A. Fargues, A. Garcia, T. Gacoin, J.P. Boilot, S. Perruchas, F. Camerel, Mechanochromic luminescence and liquid crystallinity of molecular copper clusters, Chem. Mater. 28 (2016) 8190–8200. doi:10.1021/acs.chemmater.6b03002.

[238] K. Yang, S.L. Li, F.Q. Zhang, X.M. Zhang, Simultaneous Luminescent Thermochromism, Vapochromism, Solvatochromism, and Mechanochromism in a C3-Symmetric Cubane [Cu4I4P4] Cluster without Cu-Cu Interaction, Inorg. Chem. 55 (2016) 7323–7325. doi:10.1021/acs.inorgchem.6b00922.

[239] M. Kinami, B.R. Crenshaw, C. Weder, Polyesters with built-in threshold temperature and deformation sensors, Chem. Mater. 18 (2006) 946–955. doi:10.1021/cm052186c.

[240] K. Ariga, T. Mori, J.P. Hill, Mechanical control of nanomaterials and nanosystems, Adv. Mater. 24 (2012) 158–176. doi:10.1002/adma.201102617.

[241] D.O. Olawale, K. Kliewer, A. Okoye, T. Dickens, M.J. Uddin, O.I. Okoli, Getting light through cementitious composites with in situ triboluminescent damage sensor, Struct. Heal. Monit. 13 (2013) 177–189. doi:10.1177/1475921713513976.

[242] A.L. Balch, Dynamic crystals: Visually detected mechanochemical changes in the luminescence of gold and other transition-metal complexes, Angew. Chemie - Int. Ed. 48 (2009) 2641–2644. doi:10.1002/anie.200805602.

[243] D.R.T. Roberts, S.J. Holder, Mechanochromic systems for the detection of stress, strain and deformation in polymeric materials, J. Mater. Chem. 21 (2011) 8256. doi:10.1039/c0jm04237d.

[244] X. Zhang, Z. Ma, M. Liu, X. Zhang, X. Jia, Y. Wei, A new organic far-red mechanofluorochromic compound derived from cyano-substituted diarylethene, Tetrahedron. 69 (2013) 10552–10557. doi:10.1016/j.tet.2013.10.066.

[245] X. Zhang, Z. Chi, Y. Zhang, S. Liu, J. Xu, Recent advances in mechanochromic luminescent metal complexes, J. Mater. Chem. C. 1 (2013) 3376. doi:10.1039/c3tc30316k.

[246] C. Yue, C. Yan, R. Feng, M. Wu, L. Chen, F. Jiang, M. Hong, A polynuclear d10-d10 metal complex with unusual near-infrared luminescence and high thermal stability,

Inorg. Chem. 48 (2009) 2873–2879. doi:10.1021/ic801840g.

[247] T.K. Sau, A.L. Rogach, Nonspherical noble metal nanoparticles: Colloid-chemical synthesis and morphology control, Adv. Mater. 22 (2010) 1781–1804. doi:10.1002/adma.200901271.

[248] C.M. Cobley, J. Chen, E.C. Cho, L. V Wang, Y. Xia, Gold nanostructures: a class of multifunctional materials for biomedical applications, Chem. Soc. Rev. Chem. Soc. Rev. 40 (2011) 44–56. doi:10.1039/b821763g.

[249] C. Helmbrecht, D. Lützenkirchen-Hecht, W. Frank, Microwave-assisted synthesis of water-soluble, fluorescent gold nanoclusters capped with small organic molecules and a revealing fluorescence and X-ray absorption study, Nanoscale. 7 (2015) 4978–4983. doi:10.1039/C4NR07051H.

[250] F. Cao, E. Ju, C. Liu, F. Pu, J. Ren, X. Qu, Coupling a DNA–ligand ensemble with Ag cluster formation for the label-free and ratiometric detection of intracellular biothiols, Chem. Commun. 52 (2016) 5167–5170. doi:10.1039/C5CC10606K.

[251] H. Li, J. Chen, H. Huang, J.J. Feng, A.J. Wang, L.X. Shao, Green and facile synthesis of l-carnosine protected fluorescent gold nanoclusters for cellular imaging, Sensors Actuators, B Chem. 223 (2016) 40–44. doi:10.1016/j.snb.2015.09.052.

[252] H. Wei, Z. Wang, L. Yang, S. Tian, C. Hou, Y. Lu, Lysozyme-stabilized gold fluorescent cluster: Synthesis and application as Hg(2+) sensor., Analyst. 135 (2010) 1406–10. doi:10.1039/c0an00046a.

[253] J. Xie, Y. Zheng, J.Y. Ying, Protein-directed synthesis of highly fluorescent gold nanoclusters., J. Am. Chem. Soc. 131 (2009) 888–9. doi:10.1021/ja806804u.

[254] H. Qian, M. Zhu, Z. Wu, R. Jin, Quantum sized gold nanoclusters with atomic precision, Acc. Chem. Res. 45 (2012) 1470–1479. doi:10.1021/ar200331z.

[255] D.R. Kauffman, D. Alfonso, C. Matranga, H. Qian, R. Jin, Experimental and computational investigation of Au25 clusters and CO2: a unique interaction and enhanced electrocatalytic activity., J. Am. Chem. Soc. 134 (2012) 10237–43. doi:10.1021/ja303259q.

[256] J. Zheng, P.R. Nicovich, R.M. Dickson, Highly fluorescent noble-metal quantum dots., Annu. Rev. Phys. Chem. 58 (2007) 409–431. doi:10.1146/annurev.physchem.58.032806.104546.

[257] B. Han, E. Wang, DNA-templated fluorescent silver nanoclusters, Anal. Bioanal. Chem. 402 (2012) 129–138. doi:10.1007/s00216-011-5307-6.

[258] W. Wei, Y. Lu, W. Chen, S. Chen, One-pot synthesis, photoluminescence, and electrocatalytic properties of subnanometer-sized copper clusters, J. Am. Chem. Soc. 133 (2011) 2060–2063. doi:10.1021/ja109303z.

[259] J. He, J.X. Zhang, C.K. Tsang, Z. Xu, Y.G. Yin, D. Li, S.W. Ng, Mixed-valence CuIICuI15I17 cluster builds up a 3D metal-organic framework with paramagnetic and

thermochromic characteristics, Inorg. Chem. 47 (2008) 7948–7950. doi:10.1021/ic8009207.

[260]  Q. Benito, X.F. Le Goff, S. Maron, A. Fargues, A. Garcia, C. Martineau, F. Taulelle, S. Kahlal, T. Gacoin, J.P. Boilot, S. Perruchas, Polymorphic copper iodide clusters: Insights into the mechanochromic luminescence properties, J. Am. Chem. Soc. 136 (2014) 11311–11320. doi:10.1021/ja500247b.

[261]  X. Liu, K.L. Huang, A 12-connected dodecanuclear copper cluster with yellow luminescence, Inorg. Chem. 48 (2009) 8653–8655. doi:10.1021/ic900611u.

[262]  X.M. Zhang, R.Q. Fang, H.S. Wu, A twelve-connected Cu6S4 cluster-based coordination polymer, J. Am. Chem. Soc. 127 (2005) 7670–7671. doi:10.1021/ja050284t.

[263]  Z. Wu, Y. Li, J. Liu, Z. Lu, H. Zhang, B. Yang, Colloidal Self-Assembly of Catalytic Copper Nanoclusters into Ultrathin Ribbons, Angew. Chemie - Int. Ed. 53 (2014) 12196–12200. doi:10.1002/anie.201407390.

[264]  Z. Wu, C. Dong, Y. Li, H. Hao, H. Zhang, Z. Lu, B. Yang, Self-assembly of Au15 into single-cluster-thick sheets at the interface of two miscible high-boiling solvents, Angew. Chemie - Int. Ed. 52 (2013) 9952–9955. doi:10.1002/anie.201304122.

[265]  Z. Wu, J. Liu, Y. Gao, H. Liu, T. Li, H. Zou, Z. Wang, K. Zhang, Y. Wang, H. Zhang, B. Yang, Assembly-Induced Enhancement of Cu Nanoclusters Luminescence with Mechanochromic Property, J. Am. Chem. Soc. 137 (2015) 12906–12913. doi:10.1021/jacs.5b06550.

[266]  J. Mei, Y. Hong, J.W.Y. Lam, A. Qin, Y. Tang, B.Z. Tang, Aggregation-induced emission: The whole is more brilliant than the parts, Adv. Mater. 26 (2014) 5429–5479. doi:10.1002/adma.201401356.

[267]  Z. Luo, X. Yuan, Y. Yu, Q. Zhang, D.T. Leong, J.Y. Lee, J. Xie, From aggregation-induced emission of Au(I)-thiolate complexes to ultrabright Au(0)@Au(I)-thiolate core-shell nanoclusters, J. Am. Chem. Soc. 134 (2012) 16662–16670. doi:10.1021/ja306199p.

[268]  Z. Wu, R. Jin, On the ligand's role in the fluorescence of gold nanoclusters, Nano Lett. 10 (2010) 2568–2573. doi:10.1021/nl101225f.

[269]  Z.H. Qing, X.X. He, T.P. Qing, K.M. Wang, H. Shi, D.G. He, Z. Zou, L. Yan, F.Z. Xu, X.S. Ye, Z.G. Mao, Poly(Thymine)-Templated Fluorescent Copper Nanoparticles for Ultrasensitive Label-Free Nuclease Assay and Its Inhibitors Screening, Anal. Chem. 85 (2013) 12138–12143. doi:10.1021/ac403354c.

[270]  Y. Chen, T. Yang, H. Pan, Y. Yuan, L. Chen, M. Liu, K. Zhang, S. Zhang, P. Wu, J. Xu, Photoemission mechanism of water-soluble silver nanoclusters: Ligand-to-metal-metal charge transfer vs strong coupling between surface plasmon and emitters, J. Am. Chem. Soc. 136 (2014) 1686–1689. doi:10.1021/ja407911b.

[271] X. Jia, J. Li, E. Wang, Cu nanoclusters with aggregation induced emission enhancement, Small. 9 (2013) 3873–3879. doi:10.1002/smll.201300896.

[272] K.J. Si, D. Sikdar, Y. Chen, F. Eftekhari, Z. Xu, Y. Tang, W. Xiong, P. Guo, S. Zhang, Y. Lu, Q. Bao, W. Zhu, M. Premaratne, W. Cheng, Giant plasmene nanosheets, nanoribbons, and origami, ACS Nano. 8 (2014) 11086–11093. doi:10.1021/nn504615a.

[273] Z. Tang, Z. Zhang, Y. Wang, S.C. Glotzer, N.A. Kotov, Self-Assembly of CdTe Nanocrystals into Free-Floating Sheets, Science (80-. ). 314 (2006) 274–278. doi:10.1126/science.1128045.

[274] W.M. Park, J.A. Champion, Colloidal Assembly of Hierarchically Structured Porous Supraparticles from Flower-Shaped Protein-Inorganic Hybrid Nanoparticles, ACS Nano. 10 (2016) 8271–8280. doi:10.1021/acsnano.6b01003.

[275] S. Wang, Y. Kang, L. Wang, H. Zhang, Y. Wang, Y. Wang, Organic/inorganic hybrid sensors: A review, Sensors Actuators, B Chem. 182 (2013) 467–481. doi:10.1016/j.snb.2013.03.042.

[276] Z. Liu, X. Yang, L. Huo, X. Tian, T. Qi, F. Yang, X. Wang, K. Yu, F. Ma, J. Sun, P-CuPcTS/n-SnO2organic-inorganic hybrid film for ppb-level NO2gas sensing at low operating temperature, Sensors Actuators, B Chem. 248 (2017) 324–331. doi:10.1016/j.snb.2017.04.003.

[277] P.C. Lebaron, Z. Wang, T.J. Pinnavaia, Polymer-layered silicate nanocomposites: An overview, Appl. Clay Sci. 15 (1999) 11–29. doi:10.1016/S0169-1317(99)00017-4.

[278] D.S. Lawrence, T. Jiang, M. Levett, Self-Assembling Supramolecular Complexes, Chem. Rev. 95 (1995) 2229–2260. doi:10.1021/cr00038a018.

[279] Q. Evrard, C. Leuvrey, P. Farger, E. Delahaye, P. Rabu, G. Taupier, K.D. Dorkenoo, J.-M. Rueff, N. Barrier, O. Pérez, G. Rogez, Noncentrosymmetric Cu(II) Layered Hydroxide: Synthesis, Crystal Structure, Nonlinear Optical, and Magnetic Properties of Cu 2 (OH) 3 (C 12 H 25 SO 4 ), Cryst. Growth Des. (2018) acs.cgd.7b01692. doi:10.1021/acs.cgd.7b01692.

[280] W. Michaeli, T.G. Pfefferkorn, Electrically conductive thermoplastic/metal hybrid materials for direct manufacturing of electronic components, Polym. Eng. Sci. 49 (2009) 1511–1524. doi:10.1002/pen.21374.

[281] J. Choy, High-Tc Superconductors in the Two-Dimensional Limit: [(Py-CnH2n+1)2HgI4]-Bi2Sr2Cam1CumOy (m&amp;nbsp;=&amp;nbsp;1&amp;nbsp;and 2), Science (80-. ). 280 (1998) 1589–1592. doi:10.1126/science.280.5369.1589.

[282] Y. Murashima, R. Ohtani, T. Matsui, H. Takehira, R. Yokota, M. Nakamura, L.F. Lindoy, S. Hayami, Coexistence of electrical conductivity and ferromagnetism in a hybrid material formed from reduced graphene oxide and manganese oxide., Dalton Trans. 44 (2015) 5049–52. doi:10.1039/c5dt00299k.

[283] J. Demel, P. Kubát, I. Jirka, P. Kovář, M. Pospíšil, K. Lang, Inorganic-organic hybrid materials: Layered zinc hydroxide salts with intercalated porphyrin sensitizers, J. Phys. Chem. C. 114 (2010) 16321–16328. doi:10.1021/jp106116n.

[284] I.G. Dance, K.J. Fisher, R.M.H. Banda, M.L. Scudder, Layered Structure of Crystalline Compounds AgSR, Inorg. Chem. 30 (1991) 183–187. doi:10.1021/ic00002a008.

[285] A.N. Parikh, S.D. Gillmor, J.D. Beers, K.M. Beardmore, R.W. Cutts, B.I. Swanson, Characterization of Chain Molecular Assemblies in Long-Chain, Layered Silver Thiolates: A Joint Infrared Spectroscopy and X-ray Diffraction Study, J. Phys. Chem. B. 103 (1999) 2850–2861. doi:10.1021/jp983938b.

[286] N. Sandhyarani, T. Pradeep, An investigation of the structure and properties of layered copper thiolates, J. Mater. Chem. 11 (2001) 1294–1299. doi:10.1039/b009837j.

[287] J.C. Love, L.A. Estroff, J.K. Kriebel, R.G. Nuzzo, G.M. Whitesides, Self-assembled monolayers of thiolates on metals as a form of nanotechnology, 2005. doi:10.1021/cr0300789.

[288] F. Bensebaa, T.H. Ellis, E. Kruus, R. Voicu, Y. Zhou, Characterization of Self-Assembled Bilayers: Silver−Alkanethiolates, Langmuir. 14 (1998) 6579–6587. doi:10.1021/la980718g.

[289] R.A. MacPhail, H.L. Strauss, R.G. Snyder, C.A. Elliger, Carbon-hydrogen stretching modes and the structure of n-alkyl chains. 2. Long, all-trans chains, J. Phys. Chem. 88 (1984) 334–341. doi:10.1021/j150647a002.

[290] M. Cai, J.E. Pemberton, Vibrational spectroscopy of dimethylchlorooctadecylsilane covalently bonded to ultrathin silica films immobilized on Ag surfaces., Fresenius. J. Anal. Chem. 369 (2001) 328–34. doi:10.1007/s002160000670.

[291] E.M. Kirby, M.J. Evans-Vader, M.A. Brown, Determination of the length of polymethylene chains in salts of saturated and unsaturated fatty acids by infrared spectroscopy, J. Am. Oil Chem. Soc. 42 (1965) 437–446. doi:10.1007/BF02635587.

[292] Z. Wu, J. Liu, Y. Li, Z. Cheng, T. Li, H. Zhang, Z. Lu, B. Yang, Self-Assembly of Nanoclusters into Mono-, Few-, and Multilayered Sheets via Dipole-Induced Asymmetric van der Waals Attraction, ACS Nano. 9 (2015) 6315–6323. doi:10.1021/acsnano.5b01823.

[293] P. Duan, N. Yanai, Y. Kurashige, N. Kimizuka, Aggregation-induced photon upconversion through control of the triplet energy landscapes of the solution and solid states, Angew. Chemie - Int. Ed. 54 (2015) 7544–7549. doi:10.1002/anie.201501449.

[294] Q. Benito, B. Baptiste, A. Polian, L. Delbes, L. Martinelli, T. Gacoin, J.P. Boilot, S. Perruchas, Pressure Control of Cuprophilic Interactions in a Luminescent Mechanochromic Copper Cluster, Inorg. Chem. 54 (2015) 9821–9825. doi:10.1021/acs.inorgchem.5b01546.

[295] V.W.-W. Yam, K.K.-W. Lo, Luminescent polynuclear d10 metal complexes, Chem. Soc.

Rev. 28 (1999) 323–334. doi:10.1039/a804249g.

[296] V.W.-W. Yam, Molecular design of luminescent metal-based materials, Pure Appl. Chem. 73 (2001) 543–548. doi:10.1351/pac200173030543.

[297] Y. Yuan, C.J. Zhang, M. Gao, R. Zhang, B.Z. Tang, B. Liu, Specific light-up bioprobe with aggregation-induced emission and activatable photoactivity for the targeted and image-guided photodynamic ablation of cancer cells, Angew. Chemie - Int. Ed. 54 (2015) 1780–1786. doi:10.1002/anie.201408476.

[298] Y. Sagara, C. Weder, N. Tamaoki, Tuning the thermo- and mechanoresponsive behavior of luminescent cyclophanes, RSC Adv. 6 (2016) 80408–80414. doi:10.1039/C6RA18348D.

[299] M. Krikorian, S. Liu, T.M. Swager, Columnar liquid crystallinity and mechanochromism in cationic platinum(II) complexes, J. Am. Chem. Soc. 136 (2014) 2952–2955. doi:10.1021/ja4114352.

[300] E. Carrasco, B. Del Rosal, F. Sanz-Rodríguez, Á.J. De La Fuente, P.H. Gonzalez, U. Rocha, K.U. Kumar, C. Jacinto, J.G. Solé, D. Jaque, Intratumoral thermal reading during photo-thermal therapy by multifunctional fluorescent nanoparticles, Adv. Funct. Mater. 25 (2015) 615–626. doi:10.1002/adfm.201403653.

[301] E.N. Cerõn, D.H. Ortgies, B. Del Rosal, F. Ren, A. Benayas, F. Vetrone, D. Ma, F. Sanz-Rodríguez, J.G. Solé, D. Jaque, E.M. Rodríguez, Hybrid Nanostructures for High-Sensitivity Luminescence Nanothermometry in the Second Biological Window, Adv. Mater. 27 (2015) 4781–4787. doi:10.1002/adma.201501014.

[302] S.A. Wade, S.F. Collins, G.W. Baxter, Fluorescence intensity ratio technique for optical fiber point temperature sensing, J. Appl. Phys. 94 (2003) 4743–4756. doi:10.1063/1.1606526.

[303] P. Cortelletti, C. Facciotti, I.X. Cantarelli, P. Canton, M. Quintanilla, F. Vetrone, A. Speghini, M. Pedroni, Nd3+ activated CaF2 NPs as colloidal nanothermometers in the biological window, Opt. Mater. (Amst). (2016). doi:10.1016/j.optmat.2016.11.019.

[304] J.O. Escobedo, O. Rusin, S. Lim, R.M. Strongin, NIR dyes for bioimaging applications, Curr. Opin. Chem. Biol. 14 (2010) 64–70. doi:10.1016/j.cbpa.2009.10.022.

[305] S. Jin, Y. Hu, Z. Gu, L. Liu, H.-C. Wu, Application of Quantum Dots in Biological Imaging, J. Nanomater. 2011 (2011) 1–13. doi:10.1155/2011/834139.

[306] S.A. Hilderbrand, R. Weissleder, Near-infrared fluorescence: application to in vivo molecular imaging, Curr. Opin. Chem. Biol. 14 (2010) 71–79. doi:10.1016/j.cbpa.2009.09.029.

[307] S.F. Lim, R. Riehn, C.K. Tung, W.S. Ryu, R. Zhuo, J. Dalland, R.H. Austin, Upconverting nanophosphors for bioimaging, Nanotechnology. 20 (2009). doi:10.1088/0957-4484/20/40/405701.

[308] J. Shen, L. Zhao, G. Han, Lanthanide-doped upconverting luminescent nanoparticle

platforms for optical imaging-guided drug delivery and therapy, Adv. Drug Deliv. Rev. 65 (2013) 744–755. doi:10.1016/j.addr.2012.05.007.

[309]   L. Shi, L.A. Sordillo, A. Rodríguez-Contreras, R. Alfano, Transmission in near-infrared optical windows for deep brain imaging, J. Biophotonics. 9 (2016) 38–43. doi:10.1002/jbio.201500192.

[310]   S.L. Jacques, Optical properties of biological tissues: A review, Phys. Med. Biol. 58 (2013). doi:10.1088/0031-9155/58/11/R37.

[311]   N. Bogdan, F. Vetrone, G.A. Ozin, J.A. Capobianco, Synthesis of ligand-free colloidally stable water dispersible brightly luminescent lanthanide-doped upconverting nanoparticles, Nano Lett. 11 (2011) 835–840. doi:10.1021/nl1041929.

[312]   M. Haase, H. Schäfer, Upconverting nanoparticles, Angew. Chemie - Int. Ed. 50 (2011) 5808–5829. doi:10.1002/anie.201005159.

[313]   S.H. Nam, Y.M. Bae, Y. Il Park, J.H. Kim, H.M. Kim, J.S. Choi, K.T. Lee, T. Hyeon, Y.D. Suh, Long-term real-time tracking of lanthanide ion doped upconverting nanoparticles in living cells, Angew. Chemie - Int. Ed. 50 (2011) 6093–6097. doi:10.1002/anie.201007979.

[314]   F.T. Rabouw, P.T. Prins, D.J. Norris, Europium-Doped NaYF4 Nanocrystals as Probes for the Electric and Magnetic Local Density of Optical States throughout the Visible Spectral Range, Nano Lett. 16 (2016) 7254–7260. doi:10.1021/acs.nanolett.6b03730.

[315]   F. He, P. Yang, D. Wang, N. Niu, S. Gai, X. Li, Self-assembled ??-NaGdF4 microcrystals: Hydrothermal synthesis, morphology evolution, and luminescence properties, Inorg. Chem. 50 (2011) 4116–4124. doi:10.1021/ic200155q.

[316]   C.T. Xu, P. Svenmarker, H. Liu, X. Wu, M.E. Messing, L.R. Wallenberg, S. Andersson-Engels, High-resolution fluorescence diffuse optical tomography developed with nonlinear upconverting nanoparticles, ACS Nano. 6 (2012) 4788–4795. doi:10.1021/nn3015807.

[317]   W. Liu, Z. Hao, L. Zhang, H. Wu, X. Zhang, Y. Luo, G. Pan, H. Zhao, Z. Fu, J. Zhang, Inhomogeneous-Broadening-Induced Intense Upconversion Luminescence in Tm3+and Yb3+Codoped Lu2O3-ZrO2Disordered Crystals, Inorg. Chem. 56 (2017). doi:10.1021/acs.inorgchem.7b01725.

[318]   Y. Zhu, W. Xu, G. Li, S. Cui, X. Liu, H. Song, Plasmonic enhancement of the upconversion fluorescence in YVO4:Yb3+, Er3+ nanocrystals based on the porous Ag film, Nanotechnology. 26 (2015). doi:10.1088/0957-4484/26/14/145602.

[319]   G. Chen, T.Y. Ohulchanskyy, R. Kumar, H. Ågren, P.N. Prasad, Ultrasmall Monodisperse NaYF 4 :Yb 3 $^{\chi}$ /Tm 3 $^{\chi}$ Nanocrystals with Enhanced Near-Infrared to Near-Infrared Upconversion Photoluminescence, ACS Nano. 4 (2010) 3163–3168. doi:10.1021/nn100457j.

[320]   G. Chen, J. Shen, T.Y. Ohulchanskyy, N.J. Patel, A. Kutikov, Z. Li, C.E.T. Al,

Nanoparticles with E ffi cient Upconversion for High-Contrast Deep Tissue Bioimaging, ACS Nano. 6 (2012) 8280–8287. doi:10.1021/nn302972r.

[321]   M. Wang, C. Mi, Y. Zhang, J. Liu, F. Li, C. Mao, S. Xu, NIR-Responsive Silica-Coated NaYbF 4 : Er / Tm / Ho Upconversion Fluorescent Nanoparticles with Tunable Emission Colors and Their Applications in Immunolabeling and Fluorescent Imaging of Cancer Cells, Society. (2009) 19021–19027.

[322]   C. Cao, H. Mi Noh, B. Kee Moon, B. Chun Choi, J. Hyun Jeong, Synthesis and optical properties of Ce3+/Tb3+ doped LaF3, KGdF4, and KYF4 nanocrystals, J. Lumin. 152 (2014) 206–209. doi:10.1016/j.jlumin.2013.10.054.

[323]   F. Wang, Y. Han, C.S. Lim, Y. Lu, J. Wang, J. Xu, H. Chen, C. Zhang, M. Hong, X. Liu, Simultaneous phase and size control of upconversion nanocrystals through lanthanide doping, Nature. 463 (2010) 1061–1065. doi:10.1038/nature08777.

[324]   B. Zhou, L. Tao, Y. Chai, S.P. Lau, Q. Zhang, Y.H. Tsang, Constructing Interfacial Energy Transfer for Photon Up- and Down-Conversion from Lanthanides in a Core– Shell Nanostructure, Angew. Chemie - Int. Ed. 55 (2016) 12356–12360. doi:10.1002/anie.201604682.

[325]   Z. Chen, Z. Liu, Y. Liu, K. Zheng, W. Qin, Controllable synthesis, upconversion luminescence, and paramagnetic properties of NaGdF 4:Yb 3+,Er 3+ microrods, J. Fluor. Chem. 144 (2012) 157–164. doi:10.1016/j.jfluchem.2012.08.009.

[326]   Y. Hou, R. Qiao, F. Fang, X. Wang, C. Dong, K. Liu, C. Liu, Z. Liu, H. Lei, F. Wang, M. Gao, NaGdF4 nanoparticle-based molecular probes for magnetic resonance imaging of intraperitoneal tumor xenografts in vivo, ACS Nano. 7 (2013) 330–338. doi:10.1021/nn304837c.

[327]   J. Key, J.F. Leary, Nanoparticles for multimodal in vivo imaging in nanomedicine, Int. J. Nanomedicine. 9 (2014) 711–726. doi:10.2147/IJN.S53717.

[328]   C. Liu, Z. Gao, J. Zeng, Y. Hou, F. Fang, Y. Li, R. Qiao, L. Shen, H. Lei, W. Yang, M. Gao, Magnetic/upconversion fluorescent NaGdF4:Yb,Er nanoparticle-based dual-modal molecular probes for imaging tiny tumors in vivo, ACS Nano. 7 (2013) 7227–7240. doi:10.1021/nn4030898.

[329]   L. Sudheendra, G.K. Das, C. Li, D. Stark, J. Cena, S. Cherry, I.M. Kennedy, NaGdF4:Eu3+nanoparticles for enhanced X-ray excited optical imaging, Chem. Mater. 26 (2014) 1881–1888. doi:10.1021/cm404044n.

[330]   J. a Damasco, G. Chen, W. Shao, H. Ågren, H. Huang, W. Song, Size-Tunable and Monodisperse Tm 3+ /Gd 3+ -Doped Hexagonal NaYbF 4 Nanoparticles with Engineered E ffi cient Near Infrared-to- Near Infrared Upconversion for In Vivo Imaging, ACS Appl. Mater. Interfaces. 6 (2015) 13884–13893. doi:10.1021/am503288d.

[331]   J.K. Cao, F.F. Hu, L.P. Chen, H. Guo, C. Duan, M. Yin, Optical thermometry based on up-conversion luminescence behavior of Er3+-doped KYb2F7nano-crystals in bulk glass      ceramics,      J.      Alloys      Compd.      693      (2017)      326–331.

doi:10.1016/j.jallcom.2016.09.163.

[332]   H.-T. Wong, F. Vetrone, R. Naccache, H.L.W. Chan, J. Hao, J.A. Capobianco, Water dispersible ultra-small multifunctional KGdF4:Tm3+, Yb3+ nanoparticles with near-infrared to near-infrared upconversion, J. Mater. Chem. 21 (2011) 16589. doi:10.1039/c1jm12796a.

[333]   D. Qin, W. Tang, Crystal structure, tunable luminescence and energy transfer properties of Na 3 La(PO 4 ) 2 :Tb 3+ ,Eu 3+ phosphors, RSC Adv. 7 (2017) 2494–2502. doi:10.1039/C6RA26164G.

[334]   R. Liu, D. Tu, Y. Liu, H. Zhu, R. Li, W. Zheng, E. Ma, X. Chen, Controlled synthesis and optical spectroscopy of lanthanide-doped KLaF4 nanocrystals, Nanoscale. 4 (2012) 4485. doi:10.1039/c2nr30794d.

[335]   Q. Zhan, H. Liu, B. Wang, Q. Wu, R. Pu, C. Zhou, B. Huang, X. Peng, H. Ågren, S. He, Achieving high-efficiency emission depletion nanoscopy by employing cross relaxation in upconversion nanoparticles, Nat. Commun. 8 (2017) 1–11. doi:10.1038/s41467-017-01141-y.

[336]   L.N. Puntus, V.F. Zolin, V.A. Kudryashova, V.I. Tsaryuk, J. Legendziewicz, P. Gawryszewska, R. Szostak, " SPECTROSCOPY OF CRYSTALS ACTIVATED Charge Transfer Bands in the Eu 3 + Luminescence Excitation, Text. 44 (2002) 1440–1444.

[337]   C. Li, Z. Quan, J. Yang, P. Yang, J. Lin, Highly uniform and monodisperse ??-NaYF4:Ln3+ (Ln = Eu, Tb, Yb/Er, and Yb/Tm) hexagonal microprism crystals: Hydrothermal synthesis and luminescent properties, Inorg. Chem. 46 (2007) 6329–6337. doi:10.1021/ic070335i.

[338]   K.N. Kumar, R. Padma, Y.C. Ratnakaram, M. Kang, Bright green emission from f-MWCNT embedded co-doped Bi 3+ + Tb 3+ :polyvinyl alcohol polymer nanocomposites for photonic applications, RSC Adv. 7 (2017) 15084–15095. doi:10.1039/C7RA01007A.